Title
Testing and analysis of structural steel columns subjected to blast loads

Permalink
https://escholarship.org/uc/item/6pw3v4gj

Author
Stewart, Lauren K.

Publication Date
2010

Peer reviewed|Thesis/dissertation

UNIVERSITY OF CALIFORNIA, SAN DIEGO

Testing and Analysis of Structural Steel Columns

Subjected to Blast Loads

A dissertation submitted in partial satisfaction of the

requirements for the degree Doctor of Philosophy

in

Structural Engineering

by

Lauren K. Stewart

Committee in charge:

        Professor Gilbert A. Hegemier, Chair
        Professor David J. Benson
        Professor Hyonny Kim
        Professor Vitali Nesterenko
        Professor Chia-Ming Uang

2010

The dissertation of Lauren K. Stewart is approved, and it is

acceptable in quality and form for publication on microfilm

and electronically:

_____

_____

_____

_____

                                                    Chair

University of California, San Diego

2010

DEDICATION

For my parents.

TABLE OF CONTENTS

LIST OF ABBREVIATIONS

ALE	Arbitrary Lagrangian Eulerian
ANFO	Ammonium Nitrate Fuel Oil
ANN	Artificial Neural Network
AMR	Adaptive Mesh Refinement
BG	Blast Generator
BG25	Blast Generator 25
BG50	Blast Generator 50
CCR	Column Capacity Ratio
CFRP	Carbon Fiber Reinforced Polymer
CMU	Concrete Masonry Unit
CTRS	Column Test Reaction Structure
DTRA	Defense Threat Reduction Agency
FE	Finite Element
FEA	Finite Element Analysis
FRM	Fast Running Model
HE	High Explosive
JWL	Jones-Wilkins-Lee
K&C	Karagozian and Case
KAFB	Kirtland Air Force Base
LMA	Levenberg-Marquardt Algorithm
SA	Strong Axis
SPH	Smooth Particle Hydrodynamics
TEMA	Tracking Eye Motion Analysis
TNT	Trinitrotoluene
UCSD	University of California, San Diego
URM	Unreinforced Masonry
WA	Weak Axis

LIST OF SYMBOLS

Lower Case Latin Characters

a Acceleration

$\bar{a}$ Activation function

b Waveform parameter

b_f Flange width

b_i Body forces in the ith direction

$\bar{b}$ Bias of neuron

c Cladding scale factor

e_{eff}^{p} Effective plastic strain

$\dot{e}_{eff}^{p}$ Effective plastic strain

e_{ij}^{p} Plastic strain tensor

e_{ij}^{p} Plastic strain rate tensor

f_c' Compressive strength of concrete

$f_i^{external}$ External forces at node i

$f_i^{internal}$ Internal forces at node i

f_1, f_2, f_3 Functions of cap model surfaces

f_o Initial yield surface

i Input number

i_r Reflected impulse

i_s Specific impulse

$i_{s,n}$ Specific impulse of nth BG

k von Mises yield surface constant

m Mass

m_1 Mass of impactor 1

m_2	Mass of impactor 2
m_n	Mass of nth BG
n	Number of BG
n_j	Normal vector in the j direction
n_p	Number of parameters
p	Pressure
p_o	Ambient air pressure
p_r	Peak reflected pressure
p_{so}	Peak static overpressure
t	Time
t_a	Time of arrival
t_f	Flange thickness
t_w	Web thickness
u_i	Displacement in the ith direction
$\bar{u}_i^o$	Initial displacement condition
v	Velocity
$\bar{v}_i^o$	Initial velocity condition
v_n	Velocity of nth BG
v_1	Velocity of impactor 1
v_2	Velocity of impactor 2
w	Weight per unit length
w	Weight of input i
x	Position
x_i	i^{th} input (or parameter)

Upper Case Latin Characters

$A_{n,eff}$ Effective area of nth BG

$C_{r\alpha}$ Reflection coefficient

D_i Detonation velocity

F Force

J_1 First invariant of the deviatoric stress tensor

J_2 Second invariant of the deviatoric stress tensor

L Length of column

L_n Tributary impact length of nth BG

M_{AB} Mass tensor

M_{AB}^{diag} Diagonal Mass tensor

M_{eq} Equivalent mass

$M_{n,eff}$ Effective mass of nth BG

N Number of elements

Q_{EXP} Specific energy of explosive

Q_d Heat of detonation

Q_{TNT} Specific energy of TNT

R Standoff distance

R_c Resistance of column

R_{clear} Equivalent standoff for clearing effects

$R_{cladding}$ Equivalent standoff for cladding effects

R_{eff} Effective standoff distance

R_{req} Required standoff distance

S_o Number of initial samples

T_{mises} Tension from Mises yield surface

T_n Duration of negative phase

T_p	Duration of positive phase
U	Wavefront velocity
W	Charge weight
W_{eff}	Effective explosive weight
W_{EXP}	Weight of explosive
W_{req}	Explosive weight required
W_{TNT}	Weight of TNT
Z	Scaled distance
Z_{clear}	Equivalent scaled distance for clearing effects

Greek Characters

α	Angle of incidence
$\alpha_c, \beta_c, \gamma_c, \theta_c$	Parameters for cap model
β	Parameter for strain rate effects
ε	Strain
η	Number of surface intersections
κ	Hardening parameter for cap model
λ	Hardening parameter for von Mises
ρ	Density
ρ_{max}	Explosive Density
σ_{ij}	Stress tensor
σ'_{ij}	Deviatoric stress tensor
σ_y	Yield stress
σ_1	Stress in the first principal direction
Δ	Displacement of mass
Δt	Timestep
Φ	Shape Function

Γ_u Domain of prescribed displacement

Γ_u Domain of prescribed traction

Λ Multiplier

Ω Continuum domain

LIST OF FIGURES

LIST OF TABLES

ACKNOWLEDGMENTS

Having spent a full decade of my life at UCSD, I have truly learned the significance of hard work and dedication. And, more than that, I have learned the importance of the support of others. This dissertation would in no way have been possible without the guidance, motivation and love from so many important people in my life. To all of you, I will forever be grateful and I owe a part of this accomplishment to each of you.

I would like to thank my advisor, Gil Hegemier, for giving me the opportunity, guidance, and motivation that I needed to conduct this research. Although I may have heard "*we gotta get you out, kiddo*" for one too many years, I am thankful for the experience that he afforded me at UCSD. In his own way, he pushed me to learn on my own and ultimately be respected in this field and that was worth every minute.

I would also like to thank the other members of my committee, Professor David Benson, Professor Hyonny Kim, Professor Vitali Nesterenko, and Professor Chia-Ming Uang for their time, comments and encouragement through this process.

This research would not have been possible without the help of many of others connected to this project. Dr. Karen Arnett provided organization, reason and calm and I don't know what we would have done without her. The staff at the Englekirk Center allowed me to conduct my tests and frankly did all my dirty work on a daily basis. To Dan, Steve, Darren, Alex, Lonnie, Mike, RC, Robert, Andy and Larry: Thank you guys, I truly enjoyed working with all of you.

I would also like to thank the employees of Karagozian & Case for their help and guidance over the last five years. I would especially like to thank Joe Magallanes, Simon Fu, and Youcai Wu for their dedication specifically during the crunch time. I also owe a great deal of gratitude (and my sanity) to Ken Morrill. He provided me with an indescribable amount of motivation, direction and compassion and words can't describe how appreciative I am for all of that.

Appreciation must also be given to my fellow graduate students, only they truly identified with the challenges I faced. I hope I was able to provide them support as well. I would particularly like to thank Corey Love, Gillian Cutter, Anna Lang and Don Phillippi for their friendship and listening ear when I needed it.

I could not group the next two people in the classmate category because I really consider them both to be family. This experience allowed me to gain two brothers, one older and one younger…and they both definitely fit into those roles. Mike Oesterle, along with being a great friend, provided me with so much knowledge and was always willing to help. He became someone that I could count on to watch out for me and always had the time to listen. I owe a great deal to Peter Huson as well. To Peter: I can't really find the words to describe how grateful I am for your friendship, advice, help, thoughtfulness and silliness. I want you to know how proud I am of you and that I really do believe that you got me through this.

In addition to my friends in the department, I must also thank my friends and family. Even with my crazy schedule, work ramblings, constant stress and bad moods, Rachel Wood, Mandy Beeler and Danielle Stephens loved me anyways. I now understand the meaning of best friends.

Finally, I would be nothing if not for the support of my family. Mom, Dad and Leigh: Thank you all so much for your constant love and support. Thank you for understanding the importance of this and thank you for giving me the drive to accomplish it. I hope I made you proud.

VITA

<u>Education</u>

2004   Bachelor of Science, Structural Engineering
University of California, San Diego

2006   Master of Science, Structural Engineering
University of California, San Diego

2010   Doctor of Philosophy, Structural Engineering
University of California, San Diego

<u>Experience</u>

2001   Laboratory Intern, Orbital Sciences Corporation, Pomona, CA

2002   Engineering Intern, Metropolitan Transit Board, San Diego, CA

2003   Research Intern, Pacific Earthquake Engineering Research Center,
Berkeley, CA

2004-2007   Teaching Assistant, University of California, San Diego, La Jolla, CA

2006-2010   Graduate Student Researcher, University of California, San Diego, La
Jolla, CA

2007-2009   Instructor, University of California, San Diego, La Jolla, CA

2007-Present Senior Engineer, Karagozian & Case, Burbank, CA

<u>Publications</u>

P. Krysl, W. T. Ramroth, L. K. Stewart, and R. J. Asaro. "Finite Element Modeling of Fiber Reinforced Polymer Sandwich Panels Exposed to Heat." *International Journal for Numerical Methods in Engineering* 2004; Volume 61: pp 49-68.

L.K. Stewart, G.A. Hegemier and K.B. Morrill. "Blast Simulator Testing of Steel Columns and Components." *Proceedings of the 80th Annual Shock and Vibration Symposium*. San Diego, CA. Oct. 2009.

L.K. Stewart, G.A. Hegemier and K.B. Morrill. "Simulated Blast Testing of Structural Steel Columns." *8th International Conference on Shock and Impact Loads on Structures.* Adelaide, Australia. Dec. 2010.

P.N. Huson, L.K. Stewart, R.J. Asaro and G.A. Hegemier. "Laboratory Techniques for Blast Loading of Structures with Complex Geometries." *8th International Conference on Shock and Impact Loads on Structures.* Adelaide, Australia. Dec. 2010.

Awards

2004-2007   National Defense Science and Engineering Graduate Fellow

ABSTRACT OF THE DISSERTATION

Testing and Analysis of Structural Steel Columns
Subjected to Blast Loads

by

Lauren K. Stewart

Doctor of Philosophy in Structural Engineering

University of California, San Diego, 2010

Professor Gilbert A. Hegemier, Chair

Extreme loading conditions generated by blasts that result from terrorist attacks can cause devastating consequences for structures and their occupants. In steel frame structures, the damage and failure of a structural column from a blast load can result in a progressive collapse and catastrophic failure of the entire structure. The objectives of this dissertation were to develop experimental methodologies, analysis strategies and threat assessment tools that can be used to mitigate blast hazards and predict damage in structural steel frame structures.

Typically, guidelines and methodologies are developed from conclusions drawn via field testing with live explosives, but due to the harsh environment created by explosives, collecting reliable data is problematic. In an effort to provide key answers to questions related to how structures behave during these types of explosions, the University of California, San Diego Blast Simulator was developed. The Blast Simulator consists of ultra-high speed actuators that accelerate/decelerate impacting modules toward the specimen in a controlled manner. Utilizing the transfer of momentum and energy of masses at high velocities, blast-like loads are applied to the structure without the use of explosive materials. Since no fireball is generated, specimen behavior can be observed for the full duration of the loading using high-speed photography.

For this dissertation, experiments were conducted with the Blast Simulator to study the effects of impulsive loading on typical steel W-Shapes. The objectives of the dissertation were met through an experimental and computational effort that included the characterization of column behavior, development of a testing protocol for loading of columns in both weak and strong axis directions, validation and implementation of numerical models to predict loads delivered to specimens as well as column behavior and generation of relations pertaining to Simulator operation.

Finally, the validated finite element models were incorporated into the development of a fast running, threat assessment tool using an artificial neural network that can predict the residual capacity of a blast damaged column. The fast running model allows for the analysis of steel structures in situations where a time consuming computational model may not be efficient.

1 Introduction

The extreme loading conditions generated by blasts that result from terrorist incidents can cause devastating consequences for structures and their occupants. In recent years, the United States has suffered significant attacks against its structures, both foreign and domestically, in the form of vehicle bombs, which has motivated the necessity for designing and analyzing structures to withstand these types of attacks. Typically, the development of such methodologies is driven by conclusions that have been obtained via field tests. Unfortunately, due to the harsh environment created by explosives, characterizing behaviors of structural components and collecting reliable data during a field blast event is problematic.

In an effort to provide answers to key questions related to how structures behave during a blast event and assuage the difficulty of producing high quality data, the University of California, San Diego (UCSD) Blast Simulator was developed. Utilizing the transfer of momentum and energy of masses at high velocities, blast-like loads can be applied to the structure without the use of explosive materials. The Blast Simulator

1

consists of ultra-high speed actuators that accelerate/decelerate impacting modules toward the specimen in a controlled manner. It is able to deliver a blast-like pressure pulse to the specimen, which can be recorded using high-speed photography since there is no fireball. Additionally, the Simulator is advantageous because it is capable of replicating experiments in a controlled environment with much less preparation and time than is involved in a field test.

To date, the Blast Simulator has been used to generate high-fidelity data, concerning the response of a variety of critical infrastructure elements, such as concrete columns, masonry walls and naval structures, subjected to blast loads. The objective of this dissertation is to develop experimental methodologies using the UCSD Blast Simulator to provide data for use in the development of analysis strategies and threat assessment tools that can be used to mitigate blast hazards and predict damage in structural steel frame structures.

In steel structures, the damage and loss of a structural column from a blast load could result in a progressive collapse and catastrophic failure of the entire structural system if the forces can not be redistributed around the column. Additionally, connections and other components may be damaged and the alternate force path may be severed leaving the column to carry the full load. Characterizing the capacity of the column is critical in the assessment of the structure as a whole and is the focus of this dissertation which has the following overall objectives:

- Provide methodologies and guidelines for performing experiments on steel columns oriented in the strong axis direction using the UCSD Blast Simulator.

- Develop a testing method for loading columns in the weak axis direction including the use of a loading medium to load structures with non-flat geometries.

- Validate the use of the UCSD Blast Simulator through comparisons of Simulator tests and field tests for columns in both the strong and the weak axis direction.

- Calibrate and validate numerical models to aid in the study of steel column testing with the Blast Simulator.

- Investigate the effects of unsynchronized impacts for tests with variable impact velocities.

- Develop relations for using momentum and energy to predict the behavior of columns when subjected to Blast Simulator loading.

- Generate methodologies for applying blast loads to columns in finite element models.

- Outline a testing protocol for application into future Blast Simulator steel column tests.

- Generate a fast running model for threat assessments to calculate the residual capacity of columns subjected to blast loads.

The dissertation is divided into nine chapters. Chapter 2 provides the background information related to this research. This includes an overview of blast loading environments including conventional methods for describing pressure and impulse. Next, a discussion of previous research is provided including a discussion of relevant steel column field tests. Also included is a description of the UCSD Blast Simulator and

examples of Simulator experiments. Finally, a summary of the numerical methods and material models used in the finite element modeling is presented.

Chapter 3 presents the experimental design and results from six full-scale steel column specimens tested in the UCSD Blast Simulator. It provides a full description of the testing setup, instrumentation and data analysis methodologies that were used throughout the tests. Additionally, Chapter 3 serves to provide a validation for using the Simulator for testing steel columns in the strong axis direction by comparing the tests to similar field tests.

Included in Chapter 4 is the development of a finite element model for the strong axis steel column tests described in Chapter 3. The chapter includes a thorough discussion of the material models, mesh and loading methods used in the model. Additionally, the model was calibrated and validated with the results from the experiments.

Similar to the information in Chapter 3, Chapter 5 provides the experimental design and results from the full-scale steel column tests oriented in the weak axis direction. Due to the application of pressure loads on the web and the flanges, a technique for using a loading medium to impact non-flat geometries is included along with relevant testing methodologies. Chapter 5 also functions to provide a validation for using the Simulator for these types of tests by evaluating the specimens against relevant field test specimens.

Chapter 6 gives an explanation of the finite element model development used for analyzing columns in the weak axis direction. In addition to discussing the material models and appropriate modeling configurations, the chapter includes an explanation of

the use of Smooth Particle Hydrodynamics (SPH) to model the loading medium. Finally, a brief introduction to modeling fracture of the web is included along with a summary of current and future research related to this area.

Chapter 7 serves to answer key questions related to Simulator testing and finite element analysis of steel columns in the form of numerical investigations. These investigations include an analysis of the effects of impact synchronicity on the behavior of the specimen and the effects of impactor mass and velocity as they pertain to momentum, energy and impulse. This chapter also addresses methods for applying explosive blast loads to finite element models. Additionally, Chapter 7 uses the findings from the investigations to develop and outline a loading protocol for testing steel columns with the Blast Simulator.

The information from the previous chapters was utilized in Chapter 8 to create a fast running model that was developed using an artificial neural network to predict the residual capacity of a blast damaged column. The fast running model allows for the analysis of steel structures in environments where a time consuming computational model may not be efficient. Validated finite element models were used to train the predictive model and the model was verified with a variety of test cases. A threat assessment example is included along with a discussion on future applications and modifications for the model.

The ninth and final chapter concludes the dissertation with a summary and recommendations for future research. Appendices are included at the end of the document and provide additional information that was not incorporated in the main body of the text.

2 Background

This chapter provides the fundamental background information for this dissertation. First, an introduction to explosives is given which includes a description of the explosive process and airblast characteristics pertaining to specific explosive environments. Next, a discussion of previous research is presented, including a summary of relevant field testing. The following section includes background information for simulating blast loads, specifically, an explanation of the UCSD Blast Simulator and previous Simulator research. Finally, a brief presentation of the relevant material models and numerical methods used in this dissertation is provided.

2.1 Fundamentals of Explosives

This section describes details pertaining to high explosives (HE), including a discussion of the process of explosions, descriptions of types of explosives and a background into the characteristics and parameters that describe an airblast environment including air bursts and surface bursts.

2.1.1 Explosive Process & Generation of Blast Waves

The development of blast waves in air from condensed high explosives can be summarized with the following sequence of events [1, 2]. First, the detonation of the explosion is initiated and the explosive reaction generates high temperature and high pressure gases. The gases expand at a rapid rate and push the surrounding air out of the volume it occupies. The air that has been pushed out is now compressed to form a blast wave which contains most of the energy in the explosion. As the gases expand, the pressure drops and forces the blast wave outwards from the detonation source. The blast wave moves from the source and its pressure also decreases. Eventually, as the explosive gases expand, they cool and drop slightly below atmospheric pressure. This drop below atmospheric pressure is due to the gas molecules having a momentum when the pressure returns to atmospheric generating a negative pressure that reverses the direction back toward the source. Equilibrium is then reached once the air and gases that have been pushed away from the source return.

2.1.2 Types of Explosives

Explosives are typically classified into three categories depending on how difficult it is to initiate the explosive reaction. As described in Krauthammer [3], the first type is a primary explosive which is very sensitive to shock or heat and is very easy to ignite or detonate. Some examples of primary explosives are Mercury fulminate, Lead azide and Silver azide. Secondary explosives are less sensitive than primary explosives, but are still volatile. Because they are relatively stable, they are often used in industrial and automotive applications. Nitroglycerine, Nitromethane and Trinitrotoluene (TNT) are

examples of secondary explosives. Explosives in the final class of explosives are called

tertiary explosives. They need significant initiation for an explosive reaction. Ammonium

nitrate when mixed with fuel oil (ANFO) is a common example of a tertiary explosive.

Table 2.1 gives a summary of characteristics for typical explosives including the

explosive density, ρ_{max}, the detonation velocity, D_i, and the heat of detonation, Q_d.

Table 2.1: Properties of Typical Explosives, reproduced from [3]

Explosive	ρ_{max} (g/cm^3)	D_i at ρ_{max} (km/sec)	Q_d (kJ/g)
Composition C-4	1.59	8.04	5.86
Nitroglycerin	1.60	7.58	6.30
Nitromethane	1.13	6.29	6.40
Nitrocellulose	1.66	7.30	10.60
PETN	1.77	7.98-8.26	6.12-6.32
RDX	1.76-1.80	8.7-8.75	5.13-6.19
TNT	1.64	6.95	4.10-4.55

2.2   Airblast Characteristics

This section describes the environment and parameters that describe an airblast

and how those parameters vary with respect to its environment. For this research, two

types of unconfined airblast geometry will be considered: air burst and surface burst.

2.2.1 Air Burst Explosions

The simplest type of free air burst environment is one in which the explosive

detonates in free air and is remote from any reflecting surface. The shock wave is not

reflected or amplified off the structure or ground. Figure 2.1 describes the geometry of a

free air burst. The charge is represented by the red sphere and the point of interest where

parameters are described is represented by the blue diamond. In this situation, the charge

detonates and the shock waves travels to the point of interest without interference from the structure or the ground.
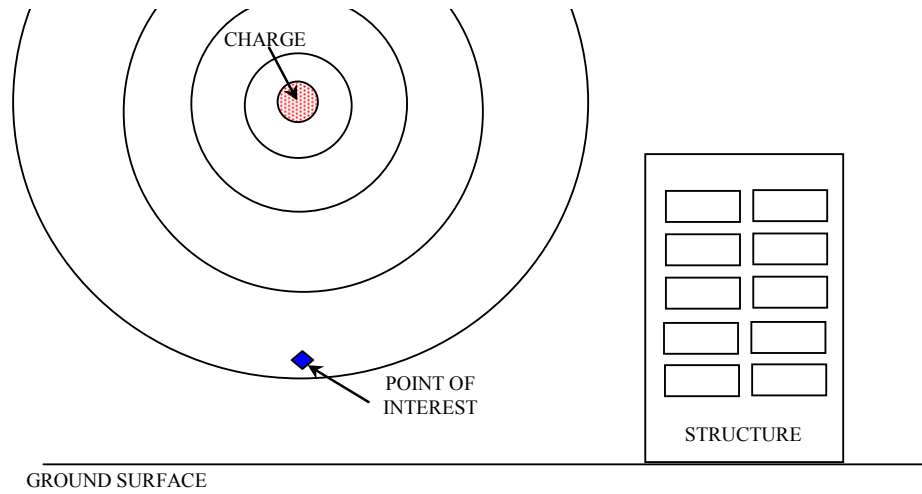
Figure 2.1: Free Air Burst Geometry
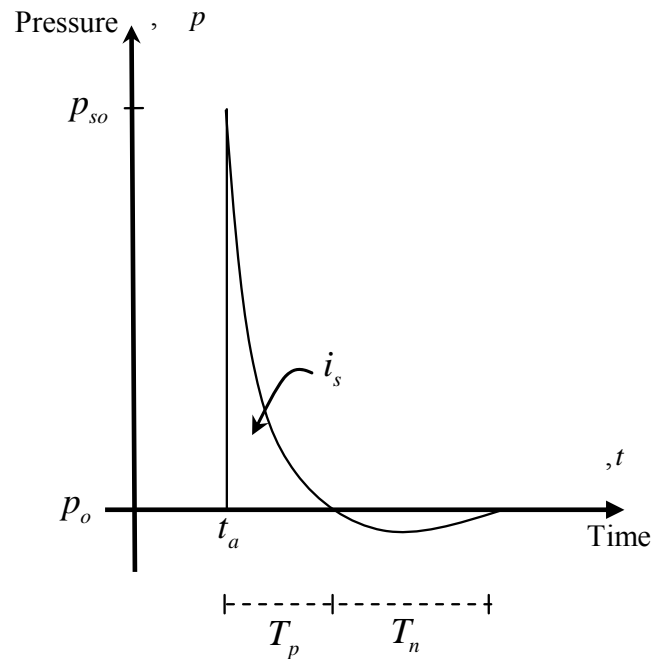
Figure 2.2: Pressure-Time History for a Blast Wave in Free Air

The general shape of a pressure-time history for a blast wave in free air without reflections is shown in Figure 2.2. In the figure, p_{so}, is the peak static overpressure at the shock front and p_o is the ambient air pressure. The time of arrival, t_a, is the time at which the shock front arrives at the target. The duration of the positive phase, T_p, is the time in which the pressure is above ambient. Similarly, the duration of the negative phase, T_n, is the time in which the pressure is below ambient.

In addition to pressure, specific impulse, i_s, is also an important blast wave parameter. Specific impulse, which from herein will be referred to as impulse, is the area under the pressure-time curve from arrival time to the end of the positive phase as given by

$$i_s = \int_{t_a}^{t_a+T_p} p(t)dt \qquad (2.1)$$

The pressure-time history is often described by an exponential function such as that given by the Friedlander equation which is shown in Equation (2.2). In the equation, b is the waveform parameter.

$$p(t) = p_{so}\left[1 - \frac{t}{T_p}\right]exp\left(-\frac{bt}{T_p}\right) \qquad (2.2)$$

Often times, linear approximations are satisfactory for representing the pressure-time history. As described in Mays and Smith [1], many methods are available for using a linear decay and two examples are shown in Figure 2.3. Method I involves a linear decay from the point of maximum pressure to the point at which the pressure goes below ambient. Method II equates the areas under the curves so that the impulse of the linear approximate is the same as that of the exponential description.
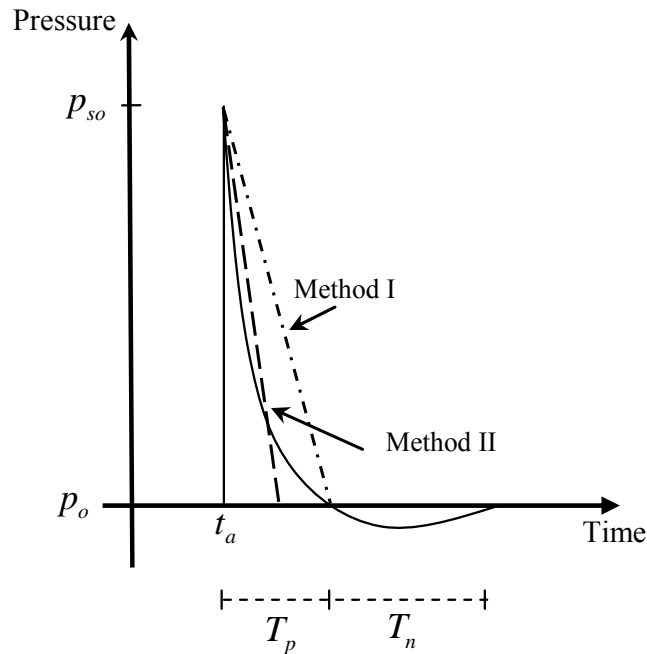
Figure 2.3: Idealization of Pressure-Time Profile

Because HEs produce different magnitudes of peak pressure, heat production and other parameters, a basis for comparison between the different explosives is needed. The universally accepted method is to use TNT as the reference explosive. The most common method of converting an explosive weight, W_{EXP}, to that of a TNT equivalent weight, $W_{TNT_{eq}}$, is to scale the mass of the explosive by a conversion factor that is calculated using the specific energy of the explosive, Q_{EXP}, to that of the specific energy of TNT, Q_{TNT}, as shown in Equation (2.3). Table 2.2 gives conversion factors for typical explosives which was reproduced from Smith and Mays [1].

$$W_{TNT_{eq}} = \frac{Q_{EXP}}{Q_{TNT}} W_{EXP} \qquad\qquad (2.3)$$

Table 2.2: Conversion Factors for Typical Explosives

Explosive	Mass Specific Energy Q_{EXP} (J/kg)	TNT Equivalent (Q_{EXP} / Q_{TNT})
Composition B	5.19	1.15
HMX	5.68	1.26
Nitroglycerin	6.70	1.48
Nitrocellulose	4.52	1.00
RDX	5.36	1.185
TNT	6.70	1.00
ANFO		0.82

Often times it is necessary to compare parameters of the same explosive type but with different masses (charge size) and distance away from point of interest (standoff). To do this, a cube root scale law formulated by Hopkinson [4] and Cranz [5] is often applied such that

$$\frac{R_1}{R_2} = \left(\frac{W_1}{W_2}\right)^{1/3}$$

(2.4)

where R_1 is the distance to the charge having equivalent TNT weight of W_1 and, similarly, R_2 and W_2 are the distance and equivalent TNT charge weight of another charge. The scaled distance, Z, is given by

$$Z \equiv \frac{R}{W^{1/3}}$$

(2.5)

Scaled distance is often used to present blast wave data and comparisons for a wide range of explosive environments. It should be noted that cube root scaling is used for spherical charges and if a charge is cylindrical and close-in, then square root scaling is more appropriate. For the purposes of this research, all charges will be assumed to be spherical, unless noted otherwise.

Graphical methods are frequently used to determine the values of blast parameters. Multiple sources, including [6], provide plots of blast parameters versus scaled distance, Z. Figure 2.4 gives one such plot that includes relations for peak static overpressure, p_{so}, specific impulse, i_s, time of arrival, t_a, and positive phase duration, T_p, which were shown in Figure 2.2. Also included in the plot is the relation for blast wavefront velocity, U.
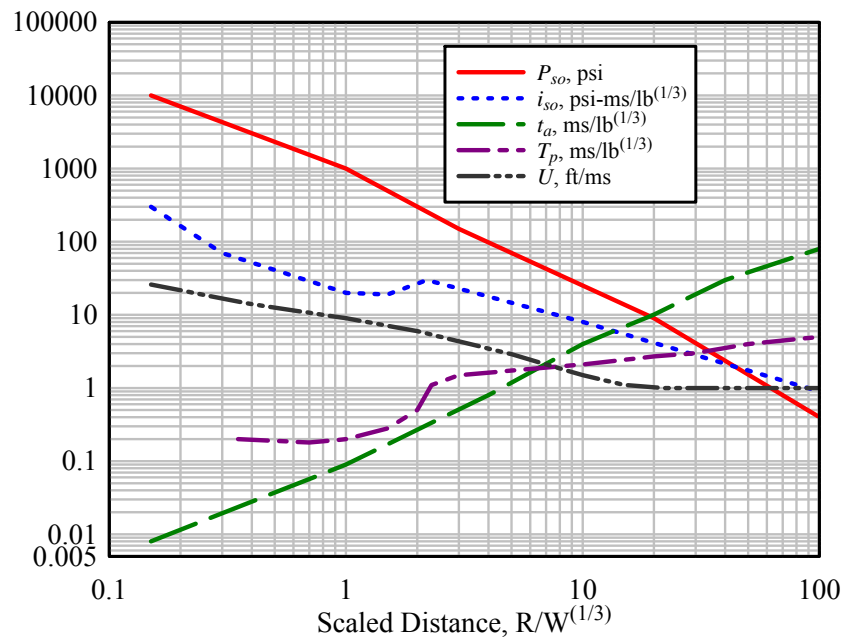
Figure 2.4: Blast Parameters for Spherical Explosions in Free Air, reproduced from [6]

Another common blast environment is that shown in Figure 2.5 which includes a charge in free air and has shock waves that travel toward the structure and towards the ground. There are two scenarios associated with this type of environment. The first is shown in where the angle of incidence, α, is between $0°$ and $40°$. In this situation, the

shock wave travels and impacts the structure before any reflections from the ground can interact with it.
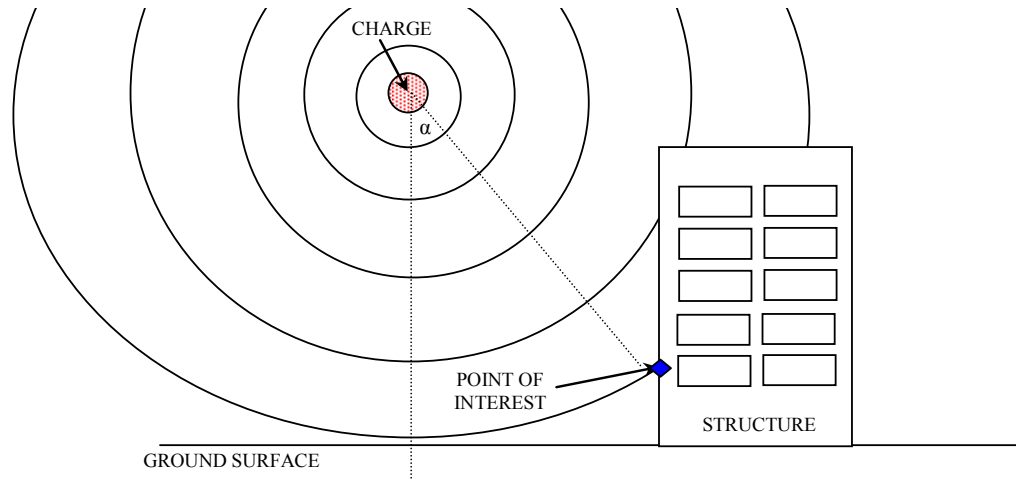
Figure 2.5: Air Blast Environment with Structural Interaction

As discussed in [1], when the wave hits the structure, it undergoes reflection when the forward moving air molecules in the blast wave are brought to rest and further compressed, inducing a reflected overpressure on the structure. The reflected overpressure, therefore, is of higher magnitude than that of the incident overpressure. An example of a typical reflected pressure-time history is shown in Figure 2.6, where p_r is the peak reflected overpressure.

The values of p_r and the corresponding impulse, i_r, can be found in many different ways. Rankine and Hugoniot [7] derived an equation for reflected overpressure in terms of peak static overpressure, p_{so}. This relation for a charge in air when the angle of incidence is zero is given in Equation (2.6).

$$p_r = 2p_{so} \left[\frac{7p_o + 4p_{so}}{7p_o + p_{so}} \right] \qquad (2.6)$$

Graphical methods are also available for determining the reflected blast parameters similar to those available for determining the incident parameters. Figure 2.7, reproduced from [6], shows peak reflected overpressure, p_r, and reflected impulse, i_r, in terms of scaled distance, Z. This graph can be used directly if the angle of incidence is zero.

If the angle of incidence is greater than zero but less than $40°$, the reflected peak overpressure can be calculated as follows

$$p_r = C_{r\alpha} \cdot p_{so} \tag{2.7}$$

where $C_{r\alpha}$ is the reflection coefficient and can be determined from Figure 2.8. The value for peak static overpressure, p_{so}, can be determined using the methods described earlier and Figure 2.4.
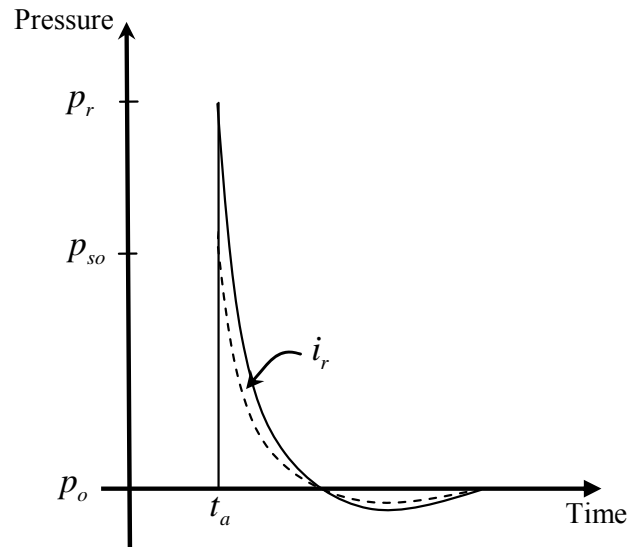
Figure 2.6: Typical Reflected Pressure-Time History
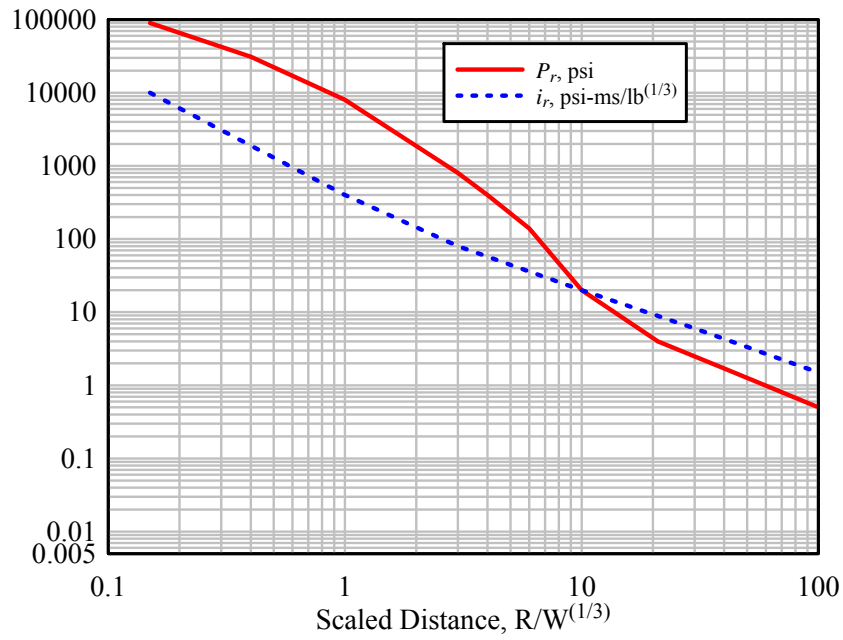
Figure 2.7: Reflected Blast Parameters, reproduced from [6]
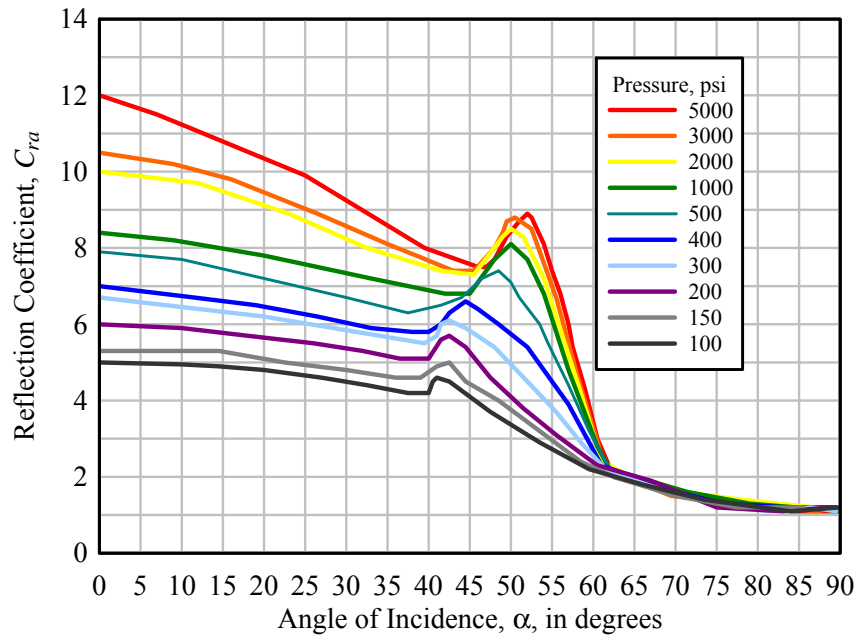
Figure 2.8: Reflected Pressure Coefficients, reproduced from [6]

The second scenario is associated with an environment in which both structural and ground interactions affect the resultant blast wave characteristics as shown in Figure 2.9; here the angle of incidence, α, is greater than $40°$. In this case, the shock wave reflects off the ground and has time to interact with the wave traveling toward the structure. This process is called Mach reflection and the resultant shock front created is known as the Mach front.

The point at which the incident wave, the reflected wave and the Mach front interact is called the triple point. For design purposes to date, it has been assumed that the Mach front is a plane wave with a uniform pressure distribution and that the magnitude of pressure is the same as that of the incident wave. Also, it is often assumed that the structure is affected solely by the Mach front. Both assumptions can produce results that do not correctly define the complex process of Mach reflection and because of this, advanced numerical simulations to calculate blast parameters will be conducted for this research.
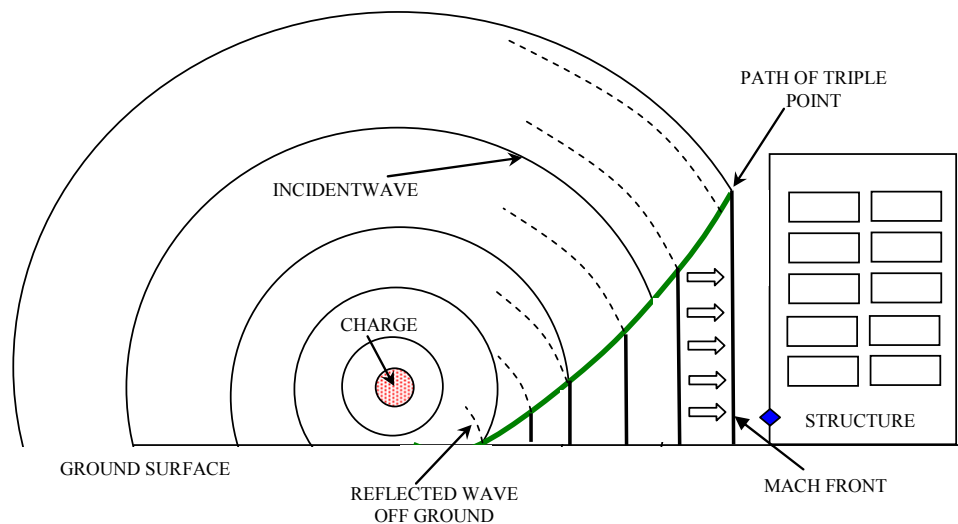
Figure 2.9: Air Burst Environment with Mach Reflection

2.2.2 Surface Burst Explosions

In a surface burst, the explosive is situated near the ground and after detonation the shock wave immediately reflects off the ground and merges with the incident wave. This produces a hemispherical blast wave that travels outward from the charge toward the structure as shown in Figure 2.10.
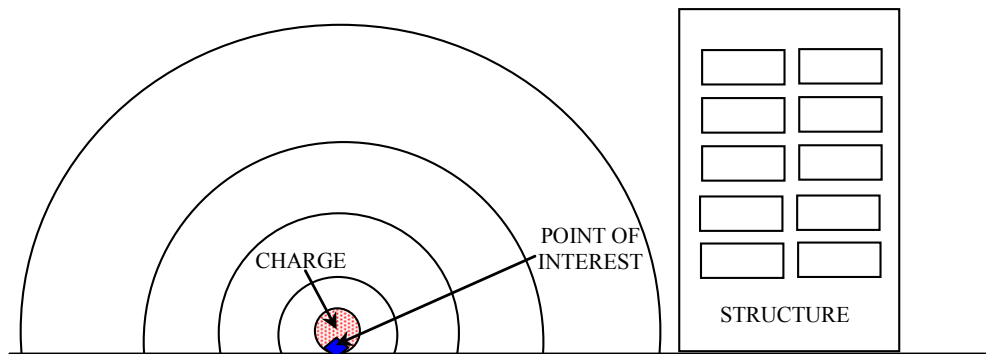
Figure 2.10: Surface Burst Environment

Mays [1] describes that there is good correlation for hemispherical bursts with free air burst data if an implication factor of 1.8 is assumed. According to Mays, surface air bursts produce blast waves that appear to come from free air bursts of 1.8 times the actual energy source. Another method for calculating blast parameters of surface bursts is similar to that described in the previous section. Army Technical Manual [6] gives a graphical procedure relating the blast parameters to scaled distance. The plot for this method is shown in Figure 2.11.
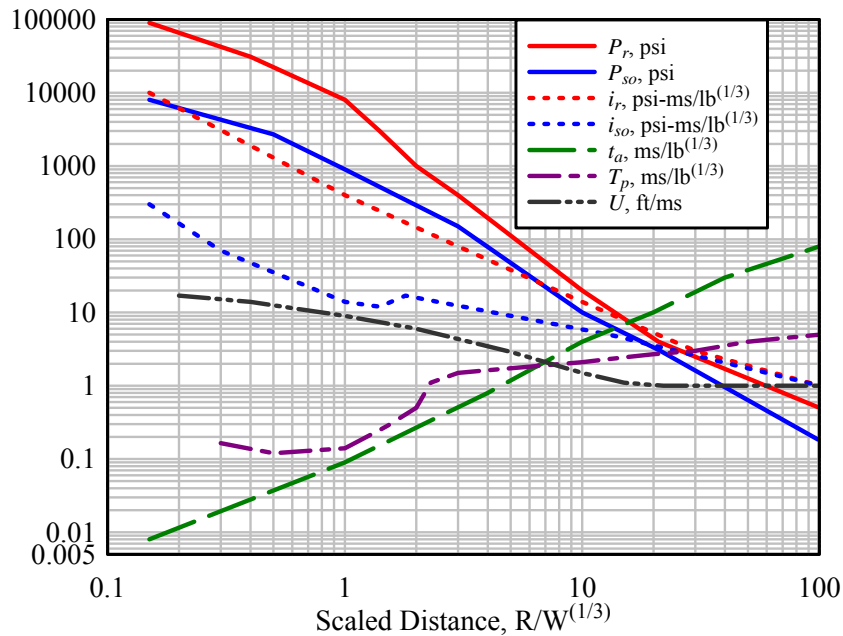
Figure 2.11: Blast Parameters for Surface Bursts, reproduced from [6]

2.3 Relevant Field Testing

This section discusses previous field research conducted on topics related to this dissertation. Specifically, two tests series are included in this section. The first set of experiments investigated the behavior of steel columns as part of a testing program by the Defense Threat Reduction Agency (DTRA). The second series of tests was also funded by DTRA, but this set looked at steel columns and beam/column connections. Due to the subject of these tests, charge sizes and standoffs have been omitted.

2.3.1 DTRA Phase I

The Defense Threat Reduction Agency initiated a test program in 2005 to study the response of steel structures to blast loadings. This study focused on steel columns and the components associated with these columns. The components included base plate

connections, column-to-beam connections and cladding. The objective for these tests was to determine what types of columns and connections were vulnerable to typical vehicle bomb attacks. This study used common connections as well as those that have been developed for seismic applications to determine their effectiveness against blast loadings.

The first phase of this program was designed to study the response of columns and base plate connections only. These tests were conducted in the Column Test Reaction Structure (CTRS), shown in Figure 2.12, at the Chestnut Test Site on Kirtland Air Force Base (KAFB), between November 18, 2004 and March 9, 2005.
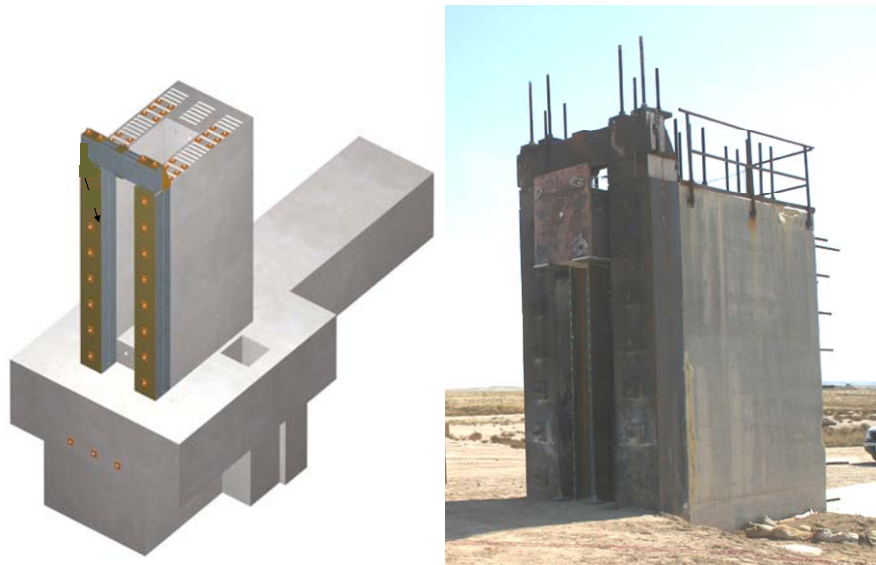
Figure 2.12: Diagram and Photo of the Column Test Reaction Structure (CTRS)

In each Phase I test, the full-scale steel column W-Shape specimen was placed into the reaction structure oriented for either a strong or a weak axis impact (Figure 2.13). The base was fixed to a baseplate and the header was connected to a steel strut system and tensioned into place with four 100-kip jacks. For three of the tests, a piece of 4 in concrete cladding was placed in front of the column which is shown in Figure 2.14. A

cylindrical ANFO charge was placed at a given standoff distance. A 100 kip axial load was placed on the specimen prior to the test. The column was instrumented with accelerometers and pressure gauges and displacements were measured after the test. A 270 kip axial load was placed on the column after each test to determine if it could carry the design capacity.

Figure 2.13: Strong Axis (left) and Weak Axis (right) Orientation

Figure 2.14: Field Tests, Phase I With (left) and Without (right) Concrete Cladding

Table 2.3 summarizes the test matrix for the six tests performed for this phase. The first five tests were performed to support the DTRA steel structures program. Test 6 was a scaled seismic section and falls out of the scope for this dissertation.

Table 2.3: Field Tests, Phase I Test Matrix

Test #	Base Plate Type	Column	Cladding	Scaled Distance, Z
1	4-bolt, 1" thick plate (A572 Gr. 50)	W14x132, A992 Gr. 50 (Weak Axis)	N/A	1.77
2	6-bolt, 1" thick plate, rebar bent over top of base plate (A572 Gr. 50)	W14x132, A992 Gr. 50 (Weak Axis)	N/A	1.15
3	Column embedded into 36x36x21" concrete base	W14x132, A992 Gr. 50 (Weak Axis)	54x126x4" concrete cladding placed in front of column	1.15
4	6-bolt, 1" thick plate, rebar bent over top of base plate (A572 Gr. 50)	W14x132, A992 Gr. 50 (Weak Axis)	54x126x4" concrete cladding placed in front of column	0.88
5	Column embedded into 36x36x21" concrete base	W14x132, A992 Gr. 50 (Strong Axis)	54x126x4" concrete cladding placed in front of column	0.88

Results and conclusions can be summarized as follows: The Test 1 event was performed using a W14x132 column with weak axis of the column facing the blast. The scaled distance was 1.77. A simple base plate connection was used in this event. Results from this event showed that very little damage occurred to the column. A permanent displacement of 1.02 in was measured after the event. The permanent displacement of the web of the column was slightly larger than that of the flanges up to the height of 5 feet. Above this height, the web and flanges had all displaced the same. No damage occurred to the base plate connection in this event.

Test 2 was a repeat of Test 1 except that the scaled distance was 1.15. This difference in standoff resulted in a larger blast loading on the column and increased the damage that the column experienced. The permanent displacement of the column flanges in this event was 2.70 in. The web experienced larger displacements than the flanges.

Even though the damage to the column was larger than the previous test, a failure to the column did not occur.

Test 3 was a repeat of the Test 2 event except that a 4-inch thick reinforced concrete cladding was placed in front of the column. Inclusion of the cladding increased the overall load applied to the test column. The results from this event showed that the overall permanent displacement of the column was 4.59 in at the column mid-height. The web had very little relative displacement with respect to the flanges. Even with the increased overall column displacement, this column was still capable of withstanding large axial loads.

Test 4 was a repeat of the Test 3 event except that the scaled distance was reduced to 0.88 to increase the loads applied to the column. The results from this test showed that the increased loading increased the permanent column displacement of the flanges to 6.56 in. The web displacement at the column mid-height was 0.5 inches more than the flanges.

The Test 5 event was a repeat of the Test 4 event except that the column orientation was rotated 90° so that the strong axis of the column was facing the blast. The results from this event showed that the maximum permanent displacement of the column along the centerline of the outer flange (directly in-line with the web) was 4.73 in at the height of 4 feet above the ground surface. The edges of the front flanges were deformed inward more than at the centerline due to the presence of the column web. The maximum displacement of the west flange was 6.98 in, and the east flange maximum was 7.4 in. Both of these maximums occurred at the height of 2.5 feet above the ground surface. Deformation of the front flanges was caused by the loads applied to them from the concrete cladding. Above the column height of 8 feet, the flanges were not deformed with

respect to the remainder of the column. This event demonstrated that, as expected, the strong axis orientation sustained less deformation than the weak axis orientation.

Overall, these tests demonstrated that the steel columns did not fail when subjected to the blast load created by the detonation of a charge with multiple scaled distances. The inclusion of cladding created more overall displacement of the column, but less deformation of the web with respect to the flanges and less rotation of the flanges (Figure 2.15). These results also demonstrated that steel columns can sustain large deformations without a failure in the steel. All of the columns in these events were able to sustain a 270-kip axial load after the tests.

Figure 2.15: Comparison of Tests With (left) and Without (right) Cladding

In the second phase of the DTRA program, Phase II, another set of six tests were conducted to study columns and connections. The tests were conducted in the CTRS between August 17, 2005 and December 15, 2005. The test columns on Tests 7-12 were fabricated using W10x49 wide flange members, and the beams connected to the columns were W16x26 wide flange members. The test setup is given in Figure 2.16.

Table 2.4 provides a summary of the test matrix for Phase II. Three different connection designs were tested: strong axis shear tab connection (Test 7 and Test 8), weak axis shear tab connection (Test 9 and Test 10), and strong axis bolted shear tab connection with wind moment plates welded to the top and bottom of the beam and to the column (Test 11 and Test 12). Concrete cladding was used on Tests 7, 9, and 11 and a glass cladding was used on Test 12, which will not be discussed in this dissertation. The explosive charge used was the same size and standoff for all tests and had a scaled distance of 1.15.
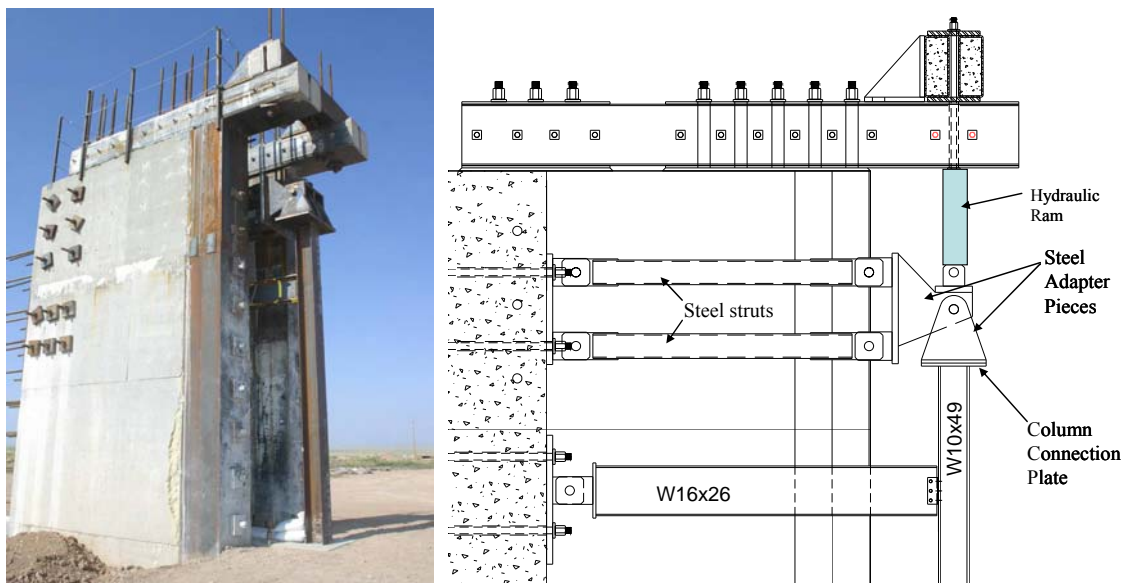
Figure 2.16: Field Test, Phase II Test Setup

Table 2.4: Field Tests, Phase II Test Matrix

Test #	Column	Beam	Connection	Cladding	Scaled Distance
7	W10x49, A992 grade 50 (Strong Axis)	W16x26, A992, grade 50	Shear Tab, Strong Axis	96" x 186" x 4" concrete	1.15
8	W10x49, A992 grade 50 (Strong Axis)	W16x26, A992, grade 50	Shear Tab, Strong Axis	N/A	1.15
9	W10x49, A992 grade 50 (Weak Axis)	W16x26, A992, grade 50	Shear Tab, Weak Axis	96" x 186" x 4" concrete	1.15
10	W10x49, A992 grade 50 (Weak Axis)	W16x26, A992, grade 50	Shear Tab, Strong Axis	N/A	1.15
11	W10x49, A992 grade 50 (Strong Axis)	W16x26, A992, grade 50	Wind Moment	96" x 186" x 4" concrete	1.15

Results and conclusions can be summarized as follows: Test 7 had a maximum permanent column displacement of 25.3 in. Buckling of the column web occurred at the column/beam connection and just above the ground level. The base plate was rotated 15°. Column posttest axial capacity was 78 kips. The beam/column connection was still intact after event. Plastic deformation occurred in the bolt holes in the web of the beam.

The Test 8 had a maximum permanent column displacement of 4.3 in. The front flanges of column were bent in the direction of the blast from the ground up to a height of 7 feet. Column posttest axial capacity was 380 kips and the beam/column connection was still intact after event.

The Test 9 had a 34.7 in maximum column residual displacement. Tearing in the column web occurred near the column/beam connection due to the beam penetrating

through the web. The anchors bolts were pulled out of concrete footing. Due to the tearing, it was assumed that the column load capacity was near zero.

The Test 10 had a maximum permanent column displacement of 16.3 in. The front flanges were deformed outward in the bottom 5 feet of the column creating tears in the K-region. A 24-in portion of the web was blown out and found approximately 800 feet behind the CTRS. The beam/column connection was still intact after the event. Plastic deformation did occur in the bolt holes in the web of the beam. The assumed column load capacity was near zero.

Test 11 showed a maximum permanent column displacement of 16.3 in. Lateral buckling of the column occurred in the front flange at the height of 5 ft above ground level and the beam was buckled behind the connection. The column post test axial capacity was 175 kips. A failure of the column/beam connection did not occur.

One important finding from these tests is shown in Figure 2.17 and Figure 2.18. Figure 2.17 shows pre and post test photos of the Test 10 without cladding and Figure 2.18 shows photos from the Test 11 with cladding. The differences in the response are clearly seen and verify the behaviors also seen in the Phase I tests; the addition of cladding increases global deformation where as the omission of cladding allows for localized failure.

Figure 2.17: Before and After Photos from Test 10 without Cladding

Figure 2.18: Before and After Photos from Test 9 with Cladding

2.4   Simulated Blast Loading

Using alternate methods to produce impulsive loading onto structures without the use of explosives has become increasingly popular in the last several years. A variety of methods for replicating these types of loads have emerged including using high speed

drop impacts [8] and shock tube testing [9, 10]. This research utilized a hydraulic actuator system to produce blast-like loads found at the University of California, San Diego. This section will discuss the UCSD Blast Simulator in detail and will describe previous simulator tests as they pertain to this dissertation.

2.4.1 UCSD Blast Simulator

The UCSD Blast Simulator [11] is the world's first hydraulically driven system that simulates blast-like loads on structures without the use of explosive materials, and thus without a fireball. This is accomplished using an array of ultra-fast computer-controlled hydraulic actuators with a combined hydraulic/high pressure nitrogen energy source. The impulsive load is created by impacting the specimen with multiple impacting modules, each of which is calibrated and controlled with respect to impact time and velocity. The modules, which are described in detail below, are accelerated to a prescribed velocity with an array of Blast Generators (BGs). The UCSD Blast Simulator Facility currently has 6 BGs, 4 of Type I, named BG25, and 2 of Type II, named BG50.

The Blast Generators consist of a hydraulic actuator, control valves, accumulators, and transducers. A schematic of a Type 1 BG (BG25) is shown in Figure 2.19, and a photo is shown in Figure 2.20 for which technical specifications are given in Table 2.5. Corresponding information for Type II is given in Figure 2.21 and Figure 2.22 and Table 2.5.
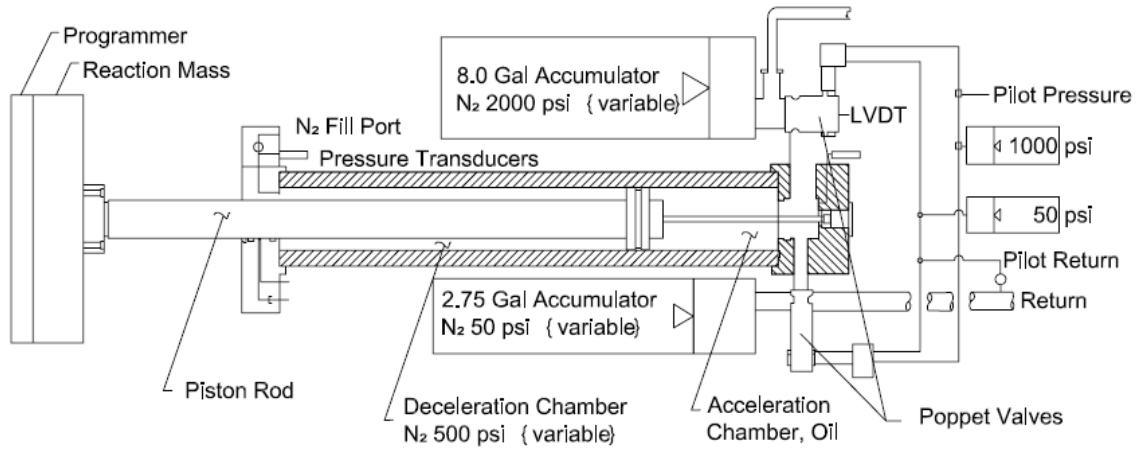
Figure 2.19: Type I BG (BG25) Schematic

Figure 2.20: Type I BG (BG25) Photo
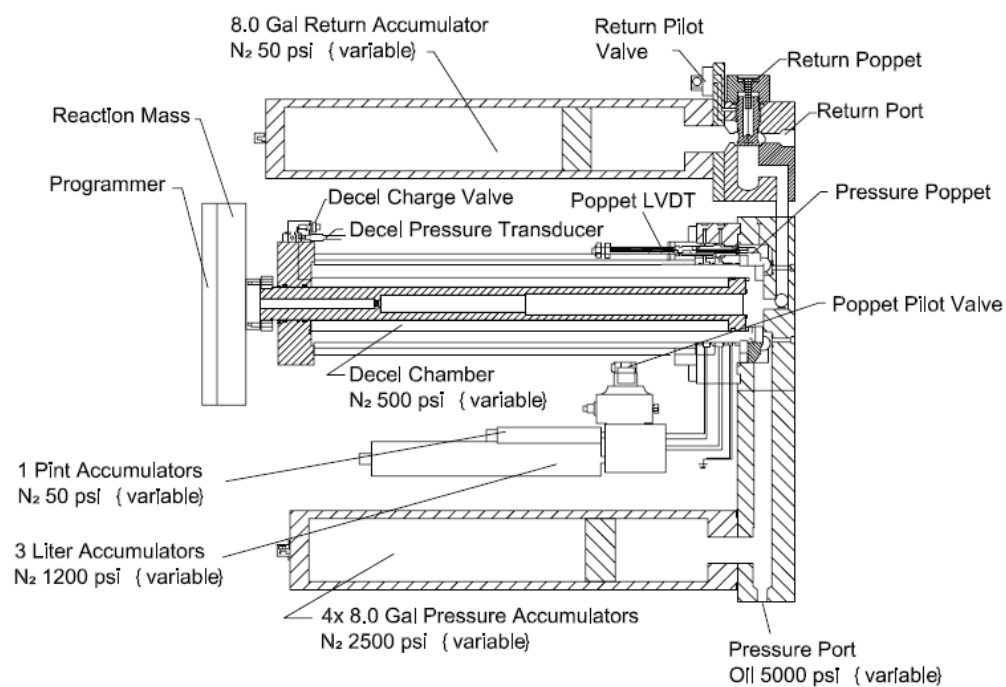
Figure 2.21: Type II BG (BG50) Schematic

Figure 2.22: Type II BG (BG50) Photo

Table 2.5: Technical Specifications for Blast Generators, reproduced from [11]

	Blast Generator, Type I (BG25)	Blast Generator, Type II (BG50)
Quantity	4	2
Maximum Kinetic Energy (with corresponding mass)	50 kg – 30kJ 100 kg – 51kJ 200 kg –76kJ 400 kg – 101kJ	100kg – 220kJ 200 kg – 310kJ 400 kg –379kJ 800 kg – 420kJ
Maximum Velocity (with 50 kg mass)	34 m/s (1300 in/s)	66 m/s (2600 in/s)
Repeatability of Velocity	4% or 0.1m/s whichever is greater	4% or 0.1m/s whichever is greater
Simultaneous Impact	+/- 0.001s	+/- 0.001s
Mass Range (Bolted to BG Rod)	50 to 400kg (including mass of piston)	100 to 800kg (including mass of piston)
Mass Range (Free Mass)	10 to 50 kg	10 to 50 kg
Shape of Mass	Variable, to match specimen	Variable, to match specimen
Programmer Impulse Time	0.5 to 5 ms	0.5 ms upward

Initially, nitrogen is compressed in the pressure accumulator along with high pressured oil. A servo-controlled high-flow valve controls the oil flow into the actuator. Once the valve has been opened at the desired rate and amount, the oil forces the piston rod/impacting mass assembly to drive outward toward the specimen. A smaller servo-controlled valve controls the outflow of the oil and thus is able to retract the actuator after impact. The force required to retract the actuator is supplied by pressurized nitrogen gas in a deceleration chamber which is specifically calibrated before each test.

For a given test, the BGs are mounted to a fixed reaction wall which is attached to a concrete slab as illustrated in Figure 2.23. Currently, the facility has the capability of

mounting BGs off both sides of the fixed reaction wall for multiple, concurrent tests. A moveable reaction wall is also attached to the slab and is used to mount specimens and fixtures. The slab as a whole is base isolated from the foundation structures to limit the energy transfer to the surrounding environment which is shown in Figure 2.24.
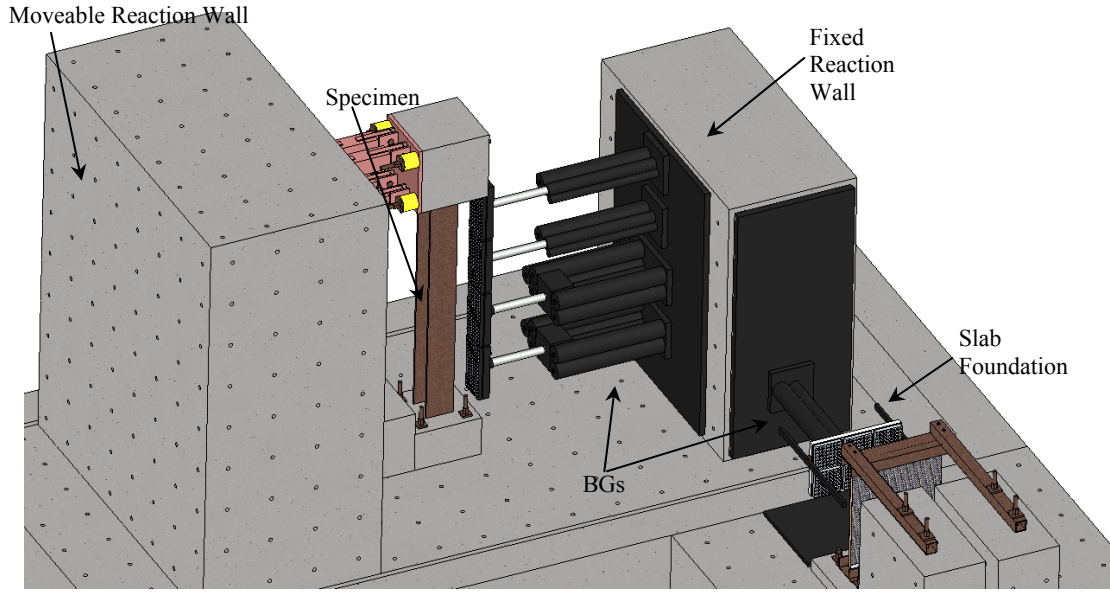
Figure 2.23: Blast Simulator Facility, BGs Mounted on Two Directions
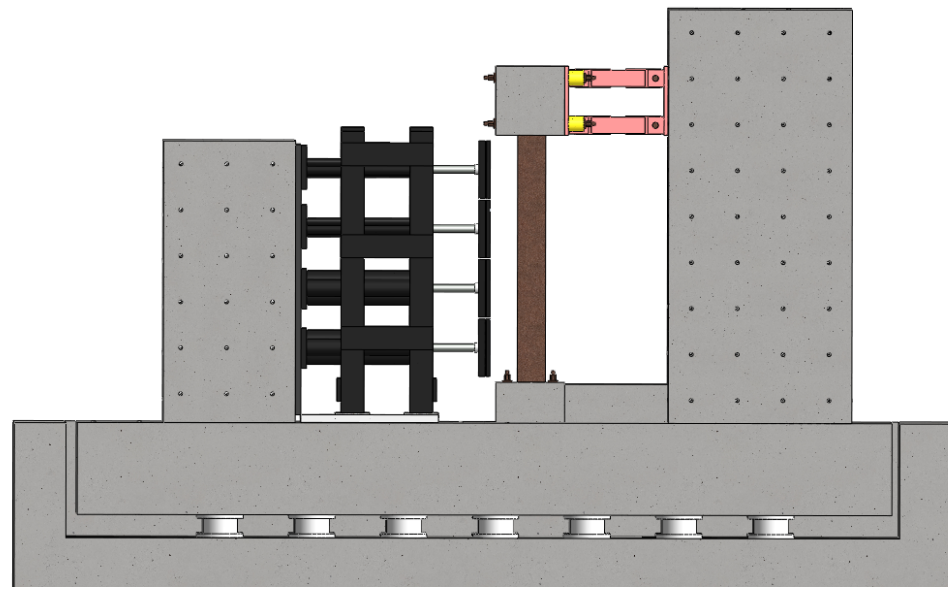
Figure 2.24: Base Isolated Foundation

Attached to the rod is the impacting module, which consists of a steel or aluminum mass, a thin aluminum backing plate, and a nonlinear, urethane material called a programmer, which is used to transfer the energy and momentum of the module to the specimen. Figure 2.25 gives a photo of a programmer. The programmer geometric and material properties help tailor the duration and magnitude of the pressure, and thus the impulse to be representative of a blast-like pulse shown in Figure 2.26.
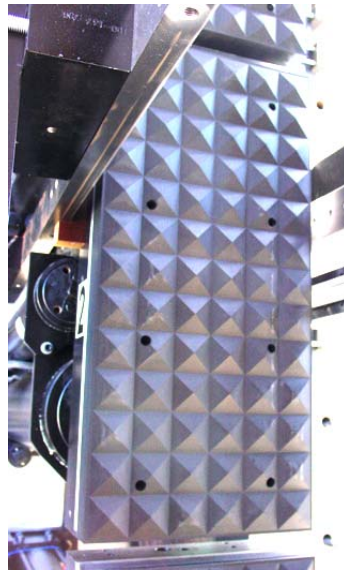
Figure 2.25: Urethane Column Programmer
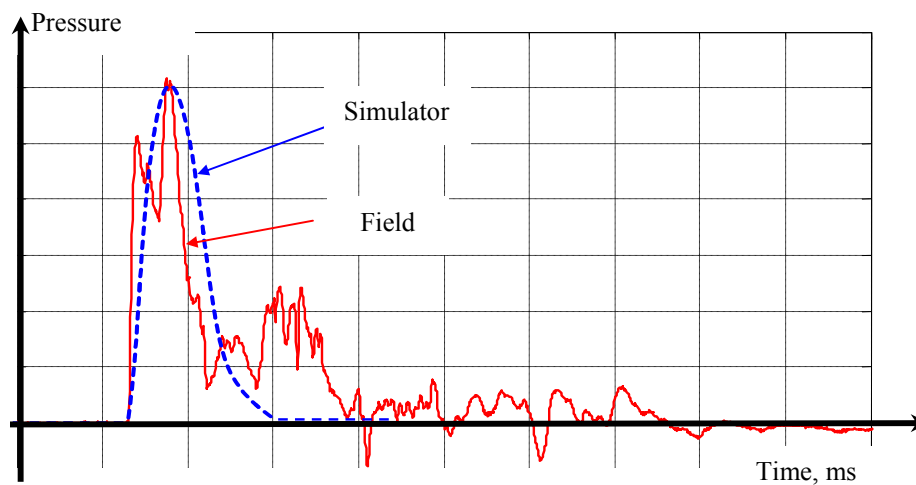
Figure 2.26: Simulated Blast Pressure Pulse

The impacting modules are supported with guiderails that also align the modules with the specimen until impact. The rails are supported on a large frame system which can be adjusted for various configurations. A photo of the frame system and rails is given in Figure 2.27.

Figure 2.27: Simulator Rail Frame System

The UCSD Simulator Facility utilizes an instrumentation system that is configured to suit the specific testing purpose. Additional information on the instrumentation used in this dissertation, as well as data analysis techniques are given in Chapter 3.

2.4.2 Previous Simulator Tests

The Blast Simulator has been used to generate high-fidelity data concerning the response of a variety of critical infrastructure elements to blast loads. The initial test

series was conducted in 2006 by Rodriguez [12] and studied the response of reinforced concrete columns (Figure 2.28) to vehicle size blast loads. This test series also utilized the Simulator to develop and verify hardening strategies for concrete columns including CFRP wraps. This particular series of tests is similar in setup to those tests discussed in this dissertation and utilized many of the same reaction fixtures and impacting modules.
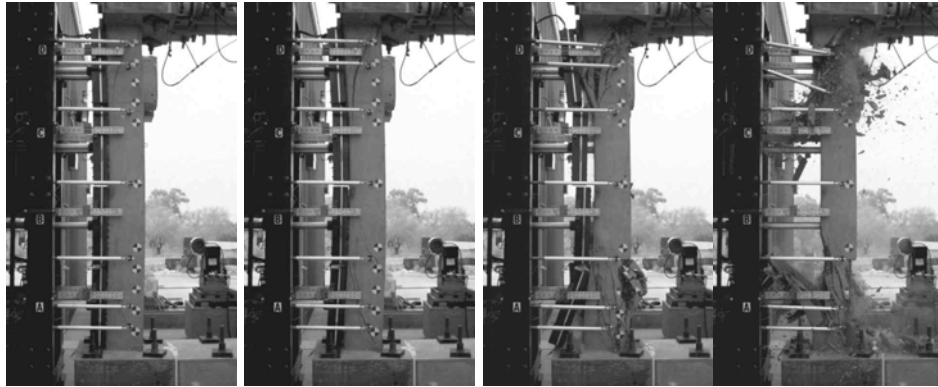
Figure 2.28: Simulator Tests of Reinforced Concrete Columns – Damage Evolution

Additionally, a variety of tests were conducted on infill CMU and URM walls by Oesterle [13] shown in brevity in Figure 2.29. These tests were particularly important because they defined a majority of the data analysis procedures that are incorporated in this dissertation.
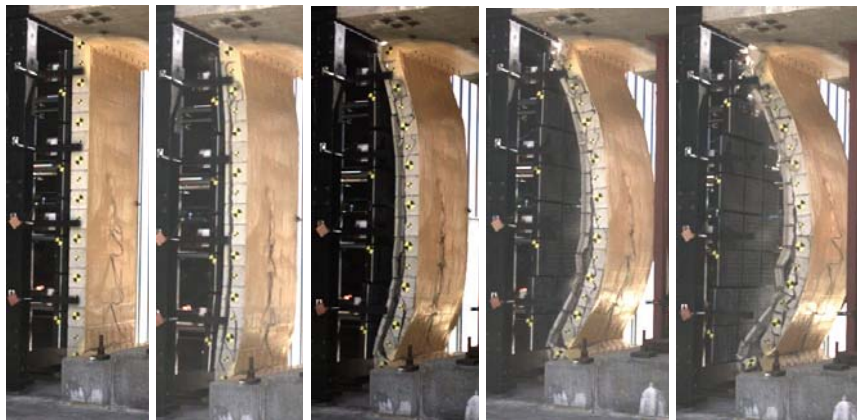
Figure 2.29: Simulator Tests of Retrofitted Wall Response

2.5 Material Models

2.5.1 Steel Plasticity Model

The material model used for steel in this dissertation is based upon a Mises-type plasticity model with strain rate effects incorporated. The model uses a von-Mises yield surface [14] together with an associated flow rule. The equation for the surface given in Equation (2.8), where k is a constant. Substituting for the definition of J_2 yields Equation (2.9) which is a function of the Cauchy deviatoric stress tensor, σ'_{ij}. This surface can be described as a cylinder with radius $\sqrt{2}k$ in principal stress space, oriented along the hydrostat as shown in Figure 2.30

$$f = J_2 - k^2 = 0 \tag{2.8}$$

$$f = \frac{1}{2}\sigma'_{ij}\sigma'_{ij} = k^2 \tag{2.9}$$
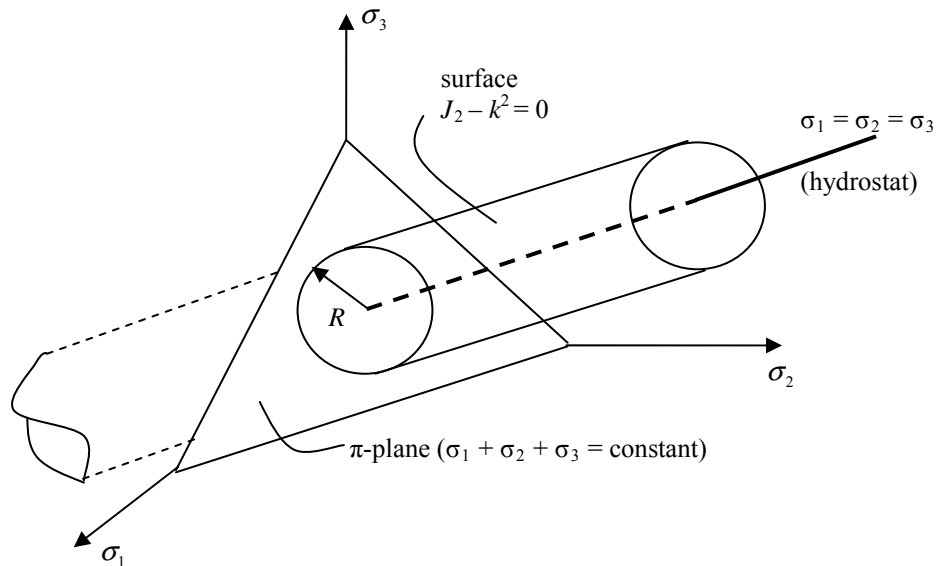
Figure 2.30: von Mises Yield Surface

For the case of uniaxial stress, the k^2 term can be found to be equal to $\frac{1}{3}(\sigma_1)_y^2$ which is defined as $\frac{1}{3}\sigma_y^2$. The equation of the yield surface can therefore be written as in Equation (2.10).

$$f = \frac{1}{2}\sigma_{ij}'\sigma_{ij}' - \frac{\sigma_y^2}{3} = 0 \qquad (2.10)$$

In the case of isotropic hardening, the current yield surface becomes a function of both the initial yield surface and some hardening parameter, λ, which is shown in Equation (2.11). This is represented by a uniform expansion of the yield surface. If strain rate effects are included as in Equation (2.12), the function is multiplied by β to account for strain rate effects or a complete table defining the yield stress versus plastic strain can be defined in computational programs for various levels of effective strain rate [5].

$$f(\sigma_{ij,}\lambda) = f_o(\sigma_{ij}) - F(\lambda) \qquad (2.11)$$

$$f(\sigma_{ij,}\lambda) = \beta\left[f_o(\sigma_{ij}) - F(\lambda)\right] \qquad (2.12)$$

The model is implemented using the Radial Return Algorithm [15] in which the deviatoric stresses are updated elastically. If the yield surface condition is met, the deviatoric stresses are accepted, if they are not, an incremental plastic strain is computed and the trial deviatoric stress state is scaled back along the radius of the yield surface.

2.5.2 Sand Plasticity Model

The sand, used in the weak axis tests, was modeled using a kinematic hardening cap model in LS-DYNA [16] with further explanation in [17]. This model has a yield condition defined by three surfaces as given in Equation (2.13) and shown in Figure 2.31

$$f_1\left(\sigma_{ij}\right)=0$$
$$f_2\left(\sigma_{ij},\lambda\right)=0 \tag{2.13}$$
$$f_3\left(\sigma_{ij}\right)=0$$
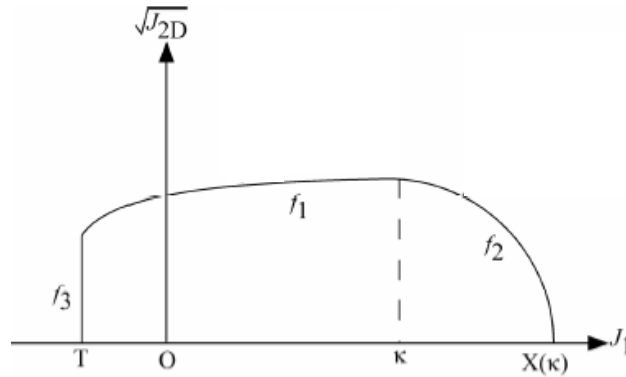
Figure 2.31: Cap Model Yield Surface in Pressure Space from [18]

The first surface, f_1, is the failure envelope surface and is defined as in Equation (2.14), where F_e is a function of the first invariant of the stress and is define in Equation (2.15). The failure surface is fixed and does not change unless kinematic hardening is present.

$$f_1 = \sqrt{J}_2 - \min\left(F_e\left(J_1\right),T_{mises}\right) \tag{2.14}$$

$$F_e\left(J_1\right) \equiv \alpha - \gamma e^{-\beta J_1} + \theta J_1 \tag{2.15}$$

The cap surface, f_2, intersects the f_1 surface at κ (the hardening parameter) and is defined by Equation (2.16). F_c in the equation is a function of both J_1 and κ and is given by the expression in Equation (2.17). $X\left(\kappa\right)$ is the intersection of the cap with the J_1 axis and $L(\kappa)$ is given in Equation (2.18). From this, the definition of T_{mises}, used in Equation (2.14) can be easily seen and is given in Equation (2.19).

$$f_2 = \sqrt{J_2} - F_c\left(J_1, \kappa\right) \tag{2.16}$$

$$F_c\left(J_1, \kappa\right) \equiv \frac{1}{R}\sqrt{\left[X\left(\kappa\right) - L\left(\kappa\right)\right]^2 - \left[J_1 - L\left(\kappa\right)\right]^2} \tag{2.17}$$

$$L\left(\kappa\right) = \begin{cases} \kappa, if\ \kappa > 0 \\ 0, if\ \kappa \leq 0 \end{cases} \tag{2.18}$$

$$T_{mises} = \left|X\left(\kappa\right) - L\left(\kappa\right)\right| \tag{2.19}$$

The final surface is the tension cutoff surface donated by f_3 in Figure 2.31 denotes the maximum tension sustainable by the soil. An associated plastic flow rule is assumed and Koiter's rule [18] given in Equation (2.20) is used to define the effective plastic strain rate, $\dot{e}_{ij}^p$, as the sum of the contribution from all the surfaces. In the equation if, for any η, either $f_\eta < 0$ or $f_\eta = 0$ and $\dot{f}_\eta < 0$, then $c_\eta = 0$. If $f_\eta = 0$ and $\dot{f}_\eta = 0$, then $c_\eta = 1$.

$$\dot{e}_{ij}^p = \sum_{\eta=1}^{N} c_\eta \Lambda_\eta \frac{\partial f_\eta}{\partial \sigma_{ij}}, \qquad \Lambda \geq 0 \tag{2.20}$$

2.6   Numerical and Computational Methods

2.6.1 The Finite Element Method

This section briefly provides an introduction to the finite element method, which is used throughout the dissertation to model the experiments conducted throughout the research. This is meant to serve as only a brief introduction and additional information can be found in a variety of sources including [16, 19, 20]. Small deformations are assumed herein for ease of presentation.

Consider a continuum with domain Ω as shown in Figure 2.32 where a prescribed displacement is given over Γ_u and a prescribed traction is given over Γ_t. For dynamic analysis, the governing equilibrium equation on the domain, Ω, is

$$\sigma_{ij,j} + b_i = \rho \ddot{u}_i \qquad i, j = 1, 2, 3 \tag{2.21}$$

with stress and displacement boundary conditions as seen in (2.22) and (2.23). Additional types of constraints, such as contacts between other parts, are also sometimes appropriate but will not be considered in this derivation.

$$\sigma_{ij} n_j = t_i \qquad on \quad \Gamma_t \tag{2.22}$$

$$u_i = \overline{u}_i(t) \qquad on \quad \Gamma_u \tag{2.23}$$

The initial conditions at $t = 0$ of the system are

$$u_i(x, 0) = \overline{u}_i^0(x) \tag{2.24}$$

$$\dot{u}_i(x, 0) = \overline{v}_i^0(x) \tag{2.25}$$
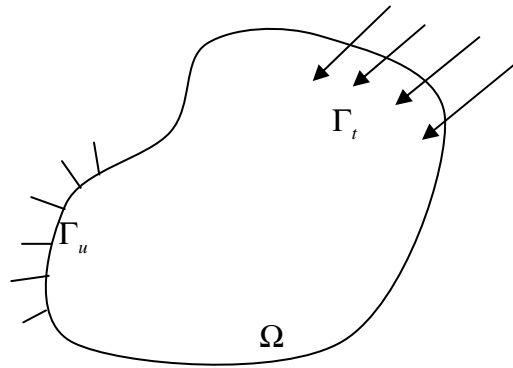
Figure 2.32: Arbitrary Continuum

In order to be a solution to the PDE given in Equation (2.21), the solution must satisfy the differential equation, the boundary conditions, and the initial conditions. Often times, complexities in the problem, such as geometry, result in an exact solution to the PDE that cannot be found or cannot be obtained in a reasonable amount of time. The finite element method allows for an approximate solution to be obtained for the PDEs. This method solves the equation using a discretized model with a finite number of degrees of freedom rather than looking for a solution for the continuum which requires infinite degrees of freedom.

The principal of virtual work can be utilized to develop the weak form from the strong form of the momentum equation given in (2.21). This principal states that if a system is given a virtual displacement, δu_i, then the total work done on the system is equal to zero shown in (2.26).

$$\int_\Omega \delta u_i \left[\rho \ddot{u}_i - \sigma_{ij,j} - b_i \right] d\Omega = 0 \tag{2.26}$$

$$\int_\Omega \delta u_i \rho \ddot{u}_i d\Omega - \int_\Omega \delta u_i \sigma_{ij,j} d\Omega - \int_\Omega \delta u_i b_i d\Omega = 0 \tag{2.27}$$

Using the chain rule the following expression can be derived:

$$\int_\Omega \left(\delta u_i \sigma_{ij} \right)_{,j} d\Omega = \int_\Omega \delta u_{i,j} \sigma_{ij} d\Omega + \int_\Omega \delta u_i \sigma_{ij,j} d\Omega \tag{2.28}$$

Rewriting (2.28) becomes

$$\int_\Omega \delta u_i \sigma_{ij,j} d\Omega = \int_\Omega \left(\delta u_i \sigma_{ij} \right)_{,j} d\Omega - \int_\Omega \delta u_{i,j} \sigma_{ij} d\Omega \tag{2.29}$$

Substitute (2.29) into the second term in (2.27).

$$\int_\Omega \delta u_i \rho \ddot{u}_i d\Omega + \int_\Omega \delta u_{i,j} \sigma_{ij} d\Omega - \int_\Omega \left(\delta u_i \sigma_{ij} \right)_{,j} d\Omega - \int_\Omega \delta u_i b_i d\Omega = 0 \tag{2.30}$$

Using the divergence theorem, the third term becomes

$$\int_{\Omega} \left(\delta u_i \sigma_{ij} \right)_{,j} d\Omega = \int_{\Gamma} \delta u_i \sigma_{ij} n_j d\Gamma = \int_{\Gamma} \delta u_i t_i d\Gamma \tag{2.31}$$

If it is forced that all boundary conditions are satisfied and forced that δu_i vanishes on Γ_u, then (2.31) becomes the following weak form formulation:

$$\int_{\Omega} \delta u_i \rho \ddot{u}_i d\Omega + \int_{\Omega} \delta u_{i,j} \sigma_{ij} d\Omega - \int_{\Omega} \delta u_i b_i d\Omega - \int_{\Gamma_t} t_i \delta u_i d\Gamma_t = 0 \tag{2.32}$$

Suppose the continuum is discretized into a mesh of finite elements connected at each node and the following finite element interpolations, with continuous shape functions, are considered:

$$u_i(\mathbf{x},t) = \sum_{A=1}^{n} u_i^A(t) \Phi_A(\mathbf{x}) \tag{2.33}$$

$$\delta u_i(\mathbf{x},t) = \sum_{B=1}^{n} \delta u_i^B(t) \Phi_B(\mathbf{x}) \tag{2.34}$$

where n is the number of nodes defining each element. Substituting (2.33) and (2.34) into (2.32) and dropping the variational term yields

$$\int_{\Omega} \Phi_B(\mathbf{x}) \rho \Phi_A(\mathbf{x}) \ddot{u}_i^A(t) d\Omega + \int_{\Omega} \Phi_{B,j}(\mathbf{x}) \sigma_{ij} d\Omega - \int_{\Omega} \Phi_B(\mathbf{x}) b_i d\Omega - \int_{\Gamma_i} t_i \Phi_B(\mathbf{x}) d\Gamma_t = 0 \tag{2.35}$$

The internal and external nodal forces and the mass matrix can be defined as follows:

$$f_{iA}^{int} = \int_{\Omega} \Phi_{A,j} \sigma_{ij} d\Omega \tag{2.36}$$

$$f_{iA}^{ext} = \int_{\Omega} \Phi_A b_i d\Omega + \int_{\Gamma_t} \Phi_N t_i d\Gamma_t \tag{2.37}$$

$$M_{BA} = \int_{\Omega} \rho \Phi_B \Phi_A d\Omega \tag{2.38}$$

The finite element equation from (2.35) in the form of Newton's Second Law:

$$\sum_A M_{BA} \ddot{u}_i^A = f_{iB}^{int} + f_{iB}^{ext} \tag{2.39}$$

In many cases, the mass matrix defined in (2.38) is not ideal. A diagonal mass matrix allows for simple mathematics without the use of a matrix solver as will be seen in the following derivation of the time-stepping method. Row-sum lumping is one of the most common methods obtained by

$$M_{BA}^{diag} = \delta_{BA} \sum_K M_{BK} \tag{2.40}$$

where the summation is over the entire row of the matrix. Additionally, for many software implementations, such as LS-DYNA [21], (2.40) is used in lumping and the mass matrix is given by

$$M_{AA}^{diag} = \int_\Omega \rho \Phi_A \left(\sum_K \Phi_K \right) d\Omega = \int_\Omega \rho \Phi_A d\Omega \tag{2.41}$$

The time stepping of this formulation can be done in a number of different ways. The following will discuss explicit time integration using the central difference method as discussed in [22]. It should be noted that LS-DYNA uses a modification of the central difference time integration for explicit runs and additional information on that implementation can be found in [16] as well as information regarding implicit analysis which will not be included in this dissertation.

Using the central difference method, the velocity and acceleration can be approximated as follows:

$$\dot{u}_{n-1/2} \approx \frac{\partial u_{n-1/2}}{\partial t} = \frac{u_n - u_{n-1}}{\Delta t} \tag{2.42}$$

$$\ddot{u}_{n-1/2} \approx \frac{\partial^2 u_{n-1/2}}{\partial t^2} = \frac{u_{n+1} + u_{n-1} - 2u_n}{\Delta t^2} \tag{2.43}$$

A finite element method for transient dynamics is developed and shown in the flowchart in Figure 2.33. It should also be noted that the flowchart above is for a simple, linear case with no strain rate effects. Additional parameters should be taken into account if these types of analysis are necessary.

1) Move one step to $t = t_n$

$$u_n = u_{n-1} + \frac{\partial u_{n-1/2}}{\partial t} \Delta t$$

2) Calculate Forces

$$\varepsilon_n = \varepsilon(u_n)$$
$$\sigma_n = E\varepsilon_n$$
$$F = F(u, \sigma, t)$$

3) Calculate Acceleration

$$a_n = \frac{\partial^2 u_n}{\partial t^2} = M^{-1} F_n$$

4) Update Velocity

$$v_{n+1/2} = \frac{\partial u_{n+1/2}}{\partial t} = \frac{\partial u_{n-1/2}}{\partial t} + a_n \Delta t$$
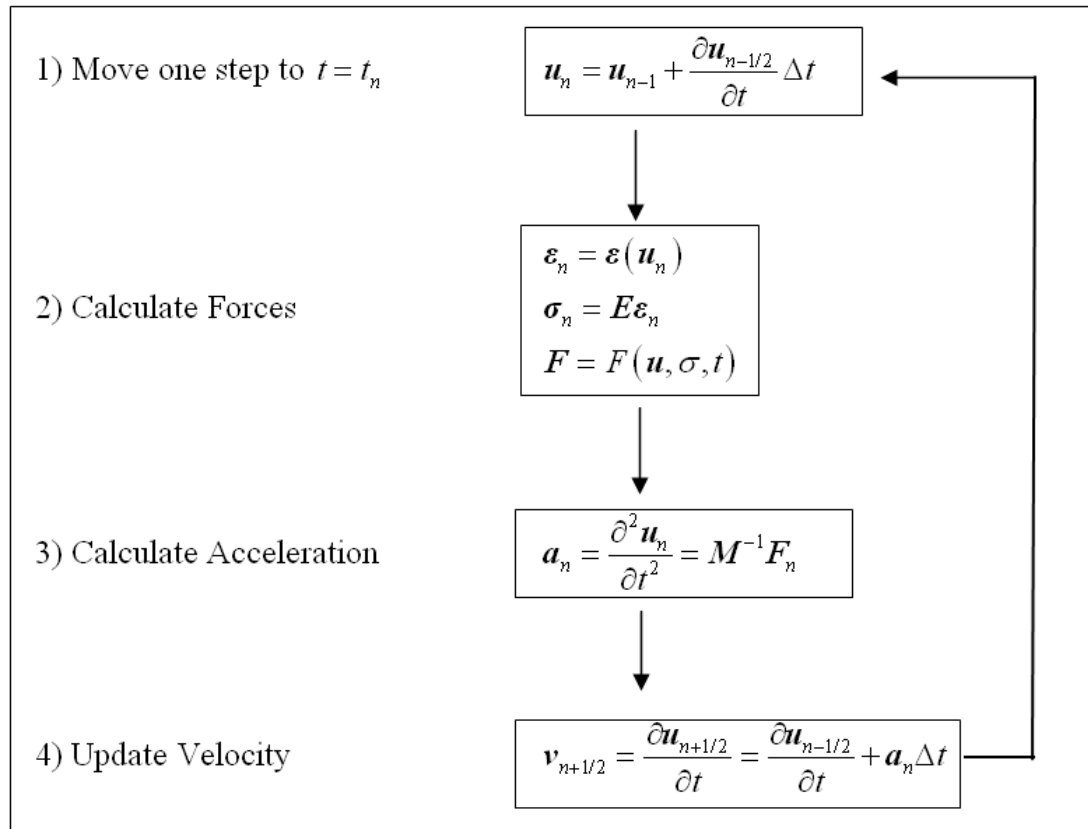
Figure 2.33: Flowchart of Explicit Finite Element Method [22]

3 Simulated Blast Loading of Strong Axis Steel Columns

This chapter presents the results from a series of simulated blast tests on as-built steel wide-flange sections impacted in the strong axis direction with uniform and variable load along the height of the column. The purposes of these tests were to characterize the behavior of the columns under various simulated blast loads, validate the simulator using data from similar field tests and to provide high quality test data which was used to improve and validate predictive computer models. Additionally, these tests were also used to develop an experimental loading protocol for future testing of columns in the strong axis direction. The first section discusses the preliminaries: test setup, specimen design and instrumentation. The second section describes the methods for data analysis. This includes the analysis of accelerometer and camera data. The following section describes the experimental test results which are used in Chapter 5 to validate computational models. Finally, a brief summary of the chapter is given.

Three uniform velocity and eight variable velocity tests were conducted on five specimens. A summary of these tests with desired target impact velocities is shown in Table 3.1. The tests were conducted on two W10x49 steel column specimens and three W14x132 specimens, which are discussed in detail in Section 3.1.2.

Table 3.1: Strong Axis Column Test Matrix

Test	Specimen	Type	Load Type	Desired Impact Velocity
SA01	1	W10x49	Uniform	157.5 in/s (4.0 m/s)
SA02	1	W10x49	Uniform	708.6 in/s (18.0 m/s)
SA03	2	W10x49	Uniform	1023.6 in/s (26.0 m/s)
SA04	3	W14x132	Variable	391.7, 325.5, 267.7, 226.4 in/s (9.9, 8.3, 6.8, 5.8 m/s)
SA05	3	W14x132	Variable	389.4, 325.5, 267.7, 226.4 in/s (9.9, 8.3, 6.8, 5.8 m/s)
SA06	3	W14x132	Variable	377.6, 322.8, 266.5, 224.4 in/s (9.6, 8.2, 6.8, 5.7 m/s)
SA07	3	W14x132	Variable	1744.1, 1389.8, 1003.9, 502.9 in/s (44.3, 35.5, 25.5, 12.8 m/s)
SA08	4	W14x132	Variable	320.5, 264.6, 213.8, 181.1 in/s (8.1, 6.7, 5.4, 4.6 m/s)
SA09	4	W14x132	Variable	1755.9, 1401.6, 1007.9, 507.9 in/s (44.6, 35.6, 25.6, 12.9 m/s)
SA10	5	W14x132	Variable	1779.5, 1425.2, 1031.5, 511.8 in/s (45.2, 36.2, 26.2, 13.0 m/s)
SA11	1	W10x49	Variable	1594.5, 1334.6, 1267.7, 972.4 in/s (40.5, 33.9, 32.3, 24.7 m/s)

3.1 Preliminaries

This section describes the details of the experimental setup for the strong axis tests. First, the test setup including reaction structure, upper link system and blast generator configurations are discussed. Next, details of the design and construction of the test specimens will be given. Finally, instrumentation details will be presented. This

includes the data acquisition system, phantom cameras, accelerometers, strain gages and displacement gages.

3.1.1 Setup

The test setup is illustrated in Figure 3.1 and Figure 3.2 with elevations of the test from the top and side. The columns were loaded with four blast generators distributed over the height of the column. For the uniform tests, four BG 25s were used and for the variable velocity tests, two BG 25s and two BG 50s were used. The center to center spacing was 31 in, which leaves a 1 in gap between each plate. At the top and bottom there was a 3 in space between the edges of the support and the steel specimen.

The impacting units vary in dimension for each of the two size specimens. For the W10x49 tests, the four impacting units were 10 in wide $\times$ 30 in tall and weighed a total of 257.5 lbs which included the weight of the steel rod and collar. The impacting units included a 10 in$\times$ 30 in $\times$ 3.75 in aluminum impacting mass and a 10 in $\times$ 30 in $\times$ 2 in programmer with a 0.5 in aluminum backing plate (Figure 3.3).

The W14x132 tests used four impacting units that were 14 in $\times$ 30 in and weighed a total of 543 and 660 lbs which included the weight of the steel rod and collar for the BG 25 and BG 50, respectively. The impacting units included a 14 in $\times$ 30 in $\times$ 3.25 in steel impacting mass and a 14 in $\times$ 30 in $\times$ 2 in programmer with a 0.5 in thick aluminum backing plate (Figure 3.4).
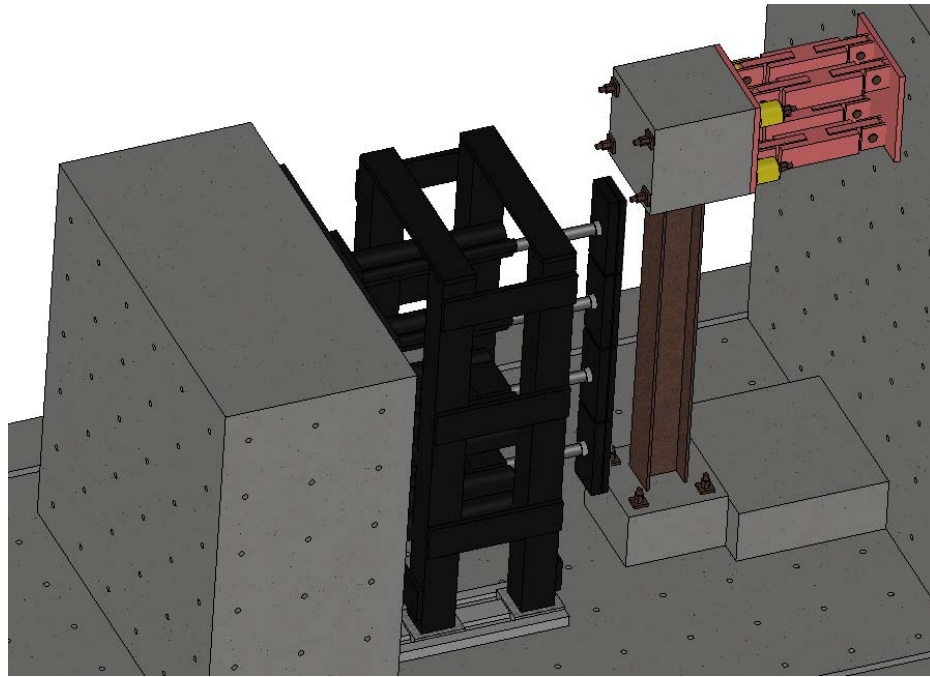
Figure 3.1: Elevation of Steel Column Strong Axis Test Setup
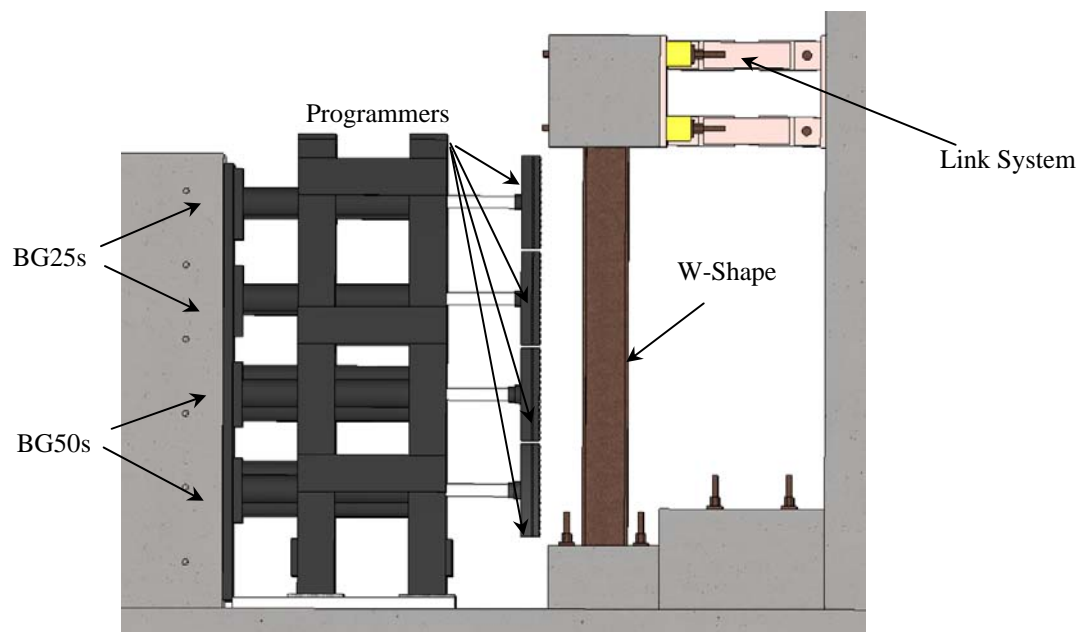
Figure 3.2: Side View of Steel Column Strong Axis Test Setup
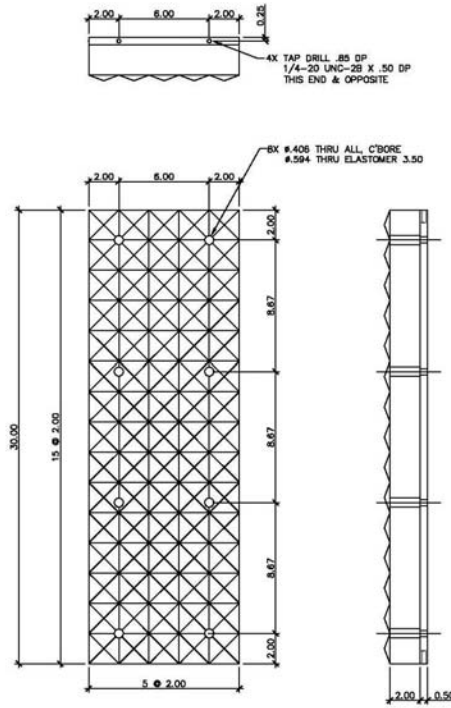
Figure 3.3: W10x49 Programmers
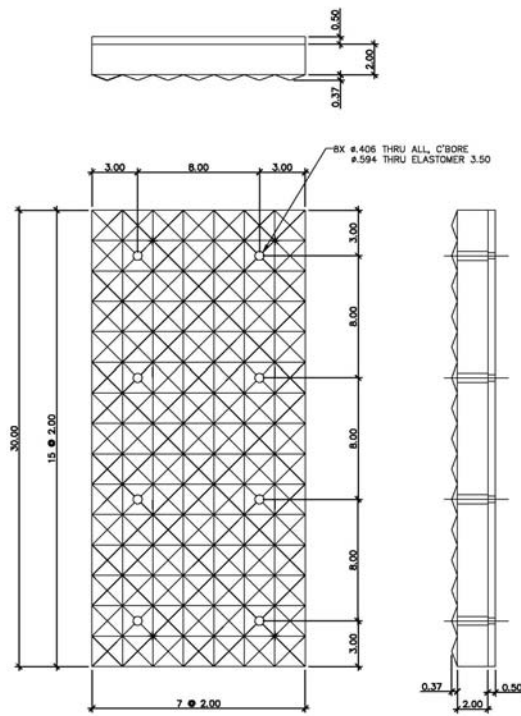
Figure 3.4: W14x132 Programmers

The boundary conditions for the tests were chosen for three reasons: they are similar to the actual behavior of a building column subjected to blast loads, they were similar to conditions applied during the DTRA Phase I field tests, and they were thought to be simple enough for ease of modeling. The connection at the base of the column was restrained in all directions simulating a "fixed" condition. It was post-tensioned to the reaction floor with four 1-3/8 in diameter rods post-tensioned to 100 kips. A 1'-9" tall × 3'-0" wide × 4'-6" long concrete spacer block transferred the shear from the specimen footing to the reaction wall.

The header was attached to a link system that allowed the column to move vertically while providing lateral and moment restraint (Figure 3.5). The link system was post-tensioned to the load stub and reaction wall. The four hollow hydraulic jacks tensioned the load stub header to the link with a 100 kip load and were left in place during the test.

Figure 3.5: Link System

3.1.2 Test Specimens

The five strong axis specimens used in this test series were constructed in June and July 2007. The specimens were identical to the columns used in the DTRA Phase I field test series, except that two of the W-Shapes chosen were smaller (W10x49). They were 10'-9" in clear height and 15'-6" in total height with the header and footer included.

The W10x49 specimens had the cross-sectional dimensions shown in Figure 3.6. The columns were fabricated from A992 grade 50 steel. The yield strength with no dynamic effects ranged from 50 ksi to 65 ksi, with a minimum ultimate tensile strength of 65 ksi. In the weak axis direction the moment of inertia was 272 in^4 and 93.4 in^4 in the strong axis direction. The area was 14.4 in^2, the depth was 9.98 in, the web thickness was 0.34 in, the flange width was 10 in and the flange thickness was 0.56 in.

The W14x132 specimens had the cross-sectional dimensions shown also in Figure 3.6. The columns were made from A992 grade 50 steel. The yield strength of the steel had a minimum of 50 ksi and a maximum of 65 ksi. The minimum ultimate tensile strength was 65 ksi. In the weak axis direction the moment of inertia was 1530 in^4 and 548 in^4 in the strong axis direction. The area was 38.8 in^2, the depth was 14.7 in, the web thickness was 0.65 in, the flange width was 14.7 in and the flange thickness was 1.07 in.
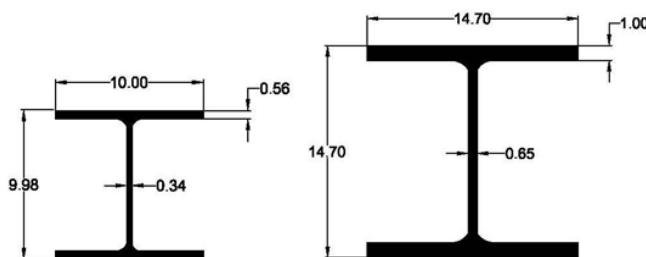
Figure 3.6: W10x49 (left) and W14x132 (right) Cross-Sectional Dimensions

Each column specimen had a concrete header attached to the top. The header prevented rotation at the top of the column. The header design was the same for all tests and is shown in Figure 3.7. The top of the column was welded to a 36 in $\times$ 36 in $\times$ 0.5 in steel plate. The weld was a 0.25 in bevel weld around the entire column. The welding rod that was used was E-70XX, which had a tensile strength of 70 ksi. The four sides of the header were confined by 0.25 in steel plates. Nelson studs were welded to the top plate and the side plates at every eight inches on center and #6 rebar hoops were installed within the header. The header created a 3 foot cube which was filled with 5,000 psi concrete. Concrete sample cylinders were acquired at the times of the concrete placement.

Figure 3.8 shows a drawing of the base of the column for the W14x132 specimen. Orientation of the column was such that the strong axis (flange) was facing the impact. A complete set of specimen drawings are shown in Appendix A. The base plate design used on the specimens consisted of a 0.5 in steel plate with the dimensions of 36 in $\times$ 36 in welded to the wide flange. The welds for this plate consisted of 0.25 in bevel welds on all sides of the column. A total of ten 0.5 in Nelson studs, 4 in long, were attached to the base plate in an array shown in Figure 3.9. The sides of the base were made from 0.25 in thick steel plates with a height of 1'-9" from the bottom of the base plate. The side plates had 0.5 in $\times$ 4 in Nelson studs centered every 8 in within the steel plates that surround the base of the column. 5,000 psi concrete was placed inside the casing and reinforced with a total of 16 #6 U-bars. Two-inch PVC was installed horizontally though the base of the column to allow four 1.375 in diameter post-tension bars to pass through it. These bars were post-tensioned to hold the base of the column to the reaction floor.
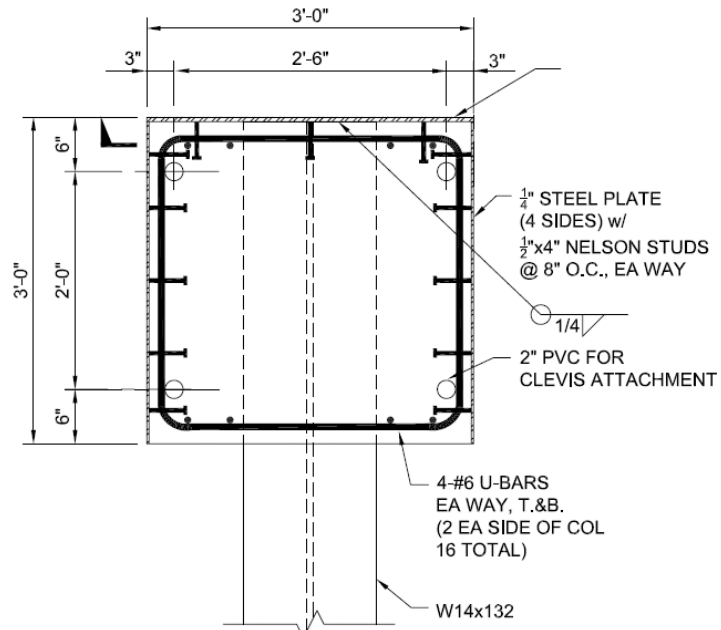
Figure 3.7: Header Design
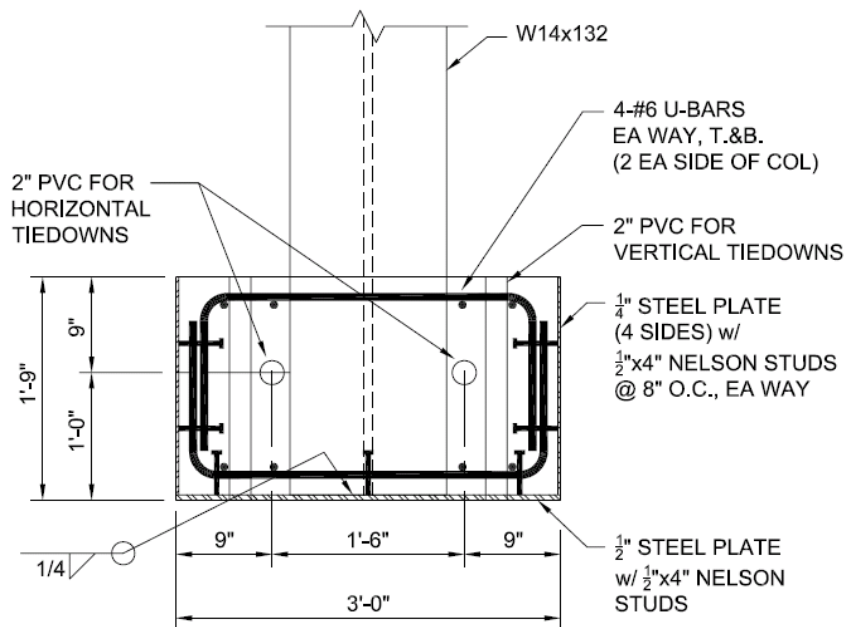
Figure 3.8: Base Design
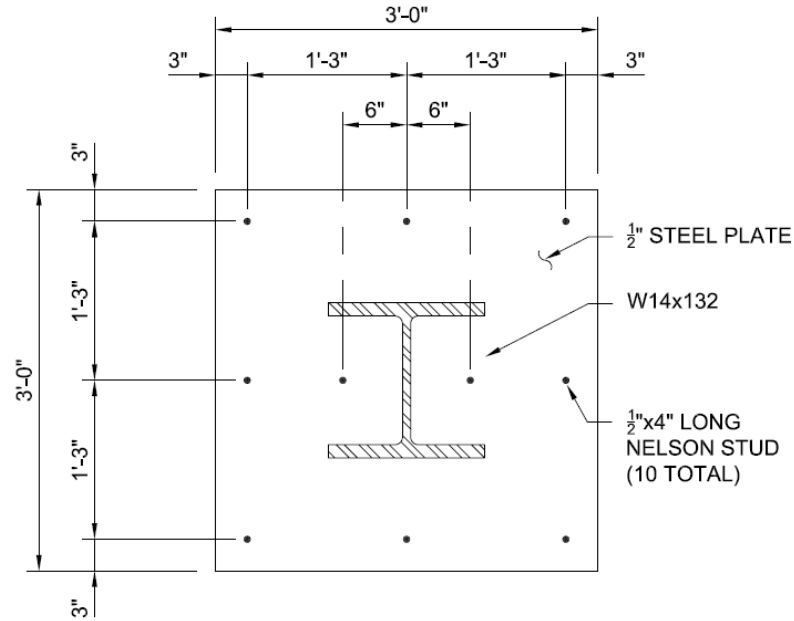
Figure 3.9: Nelson Stud Arrangement

The specimens were constructed in three phases. The first phase consisted of the steel fabrication and was done off site. Fabrication included the cutting of the W-Shapes and welding them to the steel base. The steel casings were also constructed at this time and the Nelson studs welded on. The fabricated steel specimens were shipped to Englekirk Center in June of 2007. Figure 3.10 and Figure 3.11 show the completed steel fabrication.

On June 26, 2007, rebar was placed inside the columns (Figure 3.12) and concrete was poured in each of the eleven bases. The pouring of the concrete is shown in Figure 3.13. The concrete in the base was allowed to cure for just over three weeks and on July 18, 2007 the columns were turned over with the concrete base at the top (Figure 3.14). Rebar cages were installed and concrete was poured into the header of the specimen and left to cure (Figure 3.15).

Figure 3.10: Fabricated Steel Columns and Casings

Figure 3.11: Fabricated Steel Casings with Nelson Studs

Figure 3.12: Rebar Cage in Steel Casing

Figure 3.13: Concrete Poured into Column Base

Figure 3.14: Column Specimens before Header Concrete was Poured

Figure 3.15: Concrete Poured into Column Header

3.1.3 Instrumentation

This section describes the instrumentation setup used for the strong axis column tests. For each test high speed cameras, accelerometers, strain gages and potentiometers were used to acquire data.

Data Acquisition System

A high speed data acquisition system from *Hi-Techniques* was used for all of the strong axis tests. The system sampled at 14 bits and 1 MHz. The system had 52 channels which were triggered by the MTS controller that was used to fire the blast generators.

High Speed Video

Three high speed Phantom cameras were used to record each test. These cameras provided visual evidence that was used to observe specimen behavior under impulsive loading. Figure 3.16 displays the sections of the column that were filmed in each test. Phantom 1 (shown in solid blue) recorded video in black and white. It was used to measure displacements and record velocities of the entire column. Phantom 2 and 3 were equipped with zoom lenses and recorded in color. Phantom 2 (dotted red) was focused on the bottom of the specimen and Phantom 3 (dashed green) was focused on the top. Figure 3.17 shows the placement of the cameras. The videos provide impact velocities of the BGs and visuals of the column behavior. Displacements were determined using the Track Eye Motion Analysis (TEMA*)* software package from Image Systems which can also generate velocity-time histories through differentiation of displacement.
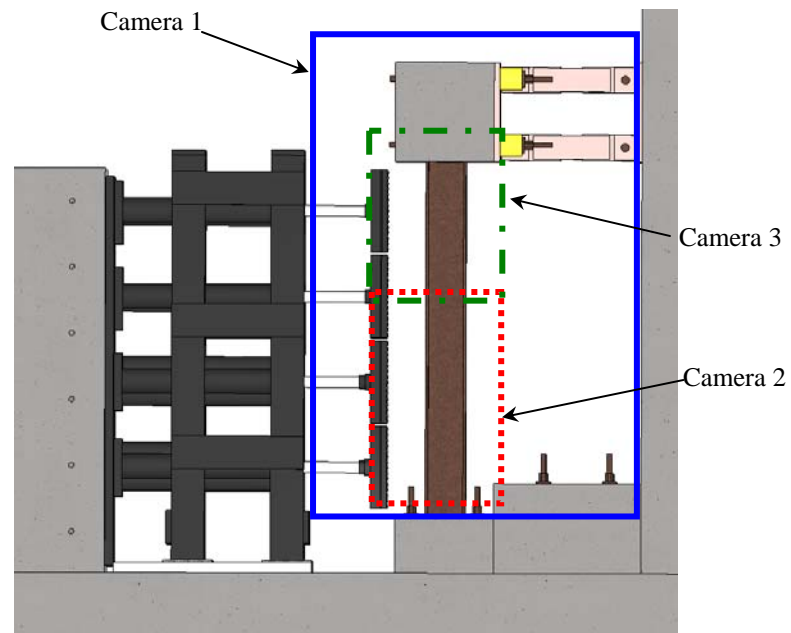
Figure 3.16: Phantom Camera Views

Figure 3.17: Phantom Camera Placement

Shock Accelerometers

Accelerations of the BGs during the test were measured with 10k g or 50k g piezoelectric shock accelerometers. One to three gages were mounted on the back of each of the four impacting plates. The cables that transmit the acceleration signal were fastened in such a way that strain relief was provided during the test.

Accelerations of the column were measured with 50k g piezoelectric shock accelerometers at five locations. One of the gages was located at the midspan and the other four were distributed over the height of the column. This corresponded to heights of 12", 38.25", 64.5", 90.75" and 117" from the bottom of the column. The locations of the accelerometers are shown in Figure 3.18. A photo of a mounted accelerometer is shown in Figure 3.19.

Strain Gages

Strains were measured in the column using post-yield, large strain measurement strain gages. Three rosettes were placed on the back (non-impact) side of the column along the midline and three were placed in the center of the flange. For each set of three, one was placed at the midspan and the two others were placed 1 foot away from the top and bottom support. The locations of the strain gages are shown in Figure 3.20.

Displacement Potentiometers

When available, displacements were also measured with a linear potentiometer at midspan. It was attached to the non-impact flange and the back movable reaction wall. The location of the potentiometer is shown in Figure 3.21.
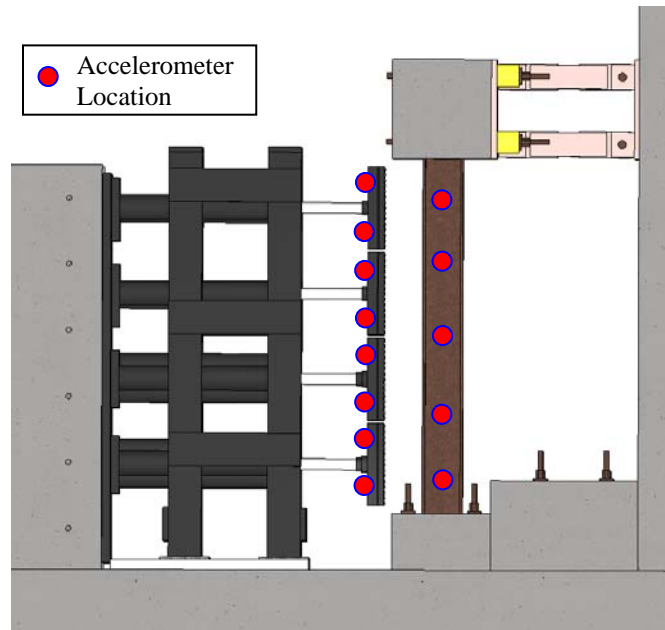
Figure 3.18: Accelerometer Locations
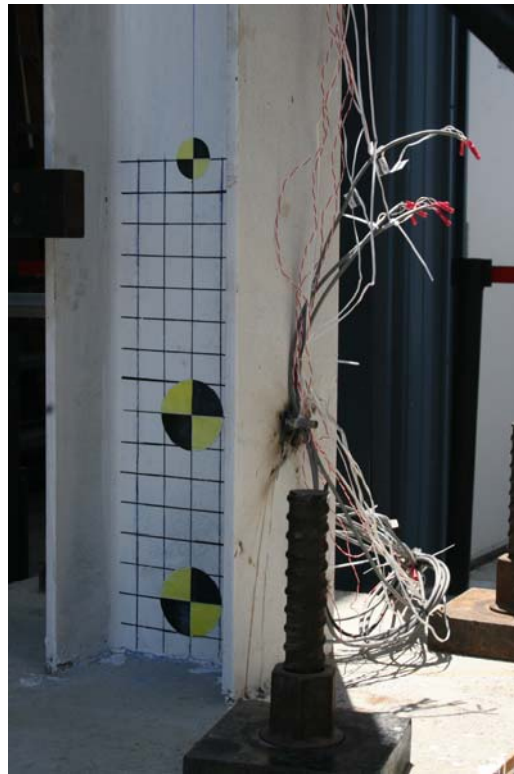
Figure 3.19: Mounted Accelerometer
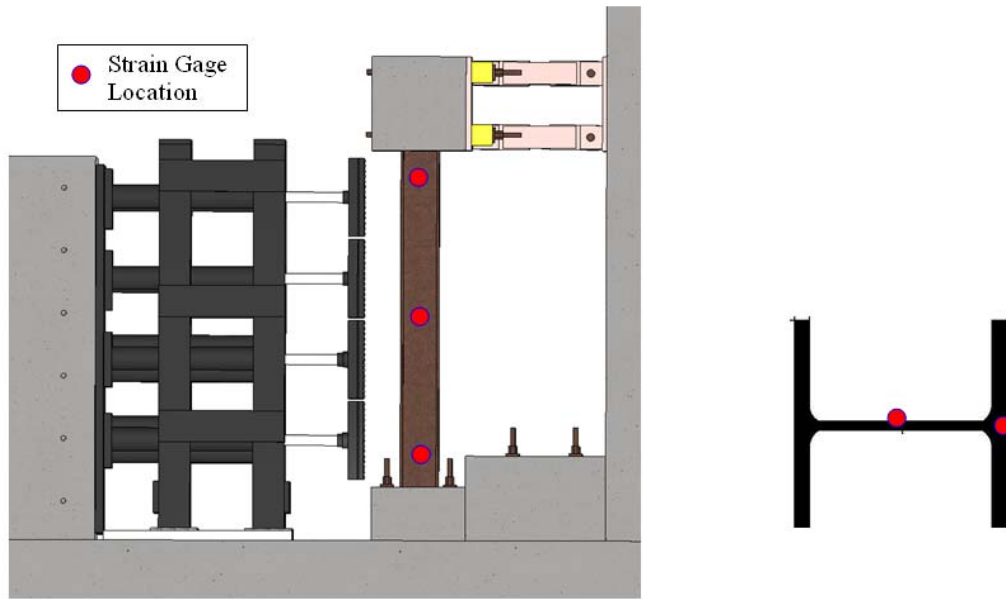
Figure 3.20: Strain Gage Locations
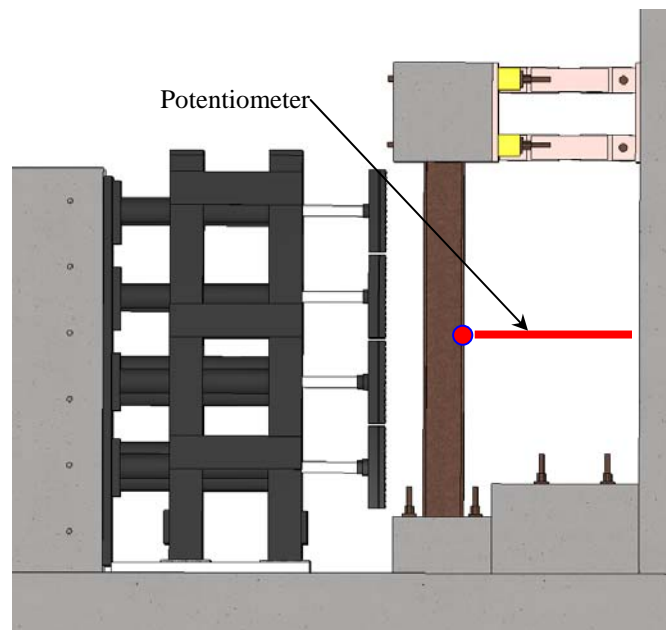
Figure 3.21: Location of the Linear Potentiometer

3.2   Data Analysis Methodologies

This section discusses the methods used to analyze data and produce important parameters for quantifying both BG and specimen behaviors. The systematic approach and examples that are given were consistently used in all strong axis tests.

3.2.1 BG Behavior

Impulse is the parameter that is used to define the load that is transferred from the BG onto the specimen over a period of time. Quantifying the impulse accurately is extremely important when using tests to validate finite element models. Two methods were used to measure the impulse for each BG. The first method employed the data from the accelerometers that are attached to each BG impacting plate. The second method used the average change in velocity of the BG at impact.

The first method initially converts the BG accelerations to an equivalent column pressure load as is discussed in [14]. The procedure here has been modified to address the variable velocity of each BG along the height of the column. For a given average acceleration time history, $a_n(t)$, for each number BG, n, the equivalent pressure, $p_n(t)$, over the corresponding impacted area can be calculated as follows:

$$p_n(t) = \frac{M_{n,eff} a_n(t)}{A_{n,eff}} \tag{3.1}$$

$$M_{n,eff} = mL_n \tag{3.2}$$

$$A_{n,eff} = b_f L_n \tag{3.3}$$

where the effective mass, $M_{n,eff}$, is found by multiplying the tributary length of impacted area, L_n, by the mass of one unit length of the steel column. The effective area, $A_{n.eff}$, is found by multiplying the tributary length by the column width, b_f. The corresponding specific impulse, $i_{s,n}(t)$, for each BG can be found using

$$i_{s,n}(t) = \int p_n(t)dt \tag{3.4}$$

It should be noted that impulse divided by area is typically called specific impulse with associated units of psi-ms. The integration of force with respect to time is often referred to as impulse with units of lb-ms, however, it is customary in the blast community to refer to specific impulse simply as impulse, and is done throughout this dissertation.

Figure 3.22 gives an example of the average acceleration-time history for one BG in this test series. Using Equation (3.1) through Equation (3.3), the corresponding pressure-time history can be computed using the geometry of the effective impact areas. From this, the impulse can be calculated using Equation (3.4). Figure 3.23 shows the pressure and impulse histories for the given acceleration in Figure 3.22.
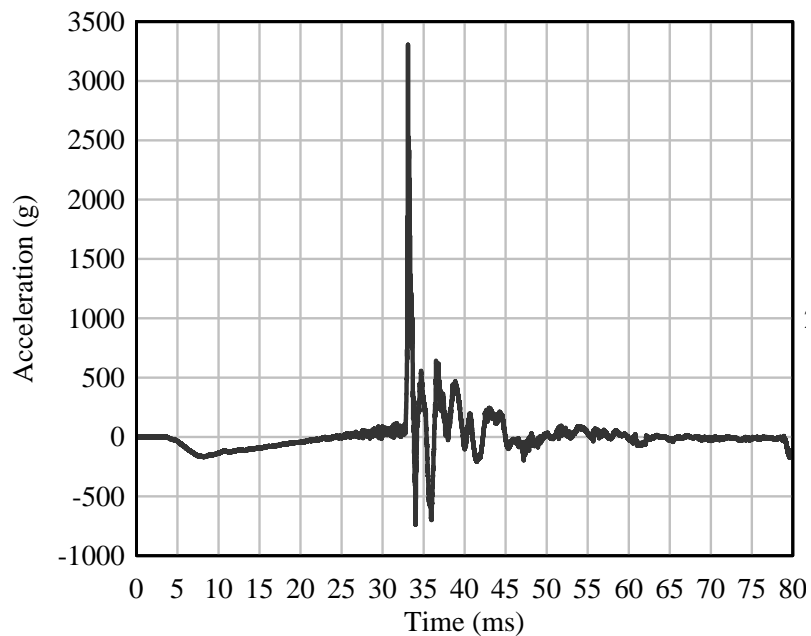
Figure 3.22: Acceleration Time-History for Single BG
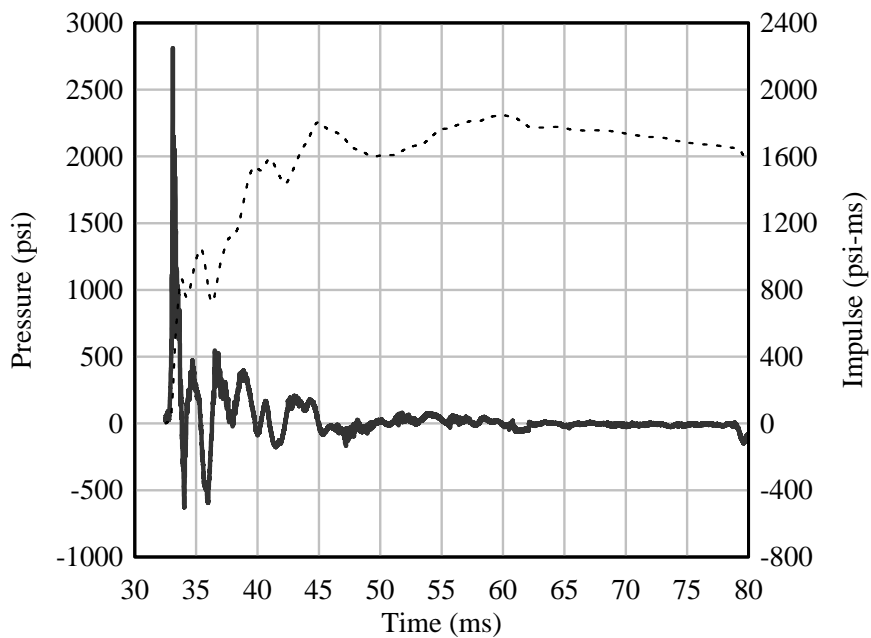
Figure 3.23: Corresponding Pressure and Impulse History for Single BG

The second method of determining the impulse is used mainly as a check of the previous method. This procedure utilizes momentum transfer to calculate the corresponding impulse. In this case, the change in BG velocity, Δv_n, during impact is scaled by the corresponding BG mass, m_n, and effective impact area, $A_{n,eff}$, to calculate the specific impulse for each BG as follows:

$$i_{s,n} = \frac{m_n \Delta v_n}{A_{n,eff}} \tag{3.5}$$

The change in velocity can be determined using three methods. The first method used the integration of the acceleration-time history of the BG impacting masses. The second method used the feedback of the control system and the third method used the displacement record generated with the TEMA software. Figure 3.24 gives an example of a velocity-time history recording from the high speed cameras. The plot shows the final velocity oscillates near zero velocity before the module decelerates and begins to retract. The change in velocity is determined by taking the average over the first two oscillations as is also shown in Figure 3.24. This method gives more accurate answers when the collision is elastic. In some cases, especially during the higher velocity impacts, the collisions behave inelastically meaning the two masses stick together during impact. Also, a large variation in masses between the impacting mass and the specimen sometimes led to multiple impact if the BG could not decelerate the mass fast enough. An example of a inelastic, multiple impact velocity-time history is shown in Figure 3.25. It is for this reason, that the momentum method should is used as a rough verification of the previous method and could produce some errors if used independently.
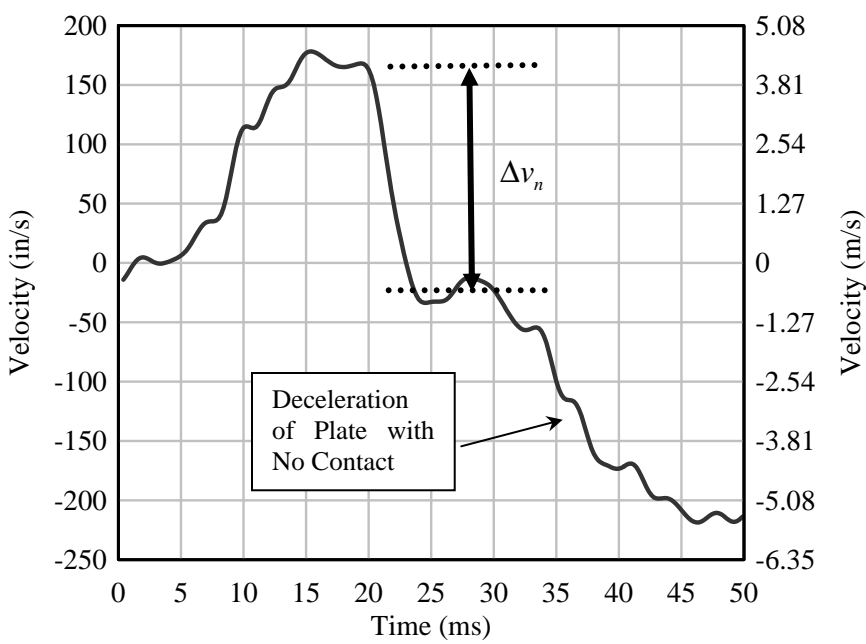
Figure 3.24: Velocity-Time History of BG at Impact – Elastic
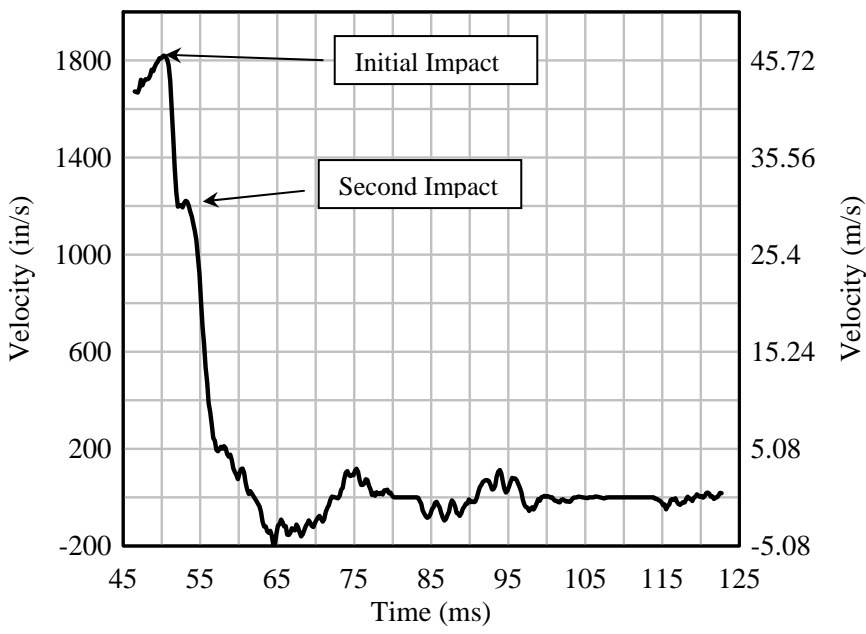
Figure 3.25: Velocity-Time History of BG Impact - Inelastic

3.2.2 Specimen Behavior

The behavior of the specimen was quantified using maximum and residual displacements at varying locations. For the strong axis tests, a global displacement of the column was one parameter that was consistently used as a measure to discuss specimen behavior. The displacements were found using two methods. The first method used the data from the high speed cameras and the TEMA software that can identify the position at each target location throughout the test. Figure 3.26 gives an example of a displacement-time history of the specimen at specified locations using the software. The second method, used as a check, integrated the acceleration-time histories from the accelerometers that were mounted on the specimen.
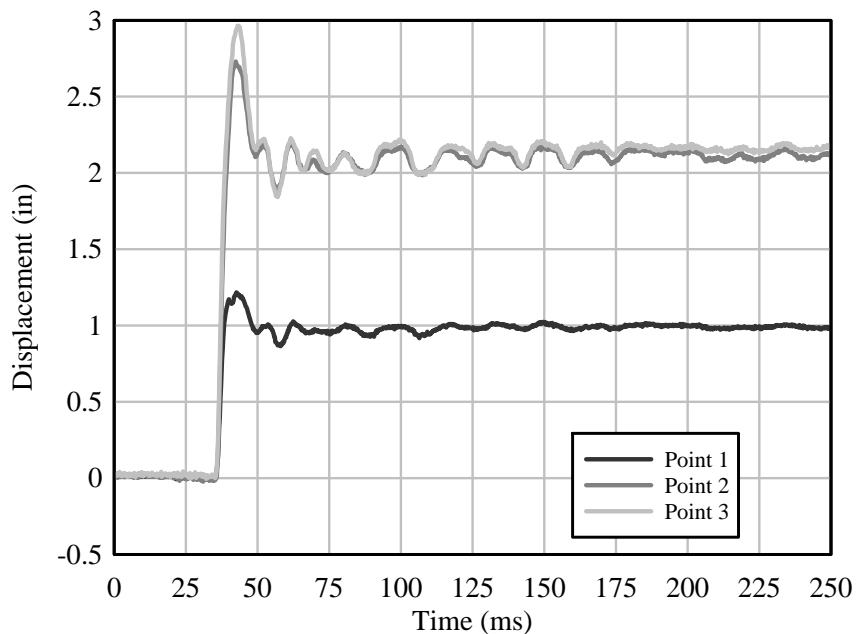
Figure 3.26: Specimen Displacements from *TEMA* Software

3.3   Test Results

Test Results from each of the eleven tests are discussed in this section. Detailed

analysis is given for Test SA01 in the following section. For the remainder of the tests, a

summary is given and any relevant or unique features are noted.

3.3.1   Test SA01

Test SA01 was the initial test conducted on Specimen 1. The test occurred on July

15, 2008. This was a low velocity test with uniform velocity. The target velocity at

impact was 4 m/s. The goal of this test was to check the system and setup with the

column remaining elastic so that it could be re-tested.

Initial Setup

The setup for Test SA01 is discussed in detail in Section 3.1.1. A photo of the

column pre-test is shown in Figure 3.27. The column was painted white to increase

contrast for the high speed camera and targets were bonded to the column and locations

recorded.

BG Behavior

Each impacting mass was instrumented with three accelerometers. The average of

each of the outputs was taken and plots of the average accelerations for each BG are

shown in Figure 3.28. It should be noted that all plots are smoothed and the peak values

may be clipped, but any corresponding tables give the recorded value. The maximum

acceleration was 232.4 g. The BGs impacted in the order 4 , 3 , 2 , 1. The total spread

from first to last impact was 0.50 ms. Table 3.2 gives a summary of peak acceleration,

impact time and duration for each BG and the average.

Figure 3.27: Test SA01 Column Pre-Test

Table 3.2: Test SA01 BG Impact Details

BG	Peak Acceleration (g)	Impact Time (ms)	Duration (ms)
1	232.4	19.75	4.81
2	159.9	19.61	6.93
3	216.5	19.58	6.67
4	222.3	19.25	3.84
Average	207.8	19.54	5.56
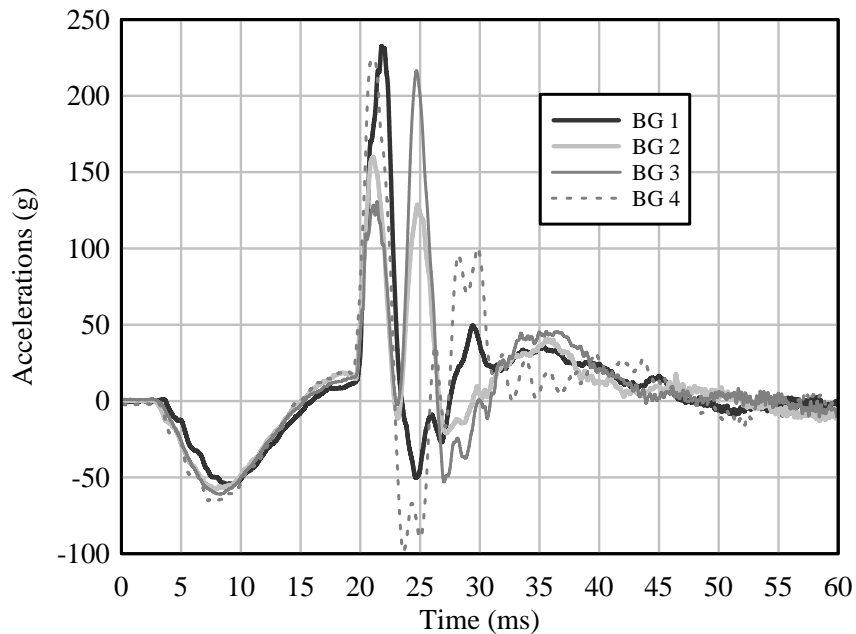
Figure 3.28: Test SA01 Average BG Accelerations

Impact velocities of the BGs were determined using two methods as discussed in Section 3.2. The first method determined impact velocity using visual data from the Phantom Cameras and the TEMA software (Figure 3.29). The second method was measured from the control system and gives the displacement of the BG mass which was converted to velocity. Table 3.3 gives a summary and average of impact velocities.

Pressure and impulse were found using the average acceleration of each BG. These time histories are shown in Figure 3.30 and Figure 3.31. The maximum pressure of 188.2 psi was found with the maximum impulse of 400.3 psi-ms using this method. These values are summarized in Table 3.4.
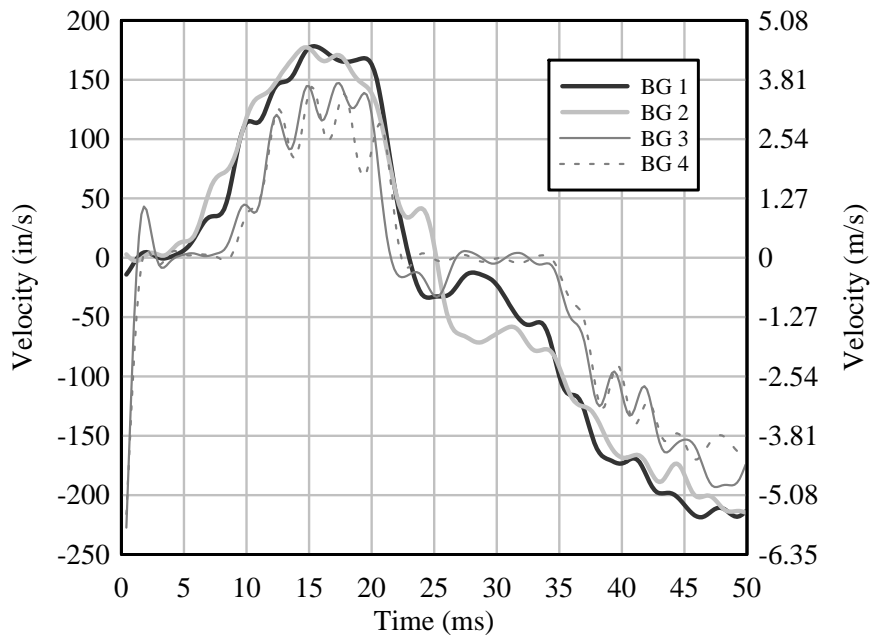
Figure 3.29: Test SA01 BG Impact Velocities from Camera Data

Table 3.3: Test SA01 BG Impact Velocities

BG	Camera Impact Velocity in/s, (m/s)	Control Impact Velocity in/s, (m/s)	Average Impact Velocity in/s, (m/s)
1	133.5 (3.4)	143.6 (3.7)	138.5 (3.5)
2	169.9 (4.3)	140.3 (3.6)	155.1 (3.9)
3	139.7 (3.5)	150.0 (3.8)	144.9 (3.7)
4	117.8 (3.0)	115.2 (2.9)	116.5 (3.0)
Average	140.2 (3.6)	137.3 (3.5)	138.8 (3.5)

Table 3.4: Test SA01 Pressures and Impulses

BG	Peak Pressure (psi)	Impulse from Accelerometer (psi-ms)
1	188.2	379.0
2	122.9	328.8
3	171.5	400.3
4	168.8	284.9
Average	162.9	348.3
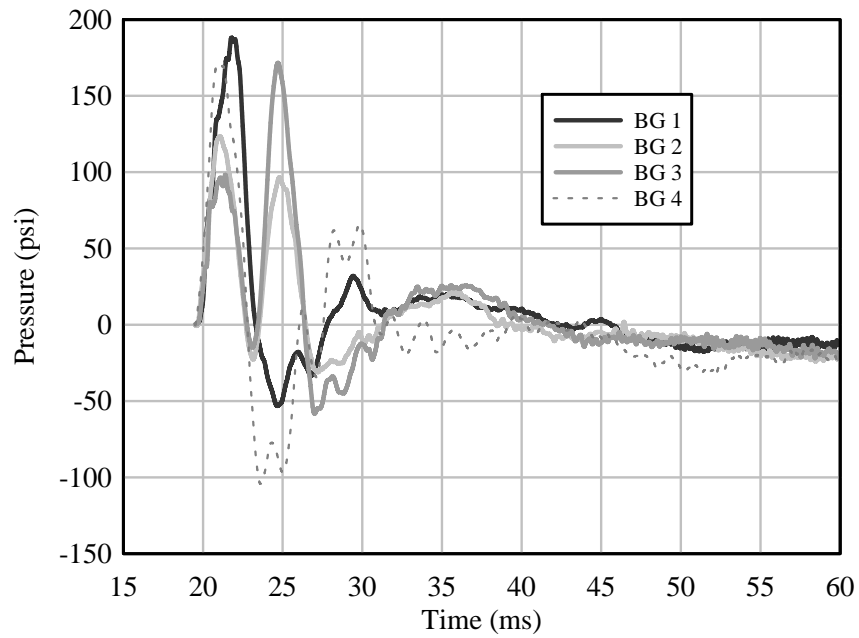
Figure 3.30: Test SA01 Pressures from Accelerometer Data
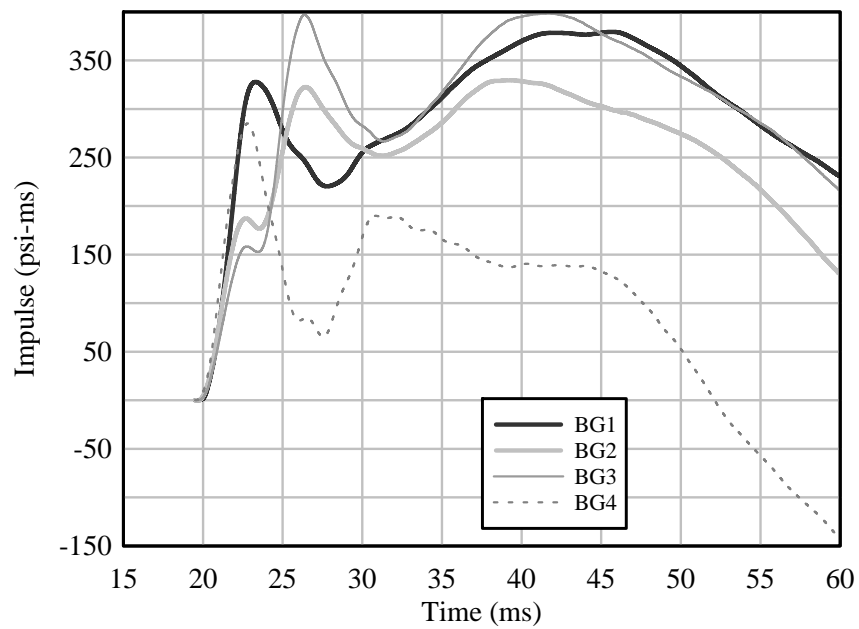
Figure 3.31: Test SA01 Impulses from Accelerometer Data

Specimen Behavior

Figure 3.32 shows the very slight progression of damage as recorded at 5,000 frames per second. In (a), the column is instrumented and the BGs are set to the correct initial position. The initial impact is shown in (b) and the synchronicity of the BGs can be seen. Figures (c) and (d) capture the slight movement of the column while the masses are in contact. Figure (e) shows that there is almost zero residual displacement of the column as the masses retract.
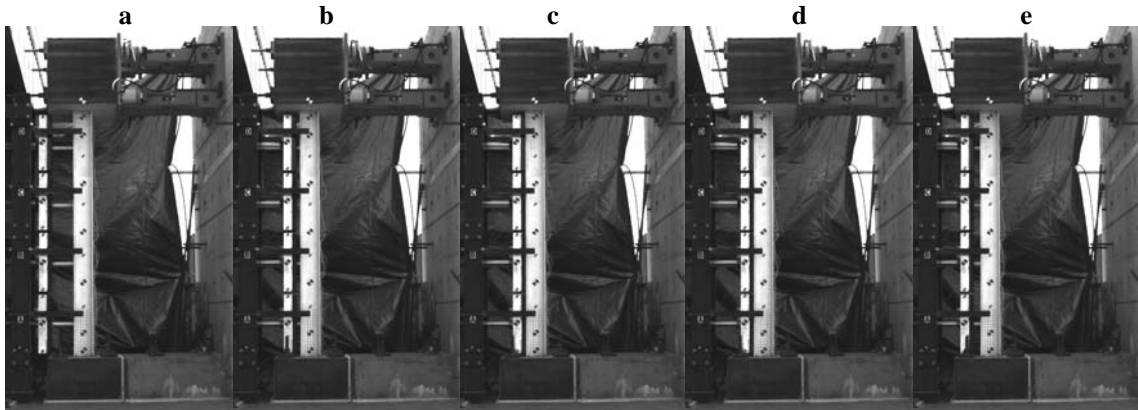
Figure 3.32: Test SA01 Progression of Damage

Accelerations of the specimen were recorded at five locations with accelerometers attached to the back (non-impact) side of the column. Plots of the accelerations are shown in Figure 3.33 with a maximum acceleration of 241.6 g at the midspan. Table 3.5 gives a summary of peak acceleration for each accelerometer.

Displacements were measured using the camera data and the tracking software and is shown in Figure 3.34. Table 3.6 gives a summary of the maximum and residual displacement at multiple locations measured with the tracking software and the accelerometers.
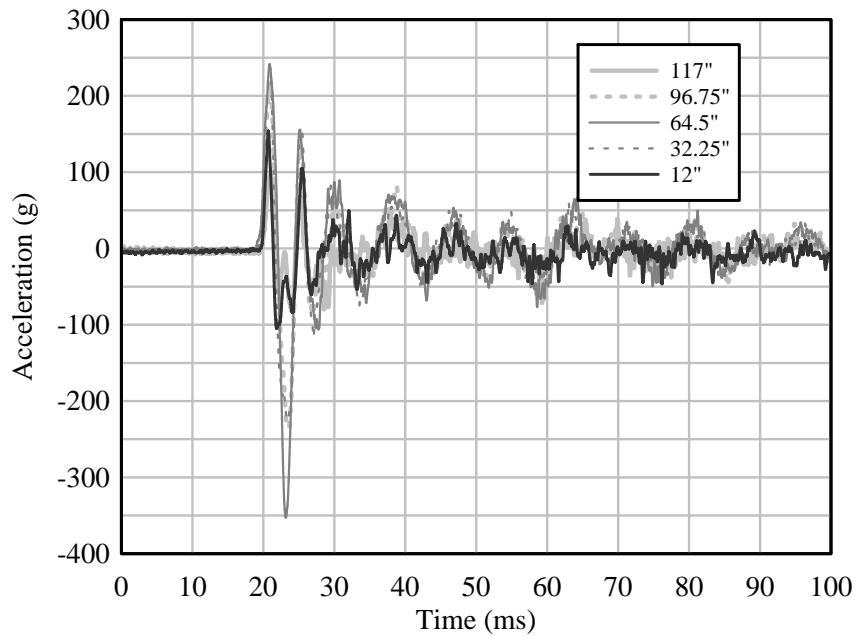
Figure 3.33: Test SA01 Specimen Accelerations

Table 3.5: Test SA01 Specimen Accelerations

Distance from Base (in)	Peak Acceleration (g)
117.0	96.3
96.75	219.1
64.5	241.6
32.25	235.8
12.0	153.9

Table 3.6: Test SA01 Specimen Displacements

Distance from Base (in)	Maximum Displacement (in)	Residual Displacement (in)
126.0	0.05	0.00
117.0	0.11	0.00
90.75	0.18	0.00
64.5	0.30	0.01
38.25	0.23	0.00
12.0	0.09	0.00
3.0	0.03	0.00
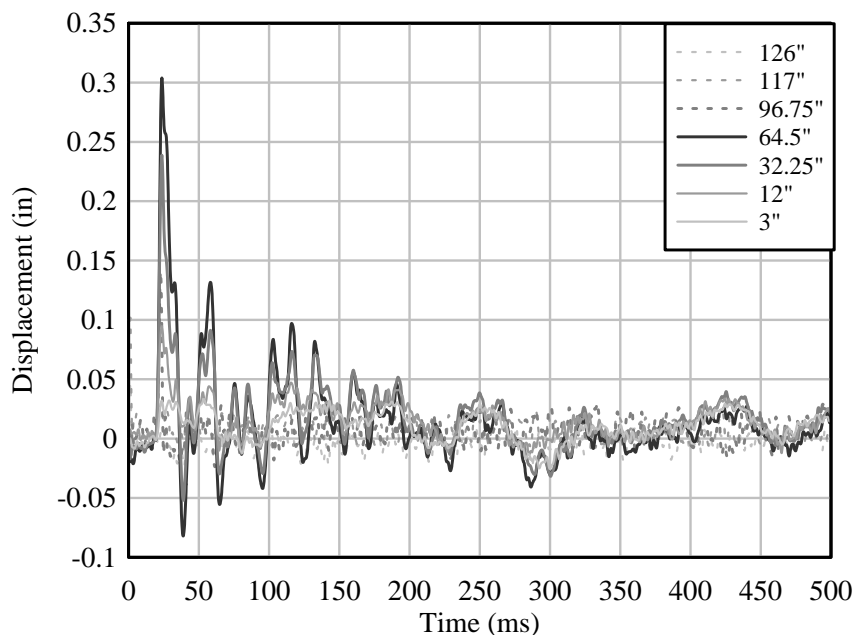
Figure 3.34: Test SA01 Specimen Displacement from Camera Data

3.3.2 Test SA02

Test SA02 was the second hit of Specimen 1 on July 18, 2008. For all purposes, it was assumed that the column remained perfectly elastic during Test SA01. The slight 0.01 in residual displacement is neglected. This test was considered a "medium" velocity test with target velocity of 18 m/s.

Initial Setup

The setup for Test SA02 is the same as Test SA01 and is discussed in Section 3.3.1. A photo of the column pre-test is shown in Figure 3.35.

Figure 3.35: Test SA02 Column Pre-Test

BG Behavior

Each impacting mass was instrumented with three accelerometers and the average of each of the outputs was taken. The maximum acceleration was 3,760 g from BG3. The BGs impacted in the order 2, 1, 3, 4. The total spread from first to last impact was 0.54 ms. Table 3.7 gives a summary of peak acceleration, impact time and duration for each BG and the averages.

Table 3.7: Test SA02 BG Impact Details

BG	Peak Acceleration (g)	Impact Time (ms)	Duration (ms)
1	2630	32.70	4.17
2	--	--	--
3	3760	33.02	2.40
4	1960	33.24	2.74
Average	2790	33.0	3.10

Impact velocities of the BGs were again determined using two methods. The first method determined impact velocity using visual data from the Phantom cameras. The second method's measurement was from the feedback of the control system which gave the displacement of the BG mass which was converted to velocity. Table 3.8 gives a summary and average of impact velocities.

Table 3.8: Test SA02 BG Impact Velocities

BG	Camera Impact Velocity in/s, (m/s)	Control Impact Velocity in/s, (m/s)	Average Impact Velocity in/s, (m/s)
1	692.6 (17.6)	710.0 (18.0)	701.3 (17.8)
2	665.3 (16.9)	658.1 (16.7)	661.7 (16.8)
3	667.2 (16.9)	712.3 (18.1)	689.8 (17.5)
4	653.7 (16.6)	655.1 (16.7)	654.4 (16.6)
Average	669.7 (17.0)	638.9 (17.4)	676.8 (17.2)

Pressures and impulses were found using the average acceleration of the BGs. The maximum pressure of 3,210 psi was recorded. The maximum impulse is 1,724 psi-ms using this method. These values are summarized in Table 3.9.

Table 3.9: Test SA02 Pressures and Impulses

BG	Peak Pressure (psi)	Impulse from Accelerometer (psi-ms)
1	2230	1714
2	--	--
3	3210	1724
4	1620	1540
Average	2350	1659

Specimen Behavior

Figure 3.36 shows the progression of damage as recorded at 5,000 frames per second. In (a), the column is undeformed and the BGs are set to the correct initial

position. The initial impact is shown in (b) and the synchronicity of the BGs can be seen. Figures (c) through (f) capture the propagation of deformation of the column while the masses are in contact with the column. Figure (g) displays the residual deformation of the specimen after the masses have retracted.

Figure 3.36: Test SA02 Progression of Damage

Accelerations of the specimen were recorded at five locations with accelerometers attached to the back (non-impact) side of the column. Table 3.10 gives a summary of peak acceleration and impact time for each accelerometer.

Table 3.10: Test SA02 Specimen Accelerations

Distance from Base (in)	Peak Acceleration (g)	Impact Time (ms)
117.0	2400	33.21
90.75	2380	32.94
64.5	2010	32.94
38.25	2360	32.76
12.0	0	--

Global displacements were measured using the camera data. The maximum displacement of 1.86 in was located at 79.3 in from the base of the column. The maximum residual displacement of 1.08 in was found at a height of 38.1 in from the base

of the column. Figure 3.37 shows the column post-test from which the residual displacement was measured. Table 3.11 and Figure 3.38 provide a summary of the maximum and residual displacement at multiple locations.

Figure 3.37: Test SA02 Column Post-Test

Table 3.11: Test SA02 Specimen Displacements

Distance from Base (in)	Maximum Displacement (in)	Residual Displacement (in)
126.9	0.42	0.16
116.6	1.04	0.63
105.1	1.30	0.73
90.4	1.66	0.80
79.3	1.86	0.95
64.5	1.76	0.94
52.0	1.81	0.94
38.1	1.60	1.08
25.5	1.26	1.09
12.0	0.80	0.63
3.0	0.30	0.30
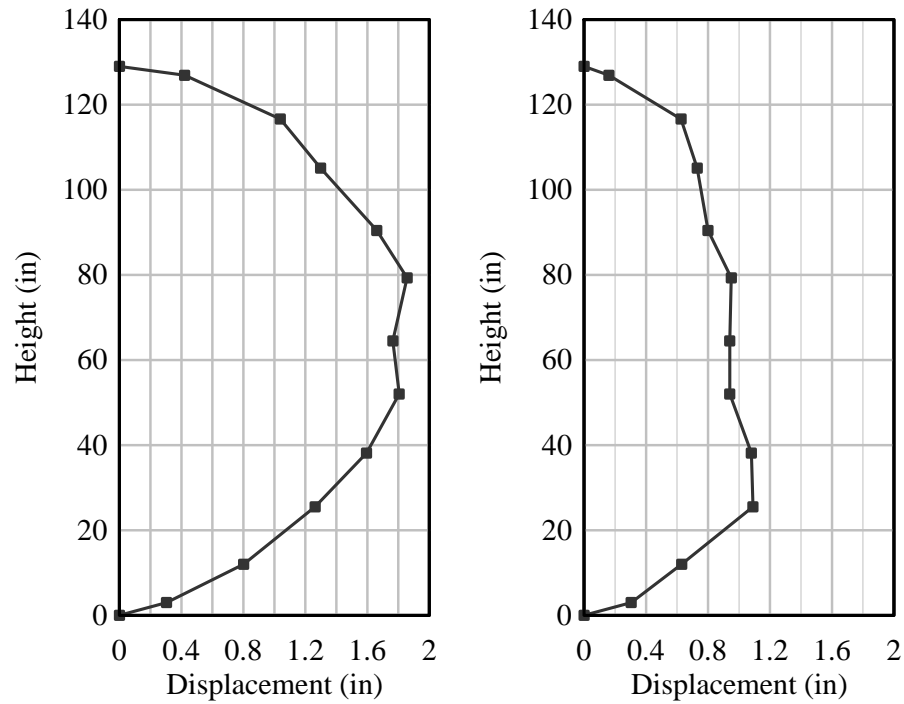
Figure 3.38: Test SA02 Maximum (left) and Residual (right) Displacements

3.3.3 Test SA03

Test SA03 was the only experiment on Specimen 2. This test used the full velocity capability of the BG25s with target impact velocity of 26 m/s. This test was the last test conducted with uniform velocity using the four BG25s.

Initial Setup

The setup for Test SA03 is discussed in detail in Section 3.1.1. Photos of the column pre-test are shown in Figure 3.39 and Figure 3.40. The column was painted to increase contrast for the high speed camera and targets were bonded to the column and locations recorded.

Figure 3.39: Test SA03 Column Pre-Test
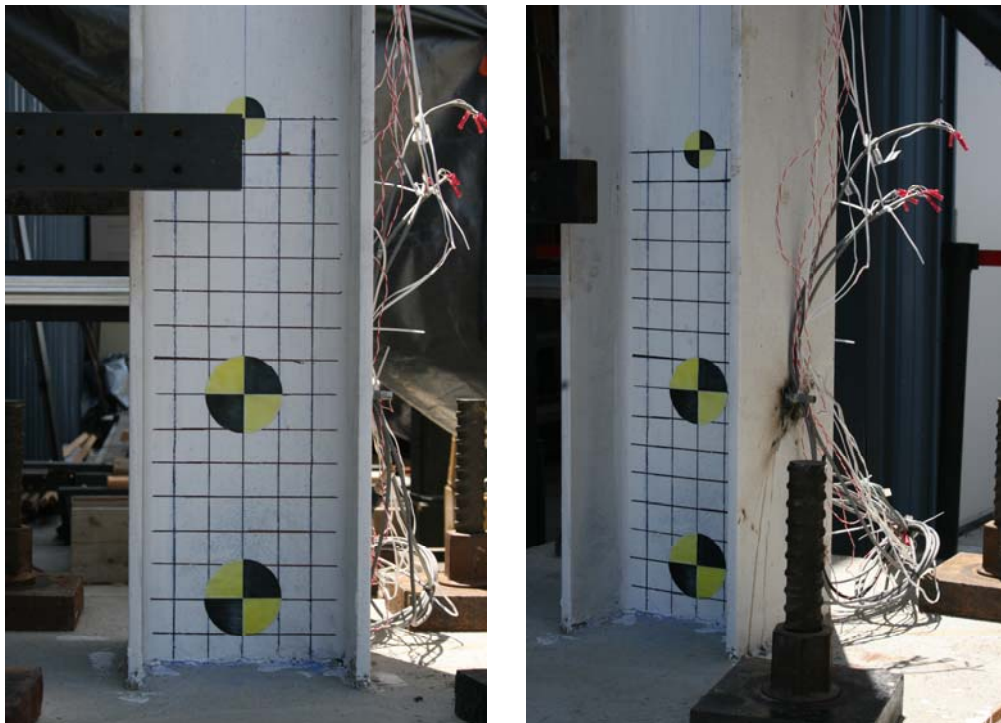
Figure 3.40: Test SA03 Column Base Pre-Test

BG Behavior

Each impacting mass was instrumented with three accelerometers. The maximum acceleration was 6,520 g. The BGs impacted in the order 3, 4, 1, 2. The total spread from first to last impact was 0.37 ms. Table 3.12 also gives a summary of peak acceleration, impact time and duration for each BG and the average.

Table 3.12: Test SA03 BG Impact Details

BG	Peak Acceleration (g)	Impact Time (ms)	Duration (ms)
1	4060	35.26	2.61
2	2150	35.58	2.60
3	6520	35.21	1.29
4	4650	35.25	2.70
Average	4350	35.32	2.30

Again, impact velocities of the BGs were determined using two methods. In the first method, impact velocity was determined using visual data from the Phantom Cameras and the TEMA software. The second method of measurement used feedback from the control system and gives the displacement of the BG mass which was converted to velocity. Table 3.13 gives a summary and average of impact velocities.

Table 3.13: Test SA03 BG Impact Velocities

BG	Camera Impact Velocity in/s, (m/s)	Control Impact Velocity in/s, (m/s)	Average Impact Velocity in/s, (m/s)
1	937.6 (23.8)	959.3 (24.4)	948.4 (24.1)
2	909.9 (23.1)	1010.0 (25.7)	960.0 (24.4)
3	903.4 (22.9)	995.4 (25.2)	949.4 (24.1)
4	901.2 (22.9)	963.3 (24.5)	932.2 (23.7)
Average	913.0 (23.2)	982.0 (24.9)	947.5 (24.1)

Pressures and impulses were found using the average acceleration of the BGs. The maximum pressure of 5,520 psi was recorded. The maximum impulse is 2,024 psi-ms using this method. These values are summarized in Table 3.14.

Table 3.14: Test SA03 Pressures and Impulses

BG	Peak Pressure (psi)	Impulse from Accelerometer (psi-ms)
1	3440	1657
2	1830	2024
3	5520	1876
4	3950	1702
Average	3680	1815

Specimen Behavior

The damage progression for this test is given in Figure 3.32. In (a), the BGs are set to the correct initial position. The initial impact is shown in (b) and the synchronicity of the BGs can be seen. Figures (c) through (f) capture the propagation of deformation of the column while the masses are in contact with the column. Figure (g) displays the residual deformation of the specimen after the masses have retracted.

Figure 3.41: Progression of Damage

Accelerations of the specimen were recorded with accelerometers attached to the back (non-impact) side of the column. A maximum acceleration of 7,480 g was recorded at the midspan. Table 3.15 gives a summary of peak acceleration and impact time.

Table 3.15: Test SA03 Specimen Accelerations

Distance from Base (in)	Peak Acceleration (g)	Impact Time (ms)
117.0	5970	35.21
90.75	5680	35.21
64.5	7480	35.21
38.25	6160	35.37
12.0	6630	35.28

The maximum displacement of 2.18 in was found at a height of 64.9 in from the base of the column. The maximum residual displacement was found to be 2.90 in, also 64.9 in from the base of the column. Table 3.16 gives a summary of the displacements. Figure 3.42 and Figure 3.43 show the column post-test. A plot of the maximum and residual displacements over the height of the column is shown in Figure 3.44.

Table 3.16: Test SA03 Specimen Displacements

Distance from Base (in)	Maximum Displacement (in)	Residual Displacement (in)
126.9	0.40	0.11
117.2	1.27	1.01
105.6	2.00	1.53
91.2	2.54	1.90
78.7	2.17	1.98
64.9	2.90	2.18
53.0	2.90	2.17
38.4	2.66	2.15
24.1	2.19	1.78
12.1	1.20	0.90
3.0	0.56	0.25
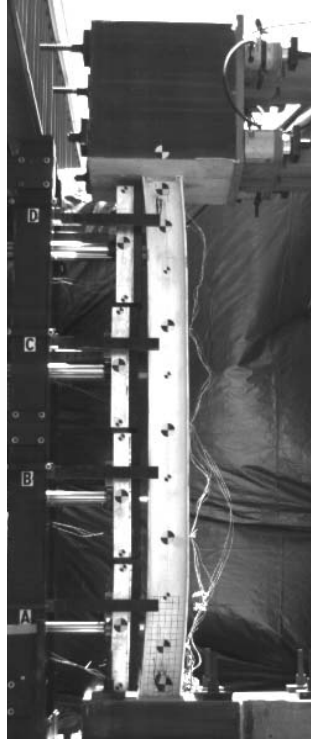
Figure 3.42: Test SA03 Column Post-Test
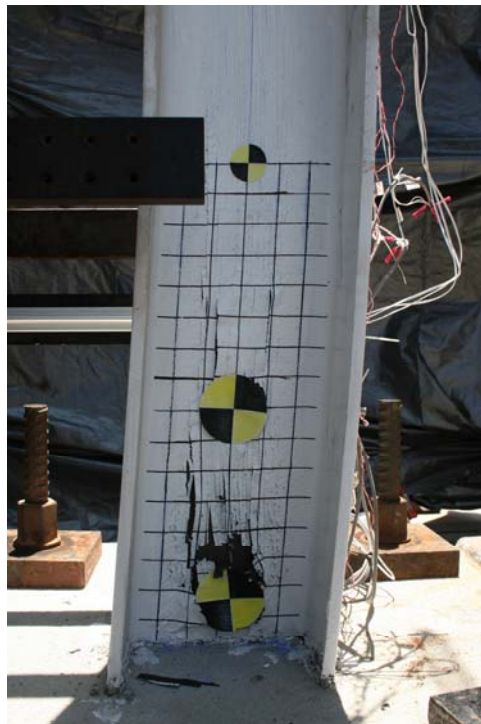
Figure 3.43: Test SA03 Column Base Post-Test
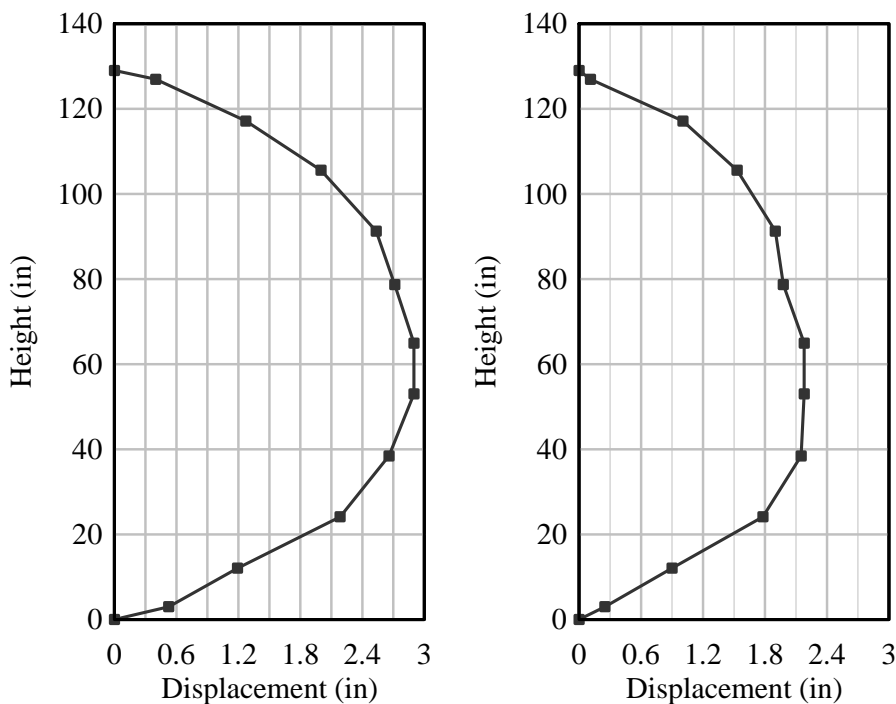
Figure 3.44: Test SA03 Maximum (left) and Residual (right) Displacements

3.3.4 Test SA04-SA06

Tests SA04 through SA06 were all conducted on the same W14x132 specimen using variable velocity. The setup is discussed in Section 3.2.2 with two BG50s and two Bg25s. The first test, Test SA04, was intended to be a low velocity test to check the synchronicity of the BGs, but unfortunately the inputs entered into the control system were incorrect and the desired impulsive loading was not executed. Also, because of the incorrect input, no data was correctly recorded and there was residual deformation after this test. Tests SA05 and SA06 were both low level velocity tests used to test the synchronicity of the BGs on the deformed specimen. Because the pressures and impulses applied to the column are unknown, only the displacements will be shown so they can be used as an input for Test SA07.

Initial Setup

The setup for the W14x132 columns for Test SA04 though Test SA06 is discussed in detail in Section 3.1.1. In addition to the instrumentation used in the previous tests, a linear potentiometer was installed to measure midspan displacement of the column.

Specimen Behavior

Figure 3.45 shows the damage after Tests SA04 through Test SA06. The displacements were not able to be recorded throughout the tests, but the residual displacements are given in Table 3.17 and Figure 3.46.
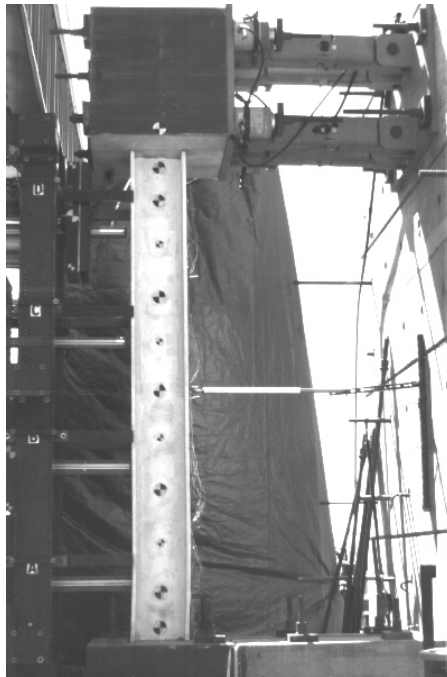
Figure 3.45: Tests SA04-SA06 Column Post-Test

Table 3.17: Tests SA04-SA06 Specimen Displacements

Distance from Base (in)	Residual Displacement (in)
126.0	0.16
117.0	0.18
90.75	0.18
64.5	0.25
38.25	0.52
12.0	0.45
3.0	0.18
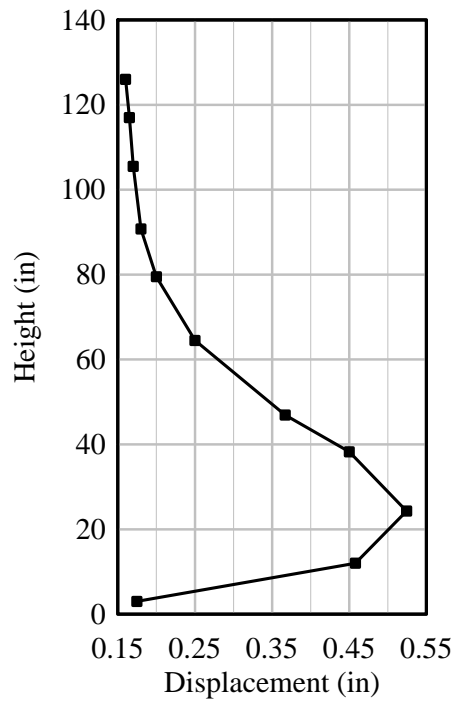
Figure 3.46: Tests SA04 - SA06 Residual Displacements

3.3.5 Test SA07

Test SA07 was the first high level impact at variable velocity. The deformed specimen impacted in Tests SA04-SA06 was used. Target velocities are given in Table 3.18. These velocities were chosen because together they create impulses that vary along the height of the column similar to that of a vehicle bomb at the curb.

Table 3.18: Test SA07 Target Impact Velocities

BG	Target Velocity in/s (m/s)
1	1744.1 (44.3)
2	1389.8 (35.3)
3	1003.9 (25.5)
4	503.9 (12.8)

Initial Setup

The setup for this test was the same for the setup described in the previous section. The specimen was initially deformed as shown in Figure 3.45.

BG Behavior

Each impacting mass was instrumented with two accelerometers. The maximum acceleration was 12,091 g. The BGs impacted in the order 4, 2, 3, 1. The total spread from first to last impact was 1.03 ms. Table 3.19 gives a summary of peak acceleration, impact time and duration for each BG and the average. Impact velocities of the BGs were determined using impact velocity from the Phantom cameras and the TEMA software. Table 3.20 gives a summary of impact velocities.

Table 3.19: Test SA07 BG Impact Details

BG	Peak Acceleration (g)	Impact Time (ms)	Duration (ms)
1	6180	53.45	5.05
2	12091	53.09	2.91
3	2573	53.42	3.25
4	848	52.42	2.84

Table 3.20: Test SA07 BG Impact Velocities

BG	Camera Impact Velocity in/s, (m/s)
1	1759.4 (44.7)
2	1456.8 (37.0)
3	982.0 (24.9)
4	443.5 (11.3)

Pressures and impulses were found using the average acceleration of the BGs. The maximum pressure of 19,040 psi was recorded. The maximum impulse is 8,057 psi-ms using this method and the values are summarized in Table 3.21.

Table 3.21: Test SA07 Pressures and Impulses

BG	Peak Pressure (psi)	Impulse from Accelerometer (psi-ms)
1	9810	6875
2	19040	8057
3	4150	5196
4	1080	1200

Specimen Behavior

Figure 3.47 shows the progression of damage as recorded at 5,000 frames per second. In (a), the column is undeformed and the BGs are set to the correct initial position. The initial impact is shown in (b) and the synchronicity of the BGs can be seen.

Figures (c) through (f) capture the propagation of deformation of the column while the masses are in contact with the column. Figure (g) displays the residual deformation of the specimen after the masses have retracted.

Figure 3.47: Test SA07 Progression of Damage

Accelerations of the specimen were recorded at five locations with accelerometers attached to the back (non-impact) side of the column. Table 3.22 gives a summary of peak acceleration and impact time.

Displacements were measured using the camera data and the tracking software. At some locations, the targets did not remain attached to the column and the displacements were estimated using the tracking software. A maximum displacement of 4.65 in was found at a height of 38.6 in from the base of the column. Figure 3.48 and Figure 3.49 show the column post-test. The maximum residual displacement of 3.98 in was found 38.6 in from the base of the column. Table 3.23 gives a summary of the maximum and residual displacement at the locations measured and plots are shown in Figure 3.50.

Table 3.22: Test SA07 Specimen Accelerations

Distance from Base (in)	Peak Acceleration (g)	Impact Time (ms)
117.0	3092	53.66
90.75	3271	53.49
64.5	9062	53.10
38.25	22740	53.23
12.0	16901	53.42

Table 3.23: Test SA07 Specimen Displacements

Distance from Base (in)	Maximum Displacement (in)	Residual Displacement (in)
125.9	0.51	0.35
116.5	1.22	0.85
104.4	2.31	1.77
89.9	3.42	2.60
77.5	4.01	3.04
64.6	4.31	3.44
52.3	4.65	3.82
38.6	4.65	3.98
25.1	4.05 (approx.)	3.33 (approx.)
12.0	2.89 (approx.)	2.42 (approx.)
3.0	1.02 (approx.)	1.12 (approx.)

Figure 3.48: Test SA07 Column Post-Test

Figure 3.49: Test SA07 Column Base Post-Test
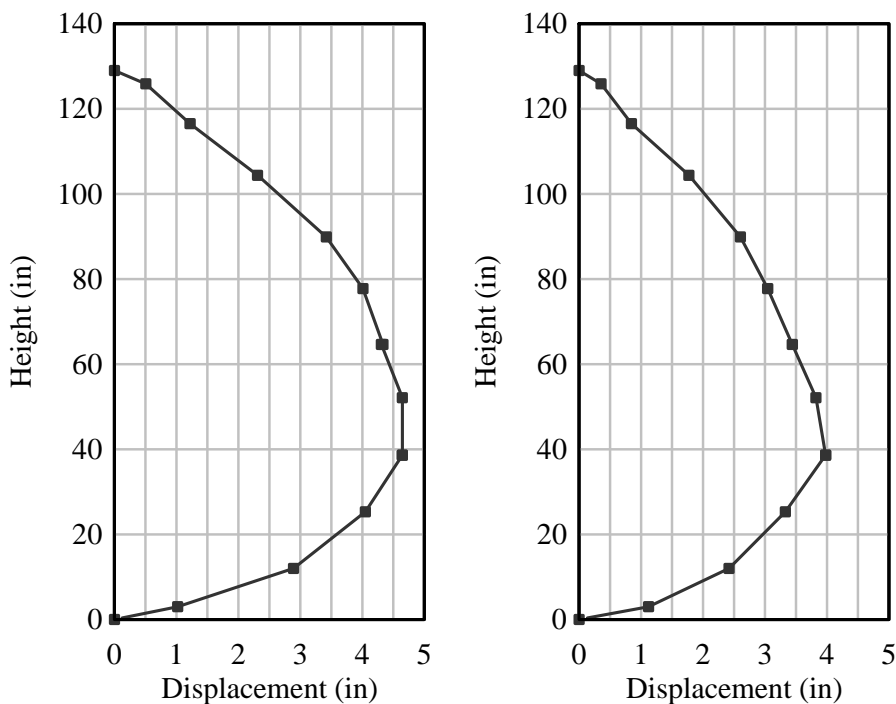
Figure 3.50: Test SA07 Maximum (left) and Residual (right) Displacements

3.3.6 Test SA08 & SA9

Test SA08 and SA09 were conducted on Specimen 4 on October 7 and 8, 2008. The first test, SA08, was a low variable velocity impact that was conducted to check the synchronicity and test setup. There was no permanent deformation after the test. Test SA09 was a high velocity impact similar to those in Test SA07, but on an undeformed specimen. The target impact velocities are shown in Table 3.24.

Table 3.24: Test SA09 Target Impact Velocities

BG	Target Velocity in/s (m/s)
1	1755.9 (44.6)
2	1401.6 (35.6)
3	1007.9 (25.6)
4	507.9 (12.9)

Initial Setup

The setup for Test SA09 is discussed in Section 3.1.1. Photos of the column pre-test are shown in Figure 3.51 and Figure 3.52. The column was painted to increase contrast and targets were bonded to the web. A linear potentiometer was used at midspan.

BG Behavior

Each impacting mass was instrumented with three accelerometers. The maximum acceleration was 18,550 g. The BGs impacted in the order 2, 1, 3, 4. The total spread from first to last impact was 2.01 ms. Table 3.25 gives a summary of peak acceleration, impact time and duration for each BG and the average.

Table 3.25: Test SA09 BG Impact Details

BG	Peak Acceleration (g)	Impact Time (ms)	Duration (ms)
1	18550	52.66	1.34
2	18325	52.14	2.70
3	1000	53.82	7.57
4	700	54.15	4.84

The impact velocities were determined using visual data from the Phantom Cameras and the TEMA software. Table 3.27 gives a summary and average of impact velocities.

Table 3.26: Test SA09 BG Impact Velocities

BG	Camera Impact Velocity in/s, (m/s)
1	1780.0 (45.2)
2	1472.5 (37.4)
3	987.5 (25.1)
4	442.0 (11.2)

Figure 3.51: Test SA09 Column Pre-Test

Figure 3.52: Test SA09 Column Base Pre-Test

The impact velocities were determined using visual data from the Phantom Cameras and the tracking software. Table 3.27 gives a summary and average of impact velocities.

Table 3.27: Test SA09 BG Impact Velocities

BG	Camera Impact Velocity in/s, (m/s)
1	1780.0 (45.2)
2	1472.5 (37.4)
3	987.5 (25.1)
4	442.0 (11.2)

Pressures and impulses were found using the average acceleration of the BGs. The maximum pressure of 33,840 psi was recorded. The maximum impulse is 7,699 psi-ms using this method. These values are summarized in Table 3.28.

Table 3.28: Test SA09 Pressures and Impulses

BG	Peak Pressure (psi)	Impulse from Accelerometer (psi-ms)
1	30020	7699
2	33840	5800
3	1280	3544
4	780	1583

Specimen Behavior

Figure 3.53 shows the damage recorded at 5,000 frames per second. In (a), the BGs are set to the correct initial position. The initial impact is shown in (b) and the synchronicity of the BGs can be seen. Figures (c) through (e) capture the propagation of deformation of the column which is greatest seen at the base. Figure (f) displays the residual deformation of the specimen after the masses have retracted.
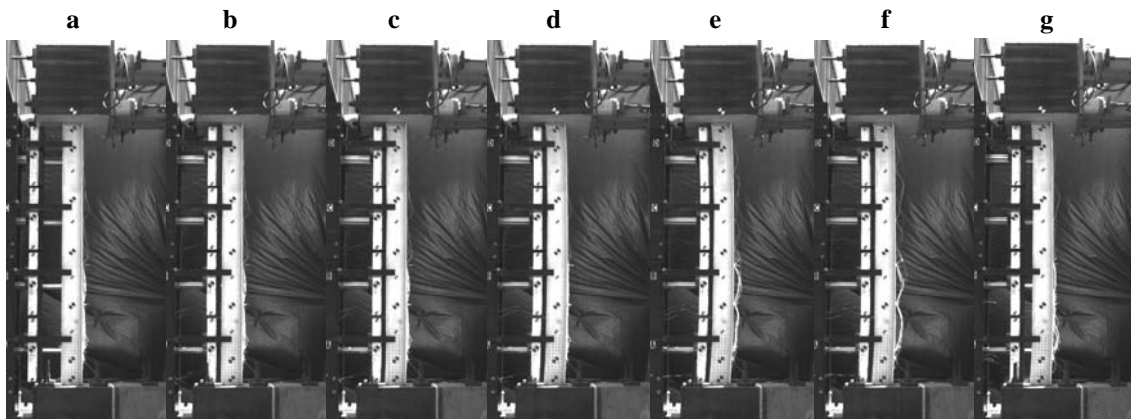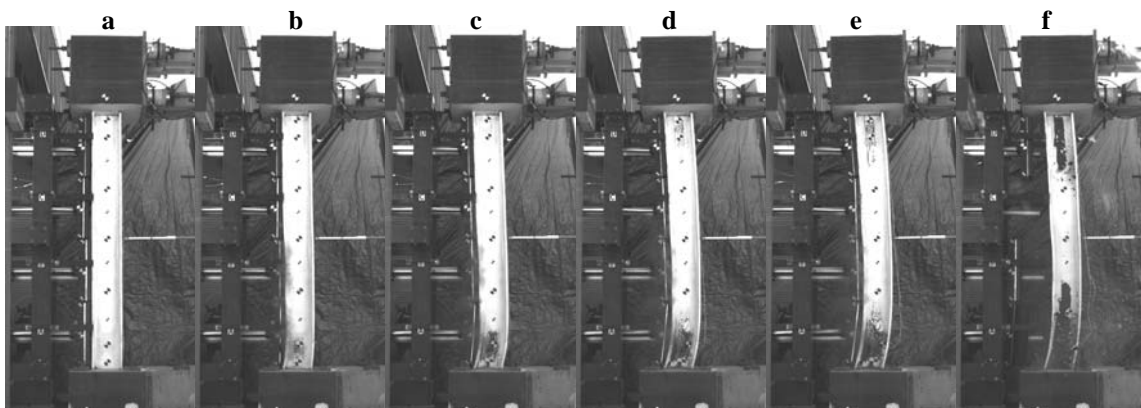
Figure 3.53: Test SA09 Progression of Damage

Accelerations of the specimen were recorded at five locations with accelerometers attached to the back (non-impact) side of the column. A maximum acceleration of 22840 g was recorded at the bottom of the column. Table 3.29 gives a summary of peak acceleration and impact time.

Table 3.29: Test SA09 Specimen Accelerations

Distance from Base (in)	Peak Acceleration (g)	Impact Time (ms)
117.0	6230	52.57
90.75	3090	52.61
64.5	7810	52.20
38.25	16160	52.20
12.0	22840	52.42

Displacements were measured using the camera data and the tracking software. The maximum displacement of 4.56 in was found at a height of 38.25 in from the base of the column. Table 3.30 gives a summary of the maximum and residual displacement at multiple locations. Figure 3.54 and Figure 3.55 shows the column post-test. Plots of the maximum and residual global displacement are shown in Figure 3.56.

Figure 3.54: Test SA09 Column Post Test

Figure 3.55: Test SA09 Column Base Post-Test

Table 3.30: Test SA09 Specimen Displacements

Distance from Base (in)	Maximum Displacement (in)	Residual Displacement (in)
126.0	0.65 (approx.)	0.56 (approx.)
117.0	1.64 (approx.)	1.47 (approx.)
103.3	2.53 (approx.)	2.11 (approx.)
89.9	3.45	2.75
78.0	3.97	3.15
64.7	4.60	3.72
52.5	4.93	4.08
38.3	4.85	4.05 (approx.)
25.1	4.12 (approx.)	3.75(approx.)
12.0	3.01 (approx.)	2.46 (approx.)
3.0	0.89 (approx.)	0.98 (approx.)
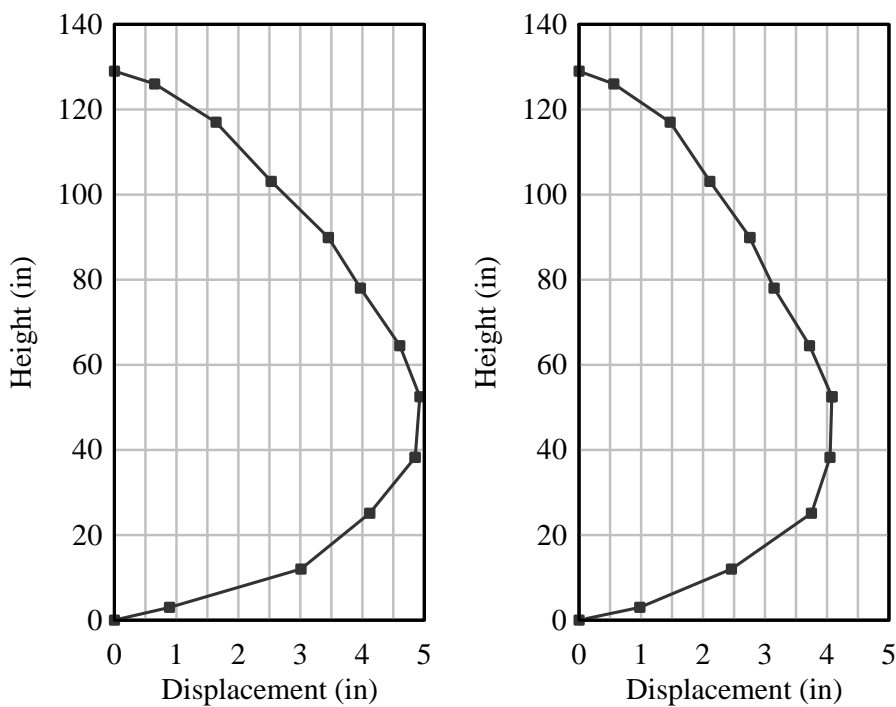
Figure 3.56: Test SA09 Maximum (left) and Residual (right) Displacements

3.3.7 Test SA10

Test SA10 was conducted on Specimen 5 on November 20, 2008. Test SA10 was a high velocity impact similar to Test SA07. The target impact velocities are shown in Table 3.31.

Table 3.31: Test SA10 Target Velocities

BG	Target Velocity in/s (m/s)
1	1779.5 (45.2)
2	1425.2 (36.2)
3	1031.5 (26.2)
4	511.8 (13.0)

Initial Setup

The setup for Test SA10 is discussed in detail in Section 3.1.1. A photo of the column pre-test is shown in Figure 3.57.

BG Behavior

Each impacting mass was instrumented with three accelerometers. The maximum acceleration was 23,470 g. The BGs impacted in the order 4, 2, 1, 3. The total spread from first to last impact was 3.45 ms.

Table 3.32 also gives a summary of peak acceleration, impact time and duration for each BG and the average and Table 3.33 gives a summary and average of impact velocities that were computed from the data from the Phantom cameras.
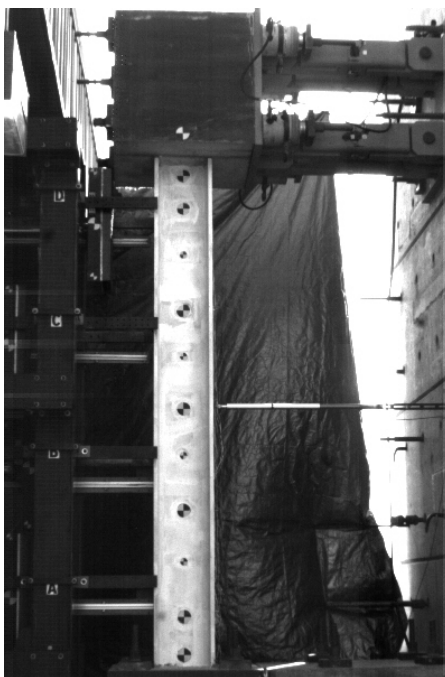
Figure 3.57: Test SA10 Column Pre-Test

Table 3.32: Test SA10 BG Impact Details

BG	Peak Acceleration (g)	Impact Time (ms)	Duration (ms)
1	23470	51.06	1.81
2	13860	50.91	2.02
3	1300	54.28	2.97
4	1360	50.83	4.25

Table 3.33: Test SA10 BG Impact Velocities

BG	Camera Impact Velocity in/s, (m/s)
1	1925.0 (48.9)
2	1621.5 (41.2)
3	1117.3 (28.4)
4	530.4 (13.5)

Pressures and impulses were found using the average acceleration of the BGs. The maximum pressure of 35,800 psi was recorded. The maximum impulse is 7796 psi-ms using this method. These values are summarized in Table 3.34.

Table 3.34: Test SA10 Pressures and Impulses

BG	Peak Pressure (psi)	Impulse from Accelerometer (psi-ms)
1	35800	7796
2	25190	3600
3	1540	3300
4	1570	2192

Specimen Behavior

Figure 3.58 shows the progression of damage recorded by the camera. In (a), the BGs are set to the correct initial position. The initial impact is shown in (b) and the synchronicity of the BGs can be seen. Figures (c) through (f) capture the propagation of deformation of the column while the masses are in contact with the column. Figure (g) displays the residual deformation of the specimen after the masses have retracted.
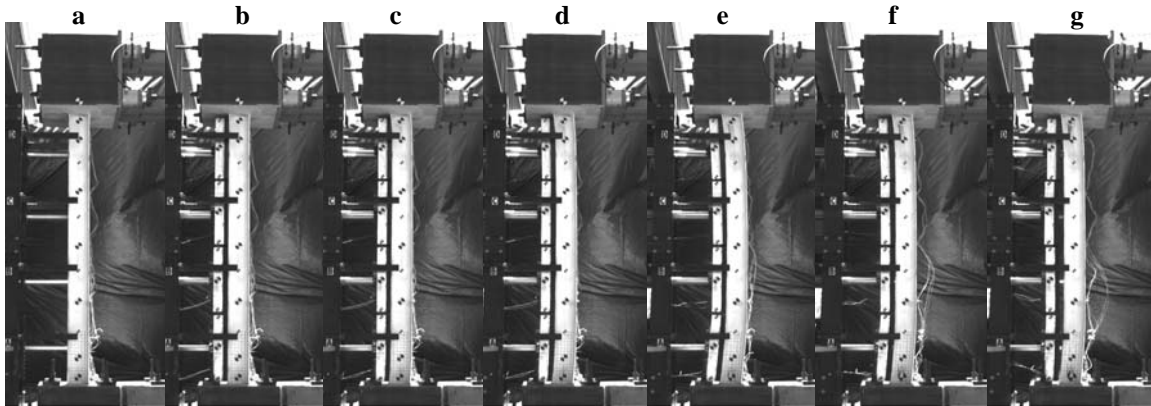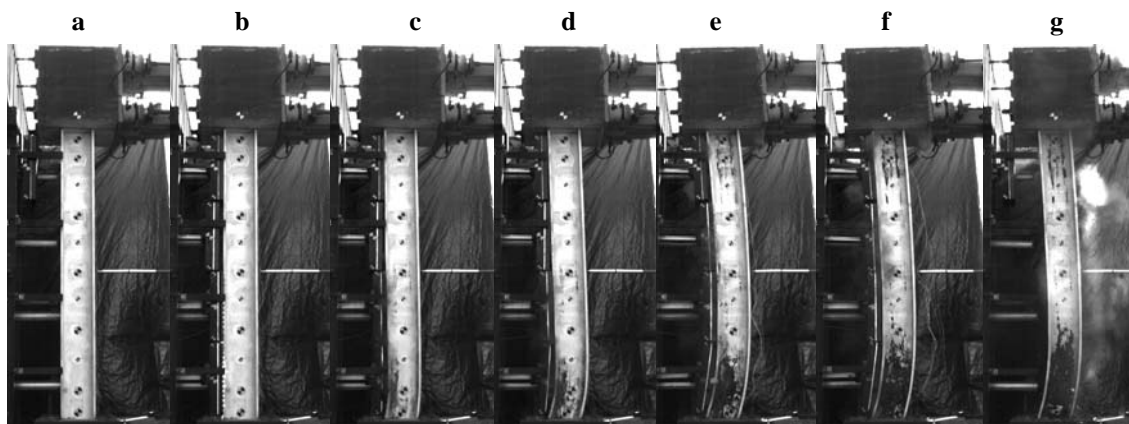

Figure 3.58: Test SA10 Progression of Damage

Accelerations of the specimen were recorded at five locations with accelerometers attached to the back (non-impact) side of the column. A maximum acceleration of 23,890

g was recorded at the bottom of the column. Table 3.35 gives a summary of peak acceleration and impact time.

Table 3.35: Test SA10 Specimen Accelerations

Distance from Base (in)	Peak Acceleration (g)	Impact Time (ms)
117.0	4090	51.31
90.75	8480	51.44
64.5	10990	51.00
38.25	15670	51.00
12.0	23890	51.17

Displacements were measured using the camera data and the tracking software, TEMA. The maximum displacement of 5.50 in was found at a height of 38.3 in from the base of the column. Table 3.36 gives a summary of the maximum and residual displacement at locations measured with the tracing software. Figure 3.59 and Figure 3.60 shows the column post-test. The maximum and residual displacements are given in Figure 3.61 and a plot of the residual displacements over the height of the column.

Table 3.36: Test SA10 Specimen Displacements

| Distance from Base (in)	Maximum Displacement (in)	Residual Displacement (in)
125.6	1.01	0.64
116.8	1.78	1.38
104.3	2.81	2.15
89.4	3.95	3.03
77.4	4.61	3.62
63.9	5.17	4.16
52.0	5.47	4.53
38.3	5.50	4.54
25.1	4.83 (approx.)	4.21 (approx.)
12.0	2.87 (approx.)	2.65 (approx.)
3.0	0.75 (approx.)	1.03 (approx.)
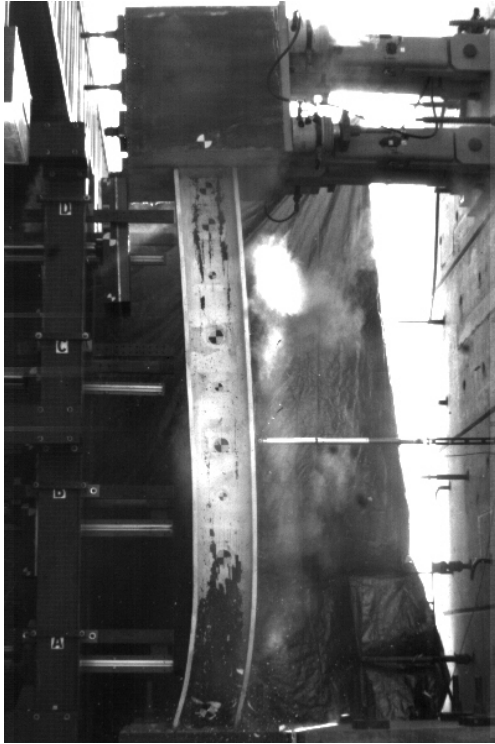
Figure 3.59: Test SA10 Column Post-Test

Figure 3.60: Test SA10 Column Base Post-Test
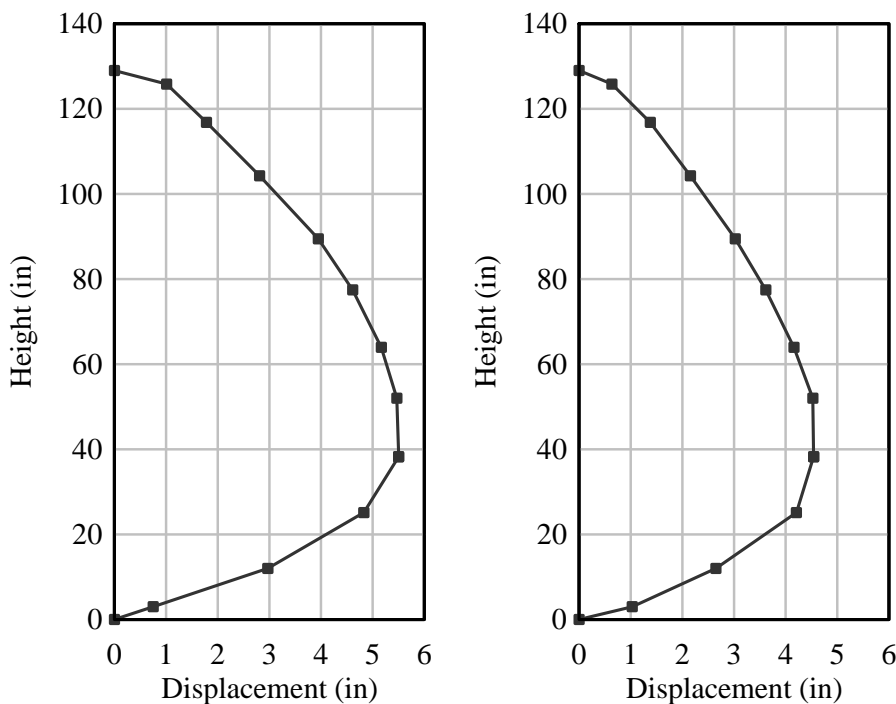
Figure 3.61: Test SA10 Maximum (left) and Residual (right) Displacements

3.3.8 Test SA11

Test SA11 was conducted on May 19, 2009 and was a re-hit of Specimen 1 with target velocities given in Table 3.37. The column had initial deformation from Test SA02.

Initial Setup

The setup for Test SA11 is discussed in detail in Section 3.1.1. Photos of the column pre-test are shown in Figure 3.62 and initial displacements are recorded in Table 3.38 and shown in Figure 3.63.

Table 3.37: Test SA11 Target Velocities

BG	Target Velocity in/s (m/s)
1	1594.5 (40.5)
2	1334.6 (33.9)
3	1267.7 (32.3)
4	972.4 (24.7)
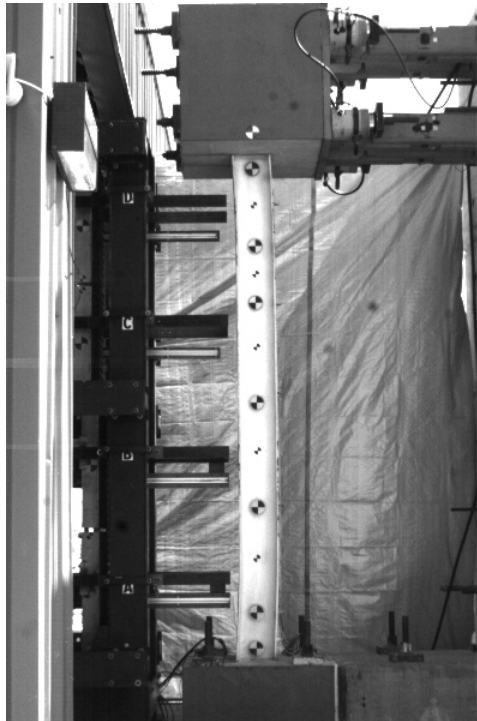
Figure 3.62: Test SA11 Column Pre-Test
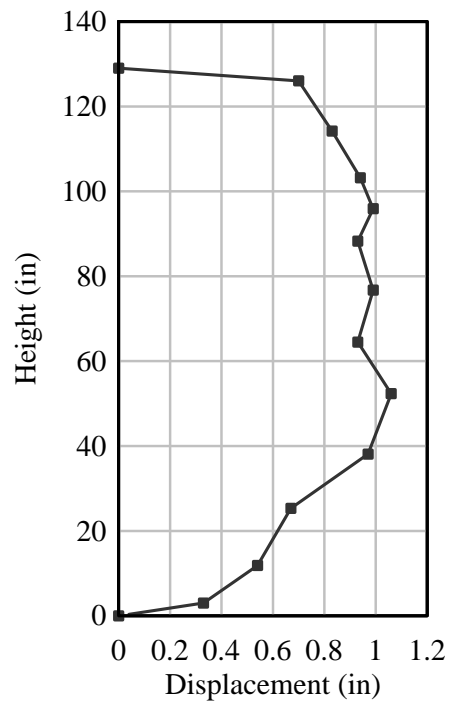
Figure 3.63: Test SA11 Initial Displacements

Table 3.38: Test SA11 Initial Displacements

Distance from Base (in)	Initial Displacement (in)
126.0	0.7
114.2	0.83
103.2	0.94
95.9	0.99
88.3	0.93
76.7	0.99
64.5	0.93
52.3	1.06
38.1	0.97
25.3	0.67
11.9	0.54
3.0	0.33

BG Behavior

The maximum recorded acceleration was 21,040 g. The BGs impacted in the order 2, 3, 4, 1. The total spread from first to last impact was 4.03 ms. Table 3.39 gives a summary of peak acceleration, impact time and duration for each BG and the average.

Table 3.39: Test SA11 BG Impact Details

BG	Peak Acceleration (g)	Impact Time (ms)	Duration (ms)
1	21040	51.09	5.68
2	7890	47.06	2.94
3	5930	47.97	2.03
4	2064	48.19	4.41

Impact velocities were determined using visual data from the Phantom Cameras and the *TEMA* software. Table 3.40 gives a summary and average of impact velocities.

Table 3.40: Test SA11 BG Impact Velocities

BG	Camera Impact Velocity in/s, (m/s)
1	1672.3 (42.5)
2	1470.5 (37.3)
3	1202.5(30.5)
4	880.7 (22.4)

Pressures and impulses, summarized in Table 3.41, were found using the average acceleration of the BGs. The maximum pressure of 38,340 psi was recorded. The maximum impulse was 7,580 psi-ms using this method.

Table 3.41: Test SA11 Pressures and Impulses

BG	Peak Pressure (psi)	Impulse from Accelerometer (psi-ms)
1	38340	7580
2	7400	3247
3	6370	3305
4	2380	1742

Specimen Behavior

The damage propagation is shown in. In (a), the column is undeformed and the BGs are set to the correct initial position. The initial impact is shown in (b) and the synchronicity of the BGs can be seen. Figures (c) through (f) capture the propagation of deformation of the column while the masses are in contact with the column. Figure (g) displays the residual deformation of the specimen after the masses have retracted.
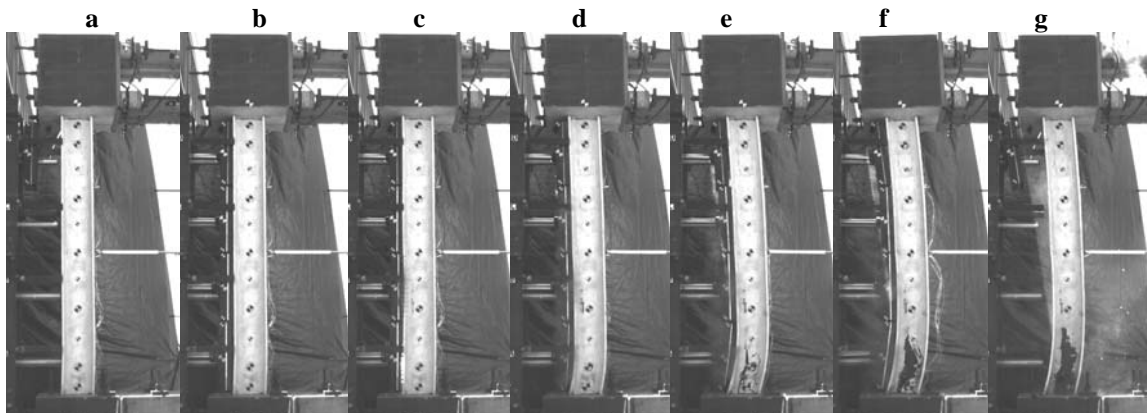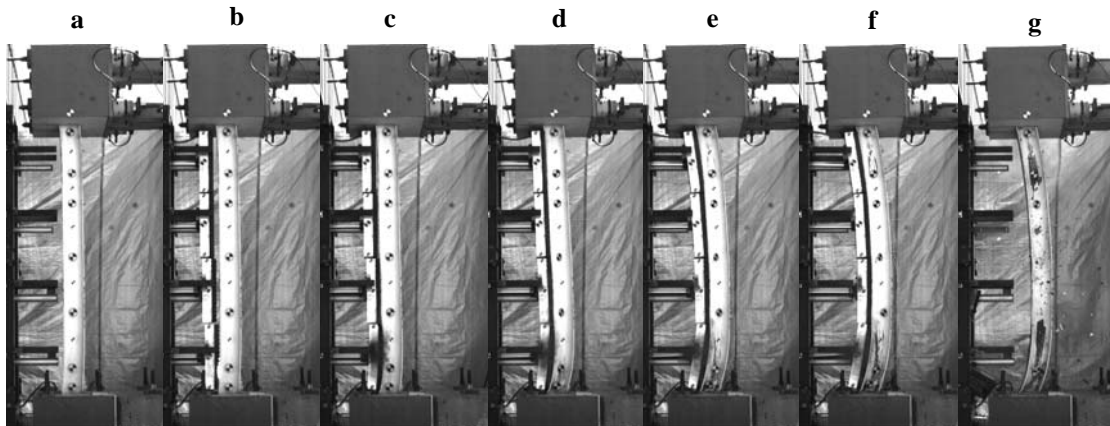

Figure 3.64: Test SA11 Progression of Damage

Accelerations of the specimen were recorded at five locations with accelerometers attached to the back (non-impact) side of the column. A maximum acceleration of 9,950 g was recorded toward the bottom of the column. Table 3.42 gives a summary of peak acceleration and impact time.

Table 3.42: Test SA11 Specimen Accelerations

Distance from Base (in)	Peak Acceleration (g)	Impact Time (ms)
117.0	6790	46.90
90.75	8610	46.65
64.5	8580	46.67
38.25	9590	46.25
12.0	7090	45.86

The maximum displacement of 7.09 in was measured at a height of 64.5 in from the base. The maximum residual displacement of 6.33 in was found at a height of 52.3 in from the base of the column. Table 3.43 gives a summary of the maximum and residual displacement at multiple locations with plots in Figure 3.65. Figure 3.66 shows the column post test. Figure 3.67, Figure 3.68, and Figure 3.69 shows the column base post test from various angles. The column web buckled up to about 6 in from the base of the column. Figure 3.70 shows the damaged concrete in the header.

Table 3.43:Test SA11 Specimen Displacements

Distance from Base (in)	Maximum Displacement (in)	Residual Displacement (in)
126.0	0.78	0.73
114.2	2.24	1.93
103.2	3.63	2.96
95.9	4.67	3.91
88.3	5.06	4.75
76.7	6.08	5.19
64.5	7.09	6.31
52.3	6.84	6.33
38.1	6.59	6.12
25.3	5.91	5.55
11.9	3.98	4.16
3.0	1.44	0.81
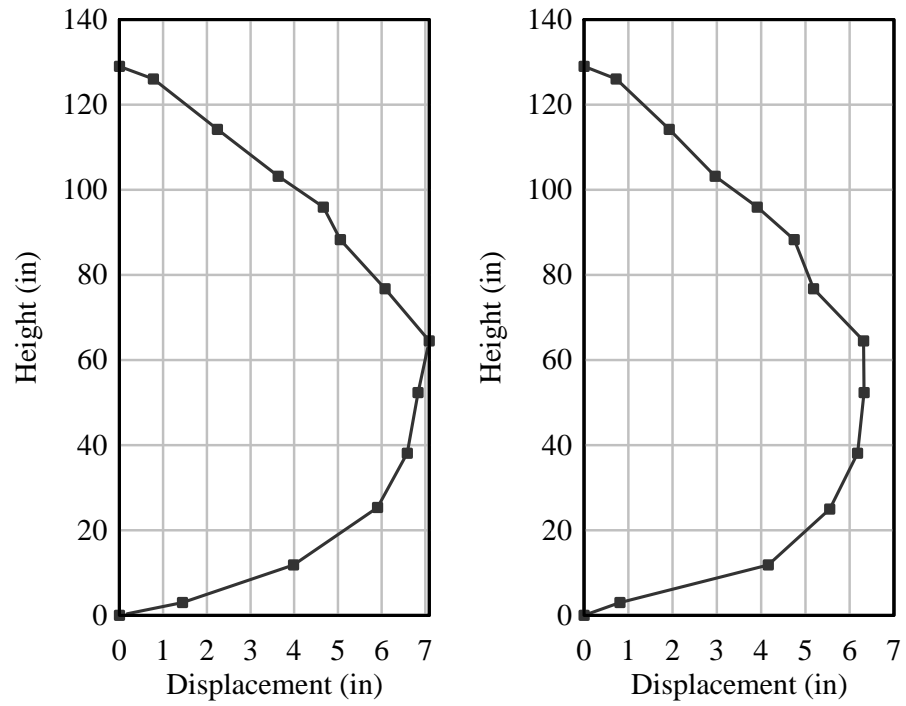
Figure 3.65: Test SA11 Maximum and Residual Displacements

Figure 3.66: Test SA11 Column Post-Test

Figure 3.67: Test SA11 Column Base Post-Test (View 1)

Figure 3.68: Test SA11 Column Base Post-Test (View 2)

Figure 3.69: Test SA11 Column Base Post-Test (View 3)
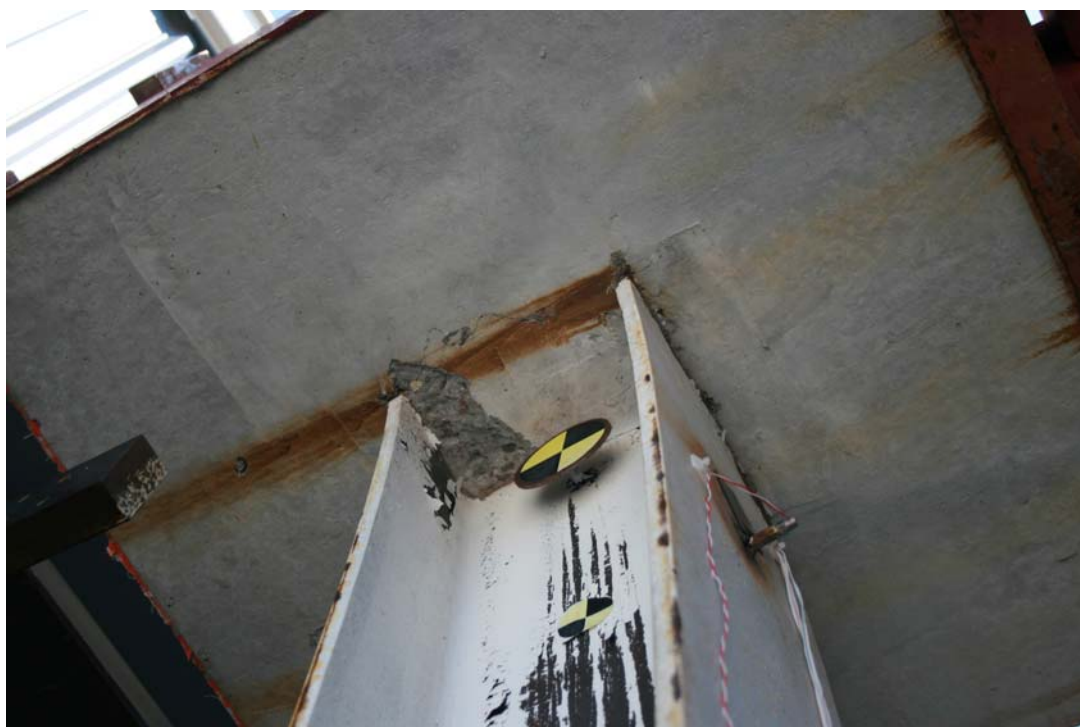
Figure 3.70: Test SA11 Column Header Post-Test

3.4   Comparison to Field Tests

The results from the DTRA test, discussed previously in Chapter 2, and the preceding tests from this chapter were compared to validate the Simulator for this type of testing. The Test 5 in the DTRA test series was a strong axis W14x132 specimen with a 4 in piece of concrete cladding placed in front of it and was similar to that of the strong axis columns tested.

Because of the harsh nature of explosive loading tests, it can be difficult to record and determine the actual pressure and impulse applied to the specimen during the test. For this reason, CTH, an Eulerian, shock physics hydrocode produced by Sandia National Laboratories [23] was utilized to calculate an approximation for the pressure and impulses felt on the face of the cladding. These impulses were then used to find a representative test from the test series for comparison.

Figure 3.71 gives multiple screen shots of the CTH calculation, which displays pressure. In this calculation the cladding was modeled as a rigid surface and tracers were placed at various locations. A cylindrical charge with equivalent weight of TNT was placed a given distance away using the scaled distance of 0.88, as was seen in the test. The explosive was modeled using the JWL model for TNT, which is an option in the CTH database. Adaptive Mesh Refinement (AMR) was used to refine the mesh as needed as the explosive waves propagated towards the structure. An example of a tracer output for pressure and impulse is shown in Figure 3.72.
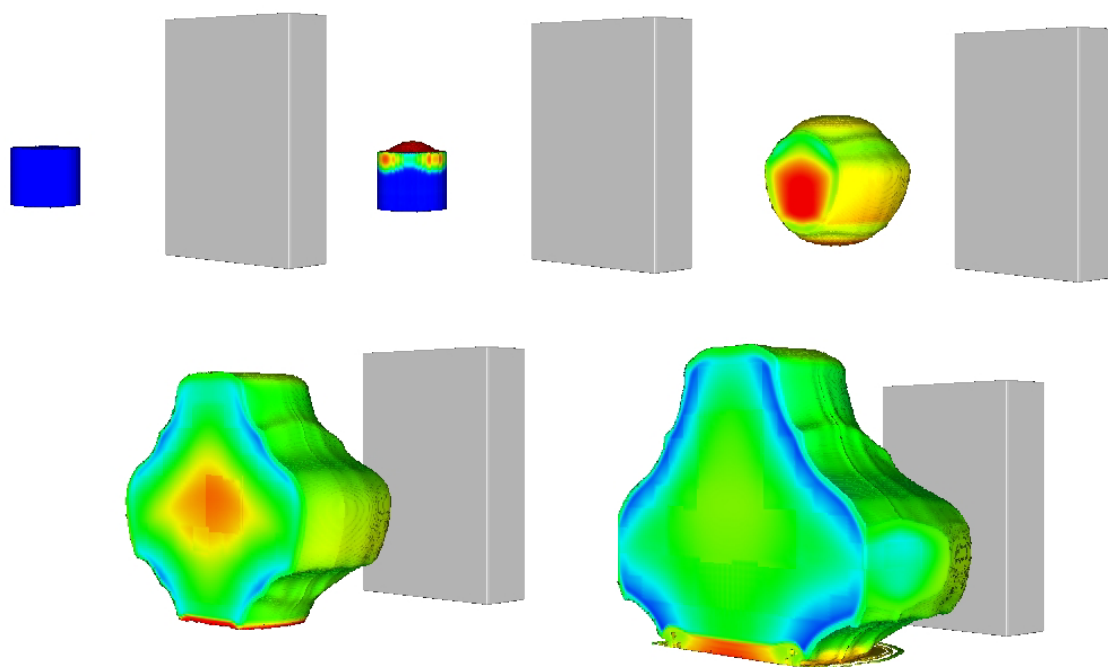
Figure 3.71: CTH Calculation for DTRA Field Test
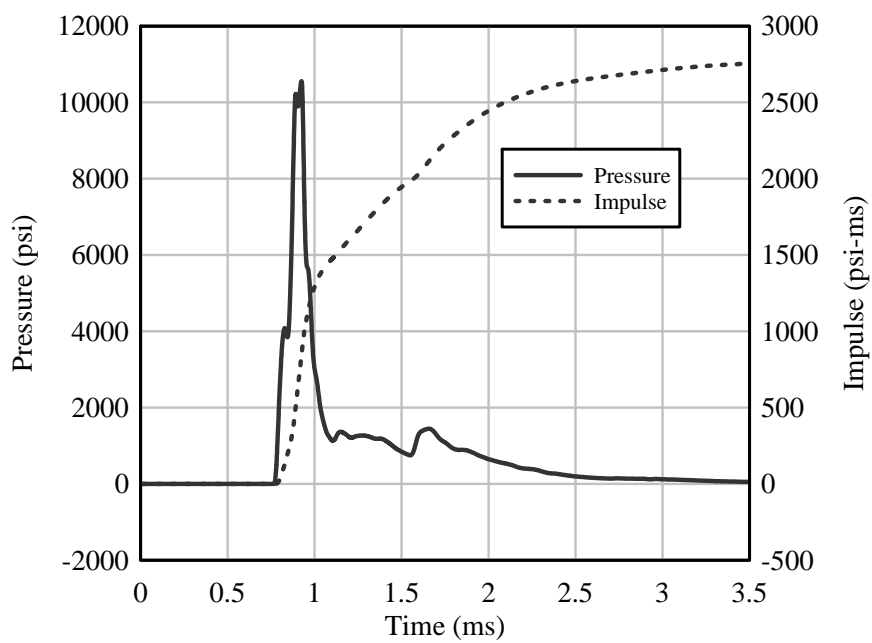
Figure 3.72: Example CTH Pressure and Impulse Output

Using the impulses generated above, it was found that Test SA10 had impulses most closely matching those of Field Test 5. The global residual displacements from Field Test 5 and the Simulator Test SA10 are plotted in Figure 3.73. The two columns behaved similarly and the overall maximum column residual displacements were within 5%, which is satisfactory for comparison of tests with live explosives where the incoming pressure and impulse is not immediately known. One note of difference between the two tests was that the flanges of Field Test 5 exhibited more bending than those from the Simulator as shown in Figure 3.74. This is thought to be due to the addition of the concrete cladding. The effects of the cladding on the behavior of the column are discussed in more detail in Chapter 8.
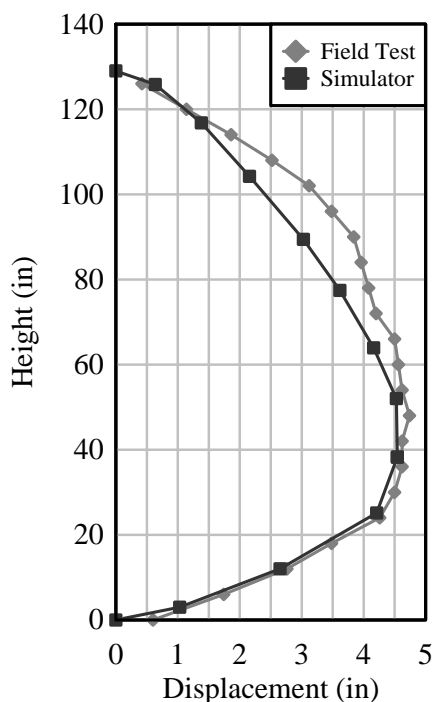
Figure 3.73: Residual Displacement Comparison of Field Test to Simulator Test

Figure 3.74: Flange Behavior Comparison of Field Test (left) to Simulator Test (right)

3.5 Summary

This chapter described the methodology of testing structural steel columns in the strong axis direction using the UCSD Blast Simulator. Initially, a description of the test setup and test specimens was included, as well as the instrumentation plan. The chapter also described the procedure for analyzing the appropriate instrumentation output, such as accelerations and velocities, to generate pressures and impulses seen on the column, highlighted through the detailed results from six experiments. Additionally, the results of high speed cameras and tracking software was included to demonstrate the capability to observe behaviors and displacements over time that would not be seen during a actual explosive event.

Also included in the strong axis tests was the incorporation of the BG25s and the BG50s together to impact the specimen with variable velocities over the height of the

column. This was done to generate a distribution of impulse over the height of the column, where the base sees more load than the top, as is seen with bombs detonated near the ground. The addition of variable velocity impact allowed these types of tests to be directly compared to actual field testing to validate that the Simulator is capable of generating forces, damage and behavior similar to those seen during an actual explosive event.

4 Development & Validation of a Finite Element Model for Columns Loaded in the Strong Axis Direction

A finite element model to predict the response of steel columns under simulated blast loads was developed as part of this dissertation. The finite element analysis was preformed with LS-DYNA [21], a three dimensional, explicit, Lagrangian finite element code that uses a central difference time integration method. LS-DYNA is a general purpose, transient, dynamic finite element program that is often used in problems with blast and impact loading. It is able to utilize state of the art constitutive models to represent material behaviors of interest, specifically steel with strain rate effects and concrete. This chapter describes the development of the finite element model and includes validation of the model by comparing to similar experiments described in Chapter 3.

4.1   Column Mesh Development

This section describes the development and selection of properties pertaining to defining the mesh parameters for the steel column experiments.

4.1.1   Shell Elements

Fully integrated shell elements with six integration points through the thickness were used to model the steel W-Shape. Shell elements were selected for the steel because, not only are they computationally accurate, they provide for a faster processing time which is critical for developing the fast running model discussed in Chapter 8. The shell elements used were 0.5 in by 0.5 in and were given the corresponding thicknesses to the column dimensions. The shell elements from the column flanges share nodes with the column web at the appropriate connection point. Figure 4.1 shows the W14x132 steel column constructed with shell elements.
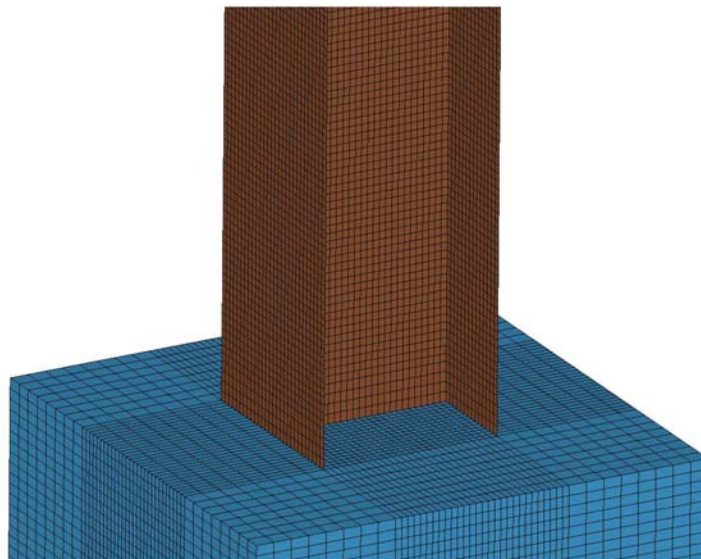
Figure 4.1: Shell Elements in Steel Column

4.1.2 Solid Elements

The model for the strong axis steel column tests used three dimensional solid elements to represent the concrete header, concrete footer, steel casing and link system. These elements were eight node brick elements with single point integration. The elements varied in size throughout the mesh. The largest element being 1 in by 1 in by 1 located in the concrete header and footer away from the steel column. Figure 4.2 shows solid elements used to model the concrete footer.
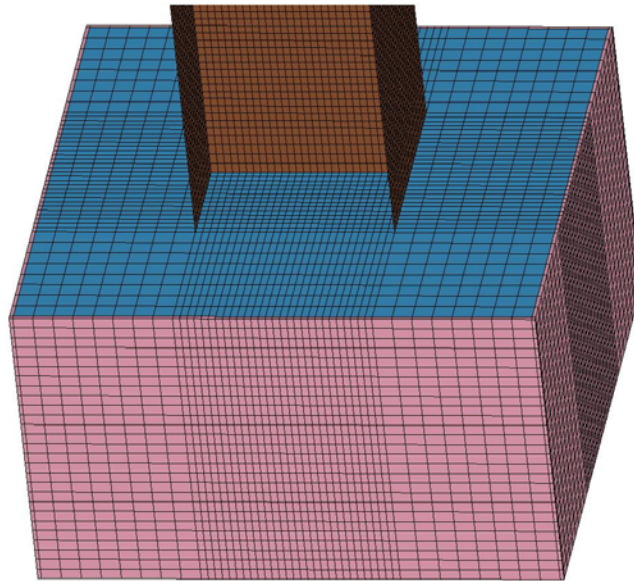
Figure 4.2: Solid Elements in Concrete Footer

4.1.3 Beam Elements

Hughes Liu beam elements with cross sectional reinforcing steel were used for modeling steel reinforcement and Nelson Studs in the concrete header and footer and are shown in Figure 4.3.
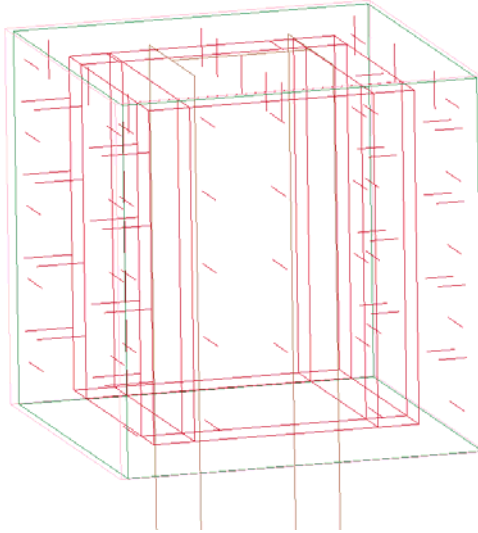
Figure 4.3: Beam Elements for Reinforcing Steel

The steel shell elements and the solid concrete elements shared common nodes and were therefore merged together. The concrete elements are also merged with any reinforcing steel inside.

4.2   Boundary Conditions

This section describes the modeling of the boundary conditions for both the base and top of the column system, with the goal of being able to accurately describe what occurred during the experiments.

4.2.1 Footer Boundary

The boundary conditions on the concrete footer were described such that the nodes on the base and the four sides were restrained in all directions, which simulated the fixed condition and are shown in Figure 4.4.
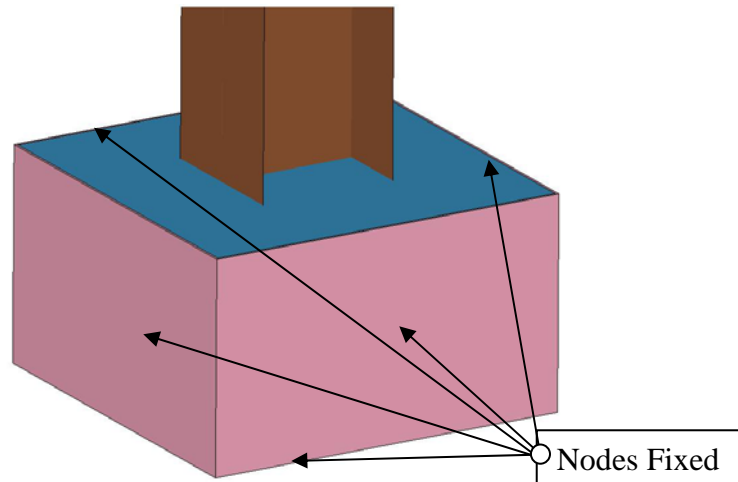
Figure 4.4: Concrete Footer Boundary Condition

4.2.2 Link System Boundary

Correctly modeling the boundary conditions on the header was crucial in developing a working model. Initially, it was assumed that the system remained fixed in the rotation and was only allowed to translate vertically and could be modeled using simple nodal restraints; however, at the higher level velocity tests, these boundary conditions were not fully met. The system began to act more like a pin connection than a fixed connection as the velocities increased.

Three main situations were identified that contributed to the boundary conditions not being consistent for all tests. The first cause that was identified is shown in Figure 4.5. In this case, the hydraulic jacks could not hold the header to the link system and a gap, and therefore rotation, occurred.
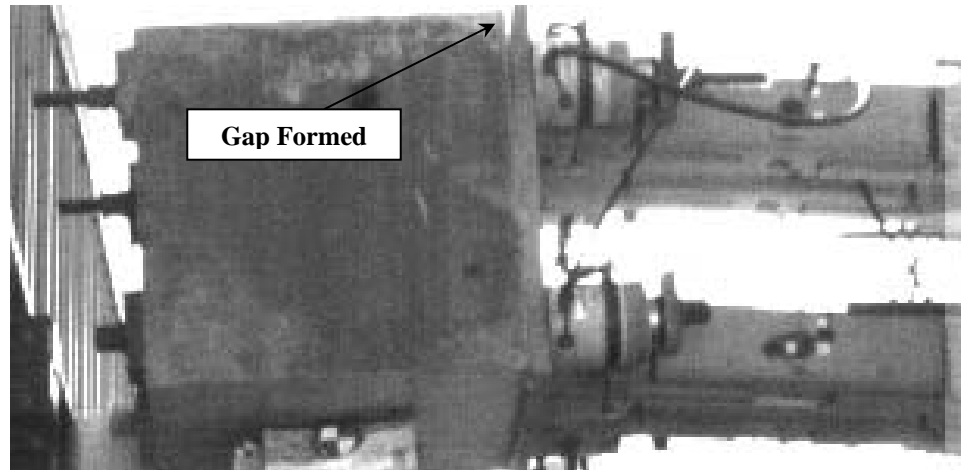
Figure 4.5: Header Pulls Away from Link System

The second scenario that contributed to the boundary condition error was the fact that, in some tests, the link system as a whole pulled off from the reaction wall. The rods that connected the link to the wall were not sufficient in fully restraining the link. It is evident that this occurs due to the visibility of a dust cloud in the camera footage which is shown in Figure 4.6.
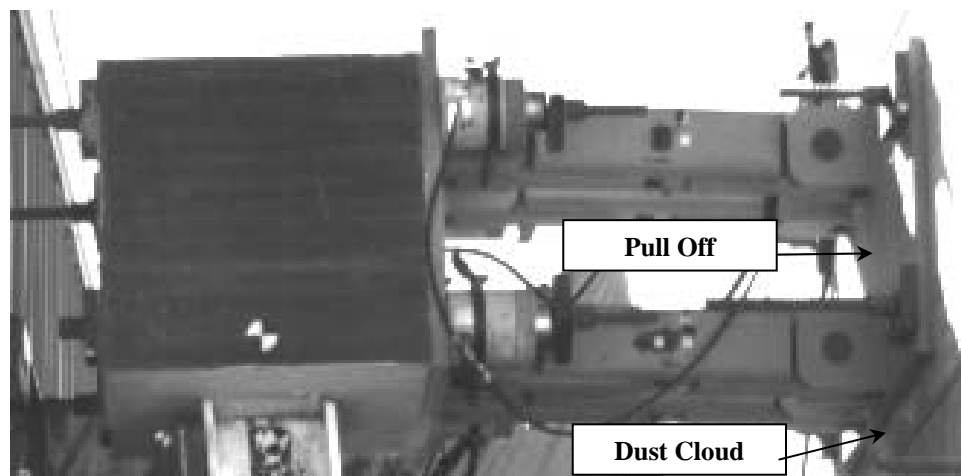
Figure 4.6: Link System Pulls Away from Reaction Wall

The last cause that was identified was that, over time, the system became loose due to opening of holes and other issues. This allowed the pins to rotate and translate

within the holes and the whole system to also rotate. An example of this rotation is shown in Figure 4.7. The upper photo was shot before impact, while the bottom photo was captured during the experiment.
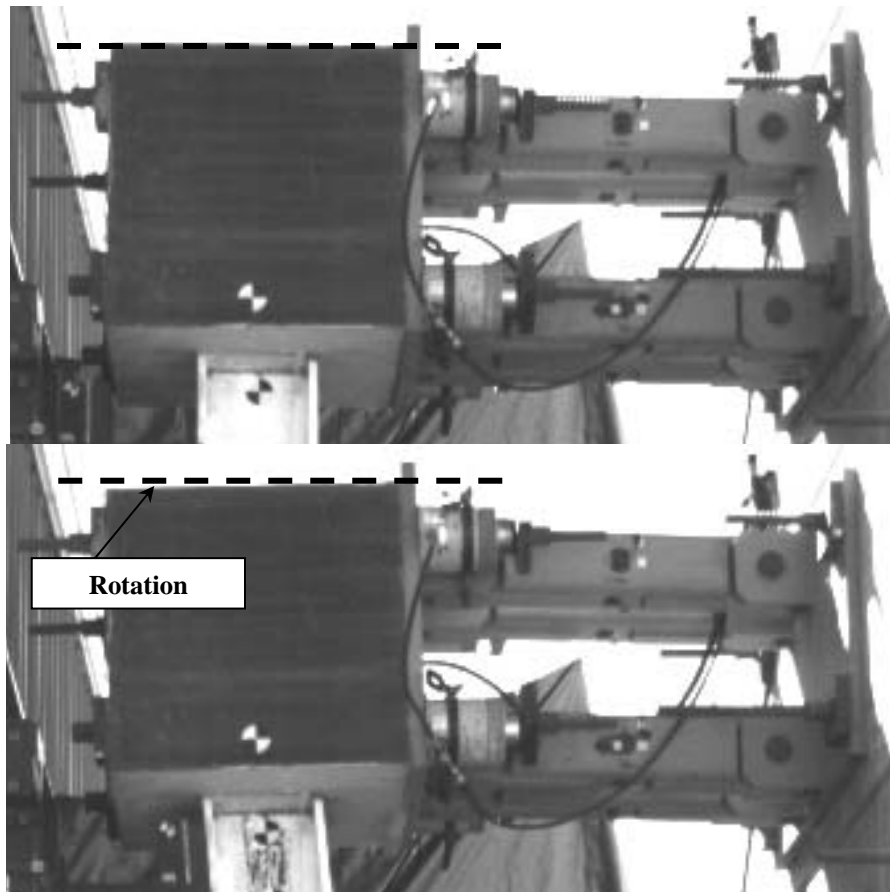
Figure 4.7: Rotation of Loose System Comparison

To incorporate these factors, the entire link system was modeled and connected to a backing plate as shown in Figure 4.8. The backing plate has a fixed restraint on the back of one side and is merged to the tabs which hold the pins on the other. There is a steel tube section connecting the two sets of pins. For both sets of pins, an *AUTOMATIC_SURFACE_TO_SURFACE contact was placed between the pin and the surrounding parts to allow rotation.
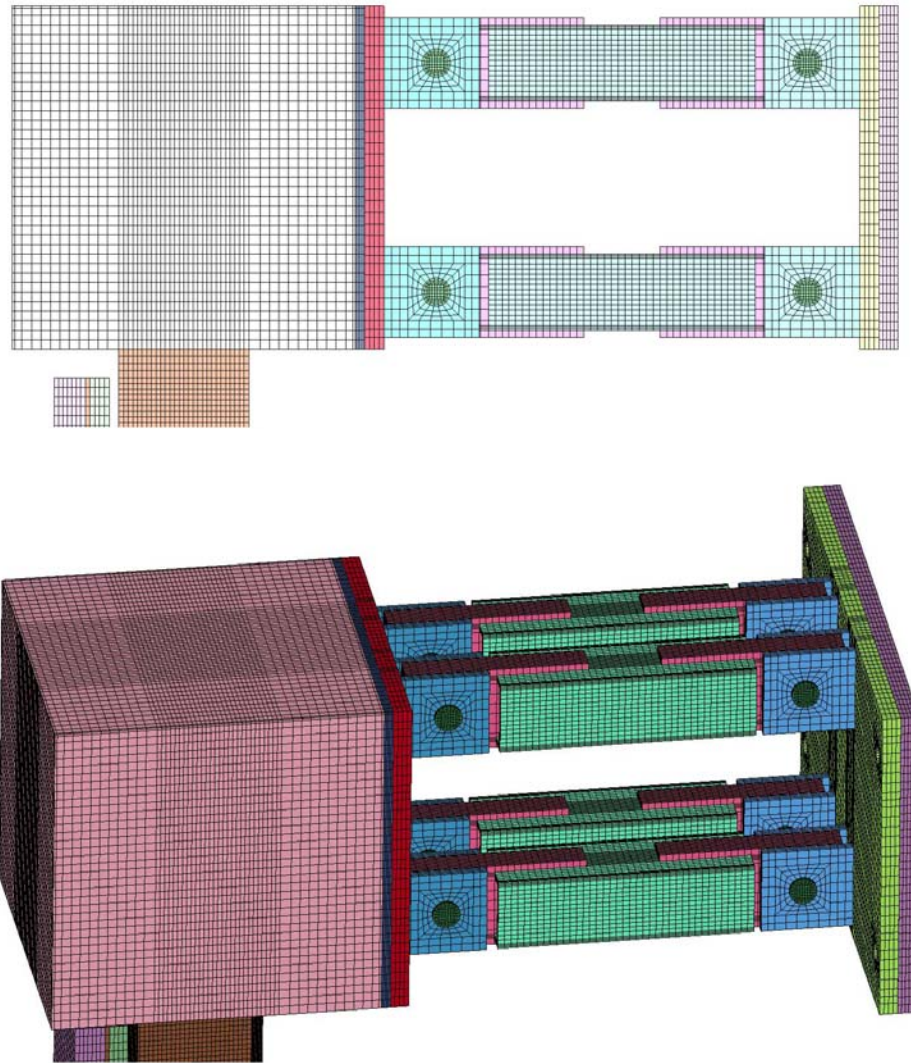
Figure 4.8: Link System Mesh

To correctly model the extra rotation for higher velocity tests, a layer of rubber elements was placed between the link and the column header and is shown in Figure 4.9. The rubber layer allowed for the link to be stiffer at small displacements as seen in the lower velocity impacts, while displacing more for the higher velocity impacts as seen in the tests. The rubber was four elements thick and was merged to the column and a

*TIED_SURFACE_TO_SURFACE contact was used to connect the rubber to the link which did not share many common nodes. The material description for the rubber is discussed in Section 4.4.4.
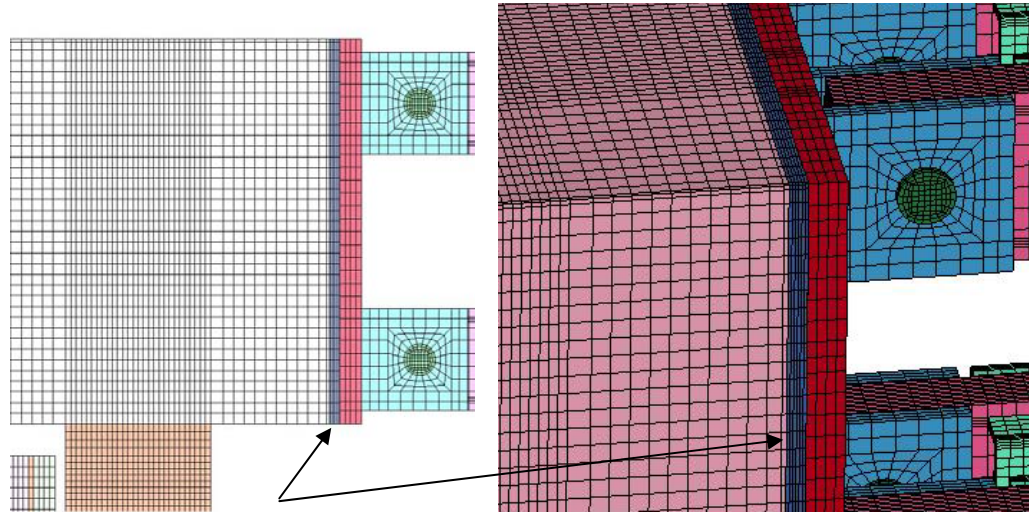
Figure 4.9: Rubber Connection Elements

4.3 Loading

Loads were applied to the column by modeling the impacting module which included the programmer, aluminum backing plate, impaction mass, rod and collar. It was found that for these tests, the pyramid system on the face of the programmer did not greatly affect the results, but greatly slowed run times and, therefore, was omitted. The rod as shown in Figure 4.10, was not fully modeled, but the density of the material was changed include the full mass of the rod.
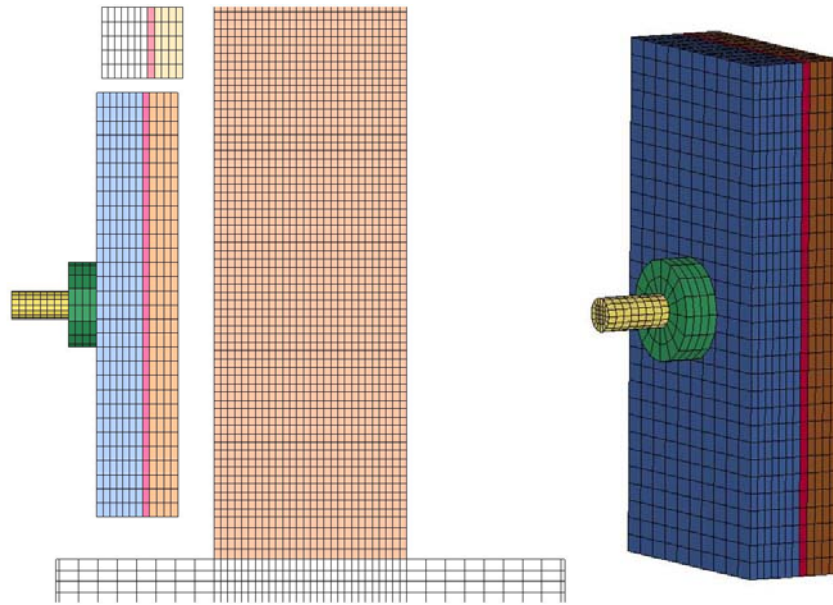
Figure 4.10: Mesh of Impacting Module

4.4 Material Models

This section describes the four main material models were used to model the strong axis tests. These materials include steel, concrete, programmer, and rubber connection elements.

4.4.1 Steel Model

To model the steel column, *MAT_PIECEWISE_LINEAR_PLASTICITY, which can incorporate strain rate effects, was used. This model allows for the input of arbitrary stress versus strain relations for various strain rates as shown in Figure 4.11 with rates increasing from 1 to 5. Intermediate values are found by interpolating between the curves and if a point falls out of range, the closest curve is utilized.
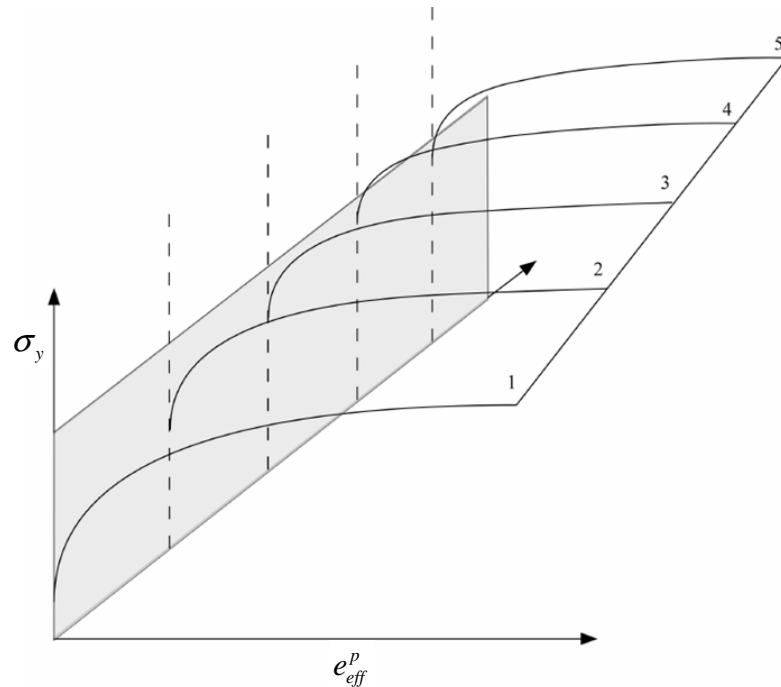
Figure 4.11: *MAT_PIECEWISE_LINEAR_PLASTICITY Model, from [21]

The values for the stress-strain relations at each given rate were found through many rounds of experimental testing conducted by Karagozian and Case [24]. Figure 4.12 shows the steel model used for the purposes of these tests. The yield stresses ranged from 52,000 psi for no rate effects to almost 78,000 psi for rates at around 100. It should be noted that no additional curves should be added. The rates for the steel column tests are in the range of 30 to 50 s^{-1}, but due to the almost immediate onset of loading, there is some high rate numerical noise in the system. The omission of the higher curves allows the model to not interpolate to unrealistic higher strain rate curves.
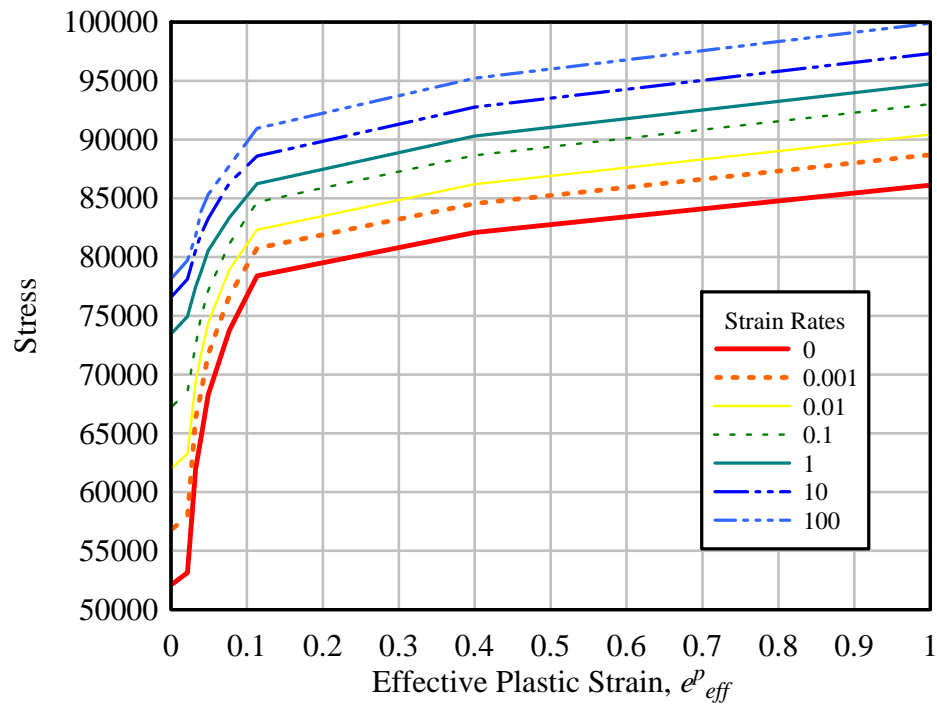
Figure 4.12: Steel Material Model

4.4.2 Concrete Model

The concrete in both the header and the footer was modeled with the K&C Concrete Model, *MAT_072 Rel 3 [25]. A background into plasticity models used for concrete is given in [26]. The K&C model is a plasticity model that decouples the volumetric and deviatoric parts of the concrete response. The volumetric part is treated with an equation of state with tabulated data that gives the pressure as a function of volumetric strain. The deviatoric response is found between three independent failure surfaces that correspond to the limit of elastic behavior, the maximum concrete strength, and the residual concrete strength. A current failure surface is found by interpolating between the three independent surfaces and more detail on this model can be found in [25].

The concrete strength was set at 5,000 psi and the density at 145 lb/ft^2. The remaining parameters, except for strain rate effects, are calculated with the strength and density. To account for strain rate effects, tabulated data was strain rates ranging from 3.0e-4 to 3.0e4 were used. The increase factors at each strain rate were determined from calibrated test data provided by K&C.

4.4.3 Programmer Model

Early on in the simulator development, an attempt was made to develop a material model for the urethane programmer [27]. At this time the research has not produced a sufficiently efficient model that can be incorporated in the finite element codes. An alternate model was developed by [13] to simulate a testing series on concrete masonry walls such that the material could impact the wall through a contact surface applied through the face of the wall and the face of the programmer material, depicted in Figure 4.15

As discussed in detail in [13], the model chosen was *MAT_057 or *MAT_LOW_DENSITY_FOAM and was selected because of the similarities between the stress-strain behavior and the energy dissipation characteristics between low density foam and the programmer.

The model requires the input of the material density and the material modulus. The unloading is governed by two factors, the HU and the SHAPE. In the LS-DYNA Keyword Manual [21], HU is defined as the hysteretic unloading factor between zero and one, where one corresponds to no energy dissipation. SHAPE is defined as the shape

factor for unloading. Shape factors greater than one increase energy dissipation and those less than one decrease energy dissipation.

The shape of the stress-strain curve (for loading) used in the wall tests is shown in Figure 4.13 and is also discussed in [13].
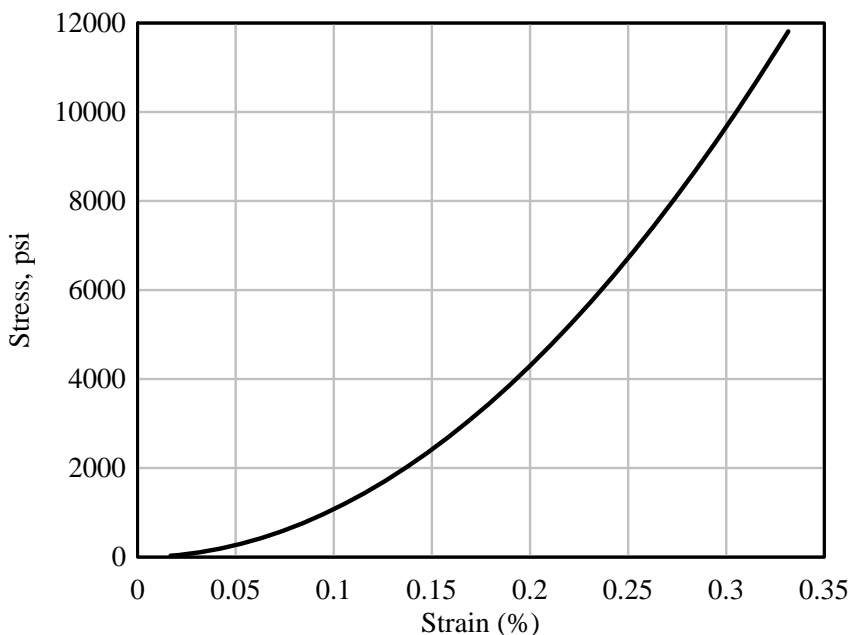
Figure 4.13: Stress-Strain Curve for Programmer Model

The model used in the steel column tests was identical to that used in the modeling of the wall tests, with two slight modifications. The material used to create the column programmer was slightly denser and less stiff than the programmers used for the previous tests. The density was modified from 0.03 lb/in^2 to 0.043 lb/in^2 and a scale factor of 2.0 was used to scale the stress-strain curve to make it stiffer than the 1.7 previously used. The initial modulus was kept the same at 2,262 psi. The HU of 0.05 and a SHAPE of 400 were also kept consistent.

4.4.4 Rubber Connection Model

The model used to represent the rubber connection elements was similar to that used for the programmer. *MAT_LOW_DENSITY_FOAM was used with parameters adjusted to match test data and incorporate the slight rotation in the system. The values of density and modulus were set to 0.043 and 2,262, respectively. A HU of 0.05 and a SHAPE of 400 was included. Finally, the stress-strain relation given in Figure 4.13 was scaled by a factor of 0.5.

4.5 Model Validation

This section describes the validation analysis of the above finite element model as compared with six of the strong axis steel column tests described in Chapter 3. The tests that were conducted as "low" velocity tests for setup validation were not modeled. For each test, all parameters except for geometry and impact velocity were kept consistent. Global maximum and residual displacement were two of the main output parameters compared in order to validate the model and comparison plots are given in each subsequent section.

4.5.1 Test SA02

A described in Section 3.3.2, Test SA02 was a W10x49 specimen loaded with four BG25s at uniform velocity. From the data analysis, the average of the impact velocity of the BGs was found to be 676.8 in/s (17.2 m/s). Each impacting module in the model, with representative equivalent weight, was given this initial velocity in the direction of the specimen. Because no acceleration was needed to reach impact velocity

from a computational standpoint, the impacting modules were started only a small distance off the flange of the column to reduce the run time. The initial configuration of the model is shown in Figure 4.14.

The masses impact the specimen though the *AUTOMATIC_SURFACE_TO_SURFACE contact shown in Figure 4.15. In this contact, the face of the impacting mass was defined as the slave set and the face of the impacted flange was described as the master set.

After impact, the modules rebound in the opposite direction, as they do during the test. To prevent any additional collisions, the elements of the impacting modules were eroded at a time of 0.012 ms. The column then was allowed to freely move to its point of maximum global displacement and rebound to its final resting point with some residual displacement. The termination time of 0.40 ms and a global damping of 2 percent was incorporated which was found to be sufficient for correctly determining the final state of the column. The progression of the run is shown in a series of screen shots in Figure 4.16.

Using the forces calculated through each contact surface, which is calculated in LS-DYNA using the rcforc ASCII output, the corresponding impulses were calculated and are summarized in Table 4.1. These impulses are comparable to those values calculated from the experimental data in the previous chapter.

Table 4.1: Test SA02 Finite Element Impulse

BG #	Impulse (psi-ms)
BG1	1761
BG2	1937
BG3	1949
BG4	1814

Displacements of the column are given in Figure 4.17 for various times throughout the run. Maximum and residual displacements at multiple locations were found along the height of the column. The results of the finite element run are summarized in Table 4.2 for the maximum and residual displacements.

The comparisons for the finite element results and Test SA02 for both maximum and residual displacements are shown in Figure 4.18 and Figure 4.19. From the plots, the maximum displacement of the finite element model was 1.86 in as compared with a displacement of 1.79 in from the experiment which corresponds to an error of 3.91%. The residual displacement of the computational model was 1.10 in and the experimental displacement was 1.09 in. The error from the residual displacements was found as 0.92%. Included in Figure 4.20 is a visual comparison from the finite element calculation and the experiment.
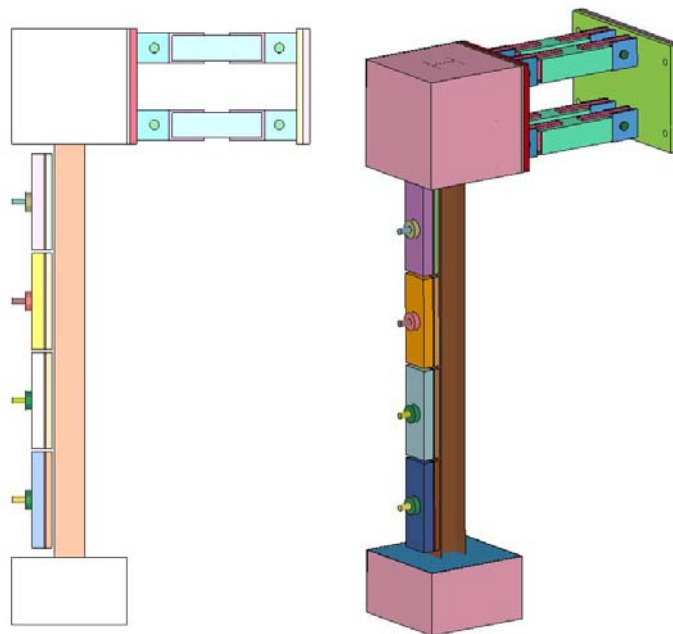
Figure 4.14: Test SA02 Finite Element Model Configuration
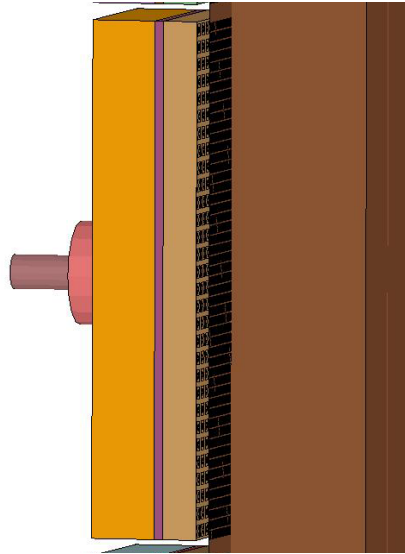
Figure 4.15: Test SA02 Impacting Mass Contact Surface

Table 4.2: Test SA02 Maximum and Residual Displacements

Distance from Base (in)	Maximum Displacement (in)	Residual Displacement (in)
126.0	0.54	0.20
117.0	0.96	0.50
103.875	1.35	0.72
90.75	1.58	0.82
77.625	1.73	0.92
64.5	1.79	1.00
51.375	1.75	1.06
38.25	1.64	1.10
25.125	1.42	1.07
12.0	0.78	0.63
3.0	0.19	0.14
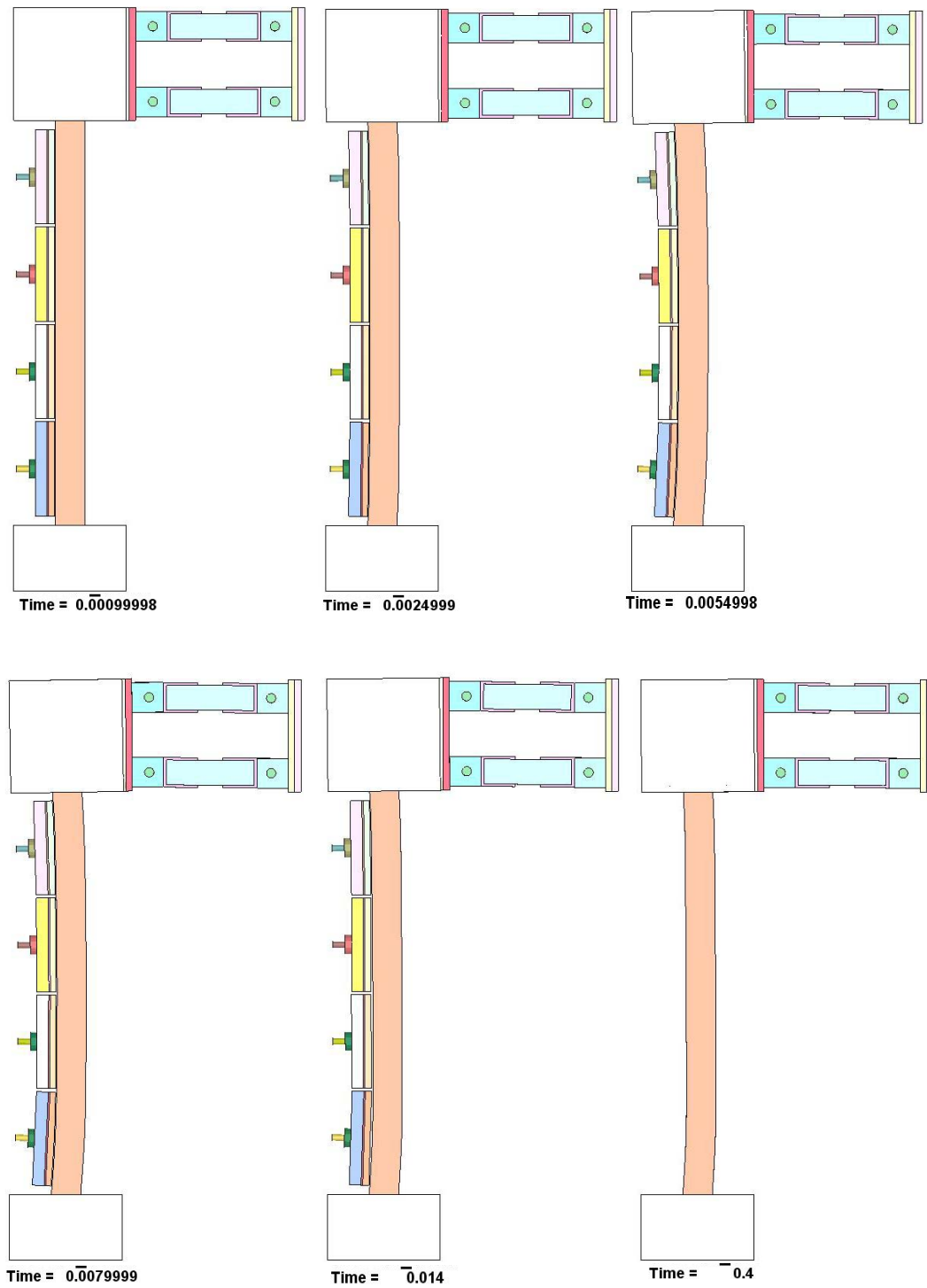
Figure 4.16: Test SA02 Finite Element Run Progression
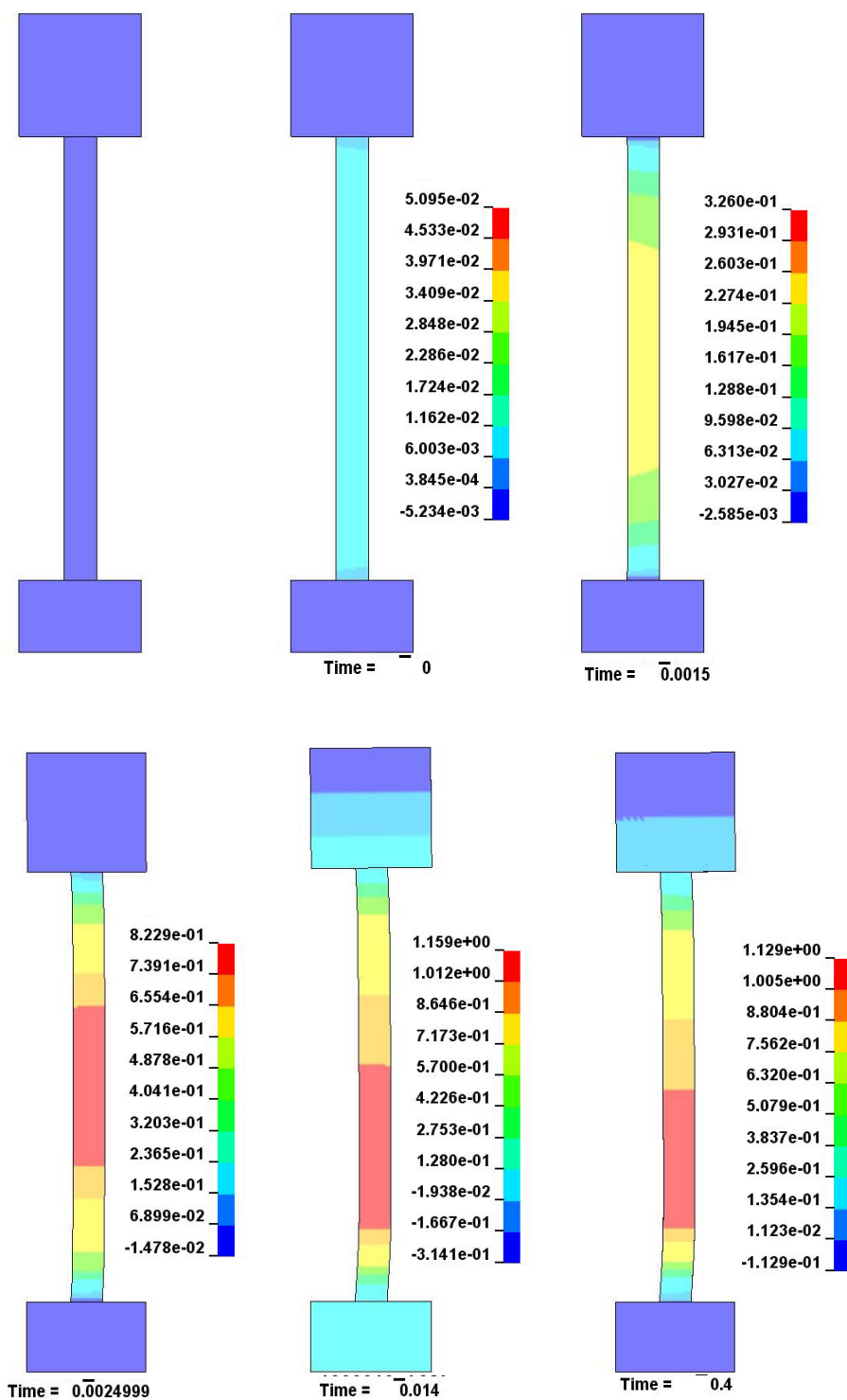
Figure 4.17: Test SA02 Finite Element Displacements
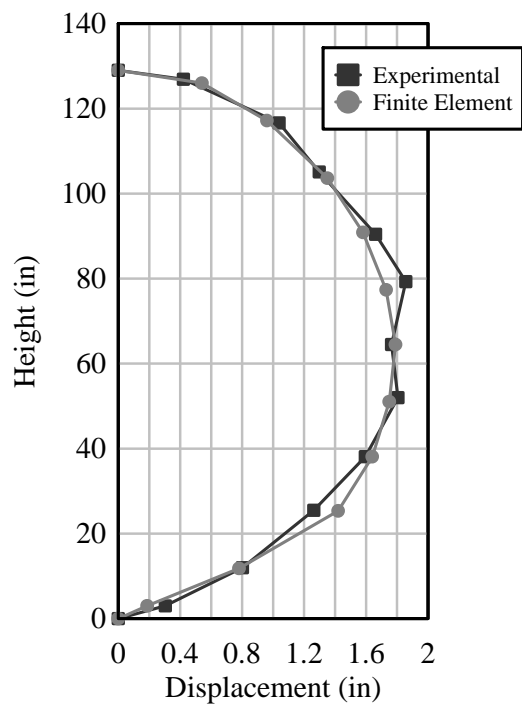
Figure 4.18: Test SA02 Maximum Displacement Comparison
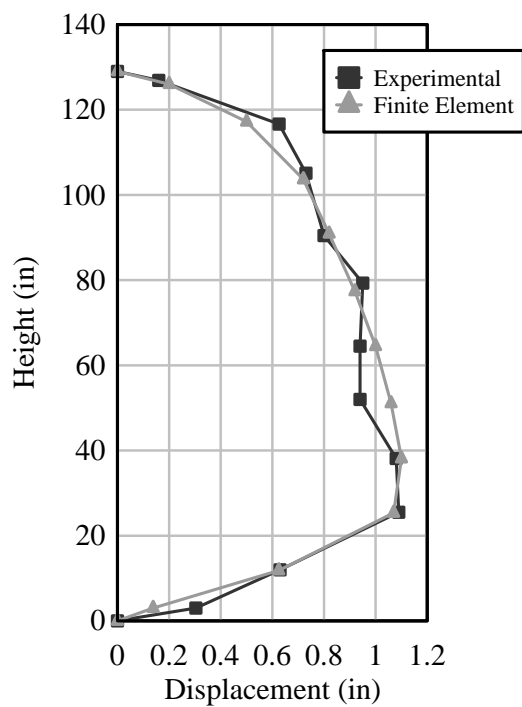
Figure 4.19: Test SA02 Residual Displacement Comparison
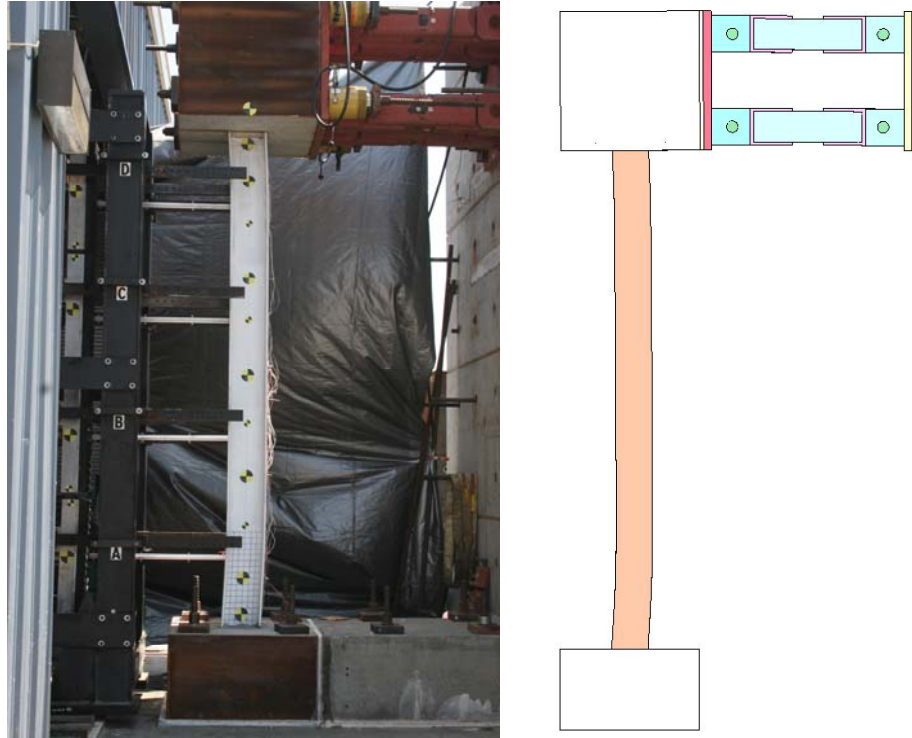
Figure 4.20: Test SA02 Visual Comparison

4.5.2 Test SA03

A described in Section 3.3.3, Test SA03 was a W10x49 specimen loaded with four BG25s at uniform velocity. From the data analysis, the average of the impact velocity of the BGs was found to be 947.5 in/s (24.1 m/s). Similar to Test SA02, each impacting module in the model, with representative equivalent weight, was given this initial velocity in the direction of the specimen. The initial configuration of the model is the same as Test SA02 and is shown in Figure 4.14.

After impact, the modules rebound in the opposite direction, as they do during the test. To prevent any additional collisions, the elements of the impacting modules were eroded at a time of 0.012 ms. The column then was allowed to freely move to its point of maximum global displacement and rebound to its final resting point with some residual

displacement. The termination time of 0.40 ms and a global damping of 2 percent were used. The progression of the run is shown in a series of screen shots in Figure 4.21.

Using the forces calculated through each contact surface, the corresponding impulses were calculated and are summarized in Table 4.3. These impulses are slightly greater than those values calculated from the experimental data in the previous chapter, and the additional impulse accounts for the greater displacements shown below.

Table 4.3: Test SA03 Finite Element Impulse

BG #	Impulse (psi-ms)
BG1	2327
BG2	2563
BG3	2476
BG4	2317

Displacements of the column are given in Figure 4.22 for various times throughout the run. Maximum and residual displacements at multiple locations were found along the height of the column. The results of the finite element run are summarized in Table 4.4.The finite element displacement results are plotted against displacements seen in the Test SA03 experiment in Figure 4.23 and Figure 4.24. From the plots, the maximum displacement of the finite element model was 3.05 in as compared with a displacement of 2.90 in from the experiment which corresponds to an error of 5.17%. The residual displacement of the computational model was 2.38 in and the experimental displacement was 2.18 in. The error from the residual displacements was found as 9.17%. Included in Figure 4.25 and Figure 4.26 are visual comparisons from the finite element calculation and the experiment.
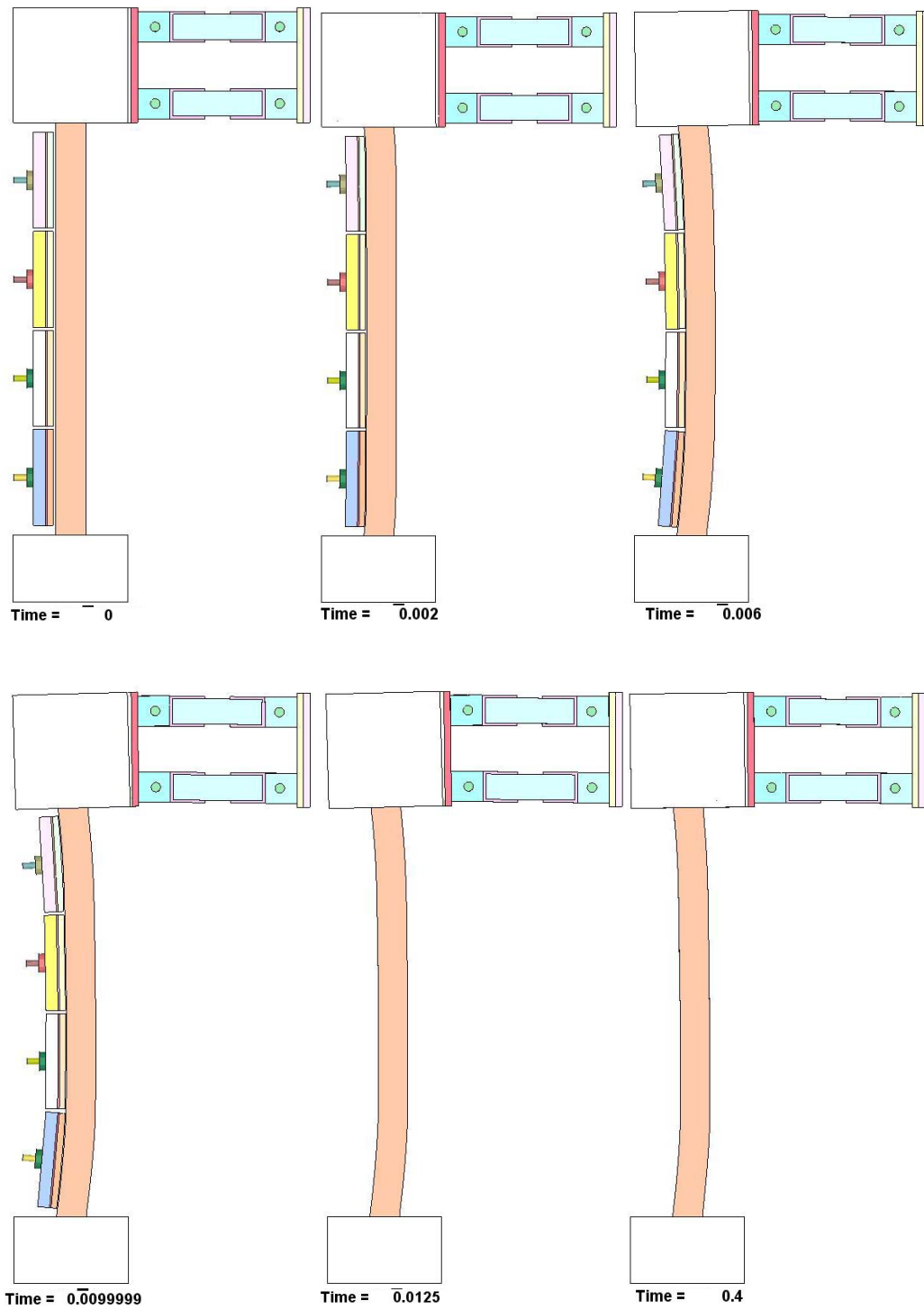
Figure 4.21: Test SA03 Finite Element Run Progression
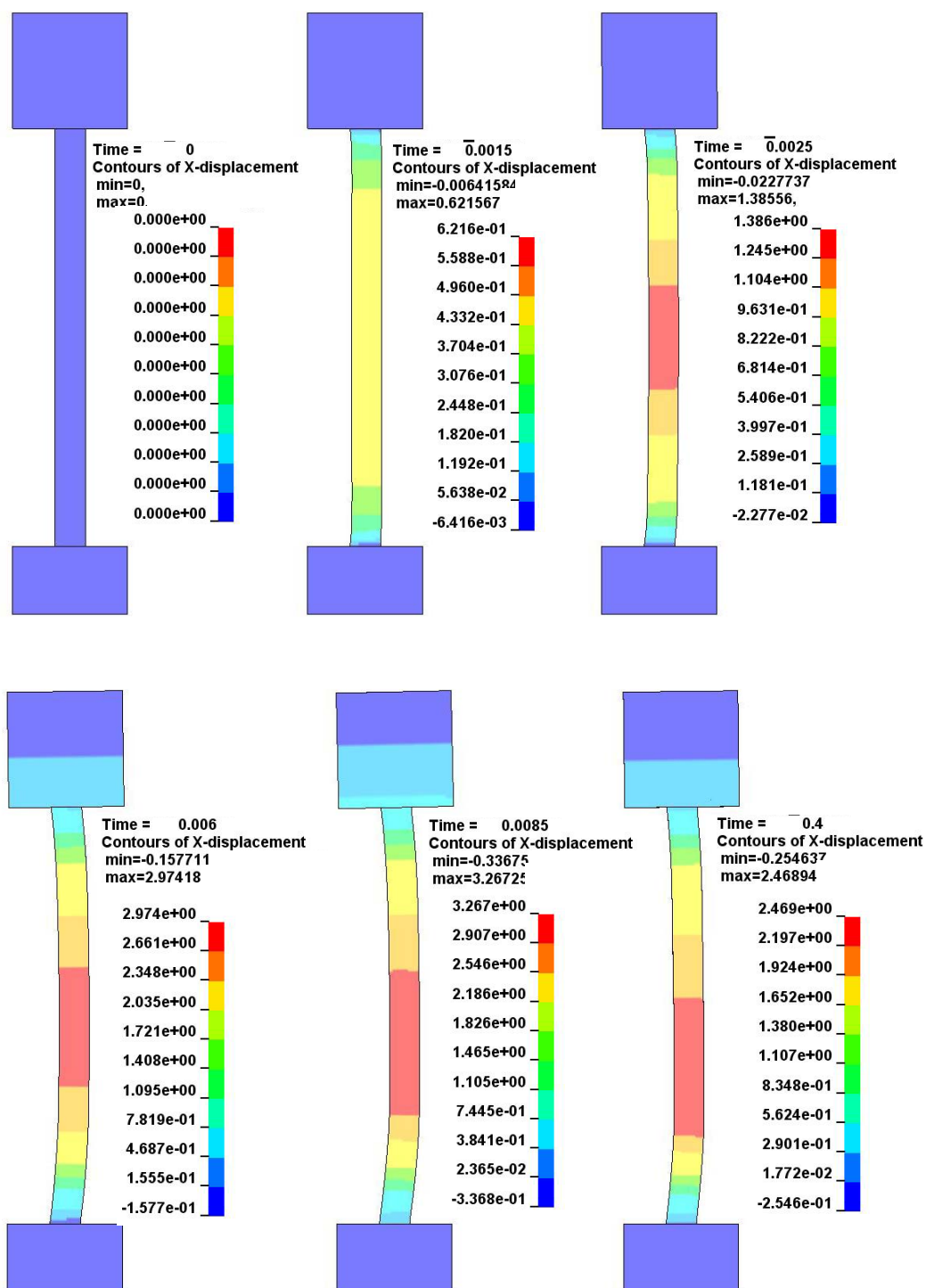
Figure 4.22: Test SA03 Finite Element Displacements

Table 4.4: Test SA03 Maximum and Residual Displacements

Distance from Base (in)	Maximum Displacement (in)	Residual Displacement (in)
126.0	0.52	0.46
117.0	1.34	1.09
103.875	2.29	1.70
90.75	2.69	1.92
77.625	2.92	2.11
64.5	3.05	2.26
51.375	3.03	2.34
38.25	2.93	2.38
25.125	2.45	2.10
12.0	1.23	1.09
3.0	0.30	0.26
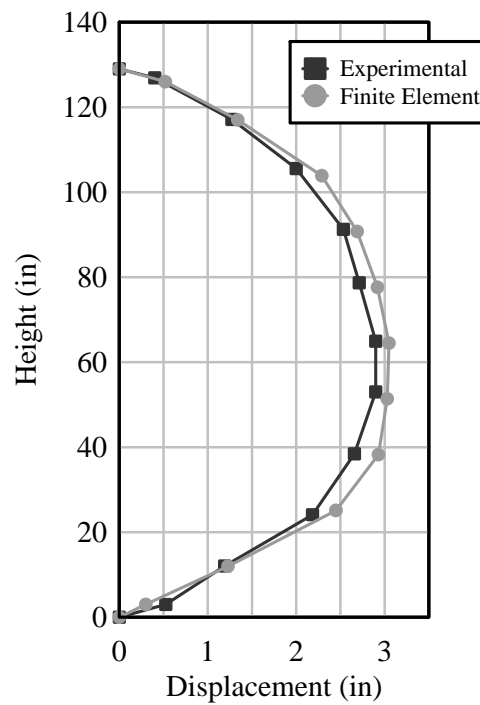
Figure 4.23: Test SA03 Maximum Displacement Comparison
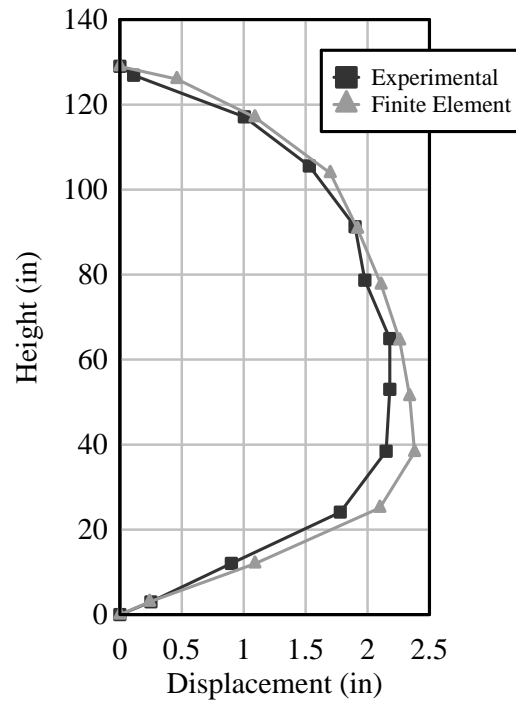
Figure 4.24: Test SA03 Residual Displacement Comparison
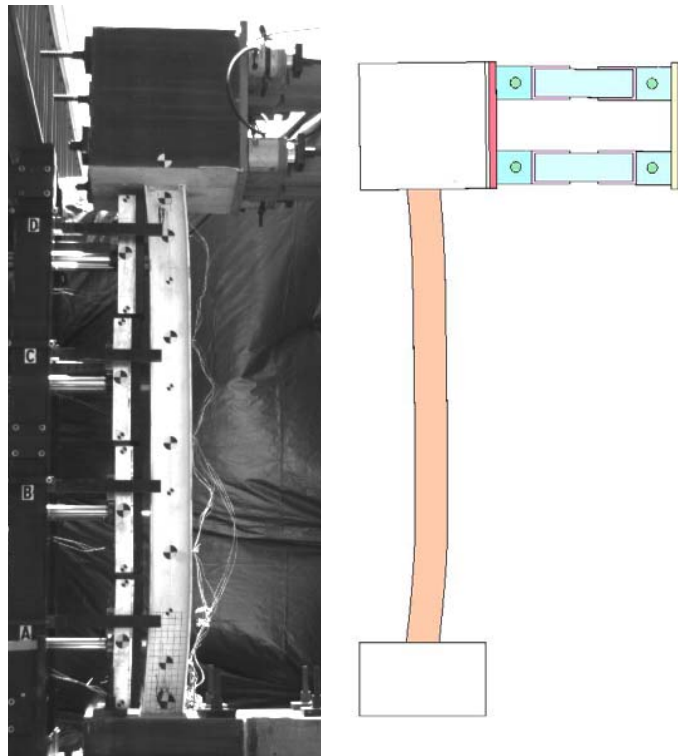
Figure 4.25: Test SA03 Visual Comparison 1
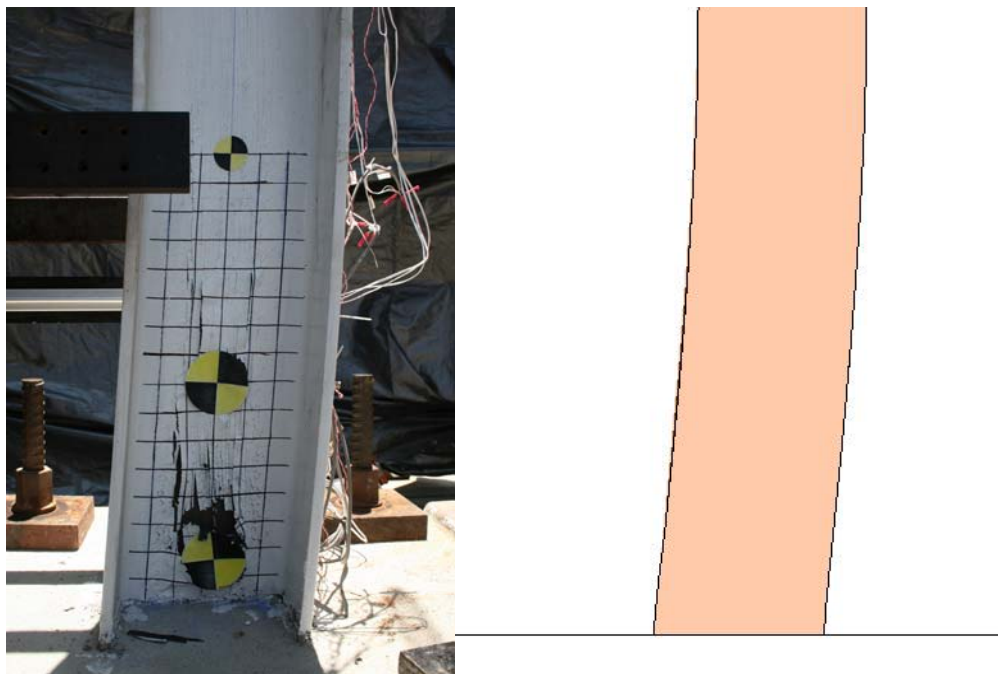
Figure 4.26: Test SA03 Visual Comparison 2

4.5.3 Test SA09

A described in Section 3.3.6, Test SA09 was a W14x132 specimen loaded with two BG50s and two BG25s at variable velocity. From the data analysis, the velocities of the BGs were found to be 1780.0 in/s (45.2 m/s), 1472.5 in/s (37.4 m/s), 987.5 in/s (25.1 m/s), and 442.0 in/s (11.2 m/s) for BG1 to BG4, respectively. Each impacting module in the model, with representative equivalent weight to account for additional mass of the rods of the BG50s, was given this initial velocity in the direction of the specimen. The modules were each given an initial position to account for the difference in velocities so that the impact would be synchronized. The initial configuration of the model is shown in Figure 4.27.

After impact, the modules rebound in the opposite direction, as they do during the test. To prevent any additional collisions, the elements of the impacting modules were

eroded at a time of 0.025 ms, which was the amount visually seen in the camera footage. The column then was allowed to freely move to its point of maximum global displacement and rebound to its final resting point with some residual displacement. The termination time of 0.40 ms and a global damping of 2 percent was incorporated which was found to be sufficient for correctly determining the final state of the column. The progression of the run is shown in a series of screen shots in Figure 4.28.

Using the forces calculated through each contact surface, the corresponding impulses were calculated and are summarized in Table 4.5. These impulses are comparable to those values calculated from the experimental data in the previous chapter.

Table 4.5: Test SA09 Finite Element Impulses

BG #	Impulse (psi-ms)
BG1	7645
BG2	7189
BG3	4345
BG4	2220

Displacements of the column are given in Figure 4.29 for various times throughout the run. Maximum and residual displacements at multiple locations were found along the height of the column. The results of the finite element run are summarized in Table 4.6 for the maximum and residual displacements.
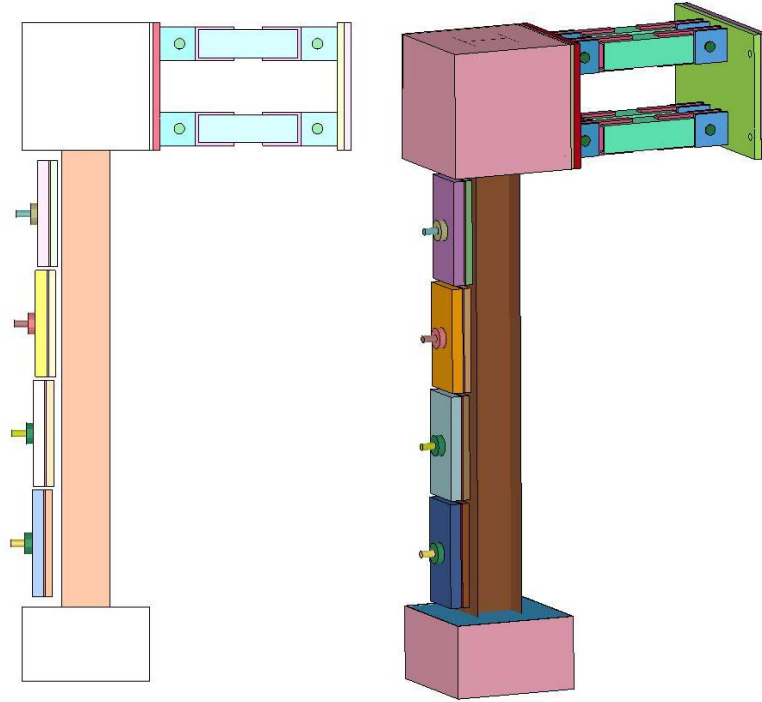
Figure 4.27: Test SA09 Finite Element Model Configuration

Table 4.6: Test SA09 Displacements

Distance from Base (in)	Maximum Displacement (in)	Residual Displacement (in)
126.0	1.16	0.89
117.0	1.71	1.30
103.875	2.48	1.90
90.75	3.13	2.45
77.625	3.71	2.98
64.5	4.13	3.41
51.375	4.39	3.75
38.25	4.51	3.99
25.125	4.09	3.73
12.0	2.36	2.18
3.0	0.68	0.61

Time =   0.0015

Time =   0.0025

Time =   0.004

Time =   0.0084999

Time =   0.0125

Time =   0.4
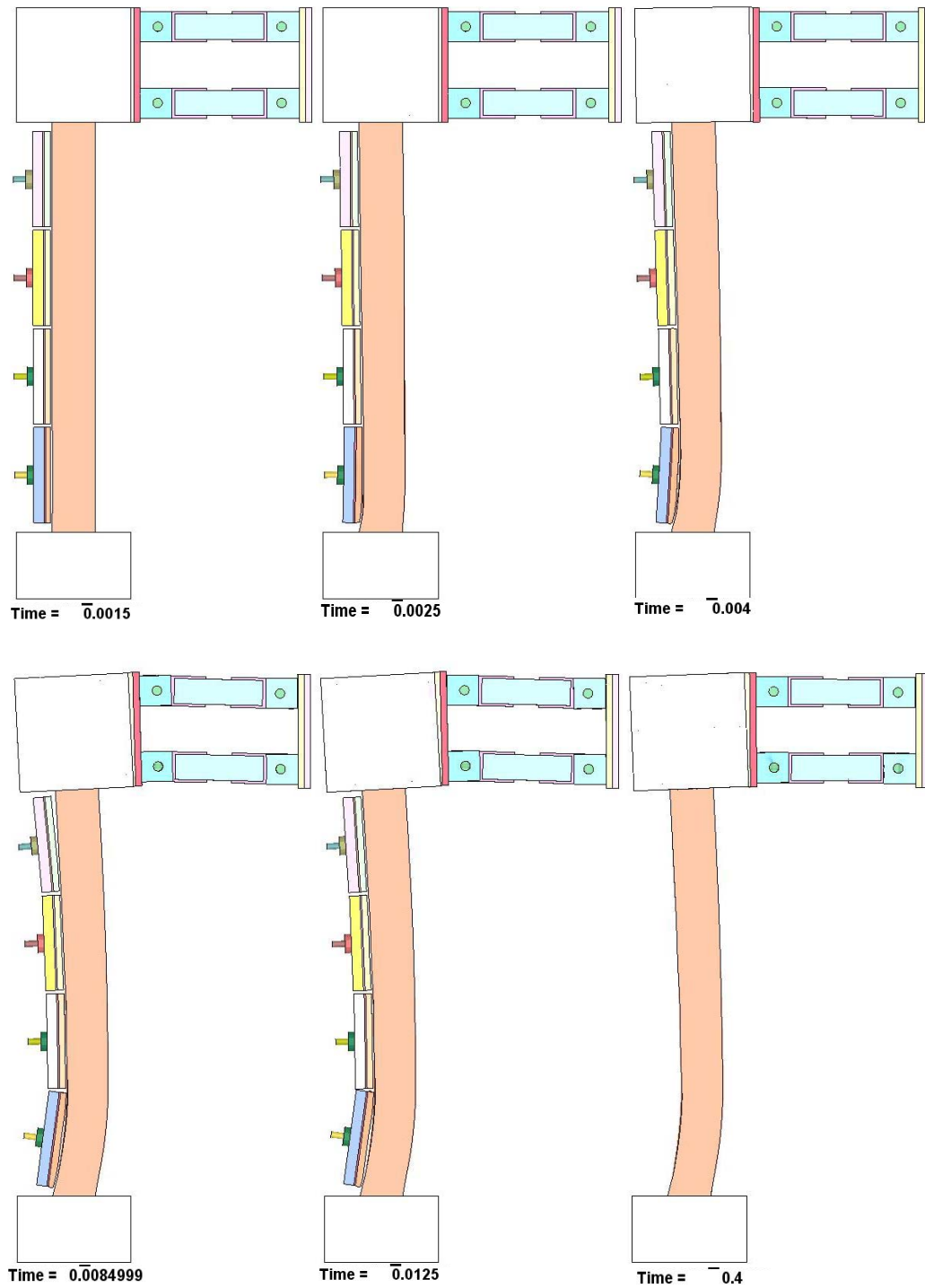
Figure 4.28: Test SA09 Finite Element Run Progression
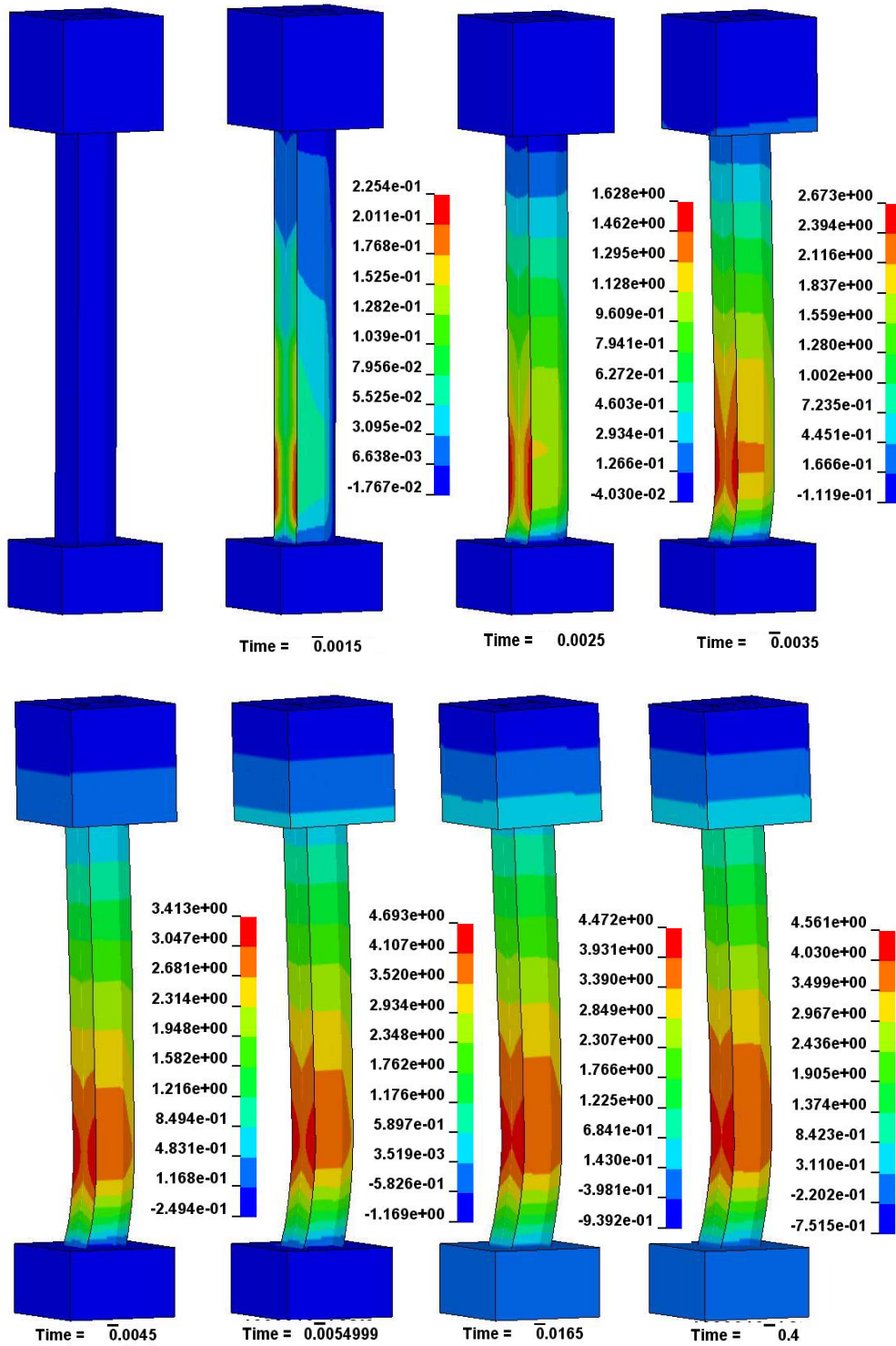
Figure 4.29: Test SA09 Finite Element Displacements

The finite element displacement results are plotted against displacements seen in the Test SA03 experiment. The comparisons for both maximum and residual displacements are shown in Figure 4.30 and Figure 4.31. From the plots, the maximum displacement of the finite element model was 4.51 in as compared with a displacement of 4.93 in from the experiment which corresponds to an error of 5.93%. The residual displacement of the computational model was 3.99 in and the experimental displacement was 4.08 in. The error from the residual displacements was found as 0.23%. Included in Figure 4.32 and Figure 4.33 are visual comparisons from the finite element calculation and the experiment.
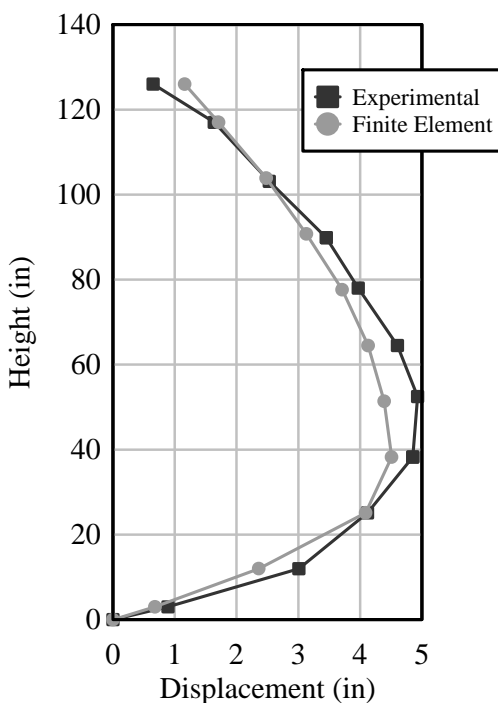
Figure 4.30: Test SA09 Maximum Displacement Comparison
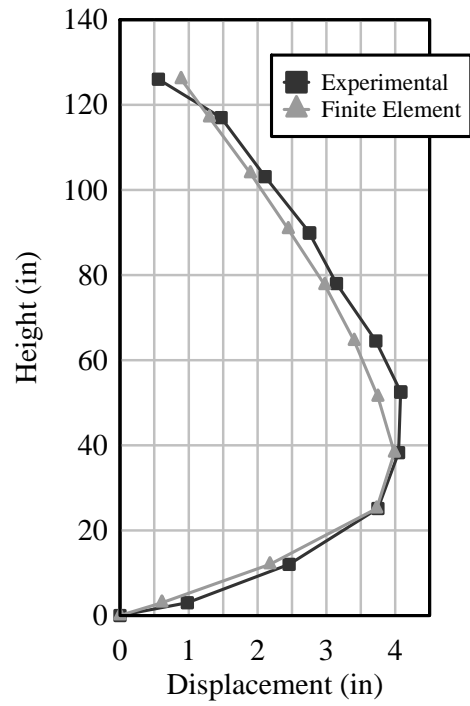
Figure 4.31: Test SA09 Residual Displacement Comparison
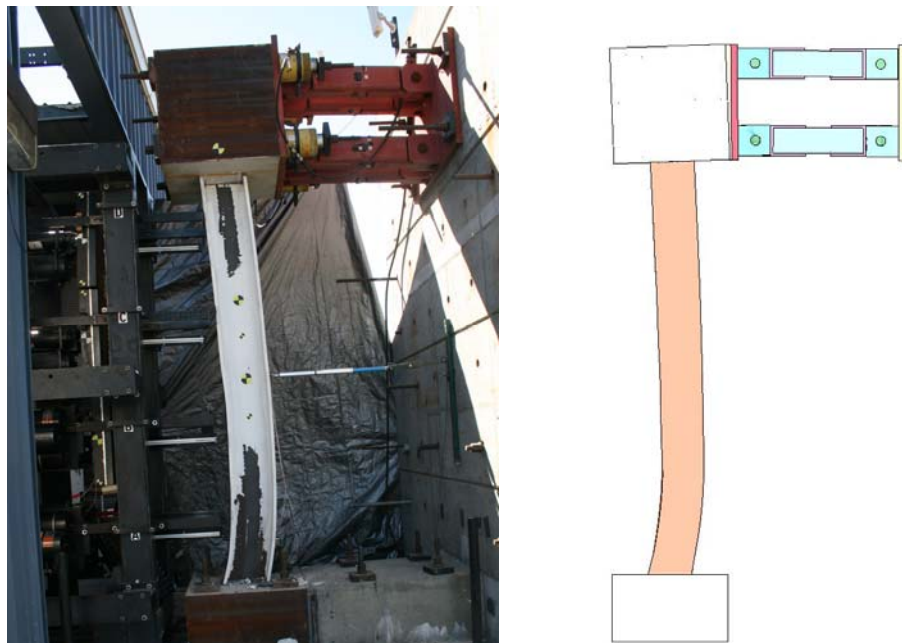
Figure 4.32: Test SA09 Visual Comparison 1
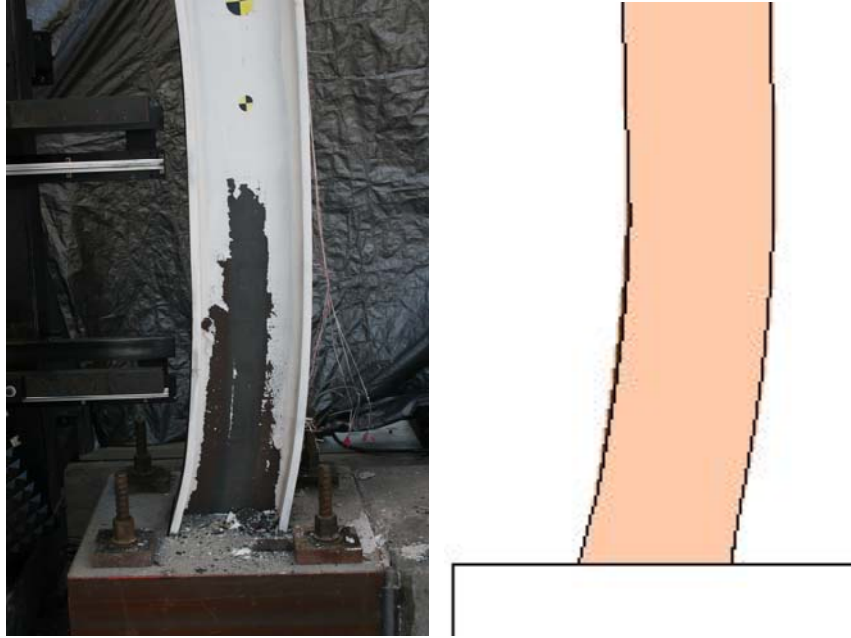
Figure 4.33: Test SA09 Visual Comparison 2

4.5.4 Test SA10

Section 3.3.7 describes the setup for Test SA10 which was a W14x132 specimen loaded with two BG50s and two BG25s at variable velocity. From the data analysis, the velocities of the BGs were found to be 1925.0 in/s (48.9 m/s), 1621.5 in/s (41.2 m/s), 1117.3 in/s (28.4 m/s), and 530.4 in/s (13.5 m/s) for BG1 to BG4, respectively. Each impacting module in the model, with representative equivalent weight to account for additional mass of the rods of the BG50s, was given this initial velocity in the direction of the specimen. The modules were each given an initial position to account for the difference in velocities so that the impact would be synchronized. The initial configuration of the model, as well as the impact process was the same as that of SA09 shown in Figure 4.27. The progression of the run is shown in a series of screen shots in Figure 4.34.

Using the forces calculated through each contact surface, the corresponding impulses were calculated and are summarized in Table 4.7. These impulses are comparable to those values calculated from the experimental data in the previous chapter.

Table 4.7: Test SA10 Finite Element Impulse

BG #	Impulse (psi-ms)
BG1	8570
BG2	8053
BG3	4940
BG4	2864

Displacements of the column are given in Figure 4.35 for various times throughout the run. Maximum and residual displacements at multiple locations were found along the height of the column. The results of the finite element run are summarized in Table 4.8 for the maximum and residual displacements. In this case, the maximum displacements occurred in the flanges as was seen in Test SA09.

The finite element displacement results are plotted with displacements seen in the Test SA10 experiment. The comparisons for both maximum and residual displacements are shown in Figure 4.36 and Figure 4.37. From the plots, the maximum displacement of the finite element model was 5.18 in as compared with a displacement of 5.50 in from the experiment which corresponds to an error of 5.82 %. The residual displacement of the computational model was 4.89 in and the experimental displacement was 4.54 in. The error from the residual displacements was found as 7.71 %.

Included in Figure 4.38 and Figure 4.39 are visual comparisons from the finite element calculation and the experiment.

Time =   0

Time =   0.0015

Time =   0.003

Time = 0.0054999

Time =   0.011

Time =   0.4

Figure 4.34: Test SA10 Finite Element Run Progression
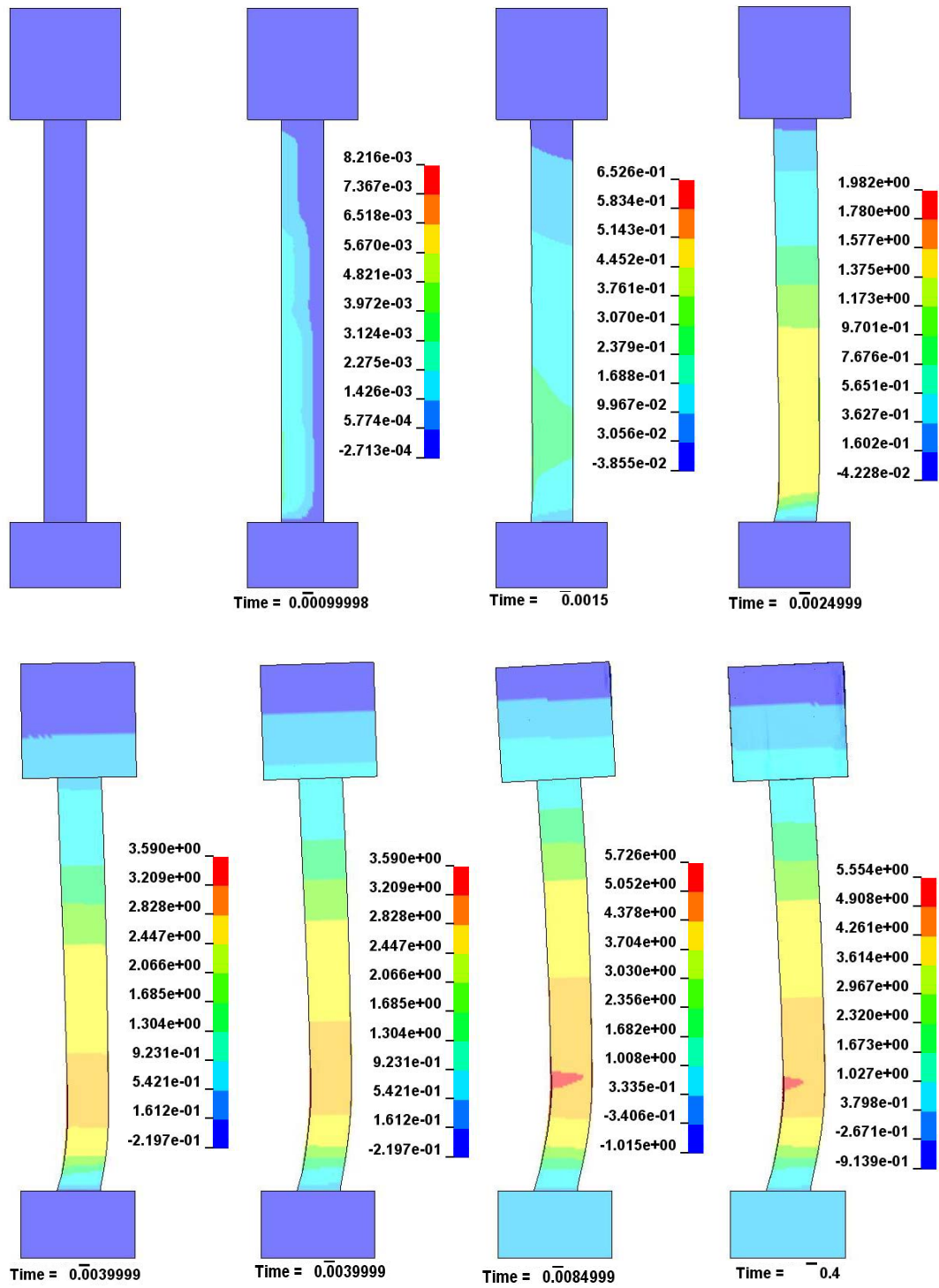
Figure 4.35: Test SA10 Finite Element Displacements

Table 4.8: Test SA10 Maximum and Residual Displacements

Distance from Base (in)	Maximum Displacement (in)	Residual Displacement (in)
126.0	1.32	1.02
117.0	1.95	1.52
103.875	2.87	2.27
90.75	3.65	2.94
77.625	4.33	3.58
64.5	4.83	4.11
51.375	5.18	4.55
38.25	5.36	4.89
25.125	4.83	4.48
12.0	2.76	2.57
3.0	0.81	0.73
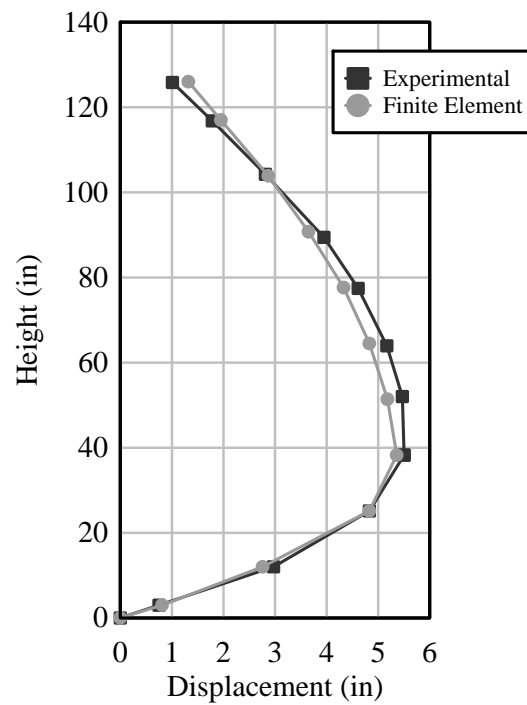
Figure 4.36: Test SA10 Maximum Displacement Comparison
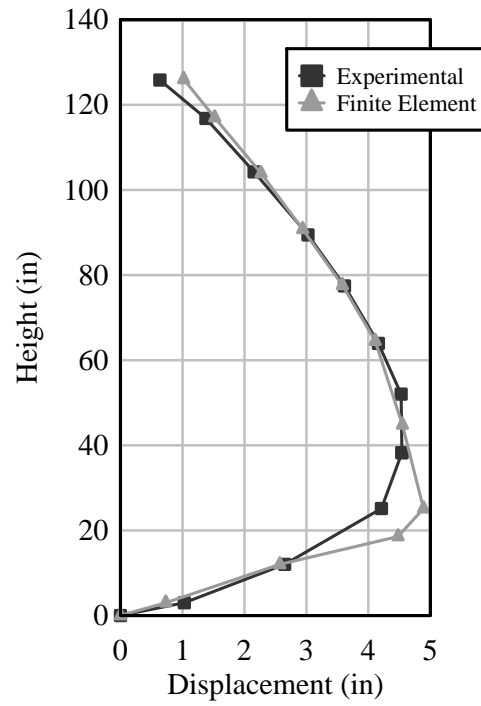
Figure 4.37: Test SA10 Residual Displacement Comparison
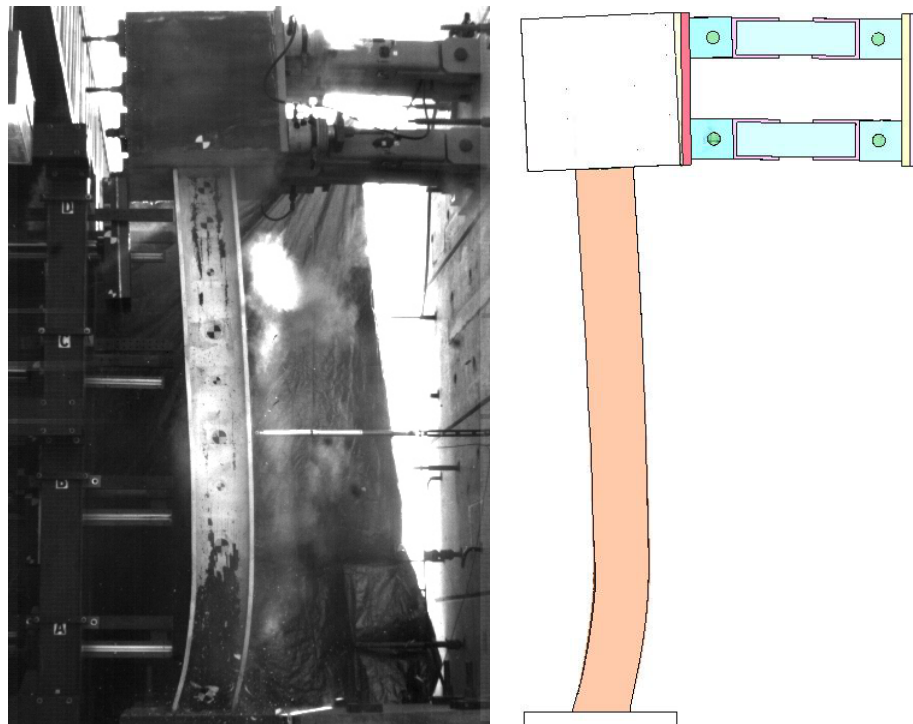
Figure 4.38: Test SA10 Visual Comparison 1
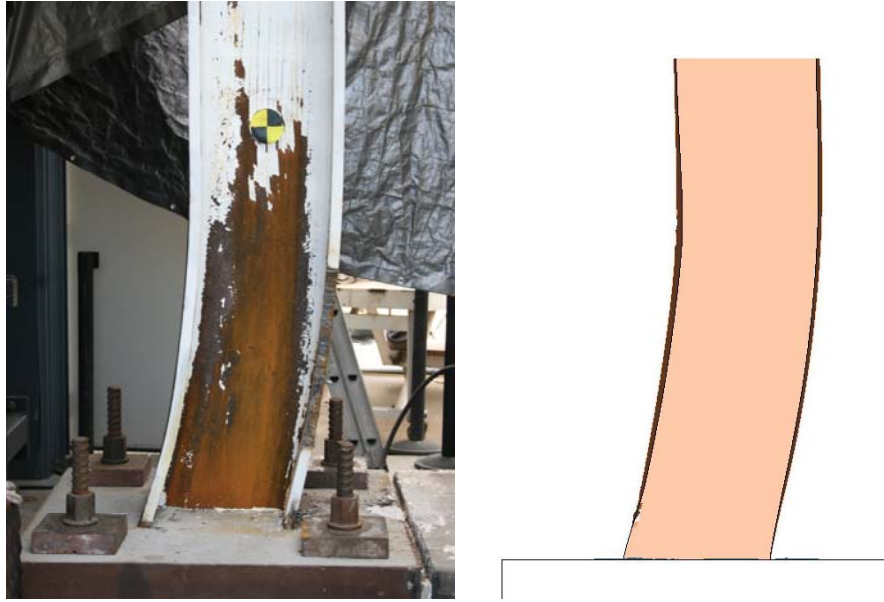
Figure 4.39: Test SA10 Visual Comparison 2

4.5.5 Test SA07

Section 3.3.5 describes the setup for Test SA07 which was a W14x132 specimen loaded with two BG50s and two BG25s at variable velocity. This test had some residual displacement from a previous hit. The initial deformation of the column was incorporated into the mesh of the model as seen in Figure 4.40 by moving nodes to the positions recorded for the residual displacements of the column web.

From the data analysis, the velocities of the BGs were found to be 1759.4 in/s (44.7 m/s), 1456.8 in/s (37.0 m/s), 982.0 in/s (24.9 m/s), and 443.5 in/s (11.3 m/s) for BG1 to BG4, respectively. The initial configuration of the model is shown in Figure 4.40 and is identical in setup to the previous test. The progression of the run is shown in a series of screen shots in Figure 4.41.
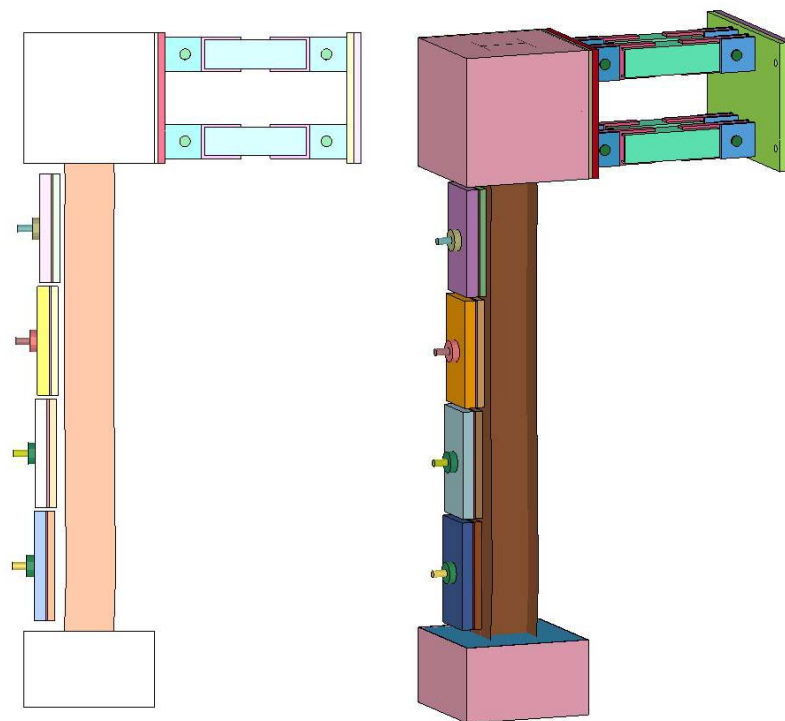
Figure 4.40: Test SA07 Finite Element Model Configuration

Using the forces calculated through each contact, the corresponding impulses were calculated and are summarized in Table 4.9. These impulses are comparable to those values calculated from the experimental data in the previous chapter.

Table 4.9: Test SA07 Finite Element Impulse

BG #	Impulse (psi-ms)
BG1	7571
BG2	7036
BG3	4362
BG4	2150

Figure 4.41: Test SA07 Finite Element Run Progression

Displacements of the column are given in Figure 4.42 for various times throughout the run. Maximum and residual displacements at multiple locations were found along the height of the column. The results of the finite element run are summarized in Table 4.10 for the maximum and residual displacements

The finite element displacement results are plotted against displacements seen in the Test SA07 experiment. The comparisons for both maximum and residual displacements are shown in Figure 4.43 and Figure 4.44. From the plots, the maximum displacement of the finite element model was 4.44 in as compared with a displacement of 4.65 in from the experiment which corresponds to an error of 4.5 %. The residual displacement of the computational model was 3.96 in and the experimental displacement was 3.98 in. The error from the residual displacements was found as 0.05 %.

Included in Figure 4.45 and Figure 4.46 are visual comparisons from the finite element calculation and the experiment.

Table 4.10: Test SA07 Maximum and Residual Displacements

Distance from Base (in)	Maximum Displacement (in)	Residual Displacement (in)
126.0	1.12	0.86
117.0	1.65	1.27
103.875	2.40	1.84
90.75	3.03	2.37
77.625	3.60	2.89
64.5	4.01	3.34
51.375	4.30	3.70
38.25	4.44	3.96
25.125	4.07	3.73
12.0	2.35	2.17
3.0	0.71	0.63
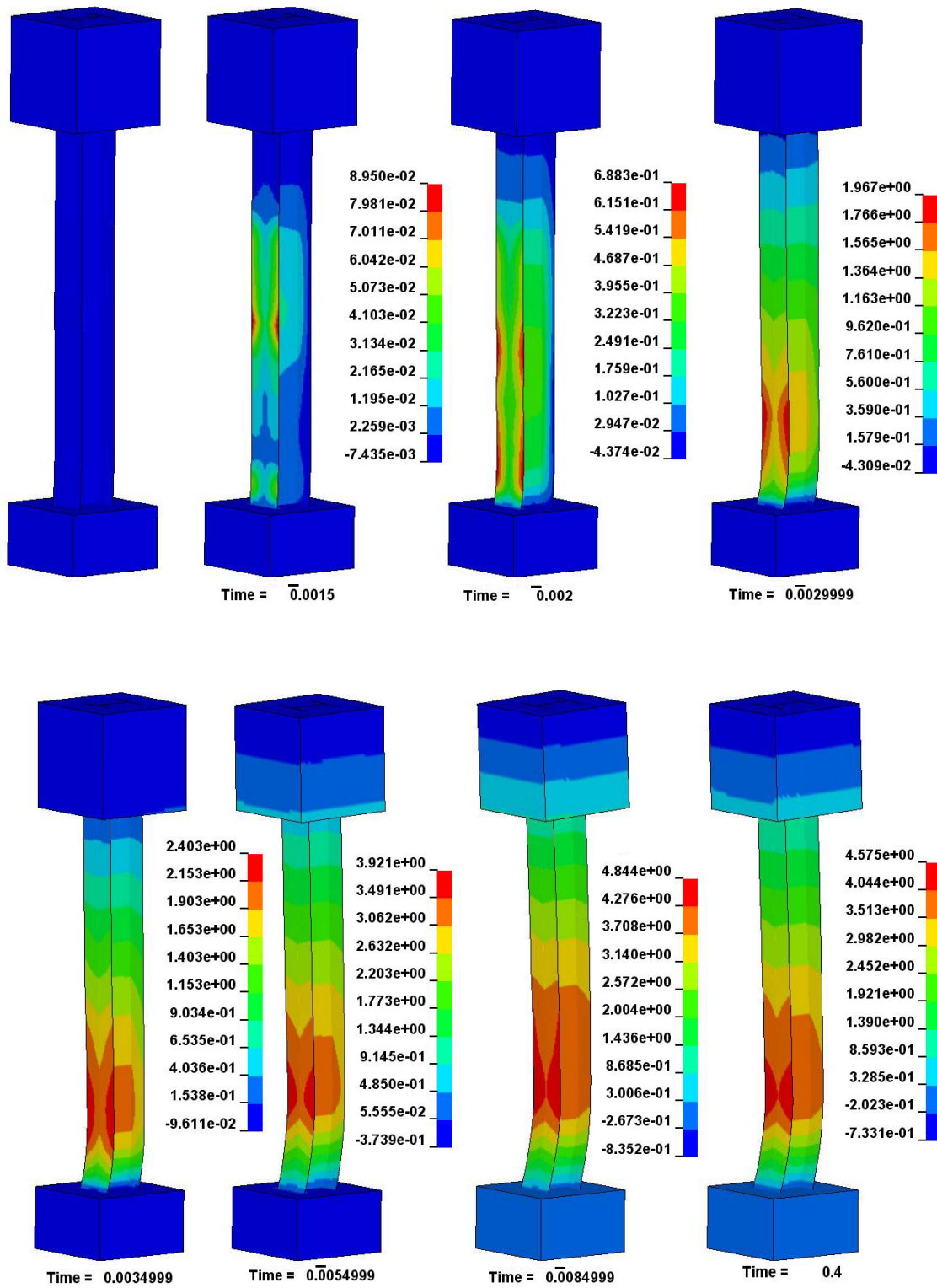
Figure 4.42: Test SA07 Finite Element Displacements
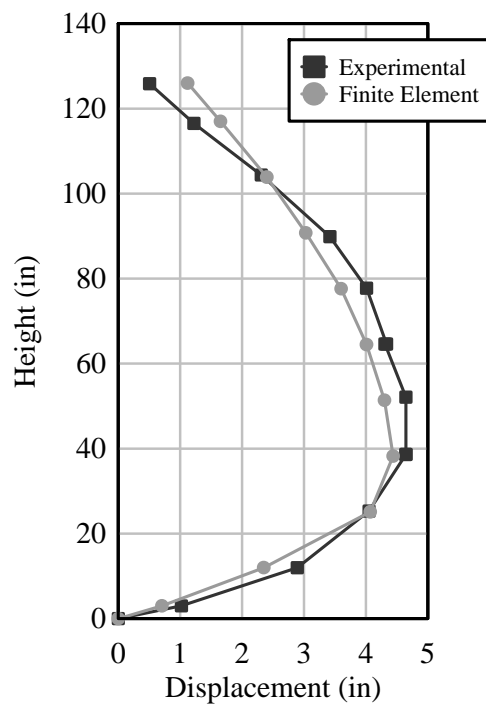
Figure 4.43: Test SA07 Maximum Displacement Comparison
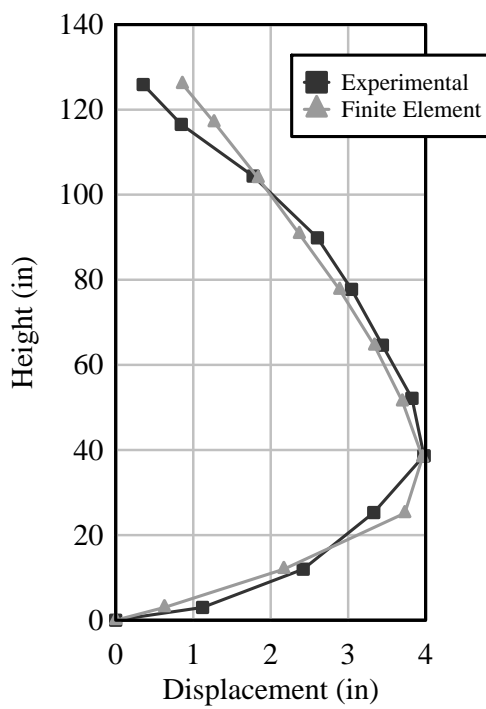
Figure 4.44: Test SA07 Residual Displacement Comparison
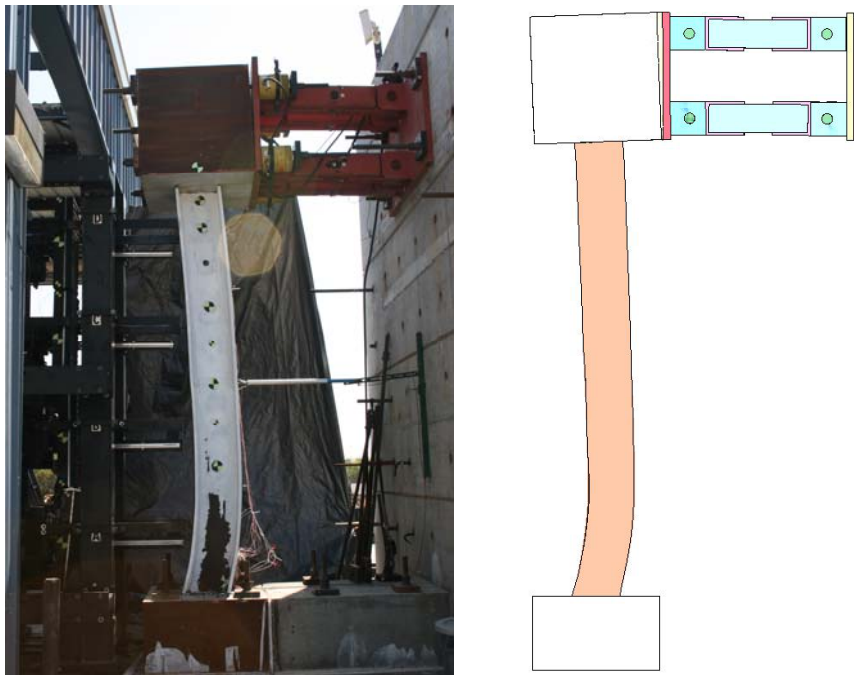
Figure 4.45: Test SA07 Visual Comparison 1
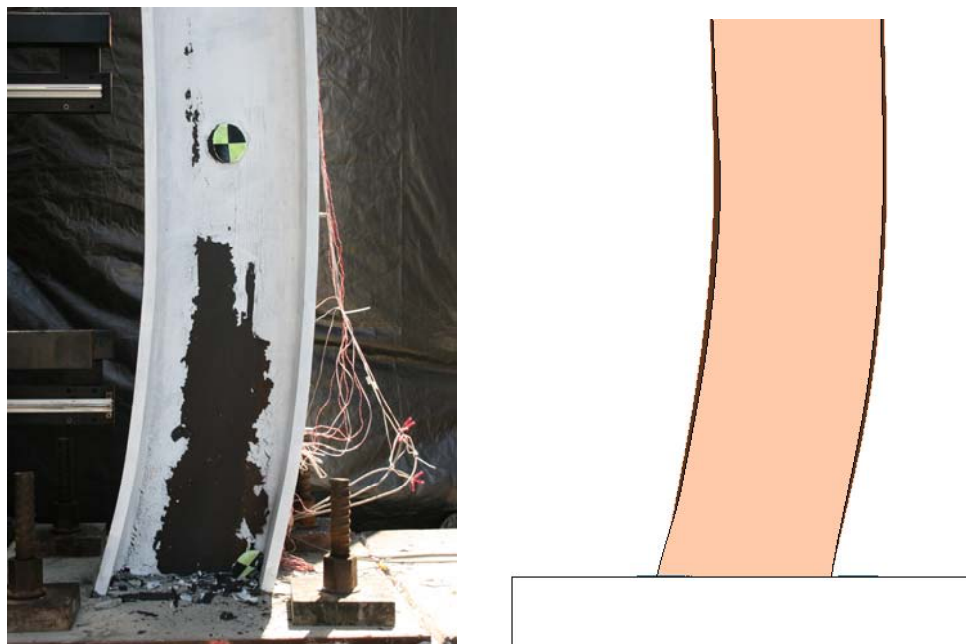
Figure 4.46: Test SA07 Visual Comparison 2

4.5.6 Test SA11

A described in Section 3.3.8, Test SA11 was a W10x49 specimen loaded with two BG50s and two BG25s at variable velocity. This test had some residual displacement from a previous hit in Test SA02. The initial deformation of the column was incorporated into the mesh of the model as seen in Figure 4.47.

From the data analysis, the velocities of the BGs were found to be 1594.5 in/s (40.5 m/s), 1334.6 in/s (33.9 m/s), 1267.7 in/s (32.2 m/s), and 972.4 in/s (24.7 m/s) for BG1 to BG4, respectively. Each impacting module in the model, with representative equivalent weight to account for additional mass of the rods of the BG50s, was given this initial velocity in the direction of the specimen. The modules were each given an initial position to account for the difference in velocities so that the impact would be synchronized.
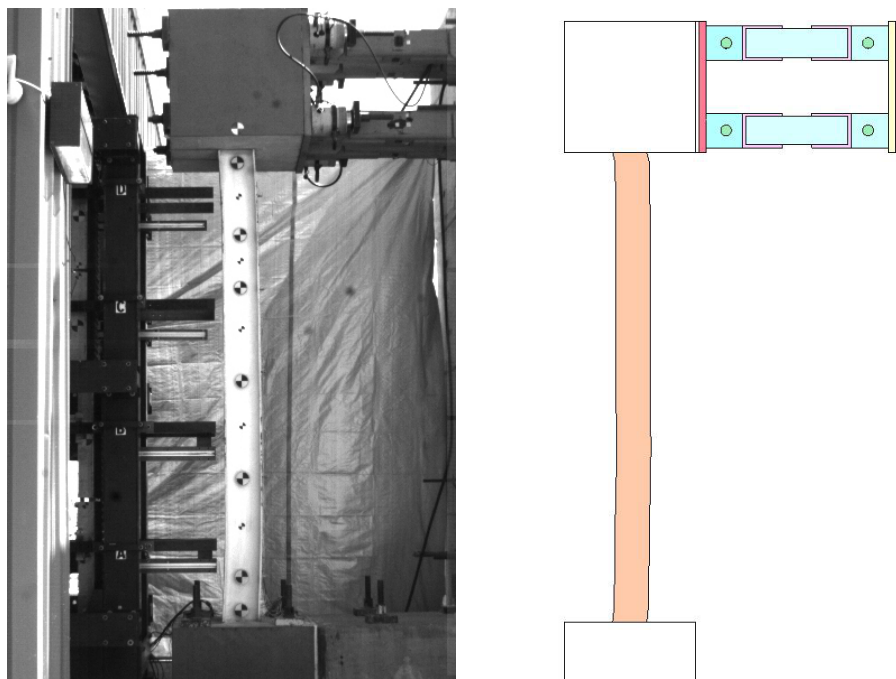
Figure 4.47: Test SA11 Initial Deformation of Experiment (left) and FE Model (right)

After impact, the modules rebounded, as they do during the test. To prevent any additional collisions, the elements of the impacting modules were eroded at a time of 0.065 ms, which was determined using visual evidence from the camera recordings. The column then was allowed to freely move to its point of maximum global displacement and rebound to its final resting point with some residual displacement. The progression of the run is shown in a series of screen shots in Figure 4.48.

Using the forces calculated through each contact surface, the corresponding impulses were calculated and are summarized in Table 4.11. These impulses are comparable to those values calculated from the experimental data in the previous chapter.

Table 4.11: Test SA11 Finite Element Impulse

BG #	Impulse (psi-ms)
BG1	5453
BG2	5234
BG3	2965
BG4	2215

Displacements of the column are given in Figure 4.49 for various times throughout the run. Maximum and residual displacements at multiple locations were found along the height of the column. The results of the finite element run are summarized in Table 4.12 for the maximum and residual displacements. The finite element displacement results are plotted against displacements seen in the Test SA11 experiment and are shown in Figure 4.50 and Figure 4.51. From the plots, the maximum displacement of the finite element model was 7.30 in as compared with a displacement of 7.09 in from the experiment which corresponds to an error of 2.96%. The residual displacement of the computational model was 6.67 in and the experimental displacement

was 6.31 in. The error from the residual displacements was found as 5.71%. Included in Figure 4.52 and Figure 4.53 are visual comparisons from the finite element calculation and the experiment.

Table 4.12: Test SA11 Maximum and Residual Displacements

Distance from Base (in)	Maximum Displacement (in)	Residual Displacement (in)
126.0	1.01	0.78
117.0	2.18	1.81
103.875	3.86	3.30
90.75	5.06	4.40
77.625	6.04	5.36
64.5	6.90	6.22
51.375	7.27	6.61
38.25	7.30	6.67
25.125	6.20	5.77
12.0	3.58	3.35
3.0	0.91	0.93

Time =   0.0015   Time = 0.0029999   Time =   0.0045

Time =   0.006   Time =   0.021   Time =   0.04

Figure 4.48: Test SA11 Finite Element Run Progression
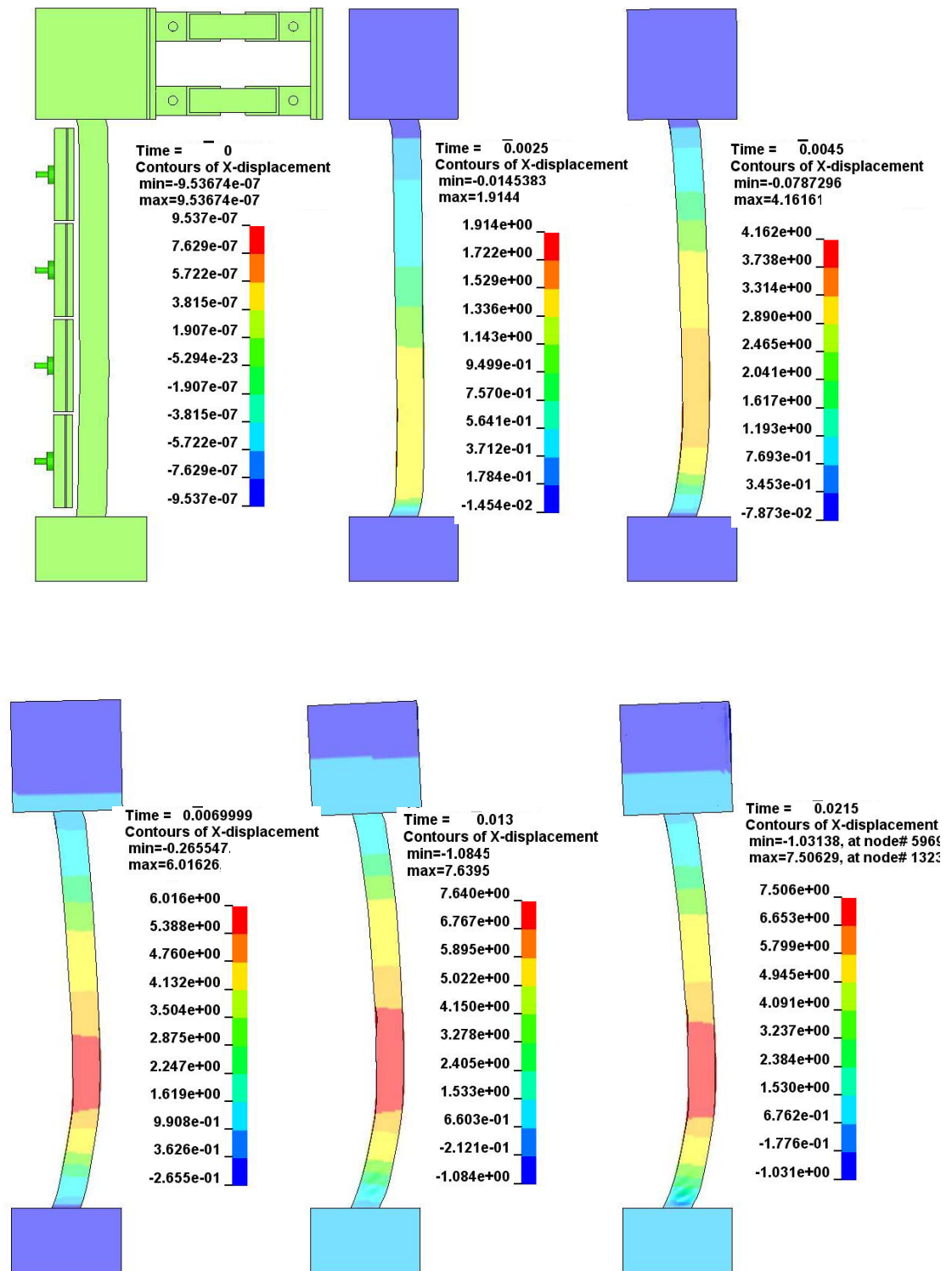
Figure 4.49: Test SA11 Finite Element Displacements
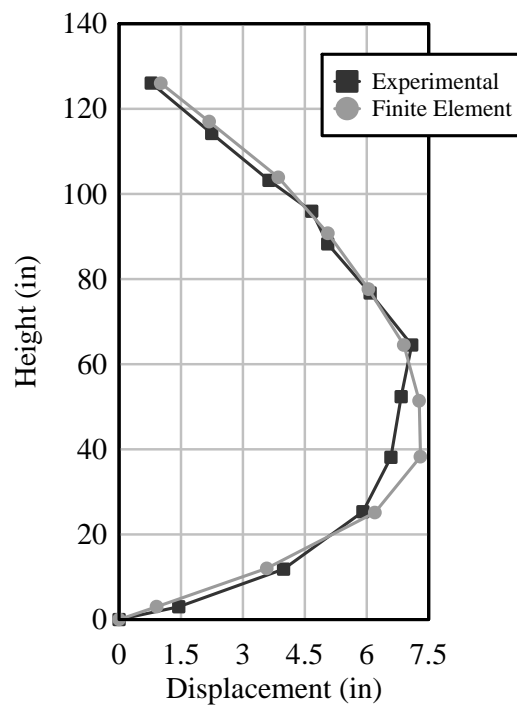
Figure 4.50: Test SA11 Maximum Displacement Comparison
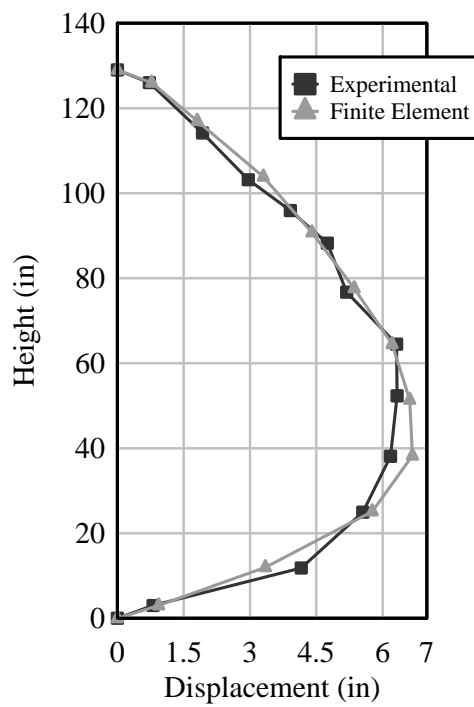
Figure 4.51: Test SA11 Residual Displacement Comparison
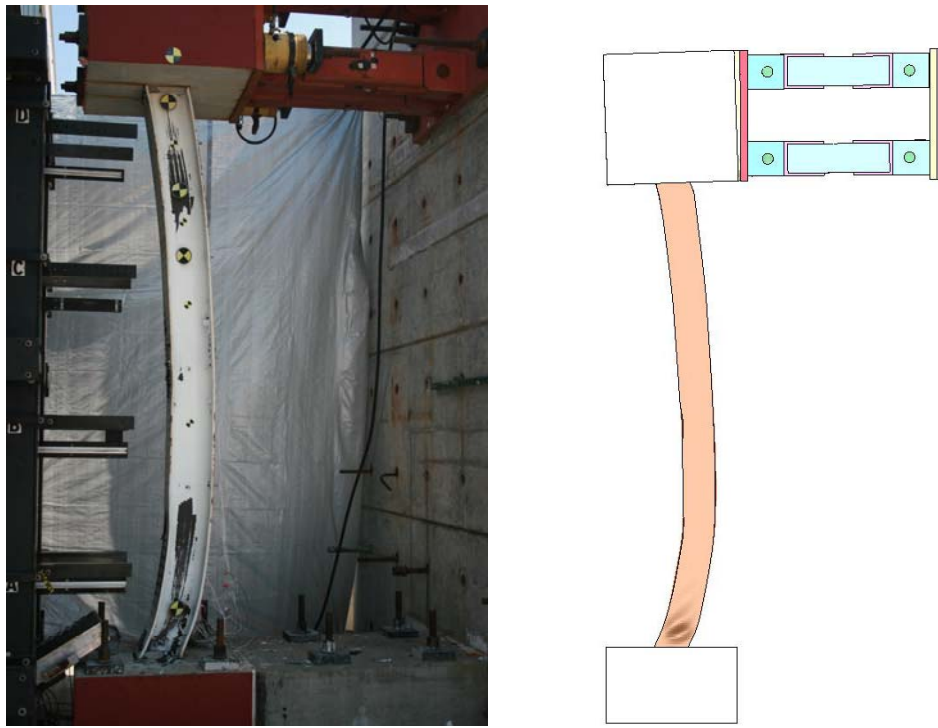
Figure 4.52: Test SA11 Visual Comparison 1
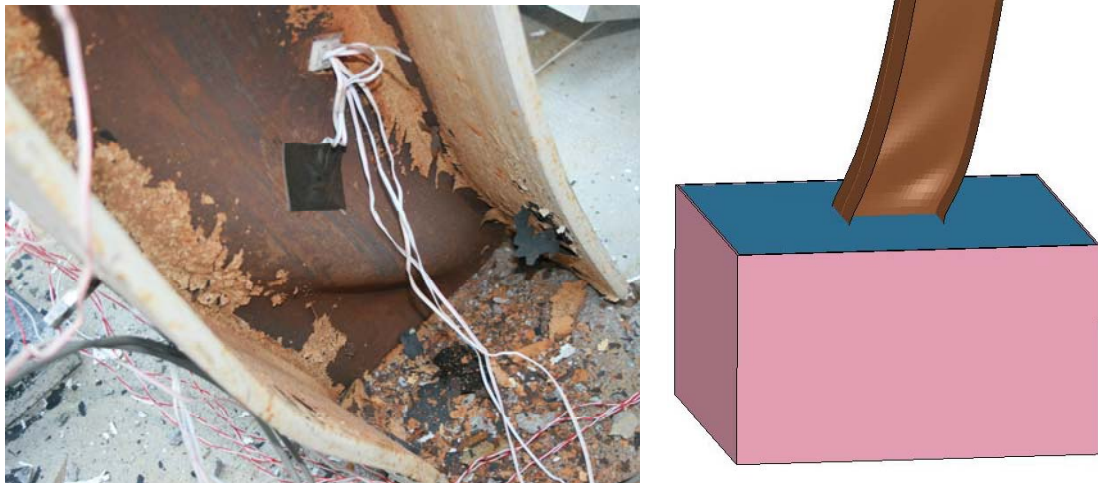
Figure 4.53: Test SA11 Visual Comparison 2

4.6 Summary

This chapter described the procedure for developing and validating a finite element model for predicting column response when loaded in the strong axis direction with the UCSD Blast Simulator. The steel columns were modeled using shell elements and used a piecewise linear isotropic model that incorporated strain rate effects. The use of this model, as well as the correct modeling of the boundary conditions proved to be critical in the overall development of the validated model.

The upper boundary was modeled to take into account the rotation and pull out of the link system through the use of a calibrated rubber pad that allowed for an increase in rotation in higher velocity tests, as was observed. The impacting module was modeled to include the rod and the collar and the programmer was simulated using a foam model that was correlated to test data in previous research [13].

The model was validated using the six tests discussed in Chapter 3 and it was found that the finite element analysis could accurately predict the local and global behavior of the column in all tests, including tests that exhibited buckling. These field tests were compared to the displacements of the model and it was observed that the model did not produce errors for maximum displacements of over 8%.

5 Simulated Testing of Weak Axis Steel Columns Subjected to Blast Loads

This chapter presents the results and analysis from a series of simulated blast tests on as-built steel wide-flange sections impacted in the weak axis direction with uniform and variable load along the height of the column. The purposes of these tests were to characterize the behavior of the columns under various simulated blast loads, validate the simulator using data from similar field tests and to provide high quality test data which was used to improve and validate predictive computer models. Additionally, these tests were also used to develop an experimental loading protocol for future testing of columns in the weak axis direction. The first section discusses the preliminaries: test setup, specimen design and instrumentation. The second section describes the methods for data analysis. This includes the analysis of accelerometer, camera and force data. The next section describes the experimental test results. Finally, a summary of the chapter is included.

One uniform velocity and five variable velocity experiments were conducted on six specimens with either sand or water as a loading medium which is further described in Section 5.1.1. A summary of these tests with desired impact velocity is shown in Table 5.1.

Table 5.1: Weak Axis Column Test Matrix

Test	Specimen	Type	Velocity Type	Loading Medium	Desired Impact Velocities
WA01	6	W10x49	Uniform	Sand	1102.4 in/s (28 m/s)
WA02	7	W14x132	Variable	Water	1574.8, 1299.2, 984.3, 629.9 in/s (40.0, 33.0, 25.0, 16.0 m/s)
WA03	8	W14x132	Variable	Water	1732.3, 1456.7, 1003.9, 708.7 in/s (44.0, 37.0, 25.5, 18.0 m/s)
WA04	9	W14x132	Variable	Sand	1732.3, 1456.7, 1003.9, 708.7 in/s (44.0, 37.0, 25.5, 18.0 m/s)
WA05	10	W10x49	Variable	Water	2362.2, 1870.1, 1378.0, 855.8 in/s (60.0, 47.5, 35.0, 22.5 m/s)
WA06	11	W10x49	Variable	Sand	2362.2, 1870.1, 1378.0, 855.8 in/s (60.0, 47.5, 35.0, 22.5 m/s)

5.1 Preliminaries

This section describes the details of the experimental setup for the weak axis tests. First, the test setup including reaction structure, upper link system and blast generator configurations are discussed. Next, details of the design and construction of the test specimens will be given. Finally, instrumentation details will be presented. This includes the data acquisition system, phantom cameras, accelerometers, strain gauges and load cells.

5.1.1 Setup

The setup for the tests is illustrated in Figure 5.1 and Figure 5.2. The columns were loaded with four blast generators distributed over the height of the column. For the W10x49 uniform tests, four BG 25s were used. The center to center spacing was 31 in, which left a 1 in gap between each plate. At the top and bottom there was a 3 in gap between the edges of the support and the impacting specimen.

The impacting units varied in dimension for each of the two size specimens and test type. For the W10x49 tests, the four impacting units were either 10 in x 30 in for the uniform velocity tests or 6 in × 30 in for the variable velocity tests. They weighed a total of 257.5 and 217 lbs for the BG25s, respectively, which included the weight of the steel rod and collar. The 6 in × 30 in impacting module for the BG50s weighed 337 lbs. The impacting units included a either a 10 in × 30 in × 3.75 in or 6 in × 30 in × 4 in thick aluminum impacting mass and either a 10 in or 6 in × 30 in × 2 in thick programmer with a 0.5 in aluminum backing plate depending on the test (Figure 5.3).

The W14x132 tests used four impacting units that were 10 in × 30 in and weighed a total of 543 and 660 lbs which included the weight of the steel rod and collar for the BG25 and BG 50, respectively. The impacting units included a 10 in × 30 in × 4.50 in steel impacting mass and a 10 in × 30 in × 2 in thick programmer with a 0.5 in aluminum backing plate (Figure 5.4).
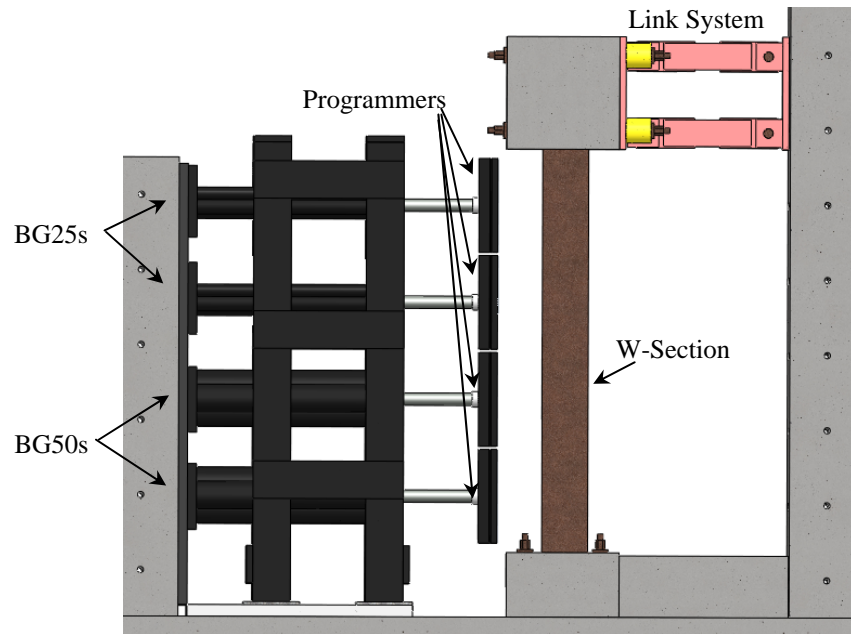
Figure 5.1: Side Elevation of Steel Column Weak Axis Test Setup
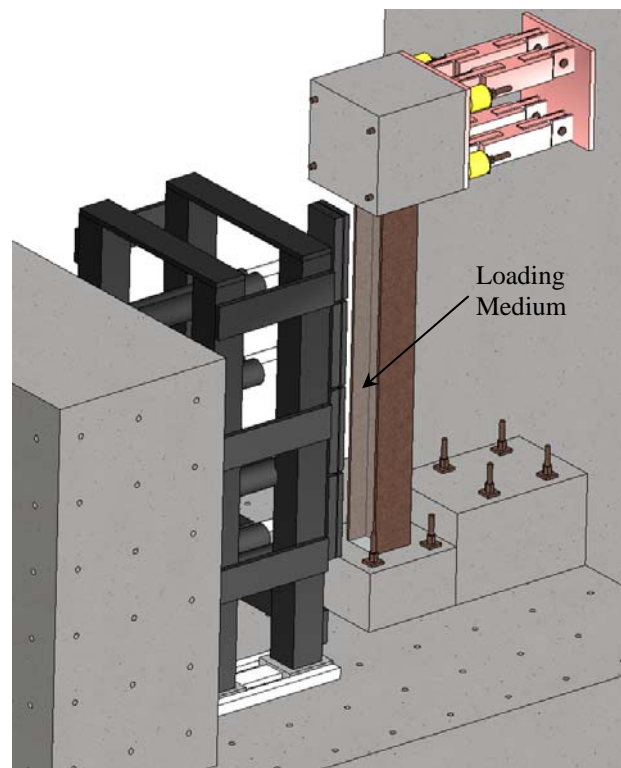
Figure 5.2: Steel Column Weak Axis Test Setup with Loading Medium
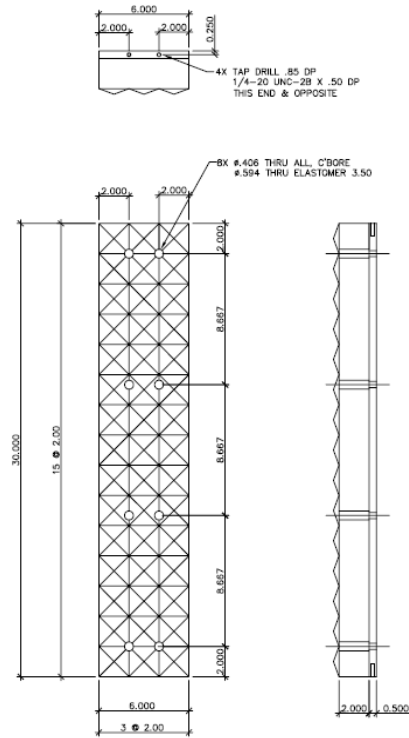
Figure 5.3: W10x49 Variable Velocity Programmer
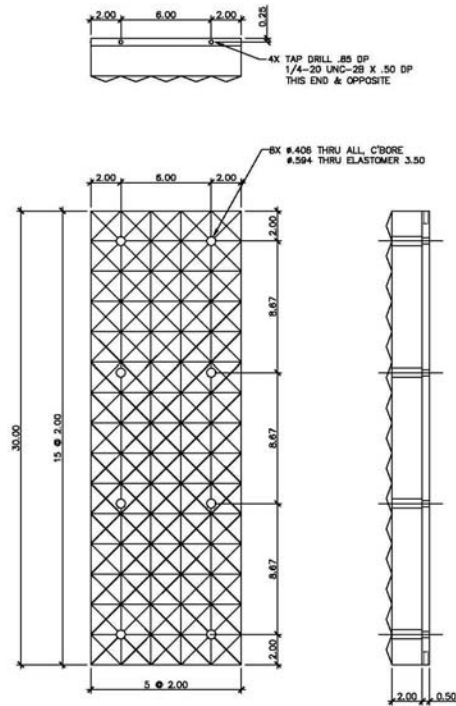
Figure 5.4: W10x49 Uniform and W14x132 Variable Velocity Programmer

Discussed in more detail in Section 3.1.1, the boundary conditions were initially chosen for three reasons: they were thought to closely mimic the actual behavior of a column subjected to blast loads, they were similar to conditions applied during the field tests, and they were thought to be simple enough for ease of modeling. The connection at the base of the column was restrained in all directions simulating a "fixed" condition.

The header was attached to a link system that was intended to allow the column to move vertically while providing lateral and moment restraint similar to the strong axis tests (Figure 3.5). The link system was post-tensioned to the load stub and reaction wall. The four hollow hydraulic jacks tensioning the load stub header to the link with 100 kip load were left in place during the test.

As shown in Table 5.2 and discussed in Section 2.3, field testing produced two types of responses depending on the test setup conditions: either the flanges remain parallel or they bend outward. In order to sufficiently load the weak axis, pressure must be imparted on both the column web and the insides of both column flanges. This cannot be done using a flat programmer on the web because that would result in a bending inward (Table 5.3). A loading medium, such as sand or water, was used to transfer the load to both the flanges and the web. The type of loading medium and specific setup is discussed for each test in Section 5.3.

Table 5.2: Flange Behavior in Field Tests
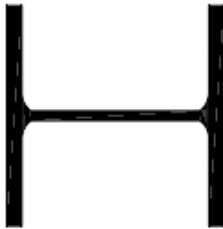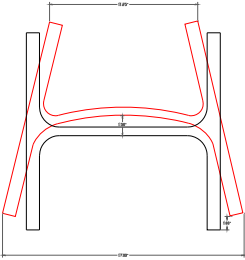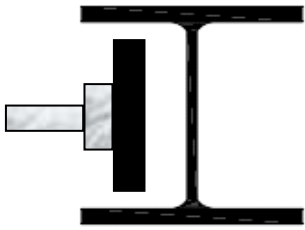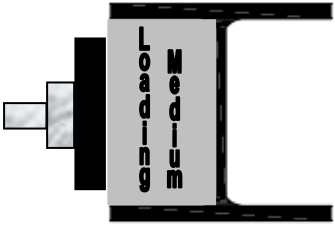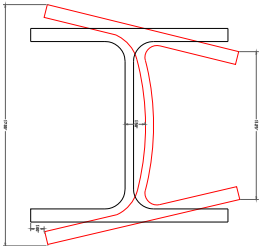
Behavior Type	Photo	Flange Behavior	Description
Behavior Type 1			Flanges remain mostly parallel.
Behavior Type 2			Flanges bend outward

Table 5.3: Predicted Flange Behavior in Simulator Tests

Test Type	Loading Description	Flange Behavior	Description
Programmer impacted on web only			Flanges bend inward (unlike field tests)
Programmer impacted on loading medium			Flanges bend outward or remain parallel (as in field tests)

5.1.2 Test Specimens

The six weak axis specimens used in this test series were constructed in June and July 2007. The specimens were identical to the columns used in the DTRA Phase I field test series, except that two of the W-section chosen were smaller (W10x49). They were 10'-9" in clear height and 15'-6" in total height with the header and footer included.

The W10x49 specimens had the cross-sectional dimensions shown in Figure 5.5. The columns were fabricated from A992 grade 50 steel. The yield strength of the steel had a minimum of 50 ksi and a maximum of 65 ksi. The minimum ultimate tensile strength was 65 ksi. In the weak axis direction the moment of inertia was 272 in^4 and 93.4 in^4 in the strong axis direction. The area was 14.4 in^2, the depth was 9.98 in, the web thickness was 0.34 in, the flange width was 10 in and the flange thickness was 0.56 in.

The W14x132 specimens had the cross-sectional dimensions shown in Figure 5.5. The columns were again fabricated from A992 grade 50 steel. The yield strength of the steel had a minimum of 50 ksi and a maximum of 65 ksi. The minimum ultimate tensile strength was 65 ksi. In the weak axis direction the moment of inertia was 1530 in^4 and 548 in^4 in the strong axis direction. The area was 38.8 in^2, the depth was 14.7 in, the web thickness was 0.65 in, the flange width was 14.7 in and the flange thickness was 1.07 in.
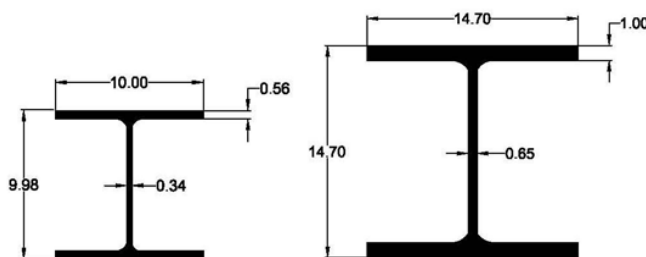
Figure 5.5: W10x49 (left) and W14x132 (right) Cross-Sectional Dimensions

Each column specimen had a concrete header attached to the top. This header prevented rotation at the top of the column. The header design was the same for all tests and is shown in Figure 5.6. The top of the column was welded to a 36 in $\times$ 36 in $\times$ 0.5 in steel plate. The weld was a 0.25 in bevel weld around the entire column. The welding rod that was used was E-70XX, which had a tensile strength of 70 ksi. The four sides of the header were confined by 0.25 in steel plates. Nelson studs were welded to the top plate and the side plates at every eight inches on center and #6 rebar hoops were installed within the header. The header created a 3 foot cube which was filled with 5,000 psi concrete. Concrete sample cylinders were acquired at the times of the concrete placement.

The base plate design used on the specimens consisted of a 0.5 in steel plate with the dimensions of 36 in $\times$ 36 in welded to the wide flange. The welds for this plate consisted of 0.25 in bevel welds on all sides of the column. A total of ten 0.5 in Nelson studs, 4 in long, were attached to the base plate in an array shown in Figure 5.7. The sides of the base were made from 0.25 in thick steel plates with a height of 1'-9" from the bottom of the base plate. The side plates had 0.5 in $\times$ 4 in Nelson studs centered every 8 in within the steel plates that surround the base of the column was 5,000 psi concrete reinforced with a total of 16 #6 U-bars. Two-inch PVC was installed horizontally though the base of the column to allow four 1.375 in diameter post-tension bars to pass through it. These bars were post-tensioned to hold the base of the column to the reaction floor. Figure 5.8 shows a drawing of the base of the column for the W14x132 specimen. Orientation of the column was such that the strong axis (flange) was facing the impact.
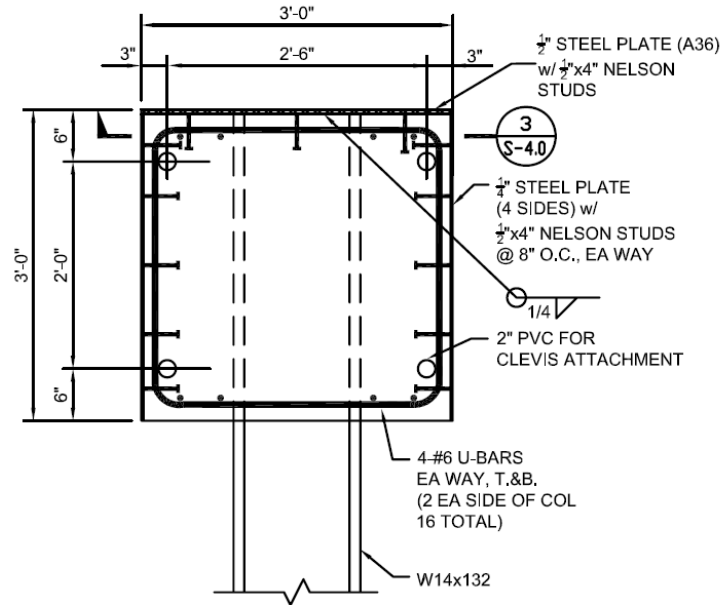
Figure 5.6: Header Design
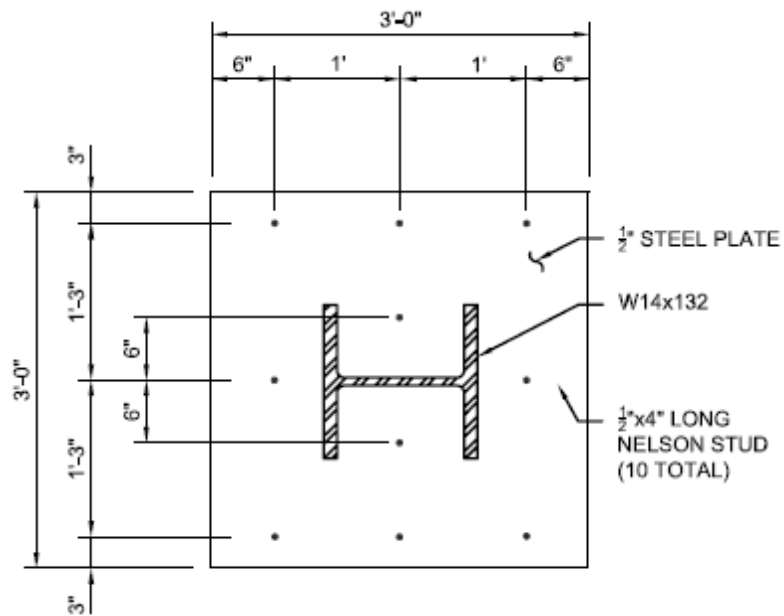
Figure 5.7: Nelson Stud Arrangement
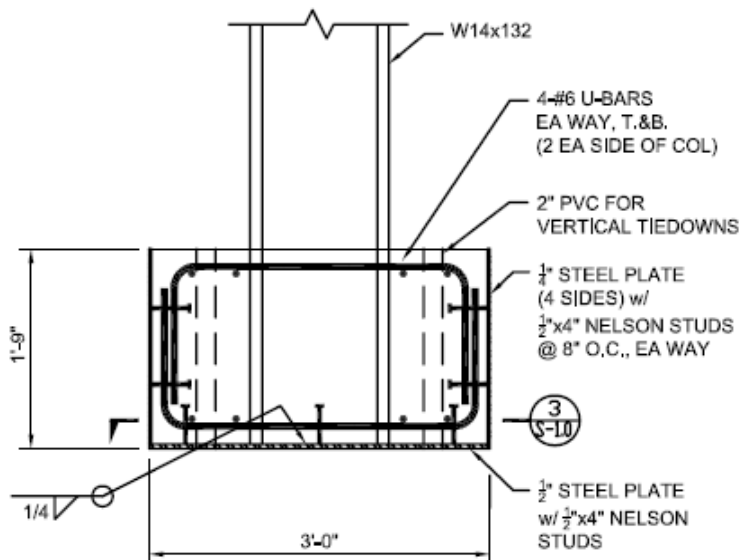
Figure 5.8: Base Design

The specimens were constructed in three phases with the specimens used for the strong axis tests. The first phase consisted of the steel fabrication and was done off site. Fabrication included the cutting of the W-Shape and welding them to the steel base. The steel casings were also constructed and the Nelson studs welded on. The fabricated steel specimens were shipped to Englekirk Center in June of 2007. Figure 3.10 and Figure 3.11 shows the completed steel fabrication.

On June 26, 2007, rebar was placed inside the columns (Figure 3.12) and concrete was poured in each of the eleven bases. The pouring of the concrete is shown in Figure 3.13. The concrete in the base was allowed to cure for just over three weeks and on July 18, 2007 the columns were lifted with a crane and turned over with the concrete base at the top (Figure 3.14). Rebar cages were installed and concrete was poured into the header of the specimen and left to cure (Figure 3.15).

5.1.3 Instrumentation

This section describes the instrumentation setup used for the strong axis column tests. For each test high speed cameras, accelerometers, strain gages and potentiometers and load cells were used and the data was recorded with the data acquisition system.

Data Acquisition

A high speed data acquisition system from *Hi-Techniques* was used for all of the steel column strong axis tests. The system samples at 14 bits and 1 MHz. The system currently has 52 channels which were triggered by the MTS controller that is used to fire the blast generators.

High Speed Video

Three high speed Phantom cameras were used to record each test. These cameras provided visual evidence of the test that was used to observe specimen behavior under impulsive loading. Figure 5.9 displays the sections of the column that were filmed in each test. Phantom 1 (shown in solid blue) records video in black and white. It was used to measure displacements and record velocities of the entire column. Phantom 2 and 3 were equipped with zoom lenses and record in color. Phantom 2 (dotted red) was focused on the bottom of the specimen and Phantom 3 (dashed green) was focused on the top. The videos provide impact velocities of the BGs and visuals of the column behavior. Displacements were determined using the Track Eye Motion Analysis (TEMA) software package from Image Systems which can also generate velocity-time histories through differentiation of displacement.

Shock Accelerometers

Accelerations of the BGs during the test were measured with 10k g or 50k g piezoelectric shock accelerometers. One to three gages were mounted on the back of each of the four impacting plates. The cables that transmit the acceleration signal were fastened in such a way that strain relief was provided during the test.

Accelerations of the column were measured with 50k g piezoelectric shock accelerometers at five locations. One of the gages was located on the back of the column at midspan. The other four were distributed over the height of the column. The locations of the accelerometers are shown in Figure 5.10.

Strain Gages

Strains were measured in the column using post-yield, large strain measurement strain gages. Three rosettes were placed on the back (non-impact) side of the column along the midline and three were placed in the center of the flange. For each set of three, one was placed at the midspan and the two others were placed 1 foot away from the top and bottom support. The locations of the strain gages are shown in Figure 5.11.

Load Cells

The dynamic load cells were used to measure pressures along the height of the column and are manufactured by Dytran Inc. The cells were piezoelectric force transducers which had capacities of 1,000 lbs and 5,000 lbs. The load cells were placed into sleeves which were welded into the web and flanges of the columns as seen in Figure 5.13 and Figure 5.14.
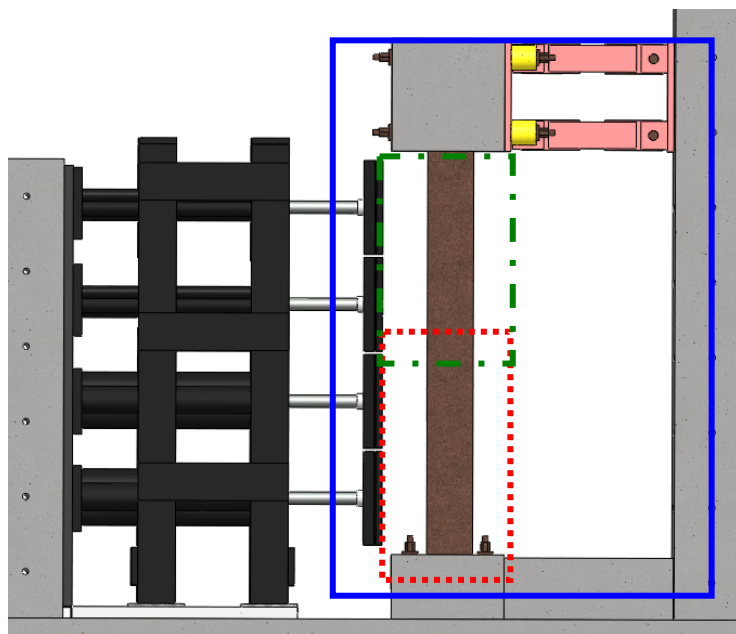
Figure 5.9: Phantom Camera Views
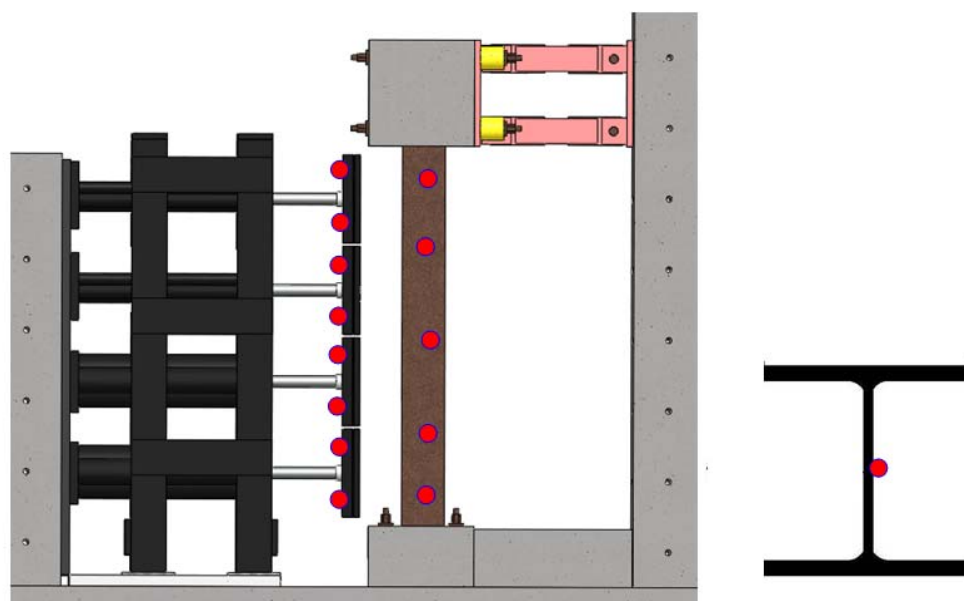
Figure 5.10: Accelerometer Locations
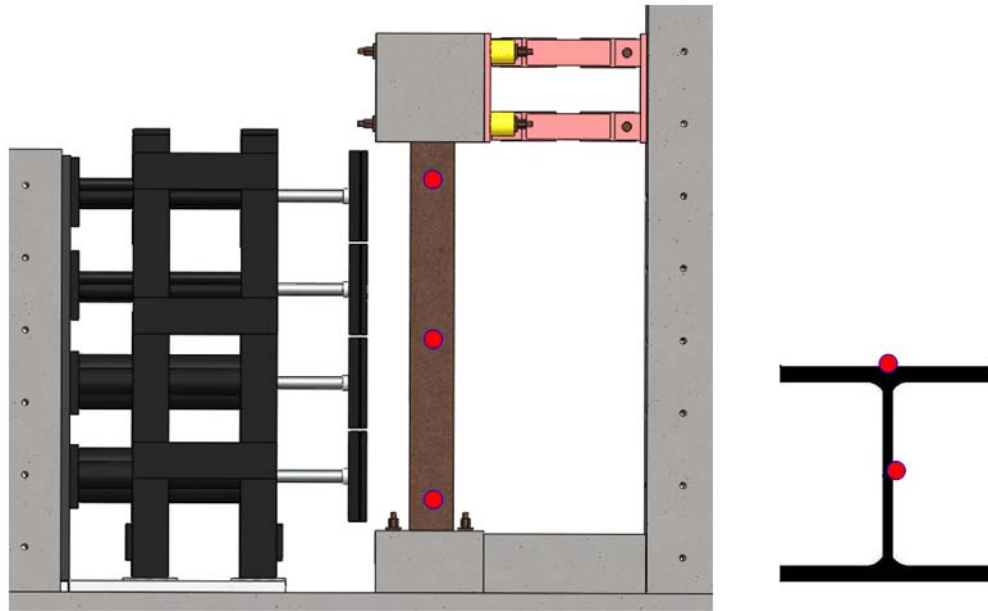
Figure 5.11: Strain Gage Locations
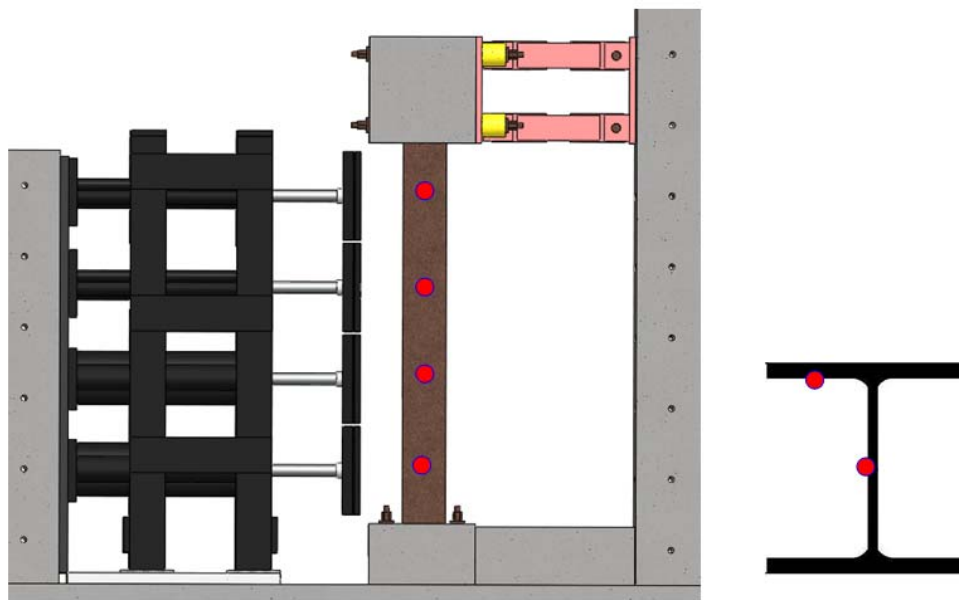
Figure 5.12: Load Cell Locations

Figure 5.13: Pressure Cell Back View

Figure 5.14: Load Cell Front View

5.2   Data Analysis Methodologies

This section discusses the methods used to analyze data to produce important parameters for quantifying both BG and specimen behaviors. The majority of the methodologies are similar to those done for the weak axis impact and are discussed in additional detail in Chapter 3.

5.2.1 BG Behavior

Like the strong axis tests, impulse is again the parameter that is used to define the load that is transferred from the BG onto the specimen. Section 3.2.1 summarizes the procedures for determining the impulse for a given data set.

Additionally, load cells were utilized to measure the forces generated on the column by the impacting module through the loading medium. The data produced from these load cells gave unrealistic pressure-time histories and impulses for loads directly applied to the column. This was thought to be due to impedance mismatch, the additional stiffness of the welded piece, the contact area of the load cell and other additional factors. The data produced from these cells is not used in any calculations in the remainder of this dissertation. Additional research is needed to correctly utilize the force-time data outputted from the cells.

5.2.2 Specimen Behavior

The behavior of the specimen was quantified using maximum and residual displacements at varying locations. For the strong axis tests, a global displacement of the column was a parameter that was consistently used as a meter to discuss specimen behavior. The displacement was found using the data from the high speed cameras as

discussed in more detail in Section 3.2.2 and the TEMA software that can identify the displacement and differentiate it to yield velocities at each target location throughout the test.

5.3 Test Results

5.3.1 Test WA01

Test WA01 was the first weak axis test on a W10x49 column. The test was conducted on August 19, 2008 and utilized four BG25s with the uniform target velocity of 28 m/s. For this test, sand was used as a loading medium as shown in Figure 5.15. The setup is discussed in detail in the next section.
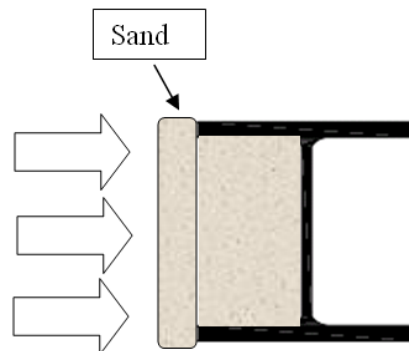
Figure 5.15: Test WA01 Loading Medium Setup

Initial Setup

In order to fill the column with a loading medium, initially the column was laid horizontally and filled with sand (Figure 5.16). The column was then wrapped with plastic wrap and tapped at the bottom and top of the specimen (Figure 5.17). Next, sand bags were laid over the top of the column so the programmers would not impact the flanges directly. The bags were then wrapped in both plastic wrap and duct tape (Figure

5.18). The column was then craned in place as shown in Figure 5.19. Figure 5.20, Figure

5.21 and Figure 5.23 show the column and column base in place before the test.

Figure 5.16: Column Laid Horizontally and Filled with Sand

Figure 5.17: Column Wrapped with Plastic Wrap

Figure 5.18: Sand Bags Laid on Top of Column

Figure 5.19: Completed Column Wrapped with Plastic and Tape

Figure 5.20: Column Craned in Place

Figure 5.21: Test WA01 Column Pre-Test

Figure 5.22: Test WA01 Column Base Pre-Test

Figure 5.23: Test WA01 Column Base Pre-Test

BG Behavior

Each impacting mass was instrumented with three accelerometers. The average of each of the outputs was taken and plots of the average accelerations for each BG were calculated. The maximum acceleration was 1,434 g. The BGs impacted in the order 4, 3, 2, 1. The total spread from first to last impact was 3.17 ms. Table 5.4 gives a summary of peak acceleration, impact time and duration for each BG and the average.

Table 5.4: Test WA01 BG Impact Details

BG	Peak Acceleration (g)	Impact Time (ms)	Duration (ms)
1	992.3	44.35	4.87
2	1461.9	43.31	2.77
3	2200.5	42.49	2.90
4	1082.6	41.18	9.33
Average	1434.3	42.83	4.97

Impact velocities of the BGs were determined using two methods and are discussed in detail in Section 3.2.1. The first method determined impact velocity using visual data from the Phantom Cameras and the TEMA software. The second velocity value was found using the method, also discussed in Section 3.21, and was used as a check of the camera velocity value. Table 5.5 gives a summary of the camera impact velocities.

Table 5.5: Summary of BG Impact Velocities

BG	Camera Impact Velocity in/s, (m/s)
1	1017.7 (25.8)
2	1037.3 (26.3)
3	1028.6 (26.1)
4	1004.2 (25.6)
Average	1021.9 (26.0)

Pressure and impulse were found using the average acceleration of the BGs and the methods discussed in Section 3.2.1. The maximum pressure was 1,260.1 psi and the average was 983.0 psi. The maximum impulse was 1,809.5 psi-ms with an average of 1,484.1 using this method. These values are summarized in Table 5.6.

Table 5.6: Summary of Pressure and Impulse

BG	Peak Pressure (psi)	Impulse (psi-ms)
1	834.0	1789.6
2	1194.8	995.5
3	1260.1	1341.6
4	643.0	1809.5
Average	983.0	1484.1

Specimen Behavior

Figure 5.24 shows the progression of damage as recorded at 5,000 frames per second. In (a), the column is undeformed and the BGs are set to the correct initial position. The initial impact is shown in (b) and the synchronicity of the BGs can be seen. Figures (c) through (e) capture the propagation of deformation of the column while the masses are in contact with the column. Figure (f) displays the residual deformation of the specimen after the masses have begun to retract.

Accelerations of the specimen were recorded at five locations with accelerometers attached to the back (non-impact) web of the column. A maximum acceleration of 5,742.2 g was found at 32.25 in from the bottom of the column. Table 5.7 gives a summary of peak acceleration and impact time for each accelerometer.
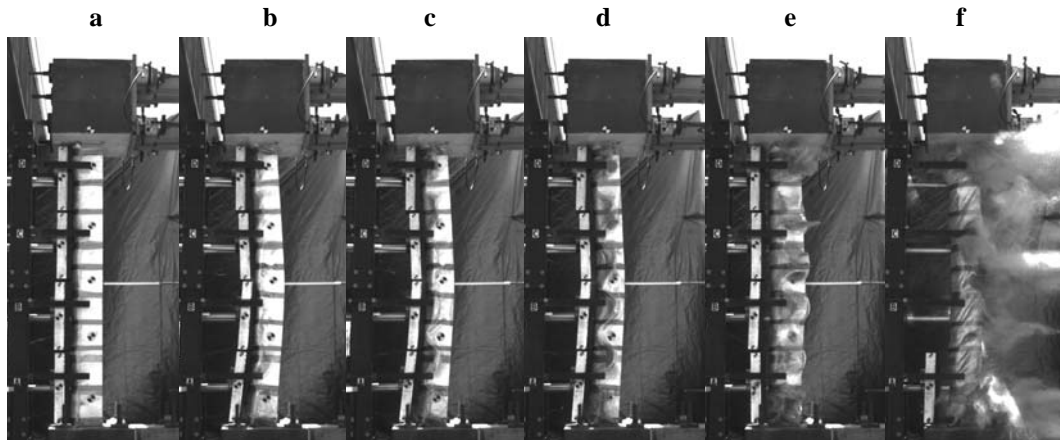
Figure 5.24: Test WA01 Progression of Damage

Table 5.7: Test WA01 Specimen Acceleration Summary

Distance from Base (in)	Peak Acceleration (g)	Impact Time (ms)
117	2359.5	42.64
96.75	3555.7	43.26
64.5	4877.7	43.51
32.25	5742.2	43.91
12	3543.5	43.64

Displacements were measured using the camera data and the tracking software, TEMA. Table 5.8 gives a summary of the maximum and residual displacement at multiple locations. Some of the values were approximated due to the sand debris blocking the targets throughout the test.

Figure 5.25 and Figure 5.26 shows the column post-test. A plot of the maximum displacements over the height of the column is shown in Figure 5.27. The maximum displacement was found to be 3.84 in at the midspan of the column. A plot of the residual displacements is given in Figure 5.27. The maximum residual displacement of 2.67 in was found at the midspan of the column.

Table 5.8: Test WA01 Specimen Displacement Summary

Distance from Base (in)	Maximum Displacement (in)	Residual Displacement (in)
117.0	0.94	0.54
104.3	-	1.19
89.4	2.87	1.64
76.8	-	2.23
64.5	3.84	2.67
51.6	-	2.37
39.2	2.87	1.89
26.7	-	1.35
12.0	0.94	0.72

Figure 5.25: Test WA01 Post-Test

Figure 5.26: Test WA01 Column Base Post-Test
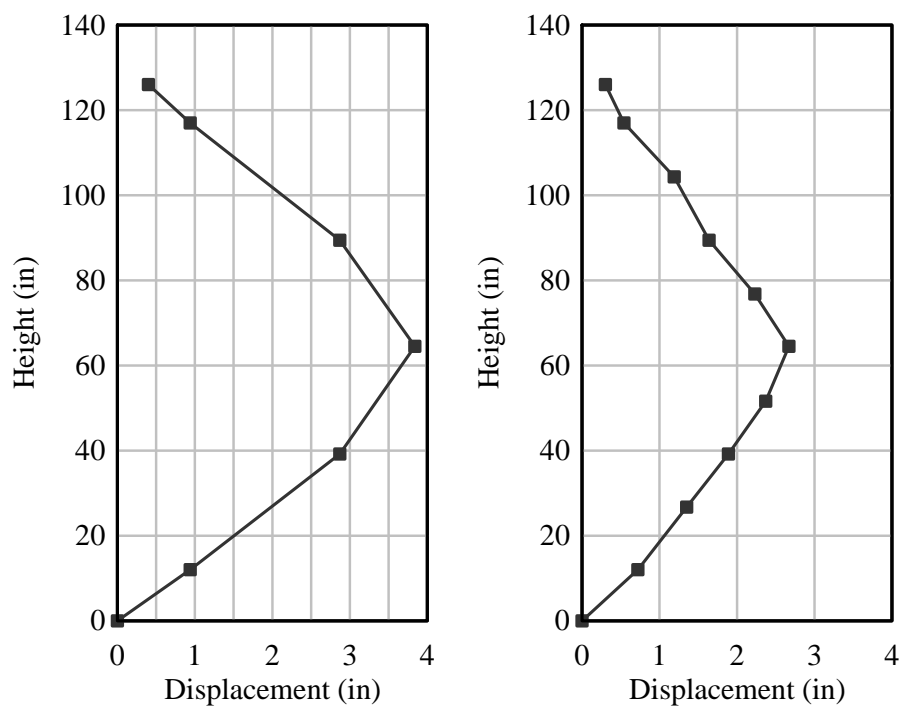
Figure 5.27: Test WA01 Maximum (left) and Residual (right) Displacements

5.3.2 Test WA02

Test WA02 was the first weak axis test on a W14x132 specimen with water used as a loading medium. The test was conducted on October 29, 2009 and was a variable velocity impact. The target velocities for this test are given in Table 5.9.

Table 5.9: Test WA02 Target Velocities

BG	Target Velocity in/s (m/s)
1	1574.8 (40.0)
2	1299.2 (33.0)
3	984.3 (25.0)
4	629.9 (16.0)

Initial Setup

The setup for Test WA02 is discussed in detail in Section 4.1.1. Photos of the column pre-test are shown in Figure 5.28 and Figure 5.29. Custom woven polyester water bladders were filled with water and strapped to the column using ratchet straps. A schematic of the water bladder placement is shown in Figure 5.30 and shows that the four bladders were placed inside the web-flange area along the height of the column. The pre-test photo is given in Figure 5.31.

Figure 5.28: Test WA02 Column with Water Bladders Attached

Figure 5.29: Custom Water Bladders
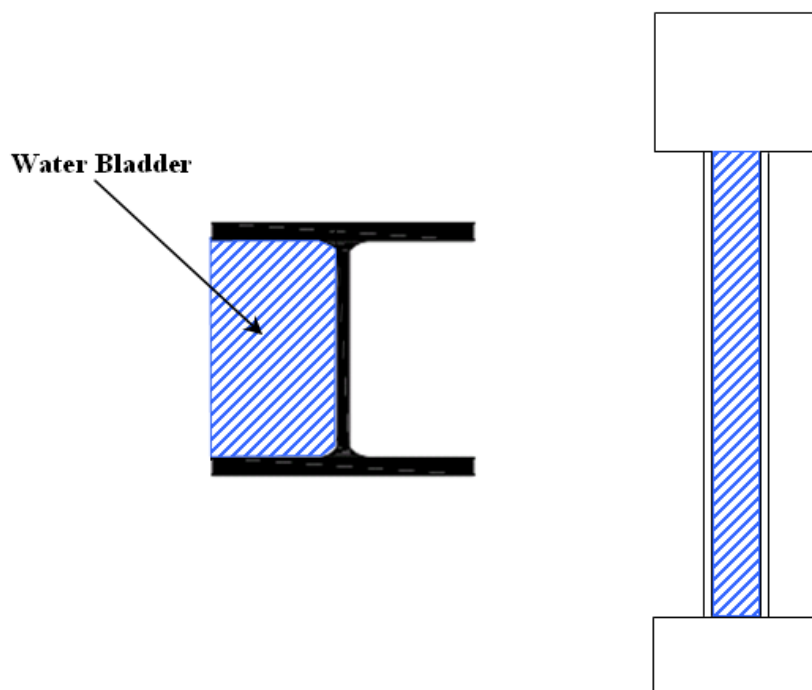
Figure 5.30: Schematic of Water Bladder Placement

Figure 5.31: Test WA02 Column Pre-Test

BG Behavior

Each impacting mass was instrumented with three accelerometers. The maximum acceleration was 3,572.6 g. The BGs impacted in the order 4, 3, 2, 1. The total spread from first to last impact was 0.86 ms. Table 5.10 gives a summary of peak acceleration, impact time and duration for each BG. The duration value was taken for the first impact only and does not include any additional impacts of the specimen.

Table 5.10: Test WA02 BG Impact Details

BG	Peak Acceleration (g)	Impact Time (ms)	Duration (ms)
1	3572.6	49.47	5.58
2	1785.1	49.34	2.75
3	1893.5	48.81	2.71
4	418.7	48.61	3.09

The use of water made determination of the impact velocities of the BGs very difficult because the water ejecta blocked the targets and hence they could not be tracked at every time interval. Approximation of the impact velocities are given in Table 5.11 and were found from using the target velocities, but will not be used for calculations in the following sections.

Table 5.11: Test WA02 BG Impact Velocities

BG	Camera Impact Velocity in/s, (m/s)
1	1574.8 (40.0)
2	1299.2 (33.0)
3	984.3 (25.0)
4	629.9 (16.0)

Pressure and impulse were found using the average acceleration of the BGs. The maximum pressure of 6163.5 psi was measured. The maximum impulse is 7,294.1 psi-ms using this method. This included all multiple impacts and long duration of pulse due to the use of the water. These values for each BG are summarized in Table 5.12. It should be noted that this is not a direct measurement of pressure and impulse on the column, but a measure of the pressure and impulse on the impacting mass due to the impacting of the water bladder.

Table 5.12: Test WA02 Pressure and Impulse

BG	Peak Pressure (psi)	Impulse from Accelerometer (psi-ms)
1	6163.5	6221.7
2	3954.7	7294.1
3	3323.5	3330.3
4	744.6	2928.5

Specimen Behavior

Figure 5.32 shows the progression of damage as recorded at 5,000 frames per second. In (a), the column is undeformed and the BGs are set to the correct initial position. The prior to initial impact is shown in (b) and the synchronicity of the BGs can be seen in (c). Shots (d) through (f) show the progression of damage and then the use of water makes it very difficult to see any additional behavior as is evident in the remainder of the camera shots.

a b c d e f
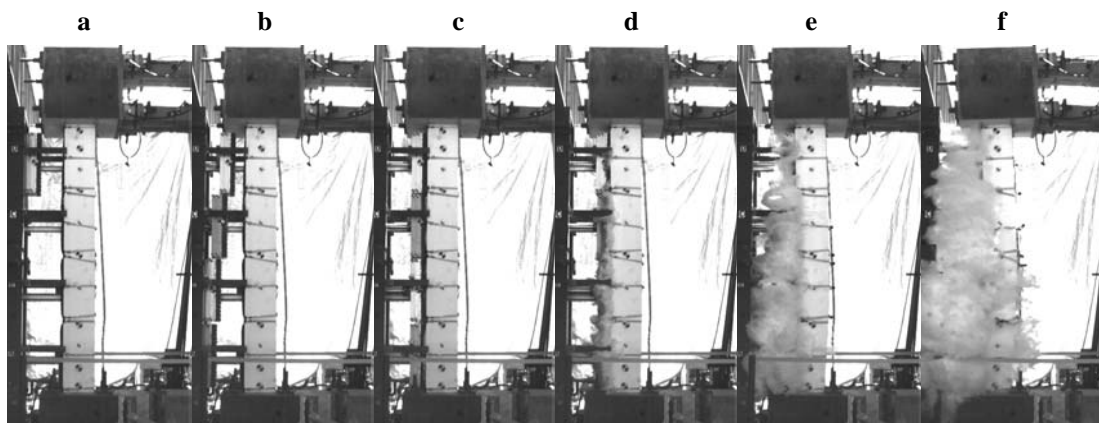
Figure 5.32: Test WA02 Progression of Damage

Accelerations of the specimen were not recorded due to a malfunction of the data acquisition system just prior to the test.

Displacements were measured using the camera data and the tracking software. Table 5.13 gives a summary of the maximum and residual displacement at various locations. Some values are given as approximations or were not able to be recorded due to the use of water.

Table 5.13: Test WA02 Specimen Displacement Summary

Distance from Base (in)	Maximum Displacement (in)	Residual Displacement (in)
126.0	0.49	0.23
117.0	0.88	0.70
106.6	1.30	1.02
96.1	1.76 (approx)	1.35
79.8	2.36	2.12
64.5	2.78	2.34
49.0	3.21 (approx)	2.97
32.0	2.37 (approx)	2.25
22.2	1.93 (approx)	1.45
12.0	1.09 (approx)	0.67
3.8	0.41 (approx)	0.31

Figure 5.33 and Figure 5.34 show the column post-test. A plot of the maximum displacements over the height of the column is shown in Figure 5.35. An approximate maximum displacement of 3.71 in was found at a height of 49.0 in from the base of the column. Figure 5.35 also gives a plot of the column residual displacements. A maximum residual displacement of 2.97 in was found at a height of 49.0 in from the base of the column. This column did not show any visible signs of localized flange bending.

Figure 5.33: Test WA02 Column Post-Test

Figure 5.34: Test WA02 Column Base Post Test
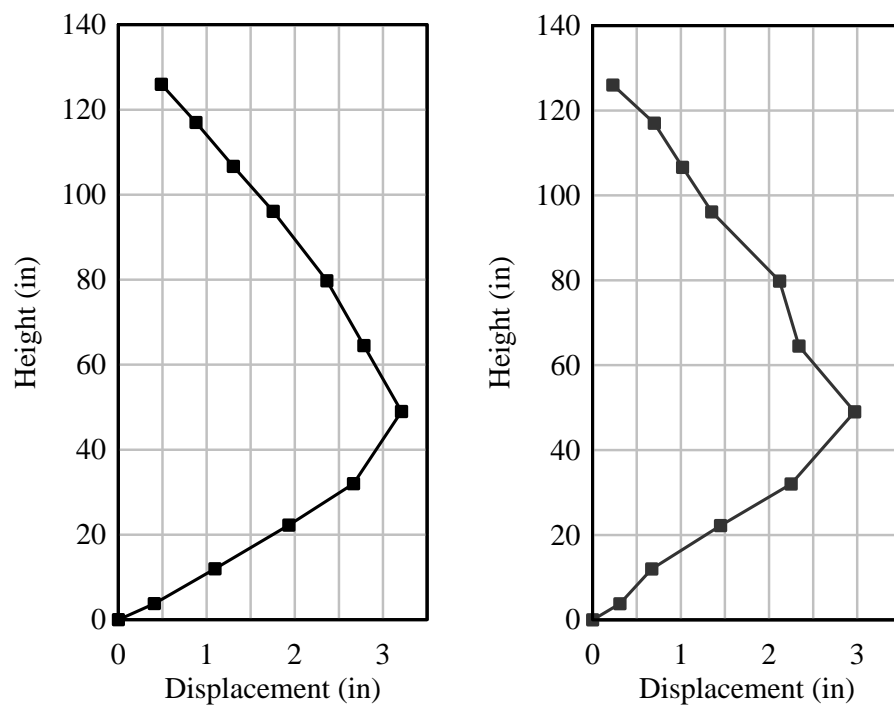
Figure 5.35: Test WA02 Maximum (left) and Residual (right) Displacements

5.3.3 Test WA03

Test WA03 was the second weak axis test on a W14x132 specimen with water used as a loading medium. The test was conducted on November 13, 2009 and was a variable velocity hit. The target velocities for this test are given in Table 5.14.

Table 5.14: Test WA03 Target Velocities

BG	Target Velocity in/s (m/s)
1	1732.3 (44.0)
2	1456.7 (37.0)
3	1003.9 (25.5)
4	708.7 (18.0)

Initial Setup

The setup for Test WA03 is discussed in detail in Section 4.1.1. Photos of the column pre-test are shown in Figure 5.36 and Figure 5.37. Again, custom water bladders were filled with water and strapped to the column using ratchet straps, similar to that done in Test WA02.

BG Behavior

The maximum acceleration of the BGs was 2,899.5 g. The BGs impacted in the order 1, 4, 3, 2. The total spread from first to last impact was 3.73 ms. Table 5.15 gives a summary of peak acceleration, impact time and duration for each BG.

Figure 5.36: Test WA03 Column Pre-Test

Figure 5.37: Test WA03 Column Base Pre-Test

Table 5.15: Test WA03 BG Impact Details

BG	Peak Acceleration (g)	Impact Time (ms)	Duration (ms)
1	2899.5	45.95	6.40
2	2264.7	49.68	2.52
3	1880.7	49.49	3.30
4	544.7	47.00	6.60

The use of water made determination of the impact velocities of the BGs difficult because the water blocked the targets and could not be tracked at every time interval. The impact velocities were approximated by using the measured values from sand Test WA04 which had similar blast profile inputs and are given in Table 5.16.

Table 5.16: Test WA03 BG Impact Velocities

BG	Camera Impact Velocity in/s, (m/s)
1	1729.6 (43.9)
2	1478.5 (37.6)
3	983.4 (25.0)
4	665.3 (16.9)

Pressure and impulse were found using the average acceleration of the BGs. The maximum pressure of 6,508.6 psi was recorded. The maximum impulse was 9,505.6 psi-ms using this method which included integration over the full duration of the impact. These values are summarized in Table 5.17. This is not a direct measurement of pressure and impulse on the column, but a measure of the pressure and impulse on the impacting mass due to the impacting of the water bladder.

Table 5.17: Test WA03 BG Pressure and Impulse

BG	Peak Pressure (psi)	Impulse (psi-ms)
1	6508.6	6210.4
2	5062.6	9505.6
3	3294.1	3624.4
4	964.4	3585.9

Specimen Behavior

Figure 5.38 shows the progression of damage as recorded at 5,000 frames per second. In (a), the column is undeformed and the BGs are set to the correct initial position. Prior to the initial impact is shown in (b) and the synchronicity of the BGs can be seen in (c). Figures (c) through (f) capture some of the propagation of deformation through the water.

Figure 5.38: Test WA03 Progression of Damage

Accelerations of the specimen were recorded at three locations with accelerometers attached to the back (non-impact) side of the column. A maximum acceleration of 23,422.4 g was recorded at 32.25 in from the bottom of the column. Table 5.18 gives a summary of the peak accelerations.

Table 5.18: Test WA03 Specimen Acceleration Summary

Distance from Base (in)	Peak Acceleration (g)
96.75	23422.4
64.5	17019.2
32.25	2341.6

Displacements were measured using the camera data and the tracking software. Table 5.19 gives a summary of the maximum and residual displacement at multiple locations. Some values were approximated due to the water blocking the column.

Table 5.19: Test WA03 Specimen Displacement Summary

Distance from Base (in)	Maximum Displacement (in)	Residual Displacement (in)
126.2	0.59 (approx)	0.16
117.0	1.30 (approx)	0.78
107.8	1.72	0.97
96.6	2.38	1.49
82.9	3.14	2.03
64.5	4.20 (approx)	2.78
50.1	4.99 (approx)	3.15
32.6	3.77 (approx)	2.41
22.5	3.16 (approx)	1.79 (approx)
12.0	1.41	1.00
3.0	0.49	0.29

Figure 5.39 and Figure 5.40 show the column post-test. A maximum displacement of approximately 4.99 in was found at a height of 50.1in from the base of the column and is shown in Figure 5.41 and also shows a maximum residual displacement of 3.15 in. The flanges buckled approximately 0.3 in inward at the base of the column.

Figure 5.39: Test WA03 Column Post-Test

Figure 5.40: Test WA03 Column Base Post-Test
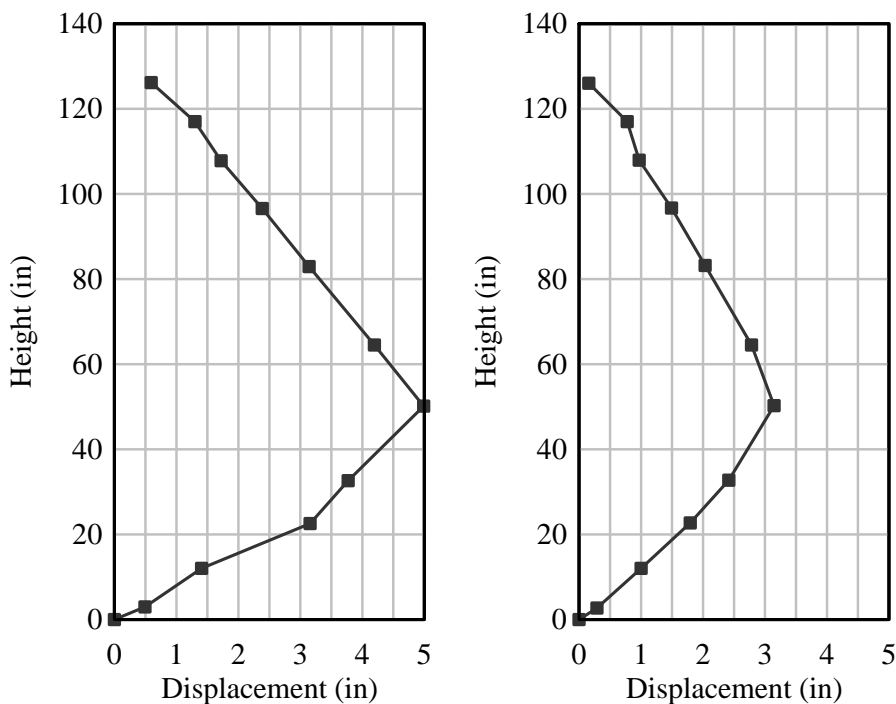
Figure 5.41: Test WA03 Maximum (left) and Residual (right) Displacements

5.3.4 Test WA04

Test WA04 was the third weak axis test on a W14x132 specimen. This test used sand as the loading medium. The test was conducted on November 20, 2009 and was a variable velocity impact. The target velocities for this test are given in Table 5.20.

Table 5.20: Test WA04 Target Velocities

BG	Target Velocity in/s (m/s)
1	1732.3 (44.0)
:2	1456.7 (37.0)
3	1003.9 (25.5)
4	708.7 (18.0)

Initial Setup

The setup for Test WA04 is discussed in detail in Section 4.1.1. The sand setup was slightly different than Test WA01; no sandbags were used as shown in Figure 5.42 and Figure 5.43. The overall column setup is shown in Figure 5.44.

Figure 5.42: Test WA04 with Sand as Loading Medium

Figure 5.43: Test WA04 Wrapped Column Specimen

Figure 5.44: Test WA04 Column Pre-Test

BG Behavior

The maximum acceleration of the BGs for Test WA04 was 1,582.6 g. The BGs impacted in the order 1, 4, 2, 3. The total spread from first to last impact was 3.41 ms. Table 5.21 gives a summary of peak acceleration, impact time and duration for each BG.

Table 5.21: Test WA04 BG Impact Details

BG	Peak Acceleration (g)	Impact Time (ms)	Duration (ms)
1	1582.6	47.39	10.45
2	1485.8	49.89	3.70
3	903.6	50.80	2.78
4	730.0	49.09	5.56

Impact velocities of the BGs were determined using visual data from the Phantom cameras and the TEMA software. Table 5.22 gives a summary of impact velocities.

Table 5.22: Test WA04 BG Impact Velocities

BG	Camera Impact Velocity in/s, (m/s)
1	1729.6 (43.9)
2	1478.5 (37.6)
3	983.4 (25.0)
4	665.3 (16.9)

Pressure and impulse were found using the average acceleration of the BGs. The maximum pressure of 3,592.8 psi was measured. The maximum impulse for the full test duration was 12,524.9 psi-ms, which should again be noted is not the direct impulse felt by the column. These values are summarized in Table 5.23.

Table 5.23: Test WA04 BG Pressure and Impulse

BG	Peak Pressure (psi)	Impulse (psi-ms)
1	3592.8	12524.9
2	3314.5	8048.6
3	1561.6	3671.9
4	1143.6	4269.2

Specimen Behavior

Figure 5.45 shows the progression of damage as recorded at 5,000 frames per second. In (a), the column is undeformed and the BGs are set to the correct initial position. The initial impact is shown in (b) and the synchronicity of the BGs can be seen. Figures (c) through (e) capture the propagation of deformation of the column while the masses are in contact with the column. Figure (f) displays the residual deformation of the specimen after the masses have retracted.
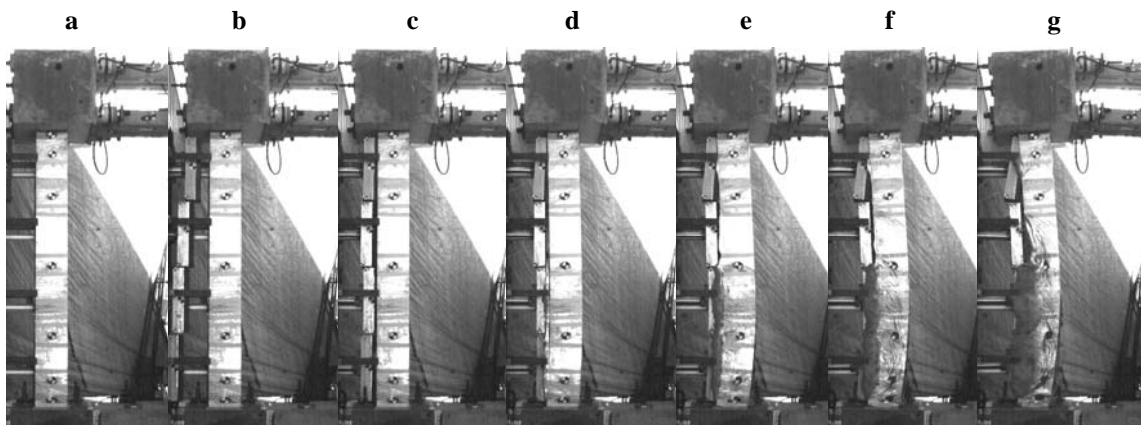
Figure 5.45: Test WA04 Progression of Damage

Accelerations of the specimen were recorded at three locations with accelerometers attached to the back (non-impact) side of the column. A maximum acceleration of 7,545.7 g was recorded at 32.35 in from the bottom of the column. Table 5.24 gives a summary of peak accelerations for each accelerometer.

Table 5.24: Test WA04 Specimen Acceleration Summary

Distance from Base (in)	Peak Acceleration (g)
96.75	2624.7
64.5	no data
32.25	7545.7

Displacements were measured using the camera data and the tracking software. Table 5.25 gives a summary of the maximum and residual displacement at multiple locations. Figure 5.46 and Figure 5.47 show the column post-test. A plot of the maximum displacements over the height of the column is shown in Figure 5.48. A maximum displacement of 5.43 in was found at a height of 47.6 in from the base of the column.

Figure 5.48 gives a plot of the column residual displacements. A maximum residual displacement of 4.01 in was found at a height of 47.6 in from the base of the column.

Table 5.25: Test WA04 Specimen Displacement Summary

Distance from Base (in)	Maximum Displacement (in)	Residual Displacement (in)
126.0	0.58	0.89
117.0	1.34	1.08
107.3	2.01 (approx)	2.02
96.8	2.91	3.07
79.1	4.32 (approx)	3.93
64.5	5.22	3.93
47.6	5.43 (approx)	4.01
32.2	4.89 (approx)	3.59
22.2	3.66 (approx)	3.21 (approx)
12.0	2.07 (approx)	1.72
3.1	0.96	0.71

Figure 5.46: Test WA04 Column Post-Test

Figure 5.47: Test WA04 Column Base Post-Test
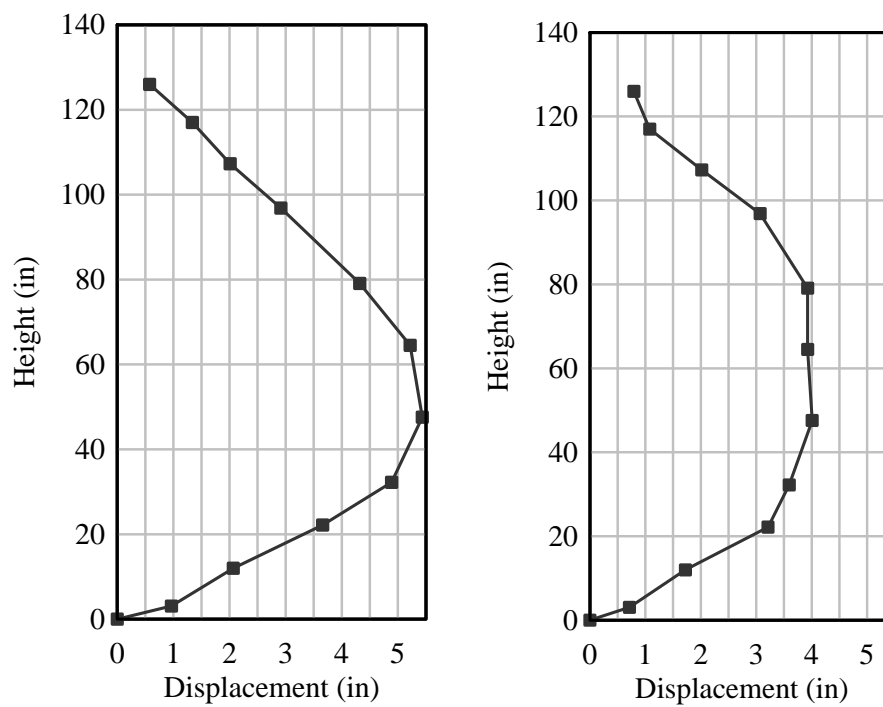
Figure 5.48: Test WA04 Maximum (left) and Residual (right) Displacements

5.3.5 Test WA05

Test WA05 was the second weak axis test on a W10x49 specimen. This test used water as the loading medium. The test was conducted on December 11, 2009 and was a variable velocity hit. The target velocities for this test are given in Table 5.26

Table 5.26: Test WA05 Target Velocities

BG	Target Velocity in/s (m/s)
1	2362.2 (60.0)
2	1870.1 (47.5)
3	1378.0 (35.0)
4	885.8 (22.5)

Initial Setup

The setup for Test WA05 is discussed in detail in Section 4.1.1. The water setup was similar to the tests in Test WA02 and Test WA03 as shown in Figure 5.49. The overall column setup is shown in Figure 5.50 with the column base shown in Figure 5.51.

BG Behavior

Each impacting mass was instrumented with three accelerometers. The maximum acceleration was 15,679 g. The BGs impacted in the order 3, 1, 2, 4. The total spread from first to last impact was 2.61 ms. Table 5.27 also gives a summary of peak acceleration, impact time and duration for each BG.

Figure 5.49: Test WA05 with Water Bladders

Figure 5.50: Test WA05 Column Pre-Test

Figure 5.51: Test WA05 Column Base Pre-Test

Table 5.27: Test WA05 BG Impact Details

BG	Peak Acceleration (g)	Impact Time (ms)	Duration (ms)
1	15679.2	42.61	1.15
2	6590.5	42.90	2.95
3	3247.7	41.91	2.58
4	895.9	44.52	18.53

Impact velocities of the BGs were determined using tracked data from the Phantom Cameras. Due to the use of water, the velocities were assumed to be the same values as those recorded in Test WA06 which had the same input blast profile. Table 5.28 gives a summary of impact velocities.

Table 5.28: Test WA05 BG Impact Velocities

BG	Camera Impact Velocity in/s, (m/s)
1	2553.7 (64.9)
2	2050.7 (52.1)
3	1273.9 (32.6)
4	840.3 (21.3)

Pressure and impulse on the mass from impact of the water bladder were found using the average acceleration of the BG impacting masses. The maximum pressure of 26,898.5 psi was recorded from BG1. The maximum impulse from impacting the water bladder was 10,581.4 psi-ms using this method. These values are summarized in Table 5.29.

Table 5.29: Test WA05 Pressure and Impulse

BG	Peak Pressure (psi)	Impulse (psi-ms)
1	26898.5	10581.4
2	11282.9	9466.1
3	3968.3	4277.7
4	1018.2	1395.5

Specimen Behavior

Figure 5.52 shows the progression of damage as recorded at 5,000 frames per second. In (a), the column is undeformed and the BGs are set to the correct initial position. The prior to the initial impact is shown in (b) and the synchronicity of the BGs can be seen in (c). Figures (d) through (f) capture some of the propagation of deformation of the column through the water.
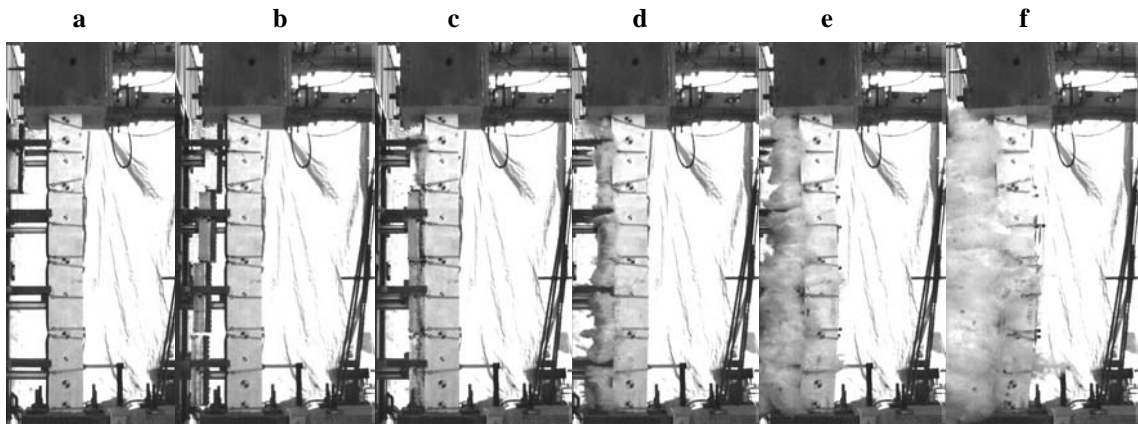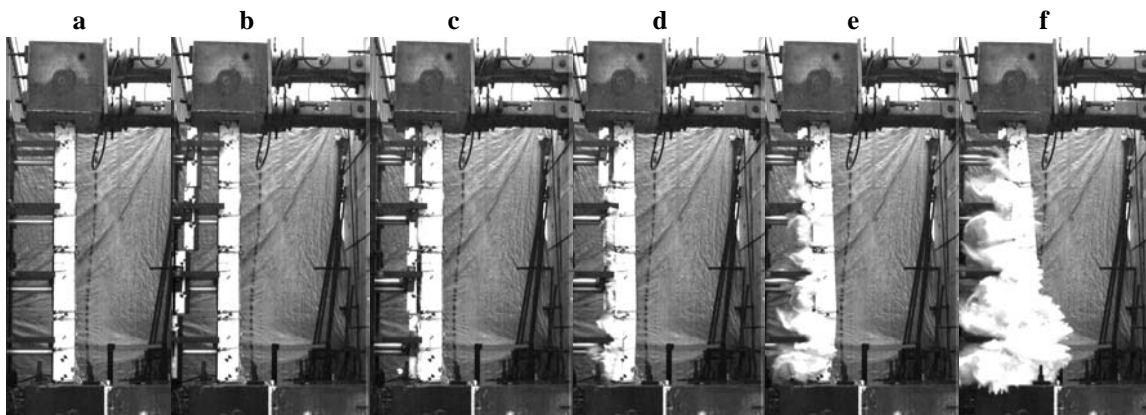
Figure 5.52: Test WA05 Progression of Damage

Accelerations of the specimen were recorded at three locations with accelerometers attached to the back (non-impact) side of the column. A maximum acceleration of 10,237.7 g was recorded at 32.25 in from the bottom of the column. Table 5.30 gives a summary of peak accelerations for each accelerometer.

Table 5.30: Test WA05 Specimen Acceleration Summary

Distance from Base (in)	Peak Acceleration (g)
96.75	10237.7
64.5	11856.7
32.25	15932.2

Displacements were measured using the camera data and the tracking software. Table 5.31 gives a summary of the residual displacements at various locations measured with the tracking software. The maximum displacements were not able to be measured because the water blocked the column for that portion of the duration of the test.

Table 5.31: Test WA05 Specimen Displacement Summary

Distance from Base (in)	Maximum Displacement (in)	Residual Displacement (in)
126.1	no data	0.31
117.0	no data	1.70
106.6	no data	3.28
96.6	no data	4.82
81.43	no data	7.09
64.5	no data	9.18
50.8	no data	10.19
32.2	no data	9.97 (approx)
21.9	no data	7.35 (approx)
12.0	no data	4.16
3.1	no data	1.66

Figure 5.53 shows the column post-test with a close up of BG2 mass, which came off of the rails as shown in Figure 5.54. Figure 5.55 and Figure 5.56 show the column base from the impact and non-impact sides, respectively. Buckling at the base of the column is shown in Figure 5.57 with a close up of the web given in Figure 5.58.Figure 5.59 gives a plot of the column residual displacements. A maximum residual displacement of 10.19 in was found at a height of 50.8 in from the base of the column.

Figure 5.53: Test WA05 Column Post-Test

Figure 5.54: Test WA05 BG2 Post Test

Figure 5.55: Test WA05 Base Post-Test (Impact Side)

Figure 5.56: Test WA05 Base Post-Test (Non-impact side)

Figure 5.57: Test WA05 Base Buckling (Non-Impact Side)

Figure 5.58: Test WA05 Column Web Post-Test
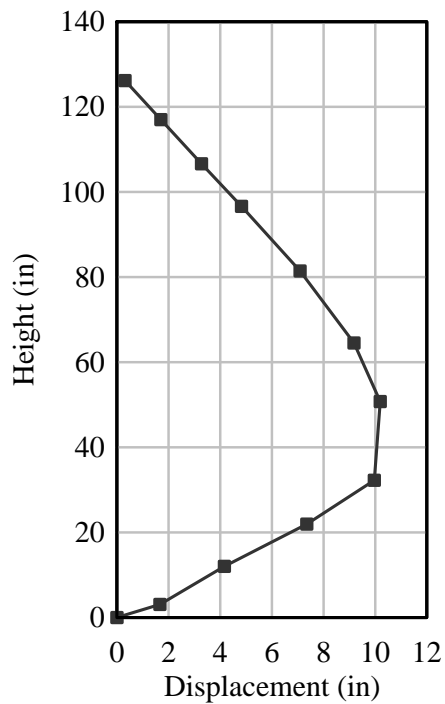
Figure 5.59: Test WA05 Residual Displacements

5.3.6 Test WA06

Test WA06 was the third weak axis test on a W10x49 specimen. This test used sand as a loading medium. The test was conducted on December 17, 2009 and was a variable velocity hit. The target velocities for this test are given in Table 5.32.

Table 5.32: Test WA06 Target Velocities

BG	Target Velocity in/s (m/s)
1	2362.2 (60.0)
2	1870.1 (47.5)
3	1378.0 (35.0)
4	885.8 (22.5)

Initial Setup

The setup for Test WA06 is discussed in detail in Section 4.1.1. The sand setup was similar to the Test WA04 as seen in Figure 5.60. The overall column setup is shown in Figure 5.61.
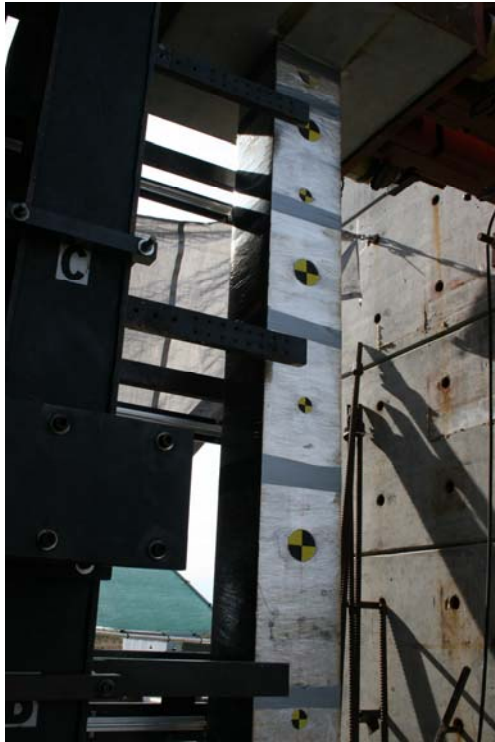
Figure 5.60: Test WA06 Column Pre-Test with Sand as Loading Medium

Figure 5.61: Test WA06 Column Pre-Test

BG Behavior

The maximum acceleration of the BGs for Test WA04 was 3,231.6 g. The BGs impacted in the order 1, 4, 3, 2. The total spread from first to last impact was 6.48 ms. Table 5.33 also gives a summary of peak acceleration, impact time and duration for each BG and the average.

Table 5.33: Test WA06 BG Impact Details

BG	Peak Acceleration (g)	Impact Time (ms)	Duration (ms)
1	3231.6	37.34	7.94
2	1900.5	43.82	21.54
3	1673.7	42.03	12.86
4	925.4	41.15	7.19

Impact velocities of the BGs were determined using visual data from the Phantom cameras and the tracking software. Table 5.34 gives a summary and average of impact velocities. Some values of velocity were approximated due to the fact that the sand blocked the targets and could not be tracked for the full time duration.

Table 5.34: Test WA06 BG Impact Velocities

BG	Camera Impact Velocity in/s, (m/s)
1	2553.7 (64.9)
2	2050.7 (52.1)
3	1273.9 (32.6)
4	840.3 (21.3)

Pressure and impulse were found using the average acceleration of the BGs. The maximum pressure of 18567.8 psi was found 1.45 ms after impact. The maximum impulse was 15584.4 psi-ms using this method. These values are summarized in Table 5.35.

Table 5.35: Test WA06 BG Pressure and Impulse

BG	Peak Pressure (psi)	Impulse (psi-ms)
1	18567.5	15584.4
2	8754.9	12456.1
3	4729.3	8523.7
4	3482.2	5678.5

Specimen Behavior

Figure 5.62 shows the progression of damage as recorded at 5,000 frames per second. In (a), the column is undeformed and the BGs are set to the correct initial position. Prior to initial impact is shown in (b) and the synchronicity of the BGs can be

seen in (c). Figures (d) through (g) capture the propagation of deformation of the column while the masses are in contact with the column.
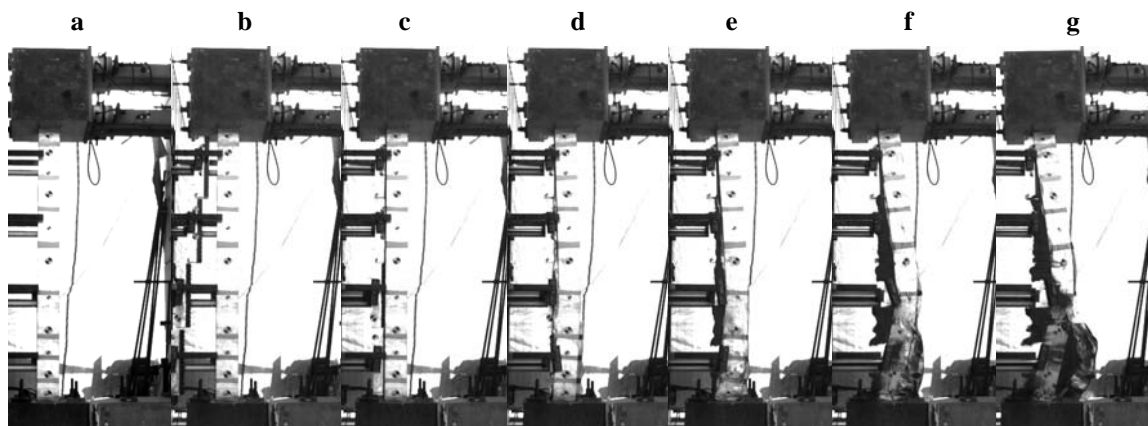
Figure 5.62: Test WA06 Progression of Damage

Accelerations of the specimen were recorded at five locations with accelerometers attached to the back (non-impact) side of the column. A maximum acceleration of 17,899.7 g was recorded at the bottom of the column. Table 5.36 gives a summary of peak acceleration for each accelerometer.

Table 5.36: Test WA06 Specimen Acceleration Summary

Distance from Base (in)	Peak Acceleration (g)
96.75	14394.7
64.5	17899.7
32.25	15354.2

Displacements were measured using the camera data and the tracking software. Table 5.37 gives a summary of the maximum and residual displacement at multiple locations.

Table 5.37: Test WA06 Specimen Displacement Summary

Distance from Base (in)	Maximum Displacement (in)	Residual Displacement (in)
125.8	0.65	0.59
117.0	1.99	1.44
107.0	3.61	2.64
96.5	5.21	4.50
80.0	7.65	6.52 (approx)
64.5	9.62	8.70
51.3	10.62 (approx)	9.37
34.4	7.91	7.44
22.9	4.91 (approx)	4.50
12.0	2.76	2.77
2.9	0.63	0.82 (approx)

Figure 5.63 and Figure 5.64 show the column post-test. Figure 5.65 shows a picture of the web being completely blown out and the flanges bent outward. The flyer plate created by the web is shown in Figure 5.66. A close up of the web fracture is given in Figure 5.67.

A plot of the maximum displacements over the height of the column is shown in Figure 5.68. A maximum displacement of 10.62 in was found at a height of 51.3 in from the base of the column. Figure 5.68 also gives a plot of the column residual displacements. A maximum residual displacement of 9.37 in was found at a height of 51.3 in from the base of the column.
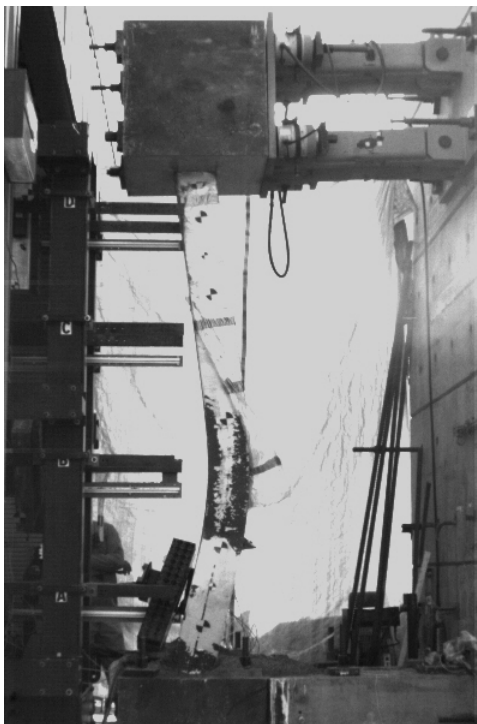
Figure 5.63: Test WA06 Column Post Test

Figure 5.64: Test WA06 Column Base Post-Test

Figure 5.65: Test WA06 Column Flanges Post-Test

Figure 5.66: Test WA06 Column Web Flyer

Figure 5.67: Test WA06 Column Web Fracture
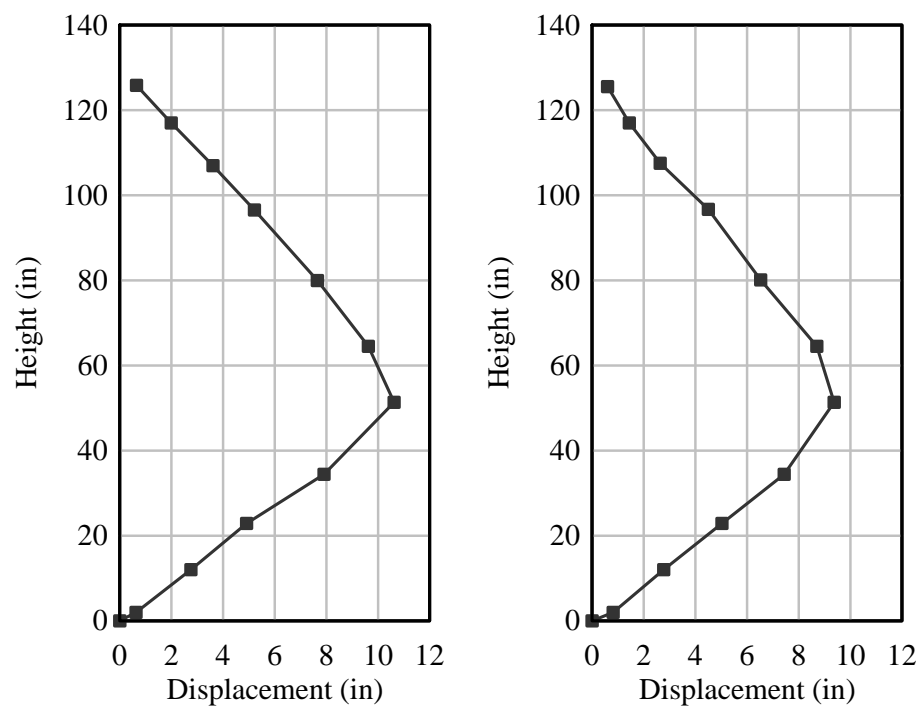
Figure 5.68: Test WA06 Maximum (left) and Residual (right) Displacements

5.4   Comparison to Field Tests

The results from the DTRA tests, discussed previously in Chapter 2, and the tests from this chapter were compared to validate the capability of the Simulator for this type of testing. Because the test setup was modified for the Field Phase II tests, there is no direct comparison for displacements; however the tests can be compared qualitatively to show similarities in the column behaviors.

Field Test 8 which was a W10x49 test specimen with a piece of cladding placed in front of it can be compared to the WA05 test done in the Simulator. Both tests had a relatively large amount of displacement, but no fracture of the web or the flanges. Figure 5.69 (field) and Figure 5.70 (lab) shows a comparison of the column post test and global deformation of the two columns.

The localized flange behavior can also be compared and is shown in Figure 5.71. In both cases, the flanges buckled up the height of the column with more localized buckling located at the base of the column.

Field Test 9 which was a W10x49 test specimen without cladding can also be compared to the WA06 test done in the Simulator. Both tests demonstrated web fracture in the k-region and subsequently had the flanges bend outward with a flyer plate created. Photos of these tests are shown in Figure 5.72, Figure 5.73 and Figure 5.74 with comparisons of the global behavior, column base and flyer plate, respectively.

Figure 5.69: Field Test 8 Pre and Post-Test Global Deformation

Figure 5.70: WA05 Pre and Post-Test Global Deformation

Figure 5.71: Field Test 8 (left) and WA05 (right) Localized Flange Behavior Comparison

Figure 5.72: Field Test 9 (left) and WA06 (right) Column Comparison

Figure 5.73: Field Test 9 (left) and WA06 (right) Column Base Comparison

Figure 5.74: Field Test 9 (top) and WA06 (bottom) Flyer Plate Comparison

5.5   Summary

This chapter described the methodology of testing structural steel columns in the weak axis direction using the UCSD Blast Simulator. This included a discussion of the use of a loading medium, such as sand or water, to distribute the loads generated by the impacting modules to both the web and the flanges of the column. The results from the six experiments were included and it was found that both loading mediums simulated the transfer of the load to the flanges; however, the use of water made tracking the column nearly impossible and, therefore, sand became the preferred loading medium for these types of tests.

The main objective of the chapter was to validate the Simulator's capability of generating blast-like loads on non-flat geometries, such as the weak axis of a column. Although no direct quantitative comparisons were available, qualitative comparisons were included for a variety of tests in which the Simulator was able to generate behavior and failures, including web fracture, very similar to those seen in the field.

6 Development & Validation of a Finite Element Model for Columns Loaded in the Weak Axis Direction

A finite element model to predict the response of steel columns under simulated blast loads in the weak axis direction was also developed as part of this dissertation and is discussed in this chapter. As with the strong axis finite element model, the analysis was preformed with LS-DYNA [21], a three dimensional, explicit, Lagrangian finite element code. This chapter describes the development of the finite element model and includes validation of the model by comparing to similar experiments described in Chapter 5.

6.1   Column Mesh Development

This section describes the development and selection of properties pertaining to defining the mesh parameters for the steel column experiments.

6.1.1 Shell Elements

Fully integrated shell elements with six integration points through the thickness were used to model the steel W-Shape. Shell elements were selected for the steel because, not only are they computationally accurate, they provide for a faster processing time which is critical for developing the fast running model discussed in Chapter 8. The shell elements used were 0.5 in by 0.5 in and were given the corresponding thicknesses to the column dimensions for the majority of the elements. The shell elements from the column flanges share nodes with the column web at the appropriate connection point. Figure 6.1 shows the W14x132 steel column constructed with shell elements.
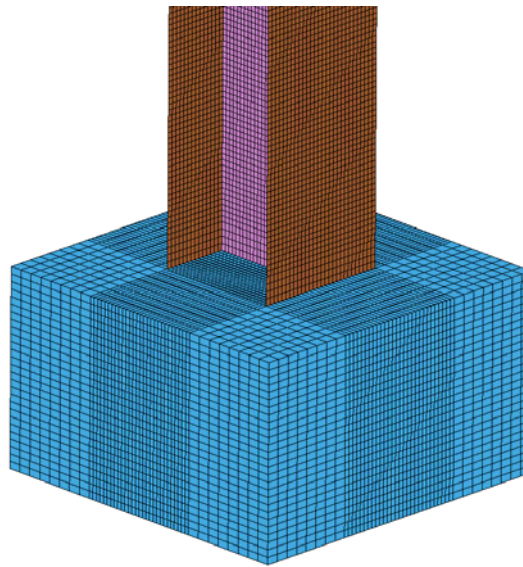
Figure 6.1: Shell Elements in Steel Column

6.1.2 Solid Elements

The model for the weak axis steel column tests used three dimensional solid elements to represent the concrete header, concrete footer, steel casing and link system. These elements were eight node brick elements with single point integration. The

elements varied in size throughout the mesh. The largest element being 1 in by 1 in by 1 in located in the concrete header and footer away from the steel column. Figure 6.2 shows solid elements used to model the concrete footer.
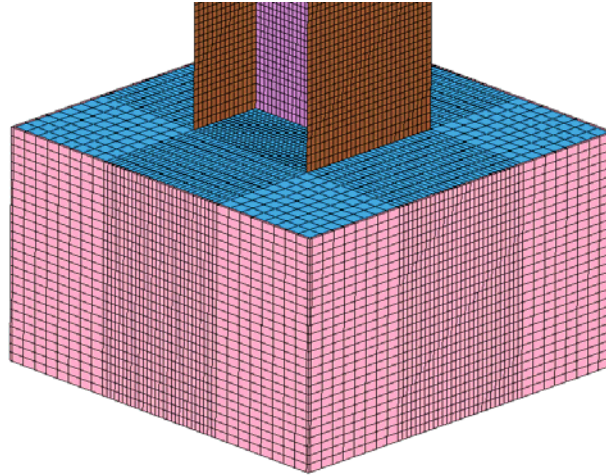
Figure 6.2: Solid Elements in Concrete Footer

6.1.3 Beam Elements

Hughes Liu beam elements with cross sectional reinforcing steel were used for modeling steel reinforcement and Nelson Studs in the concrete header and footer and are shown in Figure 6.3. The steel shell elements and the solid concrete elements shared common nodes and were therefore merged together. The concrete elements are also merged with any reinforcing steel inside.
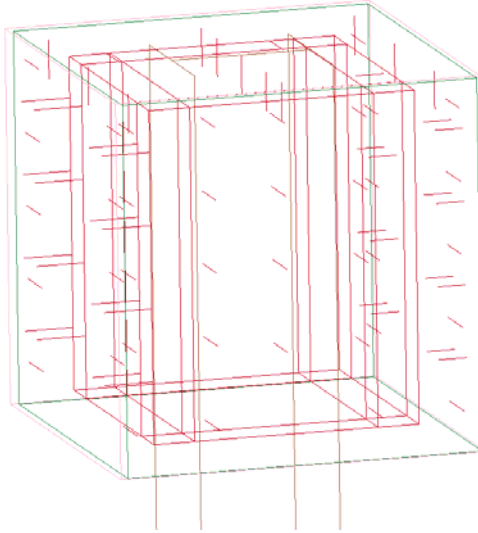
Figure 6.3: Beam Elements for Reinforcing Steel

6.1.4 SPH Elements

Smooth Particle Hydrodynamics (SPH) is an interpolation scheme developed by Lucy, Gingold, and Monaghan [28, 29] which is capable of modeling large deformations in a pure Lagrangian frame without a background spatial mesh. The particles are the computational framework on which the governing equations of continuum mechanics are resolved.

In the standard SPH method, for a function, f, the approximation of its function value at a certain location or particle, i, as well as its gradient can be expressed as a summation interpolants over the neighbor particles using a smoothing kernel function, W, with the smoothing length, h as in Equations (6.1) and (6.2).

$$\langle f_i \rangle = \sum_{j=1}^{N} \left(\frac{m_j}{\rho_j} \right) f_i W_{ij} \tag{6.1}$$

$$\langle \nabla f_i \rangle = \sum_{j=1}^{N} \left(\frac{m_j}{\rho_j} \right) f_i \nabla_i W_{ij} \tag{6.2}$$I

If the distance between particles i and j is written as r_{ij}, then W_{ij} and $\nabla_i W_{ij}$ then Equations (6.1) and (6.2) can be defined as the following, where $\boldsymbol{x}$ is the position vectors of the particles [30].

$$W_{ij} = W\left(\boldsymbol{x}_i - \boldsymbol{x}_j, h\right) = W\left(\left|\boldsymbol{x}_i - \boldsymbol{x}_j\right|, h\right) \tag{6.3}$$

$$\nabla_i W_{ij} = \frac{\boldsymbol{x}_i - \boldsymbol{x}_j}{r_{ij}} \frac{\partial W_{ij}}{\partial r_{ij}} = \frac{\boldsymbol{x}_{ij}}{r_{ij}} \frac{\partial W_{ij}}{\partial r_{ij}} \tag{6.4}$$

The conservation equations of continuum mechanics can be written as particle equations as is given in Equations (6.5), (6.6) and (6.7), where E, p and $\boldsymbol{v}$ represent the internal energy, pressure and velocity vector, respectively. Π_{ij} represents the artificial viscous pressure which is introduced to smooth the shock over several particles and prevent discontinuities. A further discussion on artificial viscosity, as well as the implementation of SPH into LS-DYNA is discussed in [16].

$$\frac{d\rho_i}{dt} = \rho_i \sum_{j=1}^{N} \frac{m_j}{\rho_j}\left(\boldsymbol{v}_i - \boldsymbol{v}_j\right) \cdot \nabla_i W_{ij} \tag{6.5}$$

$$\frac{d\boldsymbol{v}_i}{dt} = -\sum_{j=1}^{N} m_j\left(\frac{p_i}{\rho_i^2} + \frac{p_j}{\rho_j^2} + \Pi_{ij}\right)\nabla_i W_{ij} \tag{6.6}$$

$$\frac{dE_i}{dt} = \frac{1}{2}\sum_{j=1}^{N} m_j\left(\frac{p_i}{\rho_i^2} + \frac{p_j}{\rho_j^2} + \Pi_{ij}\right)\left(\boldsymbol{v}_i - \boldsymbol{v}_j\right) \cdot \nabla_i W_{ij} \tag{6.7}$$

SPH elements were used to model the sand in the weak axis tests. The model utilized the same 0.5 in x 0.5 in x 0.5 in mesh to space the SPH particles. The element masses were distributed to the particles using the solid center option which is shown in

Figure 6.4. The density was inputted using the same value as the sand model discussed in Section 2.2.1.
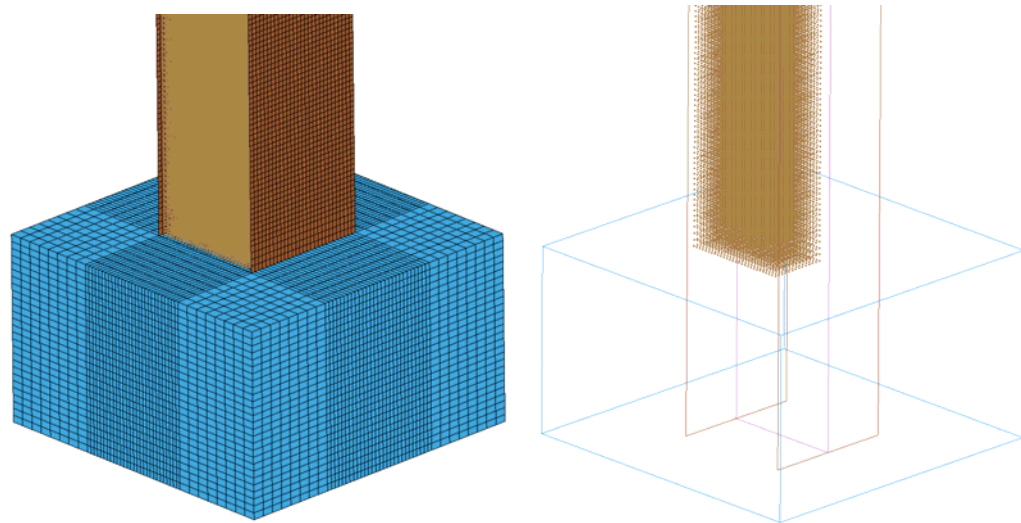
Figure 6.4: SPH Sand Elements

6.2 Boundary Conditions

This section describes the modeling of the boundary conditions for both the base and top of the column system, with the goal of being able to accurately describe what occurred during the experiments.

6.2.1 Footer Boundary

The boundary conditions on the concrete footer were modeled slightly differently than the weak axis tests for the variable velocity. This was necessary because due to the high velocity of these tests, the base lifted and rotated slightly off the base slab causing crushing of the hydro-stone which was placed in to help fix the base to the slab. To allow a slight rotation at the base, the dwidag bars were modeled with beam elements as seen in Figure 6.5. These element were tensioned and fixed to shell plates at the top and fixed

with a nodal constraint at the base. The slab and block were modeled with shell elements with nodal constrains and contacts were placed between the shells and the footer to allow rotation to develop if necessary. The boundary for the uniform velocity test, WA01, had a boundary consistent with the strong axis tests as discussed in Section 5.2.1.
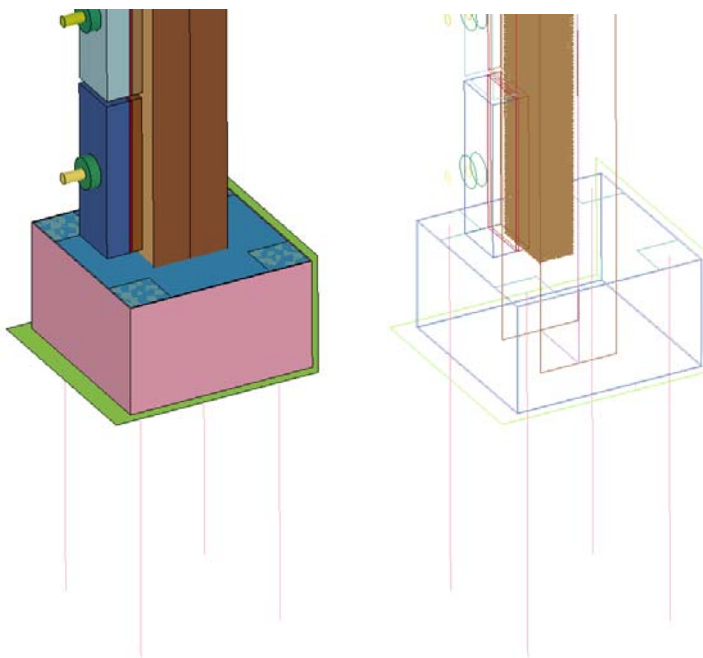
Figure 6.5: Concrete Footer Boundary Condition

6.2.2 Link System Boundary

Correctly modeling the boundary conditions on the header was crucial in developing a working model. Initially, it was assumed that the system remained fixed in the rotation and was only allowed to translate vertically and could be modeled using simple node restraints; however, at the higher level velocity tests, these boundary conditions were not fully met. The system began to act more like a pin connection than a fixed connection as the velocities increased. Three main situations were identified that

contributed to the boundary conditions not being consistent for all tests and is discussed in detail in Section 4.2.2.

To incorporate the rotation, the entire link system was modeled and connected to a backing plate as shown in Figure 6.6. The backing plate has a fixed restraint on the back of one side and is merged to the tabs which hold the pins on the other. There is a steel tube section connecting the two sets of pins. For both sets of pins, an *AUTOMATIC_SURFACE_TO_SURFACE contact was placed between the pin and the surrounding parts to allow rotation.
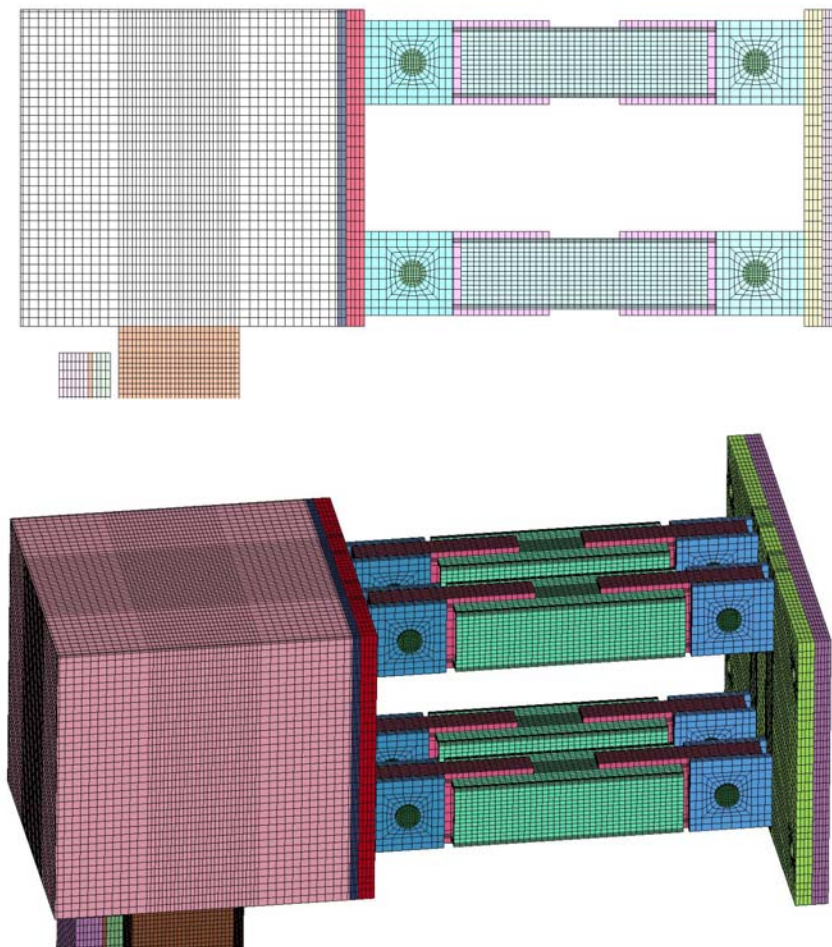
Figure 6.6: Link System Mesh

To correctly model the extra rotation for higher velocity tests, a layer of rubber elements was placed between the link and the column header and is shown in Figure 6.7. The rubber was four elements thick and was merged to the column and *TIED_SURFACE_TO_SURFACE contact was used to connect the rubber to the link which did not share many common nodes. The material description for the rubber is discussed in Section 4.4.4.
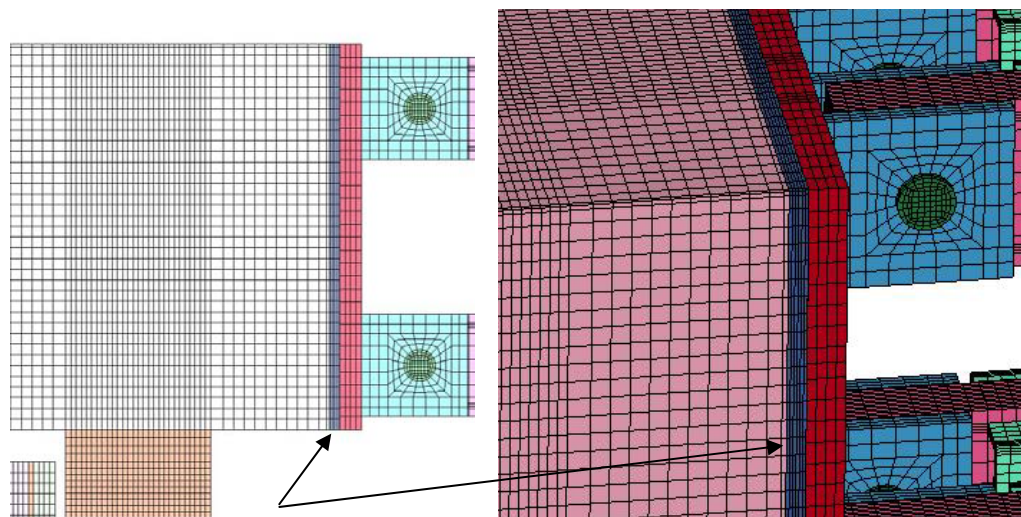
Figure 6.7: Rubber Connection Elements

6.3 Loading

Loads were applied to the SPH sand elements and the column by the modeled impacting module which included the programmer, aluminum backing plate, impaction mass, rod and collar. It was found that for these tests, the pyramid system on the face of the programmer did not greatly affect the results, but greatly slowed run times and, therefore, were omitted. The rod as shown in Figure 6.8, was not fully modeled, but the density of the material was changed include the full mass of the rod.
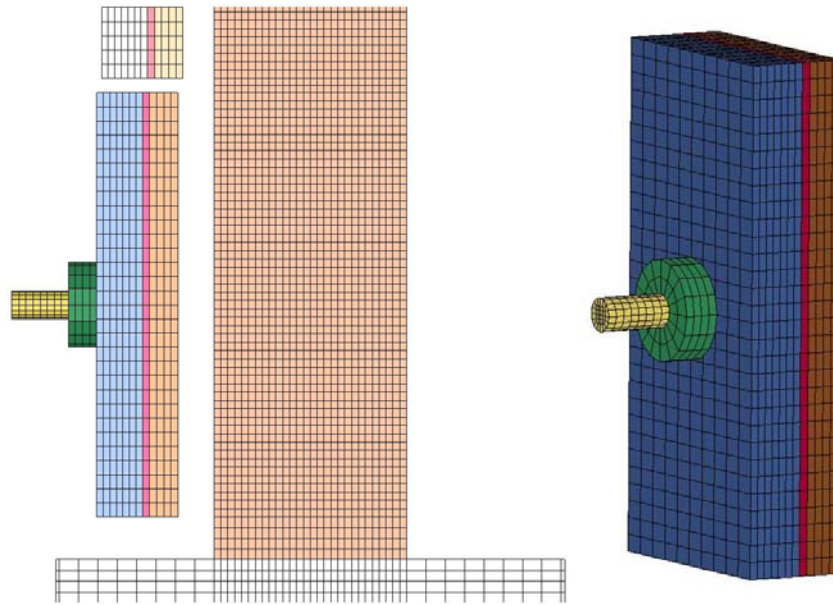
Figure 6.8: Mesh of Impacting Module

The impacting modules were allowed to impact the SPH sand particles through an *AUTOMATIC_NODES_TO_SURFACE contact which transferred the loads from the mass to the sand as shown in Figure 6.9. Another *AUTOMATIC_NODES_TO_SURFACE contact was placed between the sand particles and the column shell elements to transfer the load from the sand to the column. In both cases the SOFT=1 description was used in LS-DYNA due to the significant differences in the material stiffness and a friction factor of 0.30 was used between the sand and both other parts.
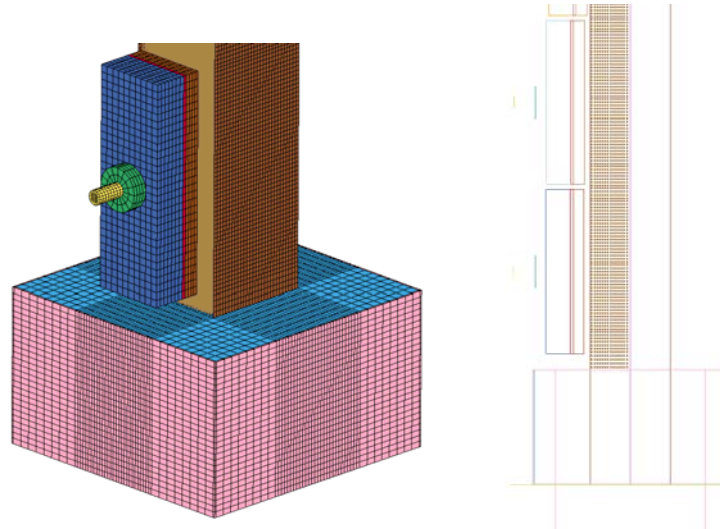
Figure 6.9: Loading of Column with Impacting Module and SPH Sand Elements

6.4   Material Models

This section describes the five main material models were used to model the strong axis tests. These materials include steel, concrete, sand, programmer, and rubber connection elements.

6.4.1   Steel Model

To model the steel column, *MAT_PIECEWISE_LINEAR_PLASTICITY, which can incorporate strain rate effects, was used. This model allows for the input of arbitrary stress versus strain relations for various strain rates as shown in Figure 6.10 with rates increasing from curves 1 to 5. Intermediate values are found by interpolating between the curves and if a point falls out of range, the closest curve is used.
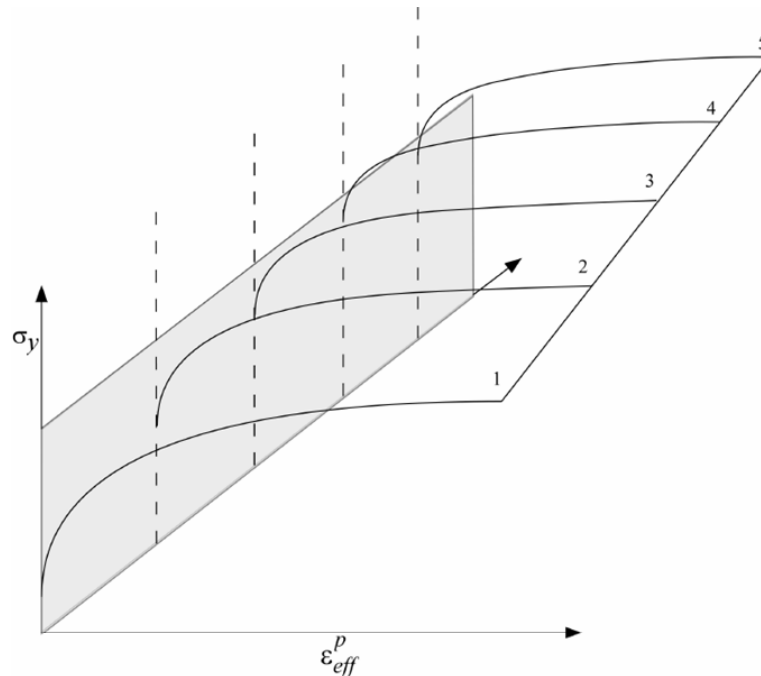
Figure 6.10: *MAT_PIECEWISE_LINEAR_PLASTICITY Model, from [21]

The values for the stress-strain relations at each given rate were found through a many rounds of experimental testing and fitting done by Karagozian and Case [24]. Figure 6.11 shows the steel model used for the purposes of these tests. The yield stresses ranged from 52,000 psi for no rate effects to almost 78,000 psi for rates at around 100. It should be noted that no additional curves should be added. The rates for the steel column tests are in the range of 30 to 50 s^{-1}, but due to the almost immediate onset of loading, there is some high rate numerical noise in the system. The omission of the higher curves allows the model to not interpolate to a much higher curve than is realistic.
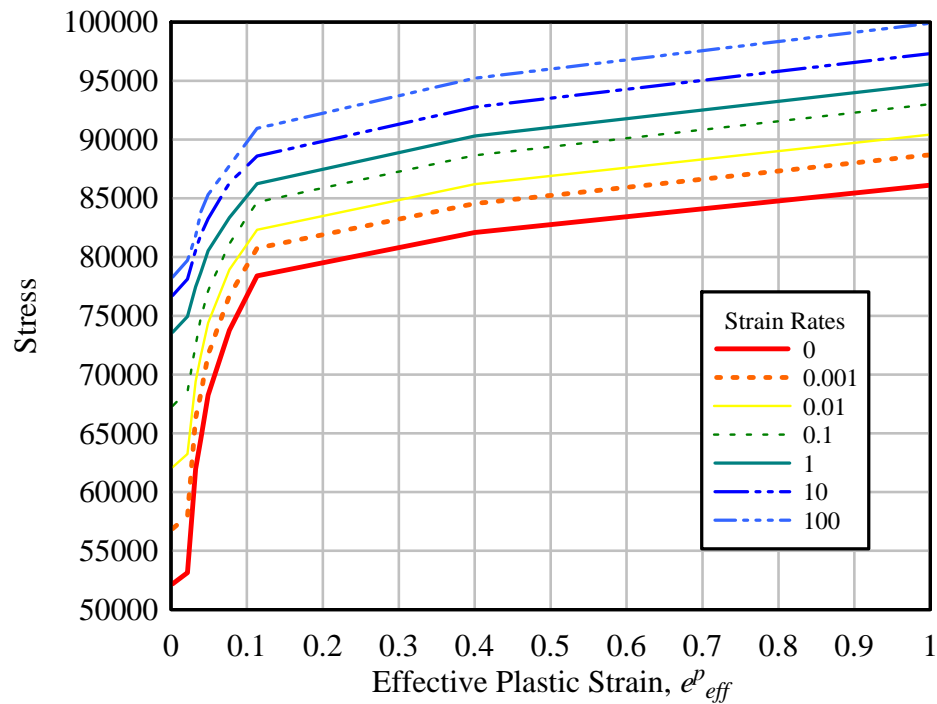
Figure 6.11: Steel Material Model

Fracture can be incorporated into the model by inputting a failure strain into the material card. At this strain, the elements are considered failed and are deleted from the calculation. Previous research done by [31] suggested using a failure strain of 0.40 based on a series of tests. This value is only valid for steel outside of the k-region and a further discussion on the difficulties associated with modeling fracture for these types of tests are given in Section 6.4.2.

6.4.2 Concrete Model

The concrete in both the header and the footer was modeled with the K&C Concrete Model, *MAT_072 Rel 3 [25]. A background into plasticity models used for concrete is given in [26]. The K&C model is a plasticity model that decouples the volumetric and deviatoric parts of the concrete response. The volumetric part is treated

with an equation of state with tabulated data that gives the pressure as a function of volumetric strain. The deviatoric response is found between three independent failure surfaces that correspond to the limit of elastic behavior, the maximum concrete strength, and the residual concrete strength. A current failure surface is found by interpolating between the three independent surfaces and more detail on this model can be found in [25].

The concrete strength was set at 5,000 psi and the density at 145 lb/ft^2. The remaining parameters, except for strain rate effects, are calculated with the strength and density. To account for strain rate effects, tabulated data was strain rates ranging from 3.0e-4 to 3.0e4 were used. The increase factors at each strain rate were determined from calibrated test data provided by K&C.

6.4.3 Programmer Model

As discussed in detail in [27], the model chosen for the programmer was *MAT_057 or *MAT_LOW_DENSITY_FOAM and was selected because of the similarities between the stress-strain behavior and the energy dissipation characteristics between low density foam and the programmer.

The model requires the input of the material density and the material modulus. The unloading is governed by two factors, the HU and the SHAPE. In the LS-DYNA Keyword Manual [21], HU is defined as the hysteretic unloading factor between zero and one, where one corresponds to no energy dissipation. SHAPE is defined as the shape factor for unloading. Shape factors greater than one increase energy dissipation and those less than one decrease energy dissipation.

The shape of the stress-strain curve (for loading) used in the wall tests is shown in Figure 6.12 and is also discussed in [13]. The model used in the steel column tests was identical to that used in the modeling of the wall tests, with two slight modifications. The material used to create the column programmer was slightly denser and less stiff than the programmers used for the previous tests. The density was modified from 0.03 lb/in^2 to 0.043 lb/in^2 and a scale factor of 2.0 was used to scale the stress-strain curve to make it stiffer than the 1.7 previously used. The initial modulus was kept the same at 2,262 psi. The HU of 0.05 and a SHAPE of 400 were also kept consistent.
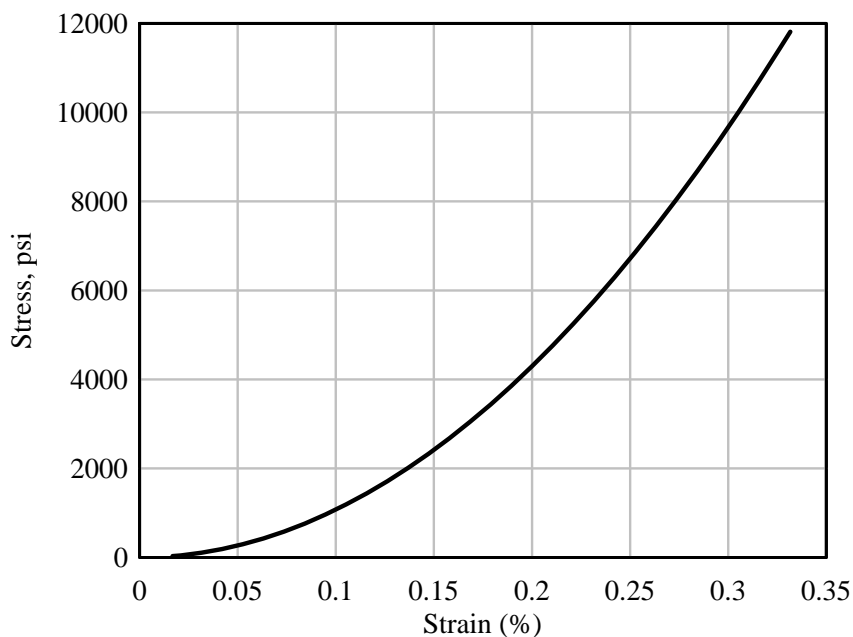
Figure 6.12: Stress-Strain Curve for Programmer Model

6.4.4 Rubber Connection Model

The model used to represent the rubber connection elements was similar to that used for the programmer. *MAT_LOW_DENSITY_FOAM was used with parameters adjusted to match test data and incorporate the slight rotation in the system. The values of

density and modulus were set to 0.043 and 2,262, respectively. A HU of 0.05 and a SHAPE of 400 was included. Finally, the stress-strain relation given in Figure 6.12 was scaled by a factor of 0.5.

6.4.5 Sand Model

The sand model used in LS-DYNA was *MAT_25 or *MAT_GEOLOGICAL_CAP_MODEL. The plasticity model used in this material card is given in Chapter 2. The model was calibrated from WES flume sand tests by [32]. The density of the sand was 0.0614 lb/in^3. The bulk modulus, the shear modulus and the failure envelope parameter, θ, were set to 1.1605 x 10^{-4} psi, 0.5915 x 10^{-4} psi, and 0.2238 radians, respectively. The values for the other two failure envelope parameters, α and γ, were set to zero.

6.5 Column Model Validation

This section describes the validation analysis of the above finite element model as compared with three of the weak axis steel column tests described in Chapter 5. Only the tests with sand as a loading medium were considered. The water tests were not modeled because the water at impact made the tracking of input velocity problematic. For each test, all parameters except for geometry and impact velocity were kept consistent. Global maximum and residual displacement were two of the main output parameters compared in order to validate the model and comparison plots are given in each subsequent section. Localized buckling, fracture, and flange behavior were also considered as part of the validation criteria.

6.5.1 Test WA01

As described in Section 5.3.1, Test WA01 was a W10x49 specimen loaded with four BG25s at uniform velocity with sand used as a loading medium. From the data analysis, the average of the impact velocity of the BGs was found to be 676.8 in/s (17.2 m/s). Each impacting module in the model, with representative equivalent weight, was given this initial velocity in the direction of the specimen. Because no acceleration was needed to reach impact velocity computationally, the impacting modules were started only a small distance off the flange of the column to reduce the run time. The sand was modeled using SPH elements including those representing the sand bags laid along the outside of the bag. The initial configuration of the model is shown in Figure 6.13.

Figure 6.13: Test WA01 Finite Element Model Configuration

The masses impact the specimen though the *AUTOMATIC_NODES_TO_SURFACE contact shown in Figure 6.14. At this point

the SPH elements dispersed around the programmers and also begin to apply pressure to the column through the additional contact as seen in Figure 6.15.

Figure 6.14: Test WA01 Impacting Mass and SPH Contact
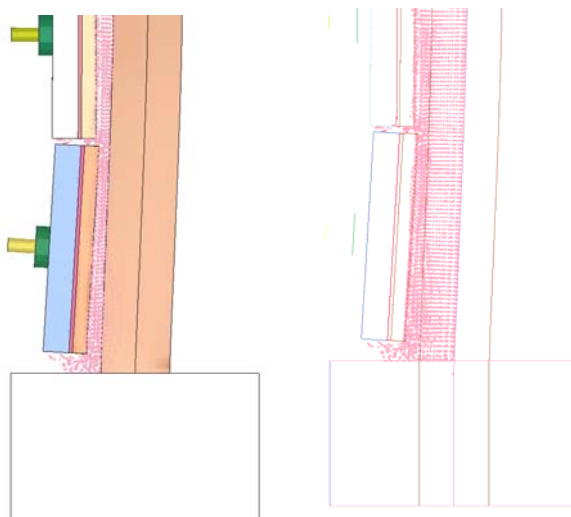
Figure 6.15: Test WA01 SPH Elements Applying Pressure on Column

After impact, the modules rebound in the opposite direction, as they do during the test. To prevent any additional collisions, the elements of the impacting modules were eroded at a time of 0.025 ms. The column then was allowed to freely move to its point of

maximum global displacement and rebound to its final resting point with some residual displacement. The termination time of 0.40 ms and a global damping of 2 percent was incorporated which was found to be sufficient for correctly determining the final state of the column. The progression of the run is shown in a series of screen shots in Figure 6.16.
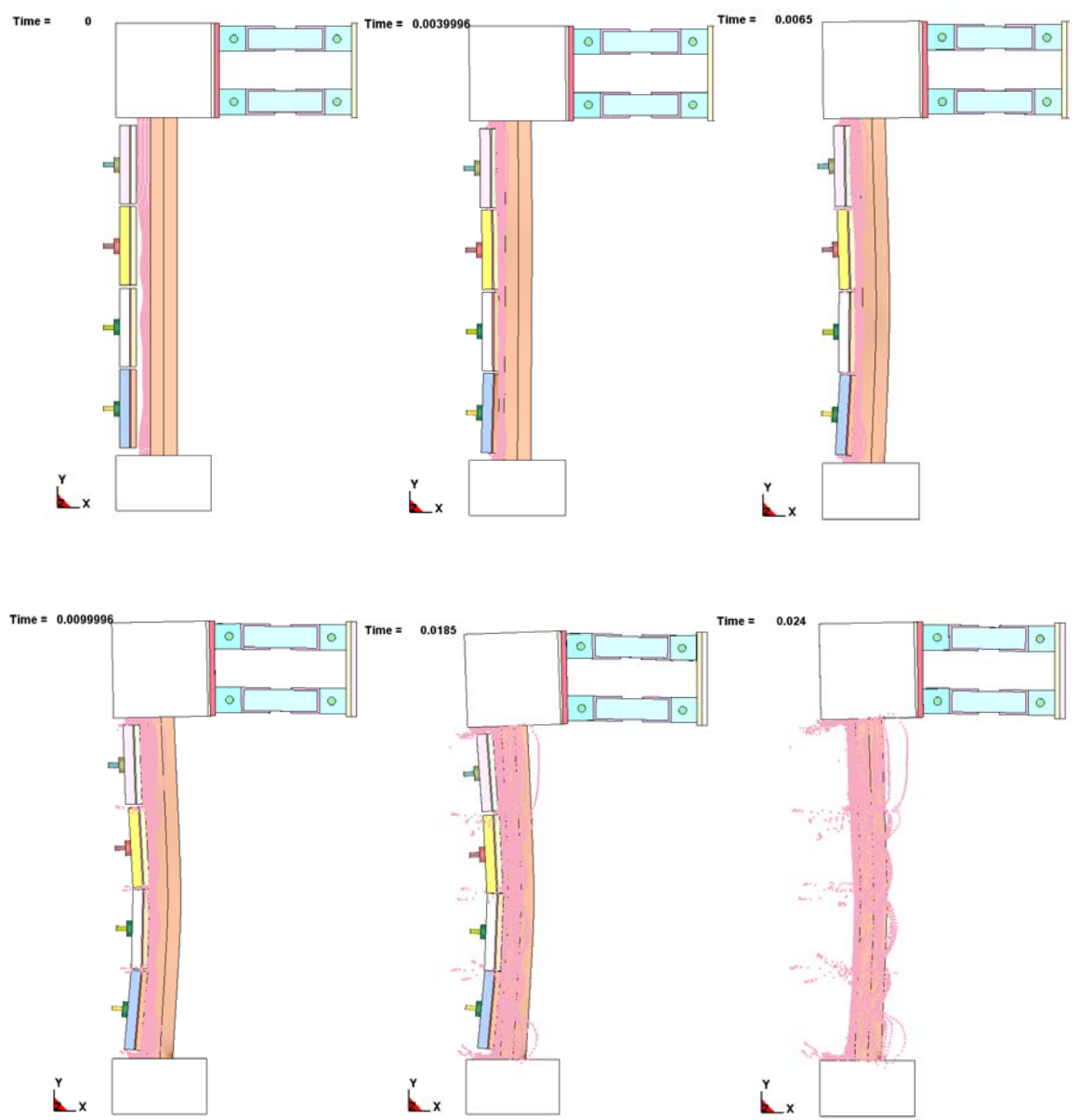
Figure 6.16: Test WA01 Finite Element Run Progression

Displacements of the column are given in Figure 6.17. Maximum and residual displacements at multiple locations were found along the height of the column. The results of the finite element run are summarized in Table 6.1.
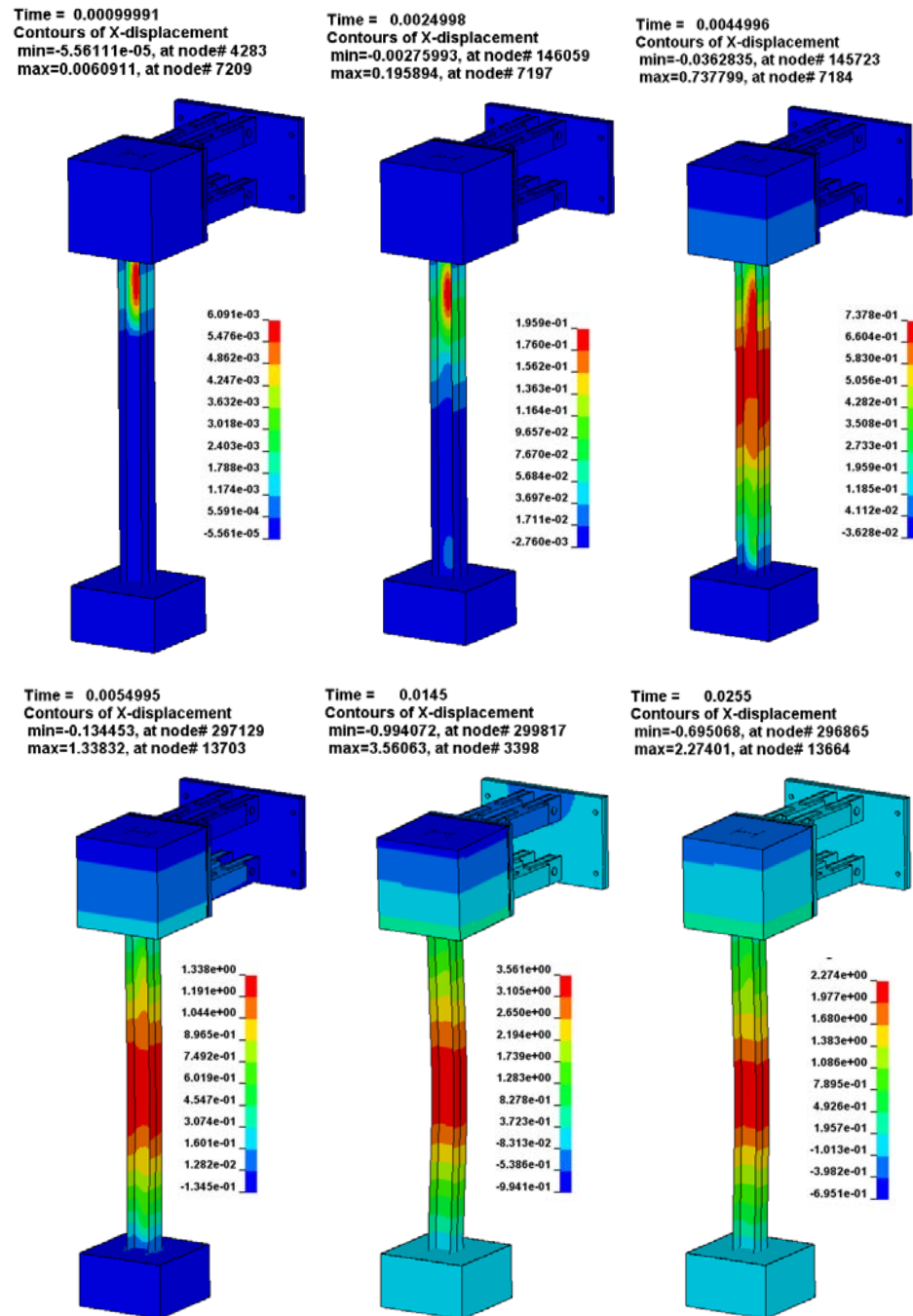
Figure 6.17: Test WA01 Finite Element Displacements

Table 6.1: Test WA01 Maximum and Residual Displacements

Distance from Base (in)	Maximum Displacement (in)	Residual Displacement (in)
126.0	0.47	0.22
117.0	1.34	0.93
103.875	2.04	1.36
90.75	2.58	1.67
77.625	3.17	2.09
64.5	3.55	2.42
51.375	3.29	2.30
38.25	2.51	1.74
25.125	1.65	1.21
12.0	0.80	0.65
3.0	0.17	0.12

The finite element displacement results are plotted with displacements seen in the Test WA01 experiment. The comparisons for both maximum and residual displacements are shown in Figure 6.18 and Figure 6.19. From the plots, the maximum displacement of the finite element model was 3.55 in as compared with a displacement of 3.84 in from the experiment which corresponds to an error of 8.17 %. The residual displacement of the computational model was 2.42 in and the experimental displacement was 2.67 in. The error from the residual displacements was found as 9.36 %. Additionally, included in Figure 6.20 and Figure 6.21 are visual comparisons from the finite element calculation and the experiment.
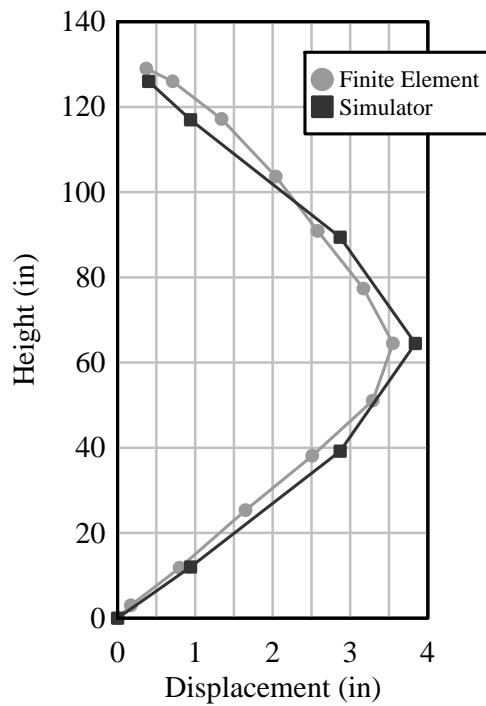
Figure 6.18: Test WA01 Maximum Displacement Comparison
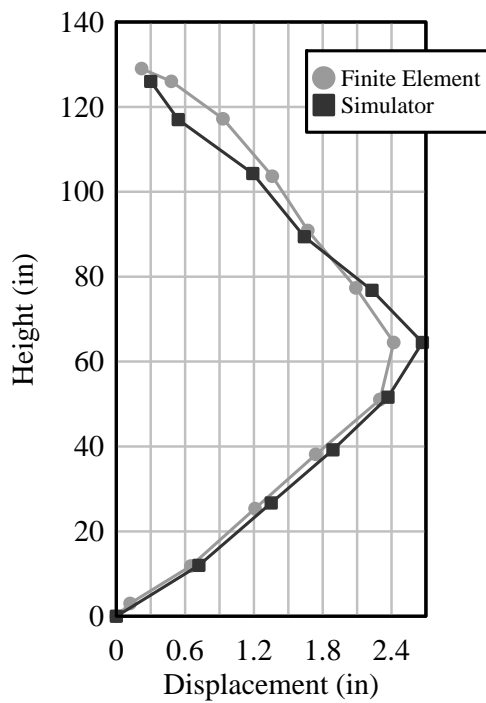
Figure 6.19: WA01 Residual Displacement Comparison
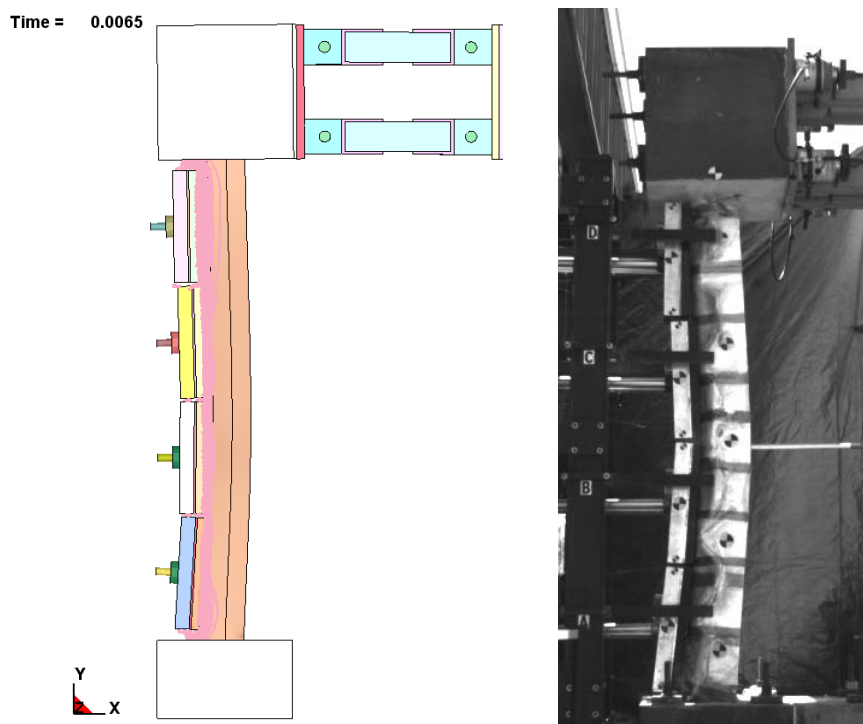
Figure 6.20: Test WA01 Visual Comparison 1
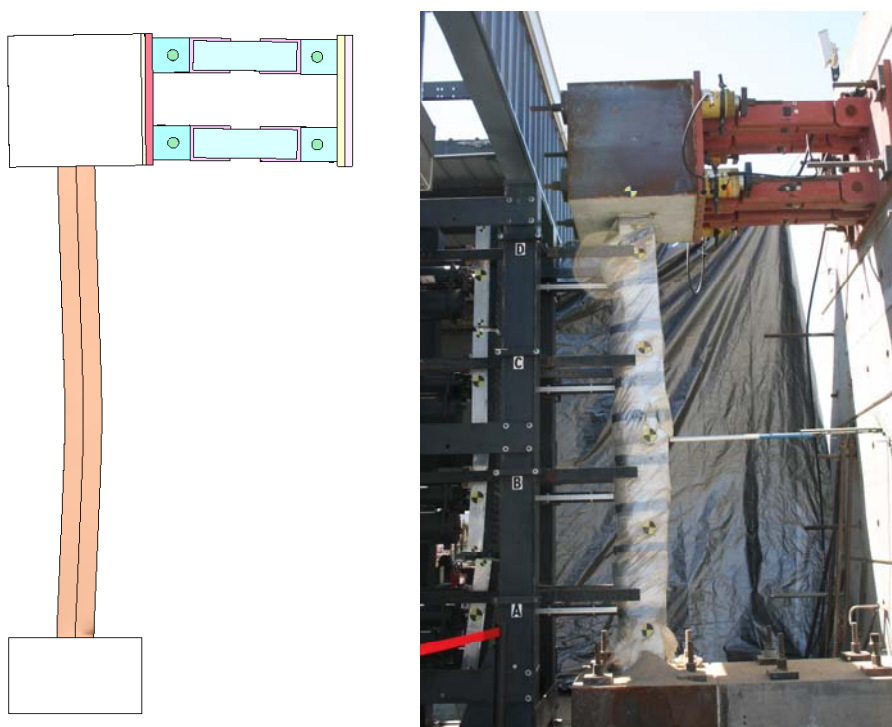
Figure 6.21: Test WA01 Visual Comparison 2

6.5.2 Test WA04

Discussed in Section 5.3.4, Test WA04 was a W14x132 specimen loaded with two BG25s and two BG50s at variable velocity. From the data analysis, the velocities of the BGs were found to be 1759.4 in/s (m/s), 1456.8 in/s (m/s), 982.0 in/s (m/s), and 443.5 in/s (m/s) for BG1 to BG4, respectively. Similar to the strong axis variable velocity tests, each impacting module in the model, with representative equivalent weight, was given this initial velocity in the direction of the specimen. The initial configuration of the model is shown in Figure 6.22.
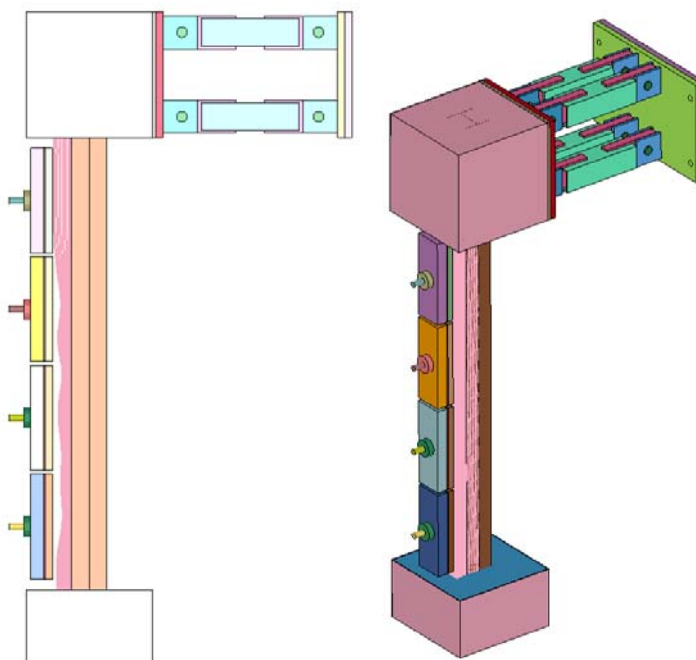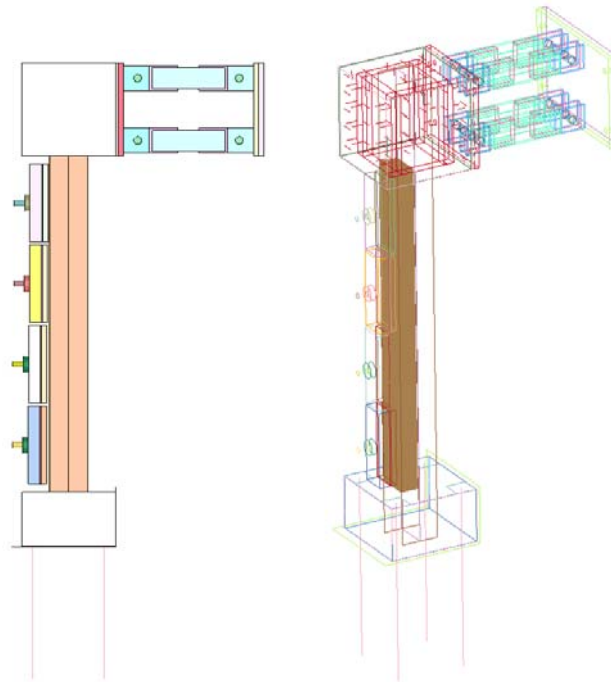

Figure 6.22: Test WA04 Finite Element Model Configuration

The masses impact the specimen though the *AUTOMATIC_NODES_TO_SURFACE contact. The SPH sand elements in this test were flush to the column flanges. As the mass travels into the sand, the SPH elements

begin to disperse around the programmers and also begin to apply pressure to the column through the additional contact.
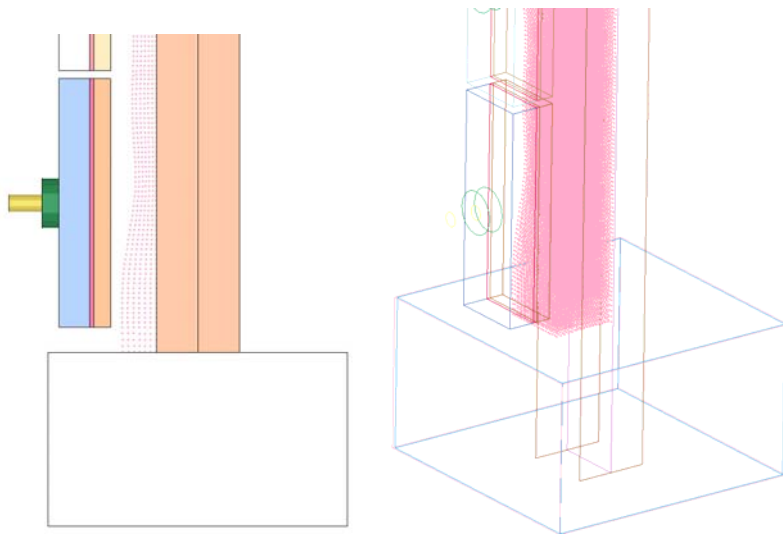
After impact, the modules rebound in the opposite direction, as they do during the test. To prevent any additional collisions, the elements of the impacting modules were eroded at a time of 0.012 ms. The column then was allowed to freely move to its point of maximum global displacement and rebound to its final resting point with some residual displacement. The termination time of 0.40 ms and a global damping of 2 percent was incorporated which was found to be sufficient for correctly determining the final state of the column. The progression of the run is shown in a series of screen shots in Figure 6.23.

Displacements of the column are given in Figure 6.24 for various times throughout the run. Maximum and residual displacements at multiple locations were found along the height of the column. The results of the finite element run are summarized in Table 6.2 for the maximum and residual displacements.

Table 6.2: Test WA04 Maximum and Residual Displacements

Distance from Base (in)	Maximum Displacement (in)	Residual Displacement (in)
126.0	1.12	1.06
117.0	1.85	1.81
103.875	2.78	2.61
90.75	3.49	3.31
77.625	4.37	3.92
64.5	4.84	4.39
51.375	4.90	4.48
38.25	4.11	3.75
25.125	3.04	2.75
12.0	1.82	1.63
3.0	1.01	0.86
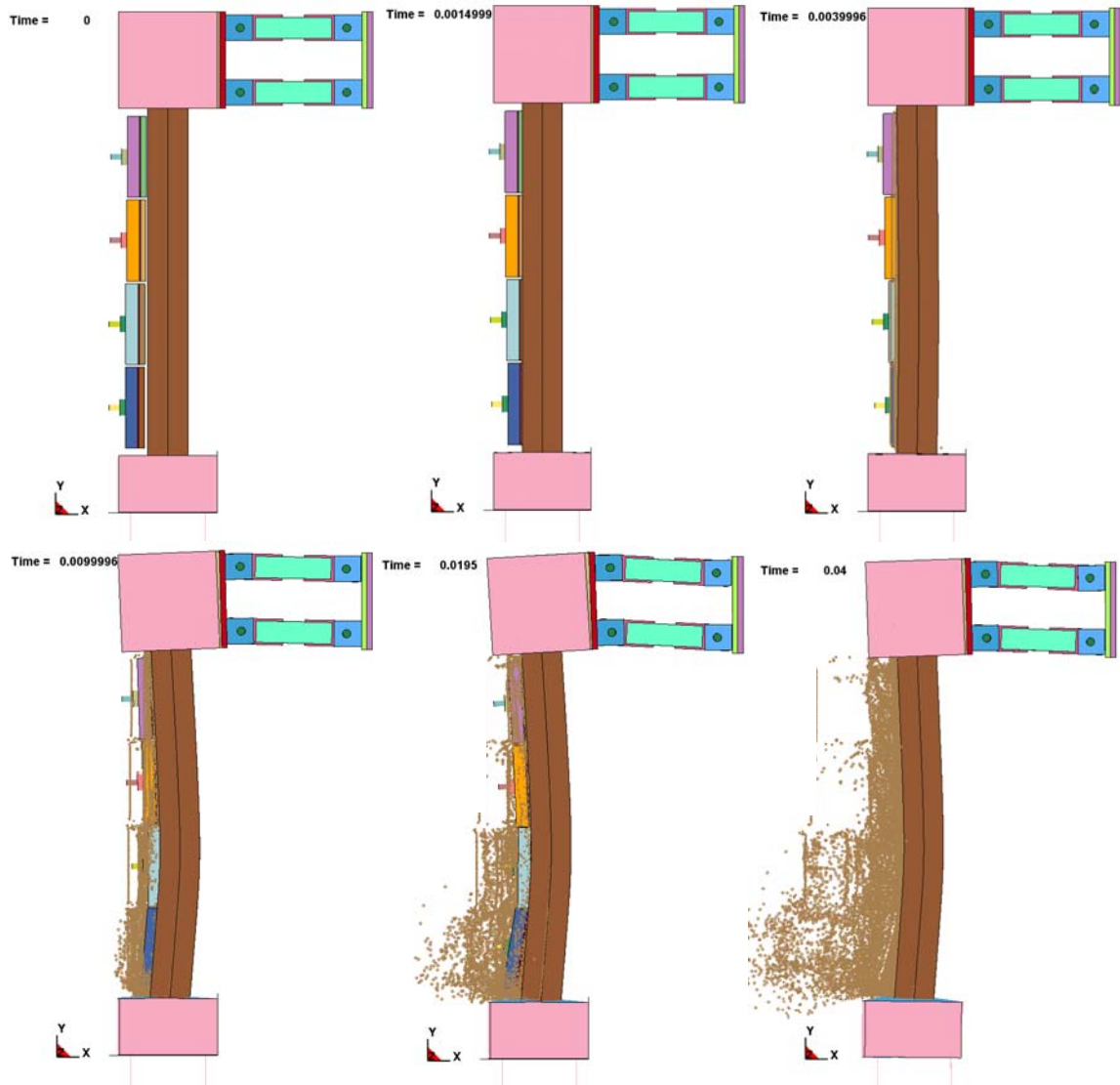
Figure 6.23: Test WA04 Finite Element Run Progression
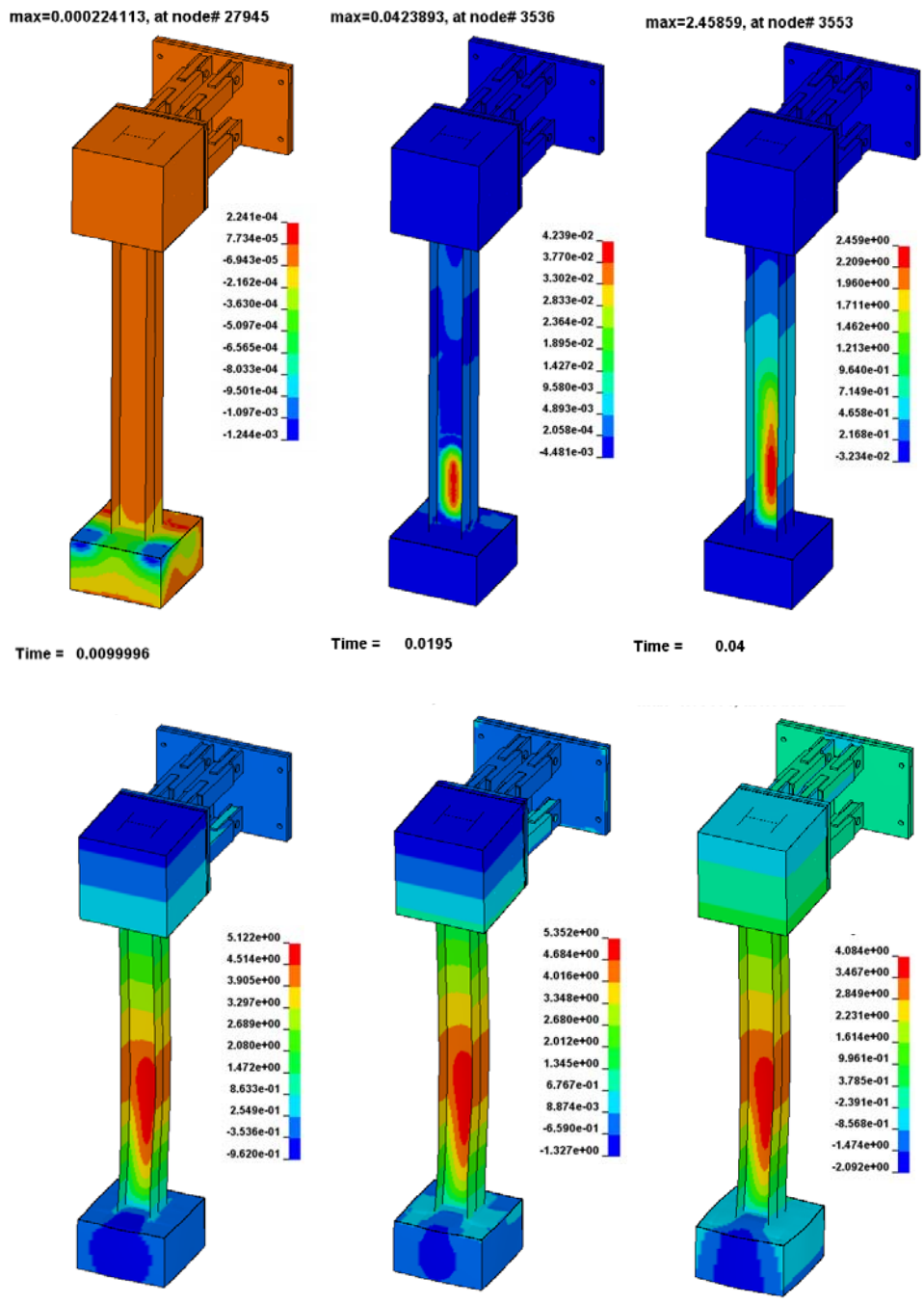
Figure 6.24: Test SA03 Finite Element Displacements

The finite element displacement results are plotted with displacements seen in the Test WA04 experiment. The comparisons for both maximum and residual displacements are shown in Figure 6.25 and Figure 6.26. From the plots, the maximum displacement of the finite element model was 4.90 in as compared with a displacement of 5.22 in from the experiment which corresponds to an error of 6.13 %. The residual displacement of the computational model was 4.48 in and the experimental displacement was 4.01in. The error from the residual displacements was found as 11.7 %. Also included, in Figure 6.27 and Figure 6.28, are visual comparisons from the finite element calculation and the experiment.
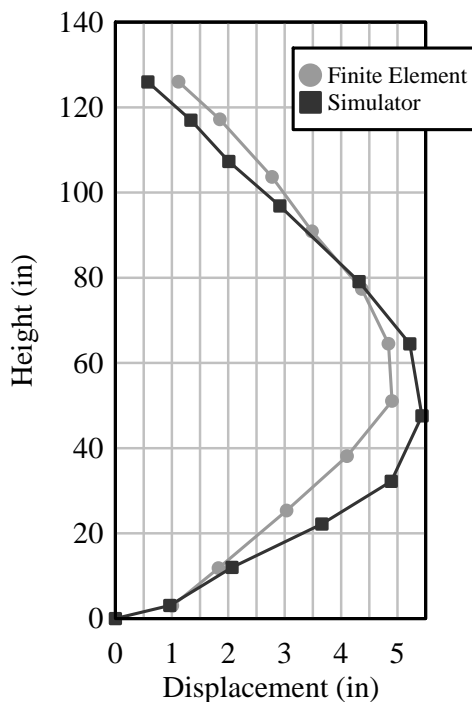
Figure 6.25: Test WA04 Maximum Displacement Comparison
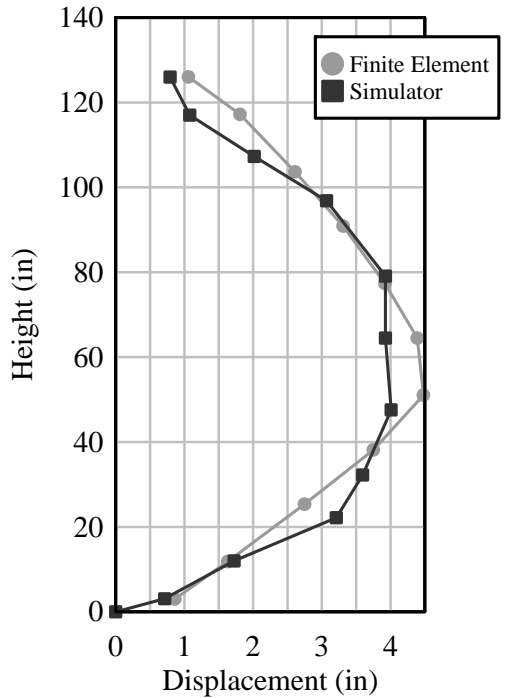
Figure 6.26: Test WA04 Residual Displacement Comparison
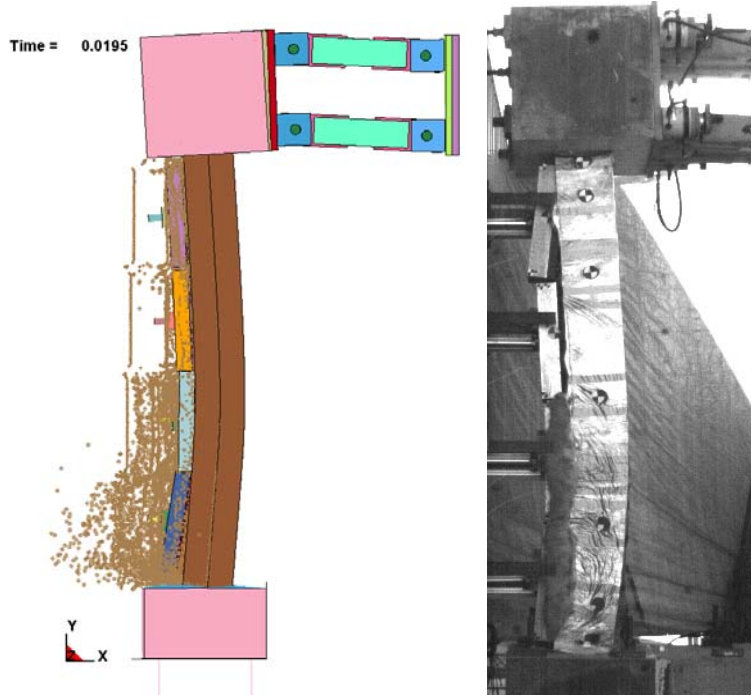
Figure 6.27: Test WA04 Visual Comparison 1
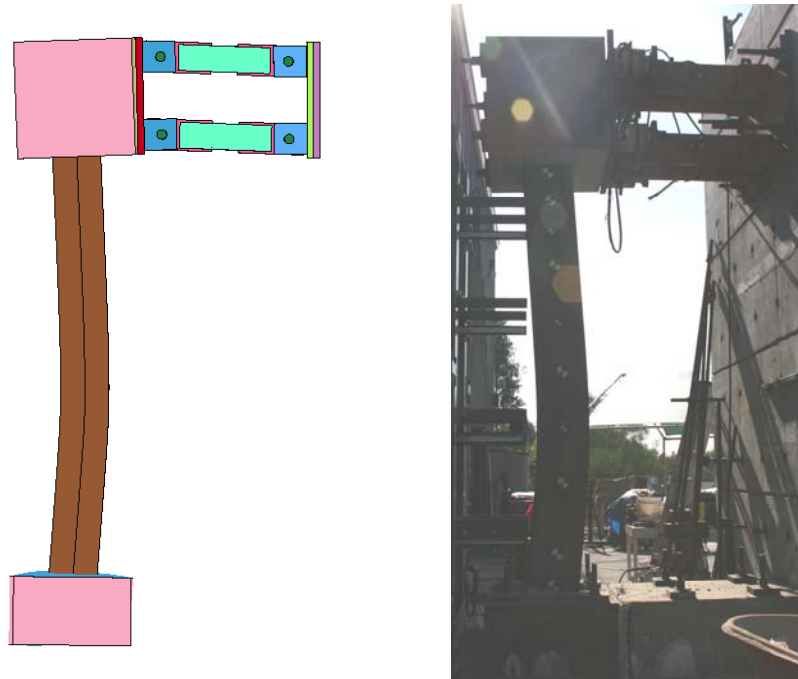
Figure 6.28: Test WA04 Visual Comparison 2

6.5.3 Tests WA06

A described in Section 3.3.6, Test WA06 was a W10x49 specimen loaded with two BG50s and two BG25s at variable velocity. From the data analysis, the velocities of the BGs were found to be 1780.0 in/s (45.2 m/s), 1472.5 in/s (37.4 m/s), 987.5 in/s (25.1 m/s), and 442.0 in/s (11.2 m/s) for BG1 to BG4, respectively. Each impacting module in the model, with representative equivalent weight to account for additional mass of the rods of the BG50s, was given this initial velocity in the direction of the specimen. The modules were each given an initial position to account for the difference in velocities so that the impact would be synchronized. The initial configuration of the model is shown in Figure 6.29.
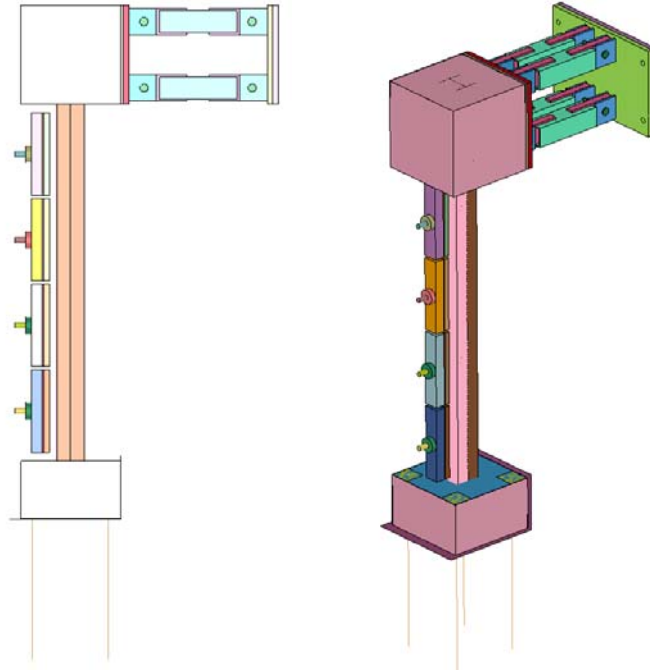
Figure 6.29: Test WA06 Finite Element Model Configuration

Initially, the model was run with the failure strain set equal to 0.40 for the web and the flanges as is consistent from the values obtained from tensile coupon testing. The progression of the run is shown in a series of screen shots in Figure 6.30 and Figure 6.31. From the analysis, no fracture of the k-region of the column was observed which was not consistent with Test WA06. The analysis was comparable, at least from a behavioral stand point to Test WA05 which was a water test at the same velocity, but did not exhibit any web fracture. A comparison of the test and the analysis with 0.40% failure strain is shown in Figure 6.33 and Figure 6.33 with views from the column front and back.
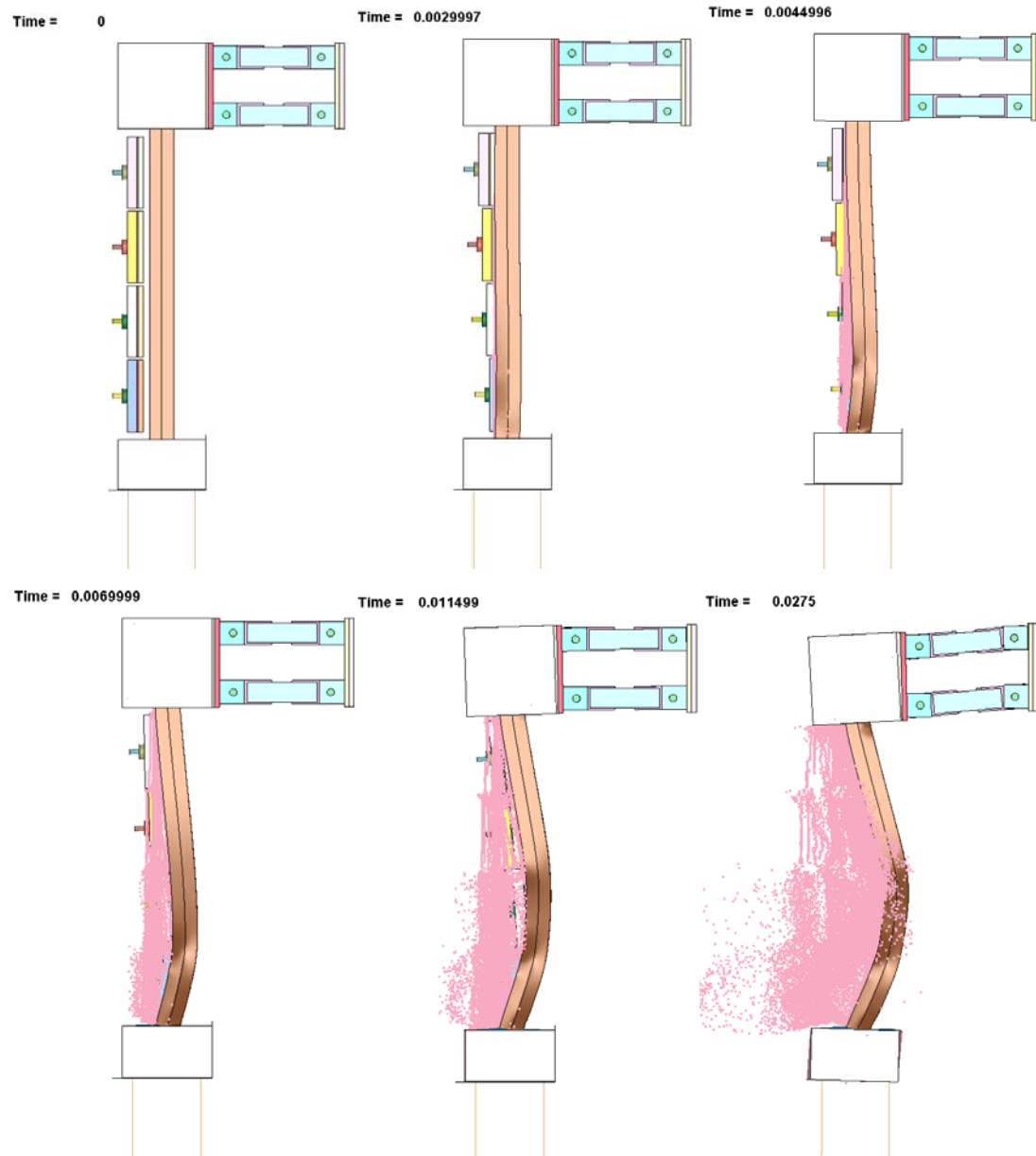
Figure 6.30: Test WA06 Finite Element Run Progression with 0.40% Failure Strain 1
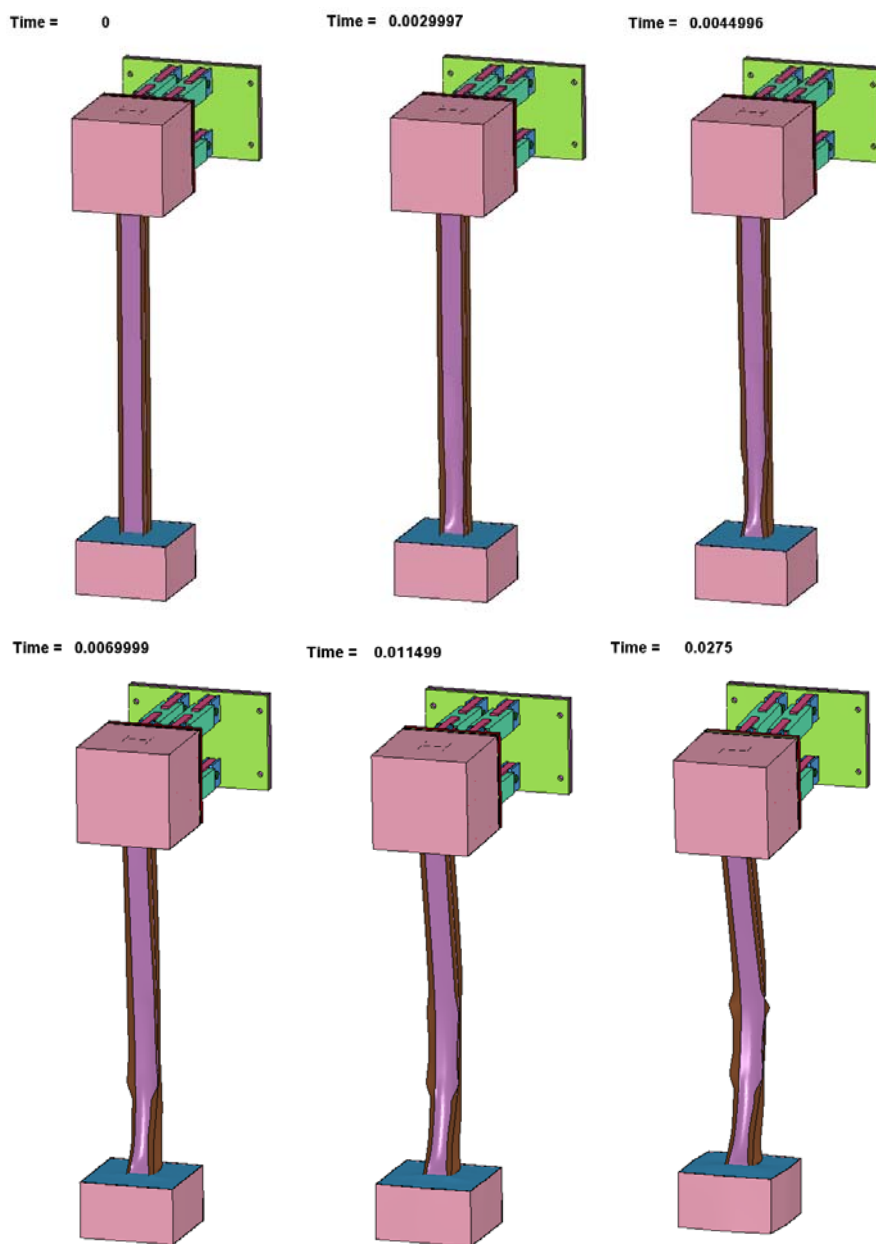
Figure 6.31: Test WA06 Finite Element Run Progression with 0.40% Failure Strain 2

Figure 6.32: Analysis with 0.40% Failure Strain (left) and WA05 (right) Comparison 1
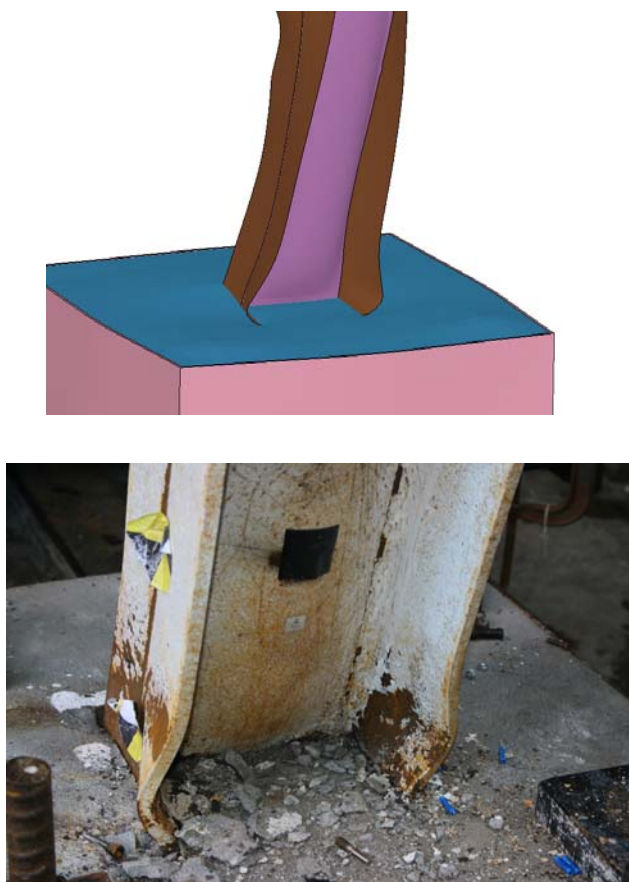
Figure 6.33: Analysis with 0.40% Failure Strain (top) and WA05 (bottom) Comparison 2

Research from Lehigh University [33] suggests that the ductility in the k-region of the column is considerably less than the surrounding steel due to the process used during the manufacturing of rolled shapes. This would indicate that the failure strain in that region would be less than the surrounding areas. The second analysis conducted on this column used a failure strain equal to 0.20% for the web and 0.40% for the flange. This would allow the web to fracture at a lower strain, but not the flanges. The results from this analysis are given in Figure 6.34. This run showed an initial fracture of the web along the k-region, with propagation along the sides. The bottom and top of the flange stay intact, and no flyer plate was created.
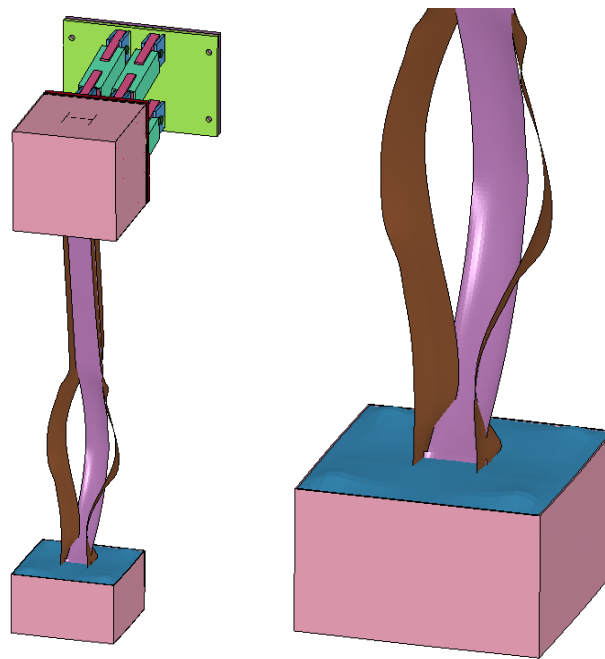
Figure 6.34: Finite Element Results from Test WA04 with 0.20 Failure Strain

The final attempt at analyzing the column included failure stain in the web at 0.18% percent. The results from this test are given in Figure 6.35. This model had failure along both sides of the web and along the bottom of the column. The top tearing was not

captured and this is thought to be because the programmer likely twisted as it broke off the rod, which caused an eccentric load to be applied to the web which the finite element model does not simulate.
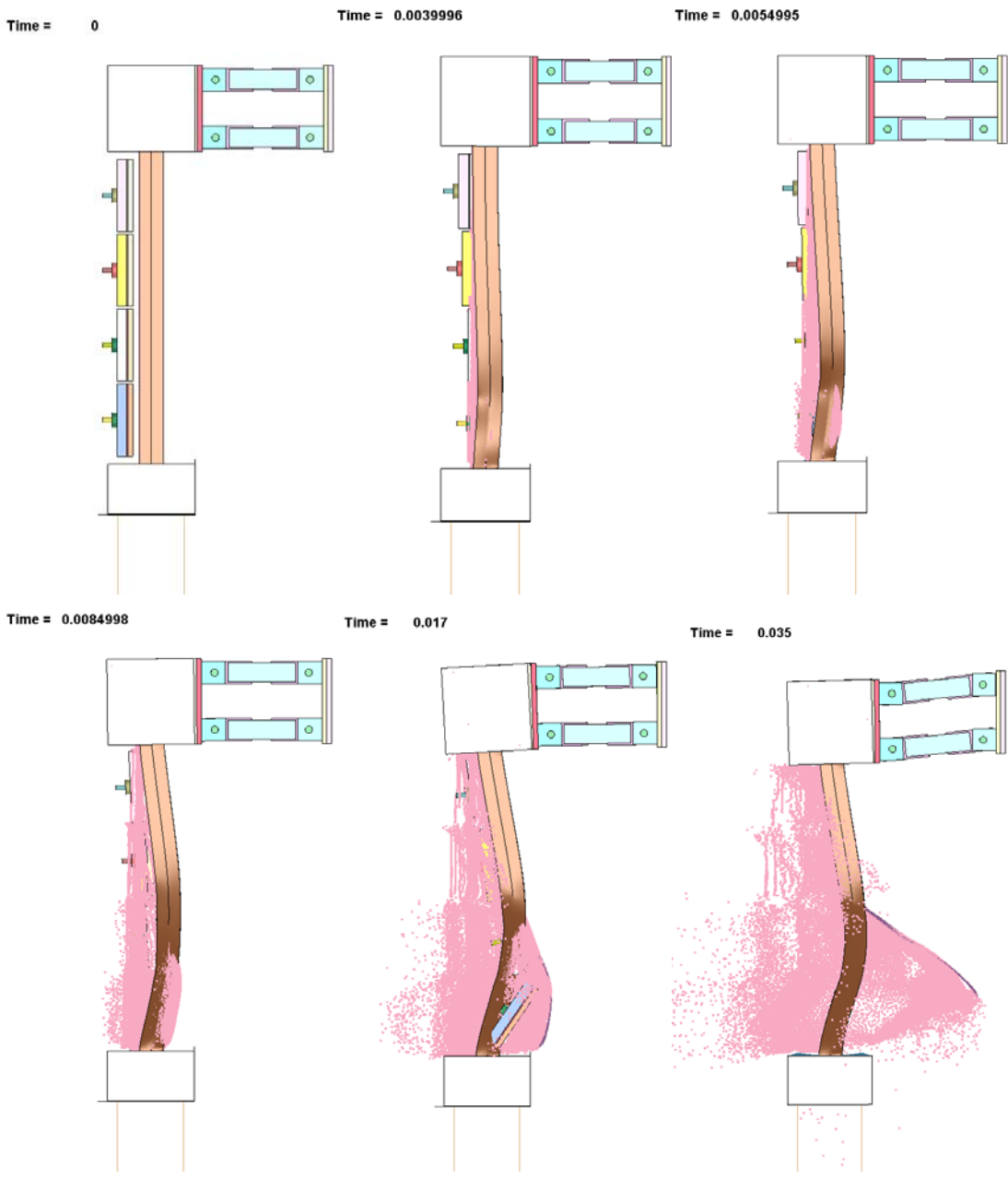
Figure 6.35: Finite Element Results from Test WA04 with 0.18% Failure Strain (side)
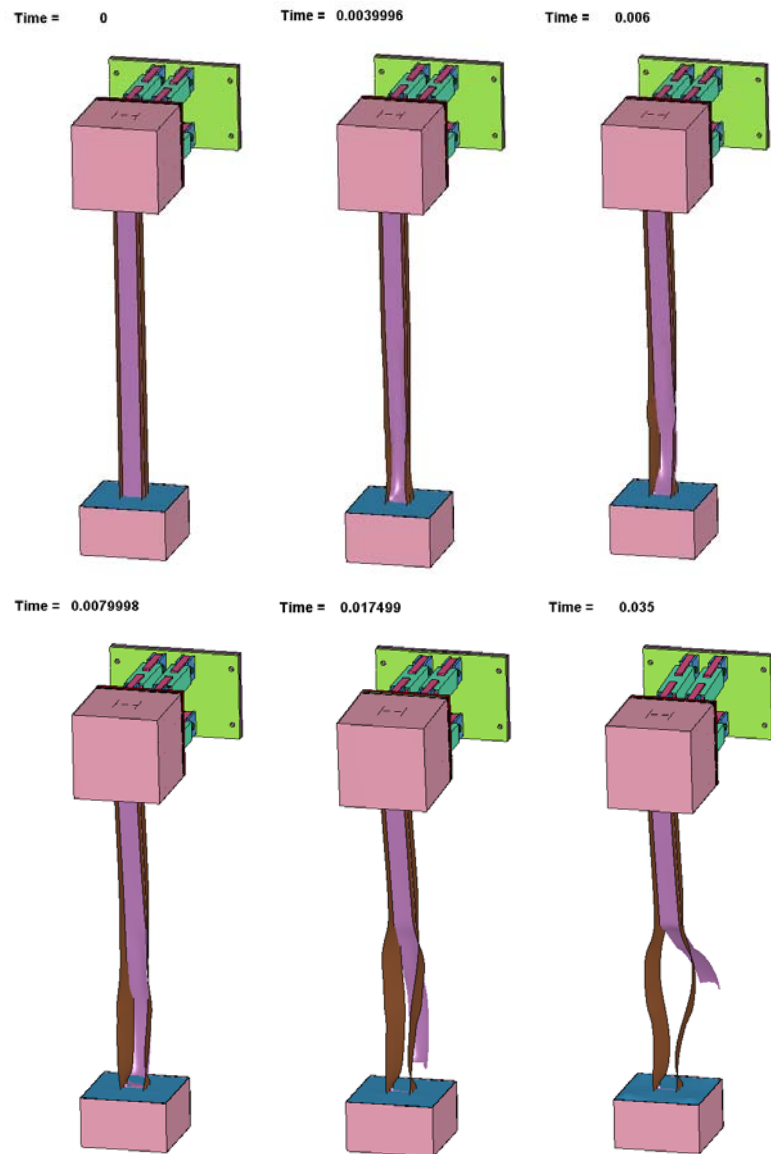
Figure 6.36: Finite Element Results from Test WA04 with 0.18% Failure Strain (front)

This failure strain was based upon a single data value from one test and was correlated to produce failure behavior that was seen for the given mesh size and model. While the model is capable of producing behaviors similar to those seen during Simulator and field tests, it is not adequately calibrated to predict fracture in other tests. Additional research is currently being conducted to validate models for predicting failure strains in the k-region and that research is discussed in Section 6.6.

Displacements of the column are given in Figure 6.37 for various times throughout the analysis with 0.18% strain to demonstrate the capabilities of generating overall behaviors for these types of experiments. Included in Figure 6.38 are visual comparisons from the finite element calculation and the experiment. In both cases, the web fractured along the k-region and continued up for about 36 to 50 in. Figure 6.39 gives a comparison of the column during the test in which the programmer and mass come off the rod and fly through the opening where the web fracture occurred.

Time = 0.00049995
Contours of X-displacement
min=-0.00116348, at node# 22591
max=0.00026989, at node# 18741

Time = 0.0014999
Contours of X-displacement
min=-0.00222206, at node# 22591
max=0.00336222, at node# 2253

Time = 0.0024998
Contours of X-displacement
min=-0.00645414, at node# 588
max=1.60639, at node# 2268

Time = 0.0054995
Contours of X-displacement
min=-0.0392551, at node# 36160
max=7.86257, at node# 2170

Time = 0.0125
Contours of X-displacement
min=-0.913996, at node# 2244
max=19.3528, at node# 8833

Time = 0.027
Contours of X-displacement
min=-0.989601, at node# 146067
max=46.8477, at node# 2248

Figure 6.37: Test WA06 Finite Element Displacements
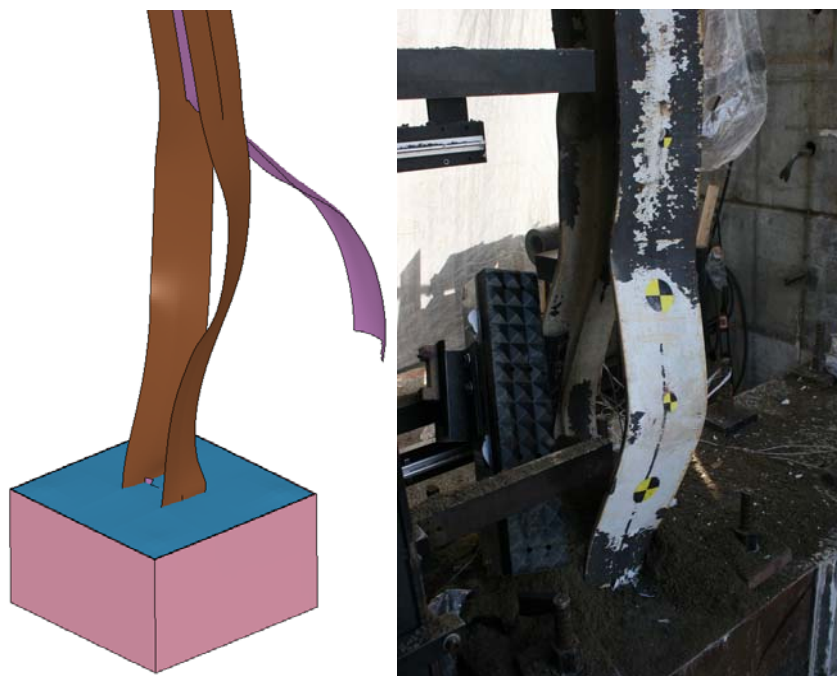
Figure 6.38: Test WA06 Visual Comparison 1

Programmer
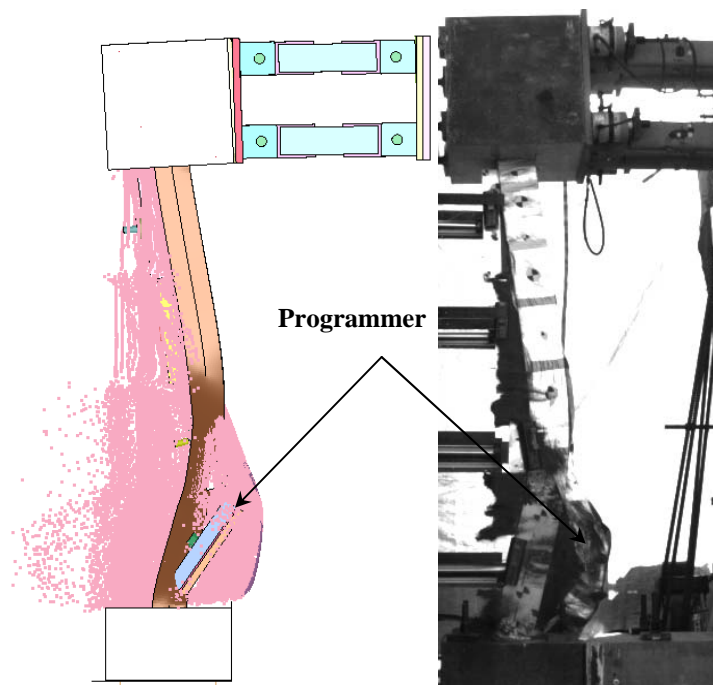
Figure 6.39: Test WA06 Visual Comparison 2

6.6   Future Research

Currently, research is being conducted using the UCSD Blast Simulator to develop a fracture model that can better predict failure in the k-region under loads with high strain rates. These tests include the use of a single programmer and 36 in section of W10x49 column as shown in the schematic in Figure 6.40. Figure 6.41 give photos from the side and Figure 6.42 from the top. The column section was placed upright and bolted to a large load plate with three load cells attached and impacted along the web with the programmer. Strain, accelerometer and camera data was collected during the tests.

To date, three tests have been conducted at three different velocities. These tests all produced failure in the k-region. The test at 25 m/s produced fracture in which the crack propagated along the height of the column, but did not completely fracture. A photo from this failure is given in Figure 6.43. Another test, at 20 m/s, caught the initiation of the crack development and is shown in Figure 6.44. It is hoped that the results from these tests, as well as future tests, will aid in the development of a material model that can better predict these types of failures.
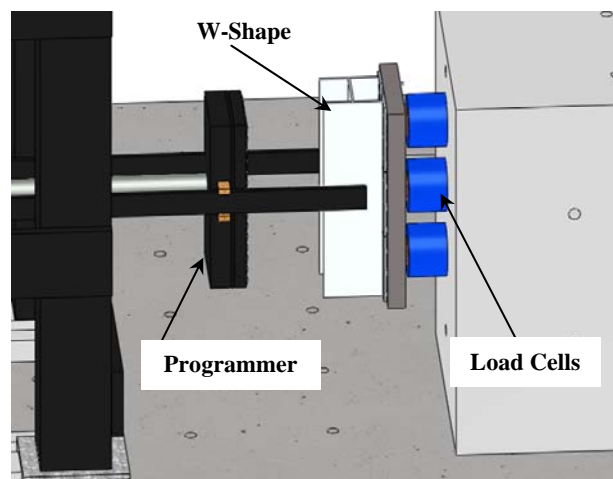
Figure 6.40: Schematic of Fracture Test Setup

Figure 6.41: Fracture Test Setup – Side View

Figure 6.42: Fracture Test Setup – Top View

Figure 6.43: Crack Propagation from 25 m/s Test

Figure 6.44: Crack Initiation from 20 m/s Test

6.7 Summary

This chapter described the development and validation of a finite element model for predicting column behavior when loaded by the UCSD Blast Simulator in the weak

axis direction. The steel columns were modeled using shell elements and used a piecewise linear isotropic model that incorporated strain rate effects. SPH elements were used to model the sand that was used as a loading medium because SPH particles can handle the large deformation and surface interactions that the sand exhibits.

The model was validated using the three sand tests discussed in Chapter 5 and it was found that the finite element analysis could accurately predict the global behavior of the column in all tests, but modeling fracture of the k-region proved to be problematic. The lack of data made it difficult to predict a failure strain that could be incorporated, with confidence, in future models. The chapter also provided a brief discussion on future testing being conducted with the goal of developing better material models for this type of failure.

The laboratory tests discussed in Chapter 5 were compared to the displacements of the finite element model and it was observed that the model did not produce errors for maximum displacements of over 12%.

7 Techniques for Steel Column Simulator Testing & Analysis

This chapter provides answers to key questions related to simulating blast loads on steel columns with the UCSD Blast Simulator in the form of finite element and shock physics hydrocode studies. These investigations include an analysis of the effects of BG synchronicity on the behavior of the specimen and the effect of BG mass and velocity as they pertain to momentum, energy and impulse. This chapter also addresses methods for applying explosive blast loads to finite element models which are used in Chapter 9 to apply loads to the fast running finite element models. Additionally, this chapter includes the development and outline of a loading protocol for testing steel columns.

7.1 Effects of BG Synchronicity on Steel Columns

7.1.1 Motivation

This section address concerns regarding the effect of the unsynchronized impact times of the BG masses on the specimen. Generally, up until now, the synchronicity of

292

the BGs was not an issue with most uniform velocity tests. This was due to fact that all BG25s utilized in the tests had uniformly designed valves. On average, all the BG25s impacted within 1 ms and this value was deemed "acceptable" for a uniform velocity test.

The addition of the BG50s created a need to investigate the effects of a non-synchronized impact which was observed in some of the experiments. In a variable velocity test, the BG50s and BG25s are fired with the control system that takes into account the standoff and start time. This process is initiated by the opening of poppet values in the accumulators. The design of the BG25s and BG50s do not utilize the same exact valve type and configuration and thus, the delay time to open the valve in each case can vary slightly. It was observed that the difference in valve delay can be as much as 3 ms.

Prior to each test, a "dry run" is conducted to get an estimate of the valve delays. This "dry run" is done by tuning the system and entering the blast profile with the appropriate input parameters, but not actually putting highly pressurized oil into the system. It is essentially a way to fire the valves and receive feedback data without firing the system and accelerating the impact module. The feedback of the pressure is used to try and estimate the time at which the valves actually open in comparison with the other BGs. This can prove problematic because there is typically not one point where the valve can be deemed open. Additionally, even if the valve delays were correctly estimated, the tuning on the actual tests needs to be conducted in the exact same manner as the "dry run". This is also difficult and can vary due to each operator and their tuning methods.

The difficulty in predicting the delay time has prompted the investigation into what spread of synchronicity should be deemed "acceptable" for variable velocity

impacts. This section also serves to provide insight into any generalizations that can be used to better predict and synchronize impacts.

7.1.2 Design of Investigation

This study utilizes the finite element model for the strong axis column described in Chapter 4. The strong axis finite element model was chosen because it is easier to predict impact and does not involve the use of a loading medium such as sand. For the study, the W10x49 column, shown in Figure 7.1, was selected because the displacements found for that size column were much more significant than those seen for the other size and therefore could produce greater differences in behavior if applicable.
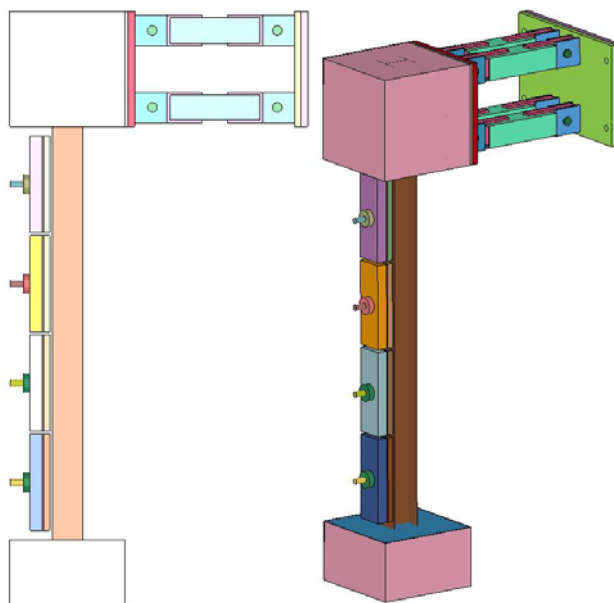
Figure 7.1: W10x49 Finite Element Specimen

Two loading scenarios were considered with different velocities shown in Table 7.1. Scenario 1 included velocities from a typical "low" velocity impact and the second scenario included velocities from a typical "high" velocity impact. In both cases, the

masses of the BGs are consistent with the experimental tests as discussed in Section 4.3.11. This section provides the results from Scenario 2. The results from Scenario 1 do not vary greatly from Scenario 2 and are given in Appendix A.

Table 7.1: BG Synchronicity Investigation Loading Velocities

BG	Loading Scenario 1 Velocities in/s (m/s)	Loading Scenario 2 Velocities in/s (m/s)
1	196.9 (5.0)	393.7 (10.0)
2	393.7 (10.0)	787.4 (20.0)
3	590.6 (15.0)	1181.1 (30.0)
4	787.4 (20.0)	1574.8 (40.0)

Two types of unsynchronized impacts were considered. The first type included tests where one BG impacts much later or earlier than the others as shown in Figure 7.2. In this case, BG 3 came in about 1ms earlier than the other three BGs.

The other unsynchronized impact type is much more common with the use of the BG50s and BG25s together. In this impact, the BG50s arrive together either both before or both after the BG25s impact. An example of this impact type is shown in Figure 7.3.

Twenty-five cases were considered for each of the loading scenarios. Four different delay times were considered, 1 ms, 3 ms, 5 ms, and 7 ms. 7 ms was chosen because that just exceeded the greatest spread of distance witnessed during an experimental test. Table 7.1 gives a summary of the finite element runs conducted.

It is important to point out that if the impacting masses, rods, velocities or periods of the structure are changed dramatically, the effects of impact arrival delay and these conclusions would likely change.
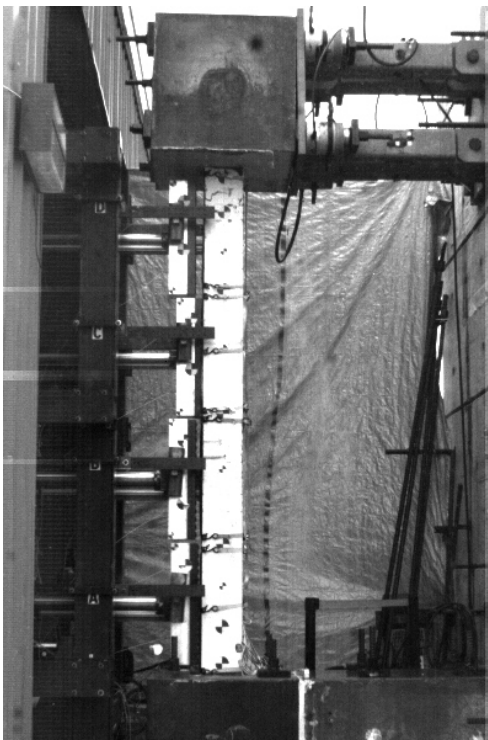
Figure 7.2: Unsynchronized Impact 1: One BG Late
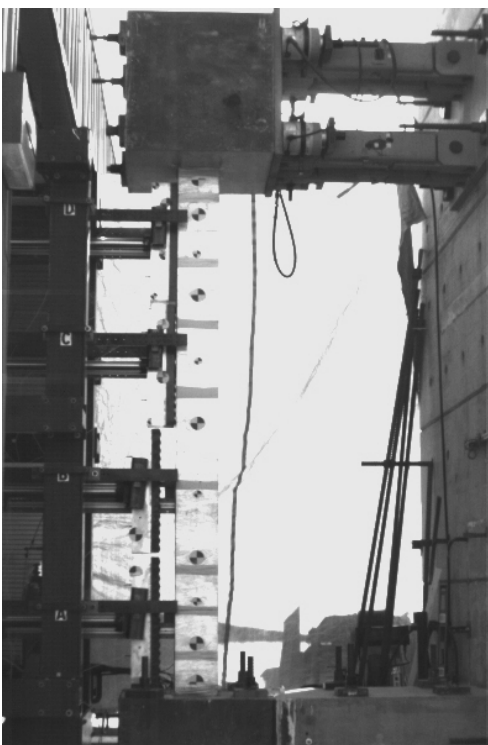
Figure 7.3: Unsynchronized Impact 1: Two BGs Late

Table 7.2: BG Synchronicity Study Test Matrix

Test #	BG Impact Description	BG1 Impact Time (ms)	BG2 Impact Time (ms)	BG3 Impact Time (ms)	BG4 Impact Time (ms)
1	BGs Synchronized	0	0	0	0
2	BG1 Late	1	0	0	0
3	BG2 Late	0	1	0	0
4	BG3 Late	0	0	1	0
5	BG4 Late	0	0	0	1
6	BG1 Late	3	0	0	0
7	BG2 Late	0	3	0	0
8	BG3 Late	0	0	3	0
9	BG4 Late	0	0	0	3
10	BG1 Late	5	0	0	0
11	BG2 Late	0	5	0	0
12	BG3 Late	0	0	5	0
13	BG4 Late	0	0	0	5
14	BG1 Late	7	0	0	0
15	BG2 Late	0	7	0	0
16	BG3 Late	0	0	7	0
17	BG4 Late	0	0	0	7
18	BG1 and BG2 Late	1	1	0	0
19	BG1 and BG2 Late	3	3	0	0
20	BG1 and BG2 Late	5	5	0	0
21	BG1 and BG2 Late	7	7	0	0
22	BG 3 and BG 4 Late	0	0	1	1
23	BG 3 and BG 4 Late	0	0	3	3
24	BG 3 and BG 4 Late	0	0	5	5
25	BG 3 and BG 4 Late	0	0	7	7

7.1.3 Investigation Results

The initial set of comparisons describes the situation in which a single BG arrives late by various times. Table 7.3 gives a summary of the maximum and residual displacements from the tests with one BG each 1 ms late. Plots of the maximum and residual displacements along the height of the column are given in Figure 7.4 and Figure 7.5.

From the plots, it can be seen that the global behavior along the height of the column is consistent for each of the five tests. The maximum error was found to be 4.40%. It was also observed that the late arrival of the BG50s introduces the greatest difference in column behavior which is due to its larger mass and velocity. The time histories of the columns displacements are given in Appendix C and additional differences are evident in these histories as well.

Table 7.4 gives a summary of the maximum and maximum residual displacements from the columns from the tests with a single BG each 3 ms late. Plots of the maximum and residual displacements along the height of the column are given in Table 7.10 and Table 7.11.

From these plots, it can be seen that the general behavior along the height of the column is consistent and the maximum error was found to be 8.97% for the maximum and 9.89 % for the residual displacement, which is more than the errors seen in the 1 ms range. It was observed that the BG1 and BG2 arriving late introduce the greatest difference in column behavior, with BG 4 introducing the least for both the maximum and residual displacements.

A summary of the maximum and maximum residual displacements of the column from the tests with a single BG each 5 ms late is given in Table 7.5. Plots of the maximum displacements along the height of the column are given in Figure 7.8. Figure 7.9 gives the residual displacements along the height of the column.

From these plots, it can again be seen that the general behavior along the height of the column is consistent and the maximum error was found to be 12.85% for the maximum and 13.55% for the residual, which is again more than the errors seen in the 1 ms and the 3 ms range. It was again observed that the BG1 or BG 2 being late introduces the greatest difference in column behavior, with BG 3 and BG 4 introducing the least for both the maximum and residual displacements.

The last comparison in this series is given in Figure 7.6 with a summary of the maximum and maximum residual displacements from the columns from the tests with a single BG each 7 ms late. Plots of the maximum displacements along the height of the column are given in Figure 7.10 and Figure 7.11 gives the residual displacements along the height of the column.

From these plots, it can again be seen that the general behavior along the height of the column is consistent and the maximum error was found to be 19.79% for the maximum and 21.61% for the residual displacement. These values are again more than the errors seen in the 1 ms, 3 ms range, or 5 ms range. It was also again observed that the BG1 or BG 2 being late introduces the greatest difference in column behavior, with BG 3 and BG 4 introducing the least for both the maximum and residual displacements.

Table 7.3: Displacement Comparison for a Single BG 1 ms Late

Test #	Test Description	Maximum Displacement (in)	Maximum Displacement Error (%)	Residual Displacement (in)	Residual Displacement Error (%)
1	BGs Synchronized	5.91		5.46	
2	BG1 1 ms Late	5.76	2.53%	5.22	4.40%
3	BG2 1 ms Late	6.10	3.21%	5.62	2.93%
4	BG3 1 ms Late	5.85	1.02%	5.50	0.73%
5	BG4 1 ms Late	5.99	1.35%	5.50	0.73%

Table 7.4: Displacement Comparison for a Single BG 3 ms Late

Test #	Test Description	Maximum Displacement (in)	Maximum Displacement Error (%)	Residual Displacement (in)	Residual Displacement Error (%)
1	BGs Synchronized	5.91		5.46	
2	BG1 3 ms Late	5.38	8.97%	4.94	9.52%
3	BG2 3 ms Late	5.39	8.79%	4.92	9.89%
4	BG3 3 ms Late	5.60	5.25%	5.10	6.59%
5	BG4 3 ms Late	5.96	0.84%	5.52	0.73%

Table 7.5: Displacement Comparison for a Single BG 5 ms Late

Test #	Test Description	Maximum Displacement (in)	Maximum Displacement Error (%)	Residual Displacement (in)	Residual Displacement Error (%)
1	BGs Synchronized	5.91		5.46	
2	BG1 5 ms Late	5.15	12.85%	4.72	13.55%
3	BG2 5 ms Late	5.16	12.69%	4.60	15.75%
4	BG3 5 ms Late	5.53	6.43%	5.05	7.51%
5	BG4 5 ms Late	5.98	1.18%	5.49	0.59%

Table 7.6: Displacement Comparison for a Single BG 7 ms Late

Test #	Test Description	Maximum Displacement (in)	Maximum Displacement Error (%)	Residual Displacement (in)	Residual Displacement Error (%)
1	BGs Synchronized	5.91		5.46	
2	BG1 7 ms Late	4.74	19.79%	4.28	21.61%
3	BG2 7 ms Late	5.10	13.71%	4.56	16.48%
4	BG3 7 ms Late	5.61	5.08%	5.24	4.03%
5	BG4 7 ms Late	5.86	0.85%	5.41	0.92%
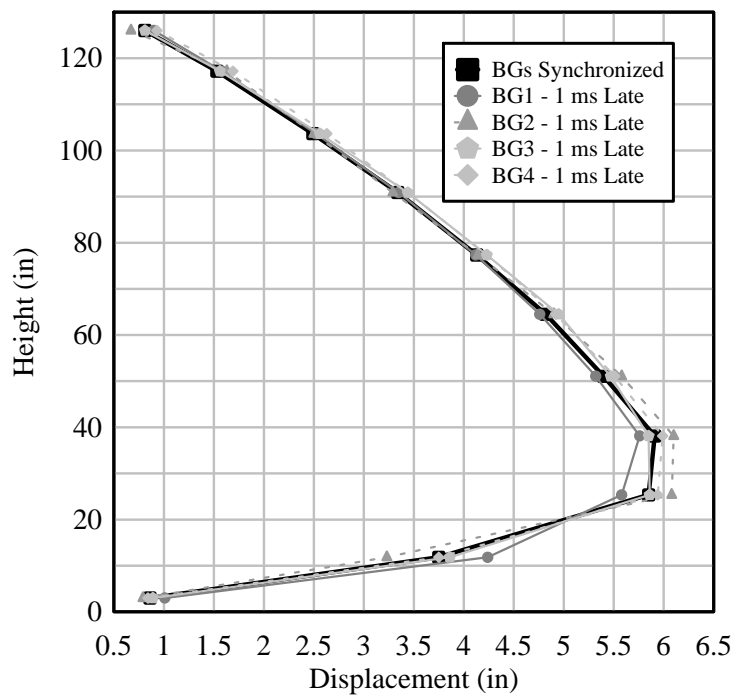
Figure 7.4: Maximum Displacements of Single BG, 1 ms Late
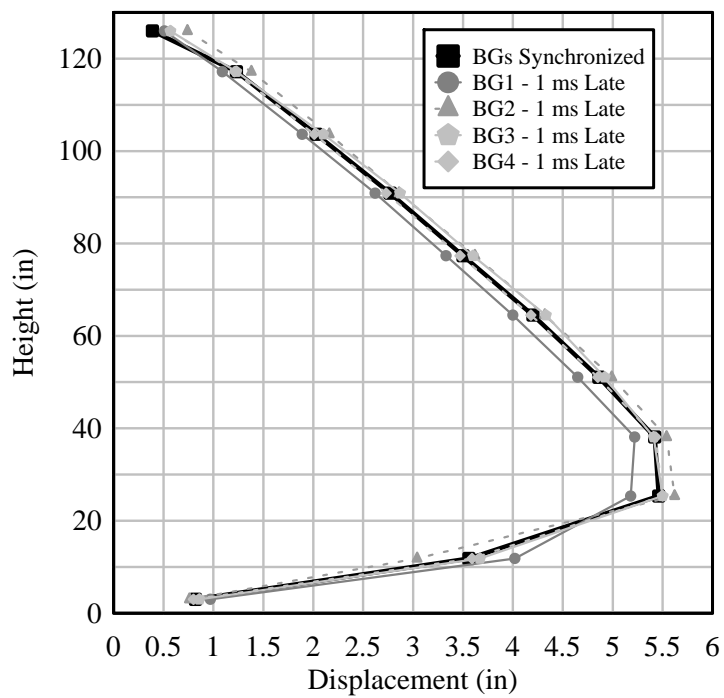
Figure 7.5: Residual Displacements of Single BG, 1 ms Late
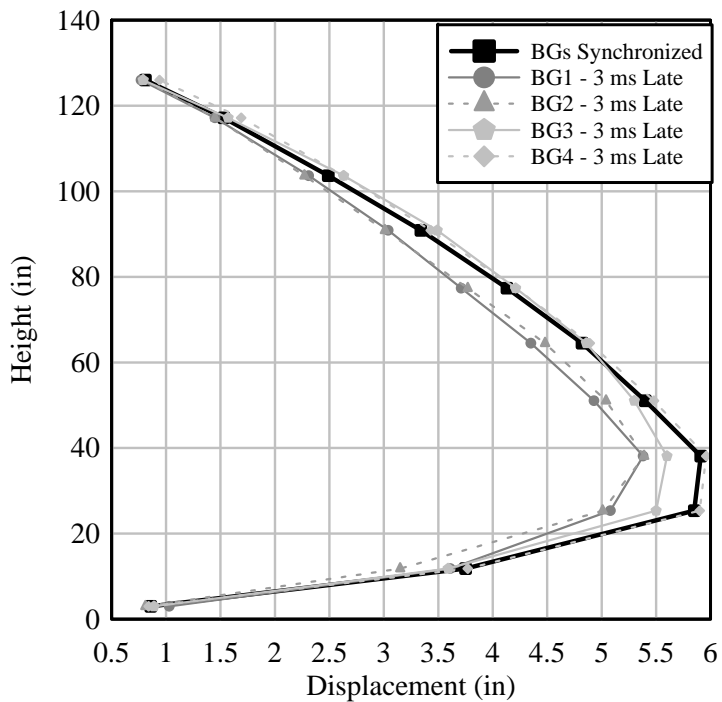
Figure 7.6: Maximum Displacements of Single BG, 3 ms Late
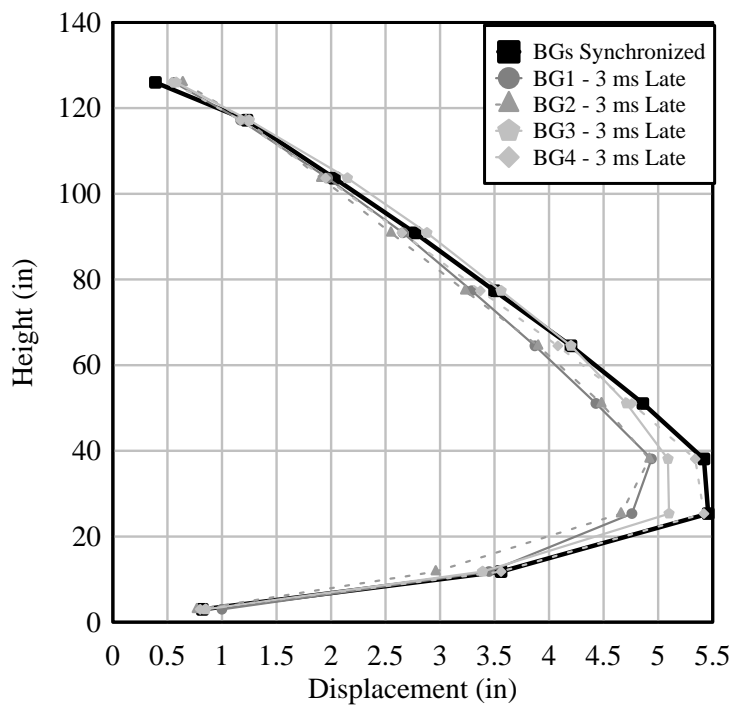
Figure 7.7: Residual Displacements of Single BG, 3 ms Late
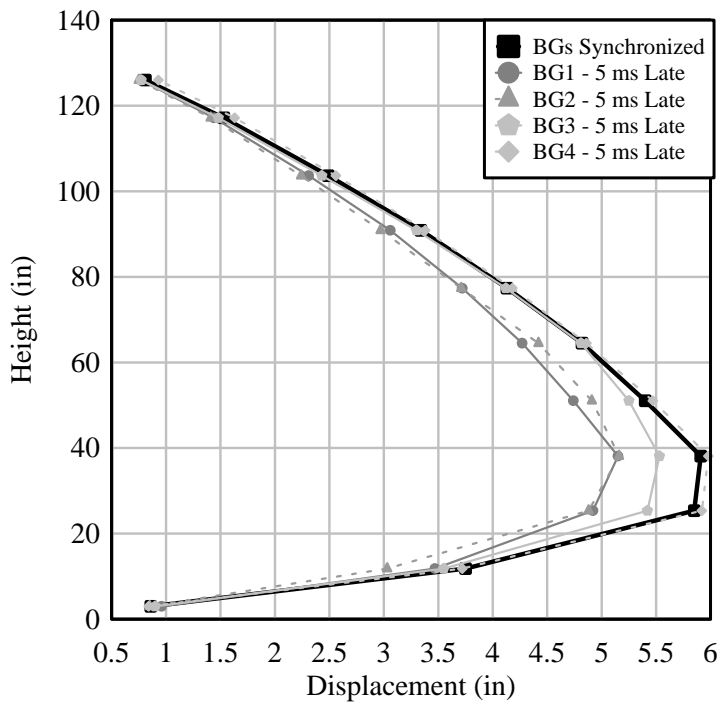
Figure 7.8: Maximum Displacements of Single BG, 5 ms Late
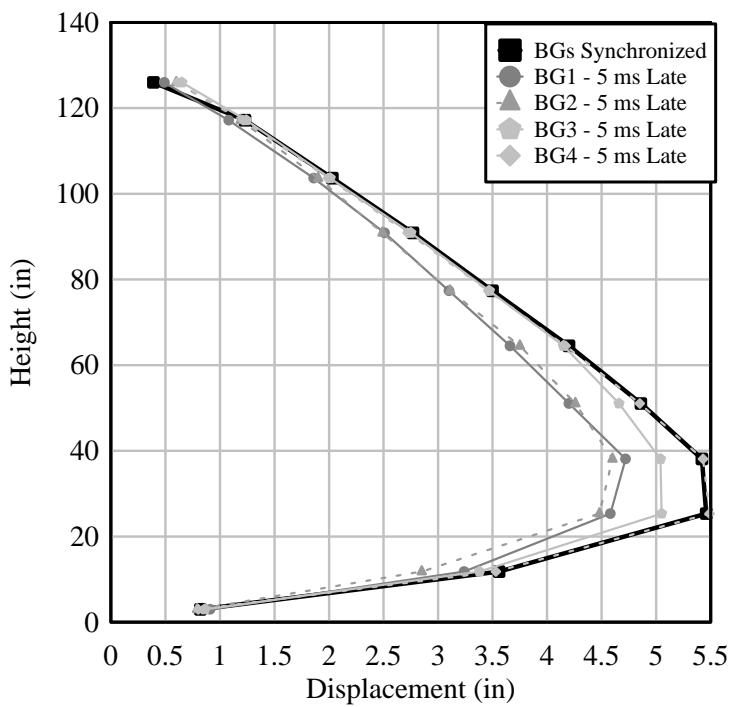
Figure 7.9: Residual Displacements of Single BG, 5 ms Late
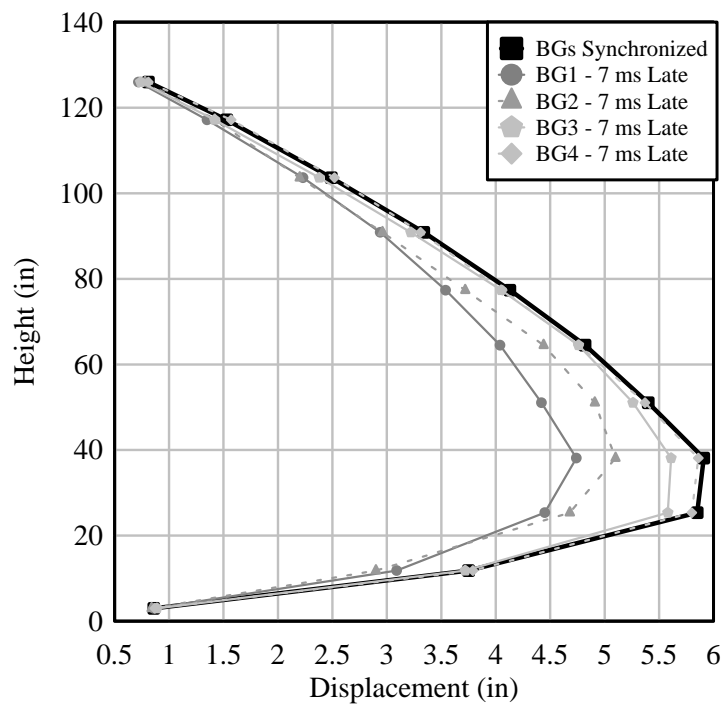
Figure 7.10: Maximum Displacements of Single BG, 7 ms Late
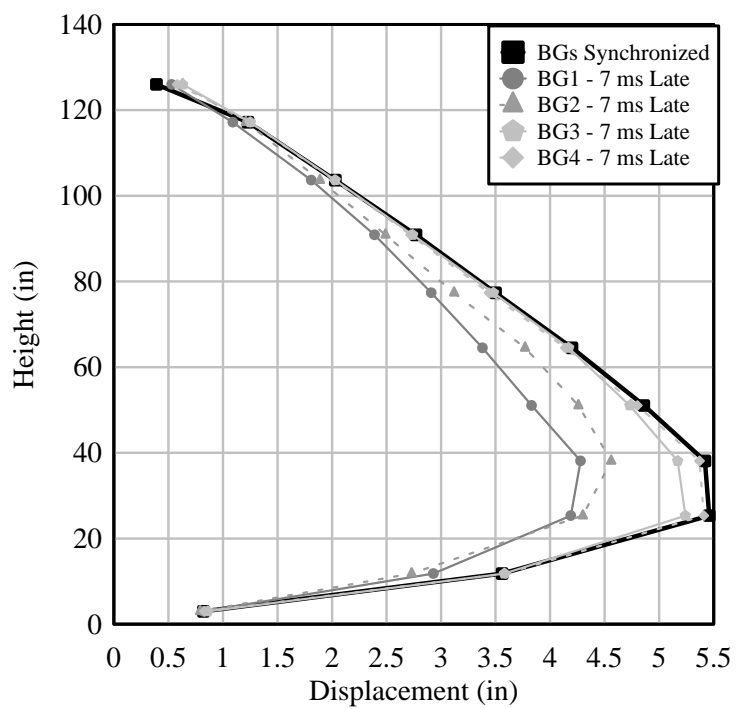
Figure 7.11: Residual Displacements of Single BG, 7 ms Late

The second set of comparisons dealt with the situation where two BGs impact late together, which is a typical occurrence due to the non-uniform valves in the system. Table 7.8 gives a summary of the maximum displacements when the BG50s (BGs 1 & 2) arrive late. The maximum and residual displacements all had errors well under 10.0% for all of the delay times.

Plots of the maximum displacements along the height of the column are given in Figure 7.12. Figure 7.13 gives the residual displacements along the height of the column. In this case, the time delay does contribute to additional error but not as significantly in the case where a single BG arrived late.

The last situation that was considered was when two BG25s impact late together. Table 7.7 gives a summary of the maximum displacements when the BG25s (BGs 3 & 4) arrive late. Plots of the maximum displacements along the height of the column are given in Figure 7.14. Figure 7.15 gives the residual displacements along the height of the column. In this case, all displacements were within 10% of the synchronized impact. There was not a significant difference between the BG25s arriving late or the BG50s arriving late.

Table 7.7: Displacement Comparison for BG 50s Arriving Late

Test #	Test Description	Maximum Displacement (in)	Maximum Displacement Error (%)	Residual Displacement (in)	Residual Displacement Error (%)
1	BGs Synchronized	5.91		5.46	
2	BG1 & BG2 1 ms Late	6.29	6.42%	5.88	7.69%
3	BG1 & BG2 3 ms Late	6.05	2.35%	5.74	5.13%
4	BG1 & BG2 5 ms Late	5.52	6.26%	5.21	4.56%
5	BG1 & BG2 7 ms Late	5.41	8.46%	5.03	8.43%

Table 7.8: Displacement Comparison for BG 25s Arriving Late

Test #	Test Description	Maximum Displacement (in)	Maximum Displacement Error (%)	Residual Displacement (in)	Residual Displacement Error (%)
1	BGs Synchronized	5.91		5.46	
2	BG3 & BG4 1 ms Late	5.88	0.51%	5.41	0.92%
3	BG3 & BG4 3 ms Late	5.59	5.42%	5.05	7.51%
4	BG3 & BG4 5 ms Late	5.51	6.77%	4.98	8.79%
5	BG3 & BG4 7 ms Late	5.56	5.92%	5.06	7.33%
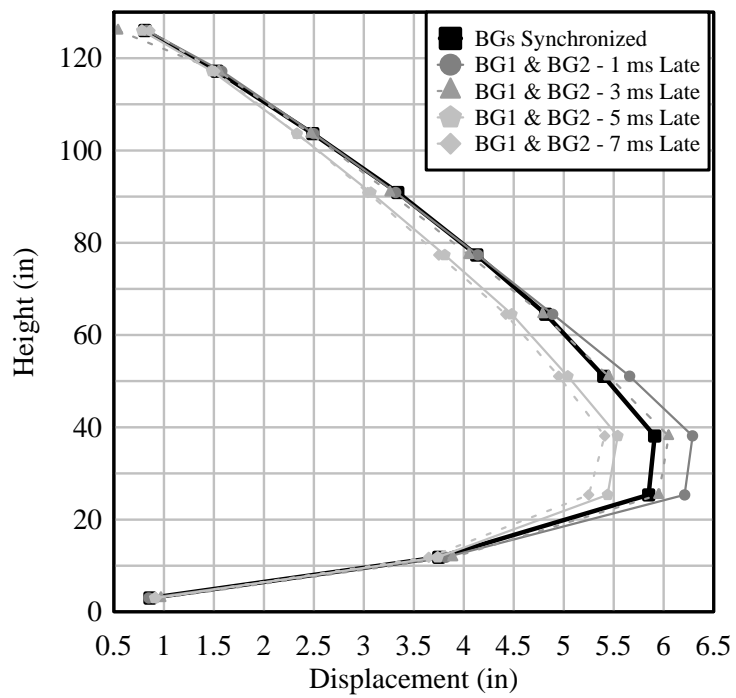
Figure 7.12: Maximum Displacements of BG50s Arriving Late
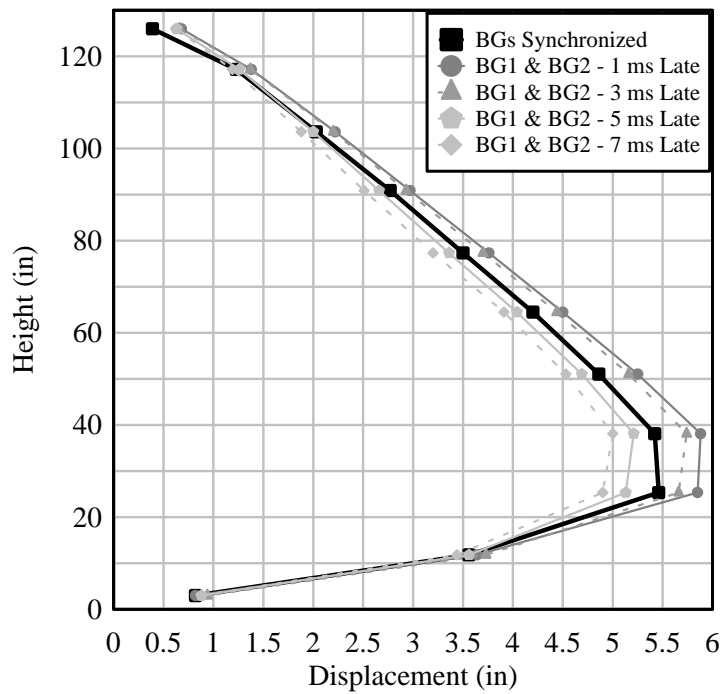
Figure 7.13: Residual Displacements of BG50s Arriving Late
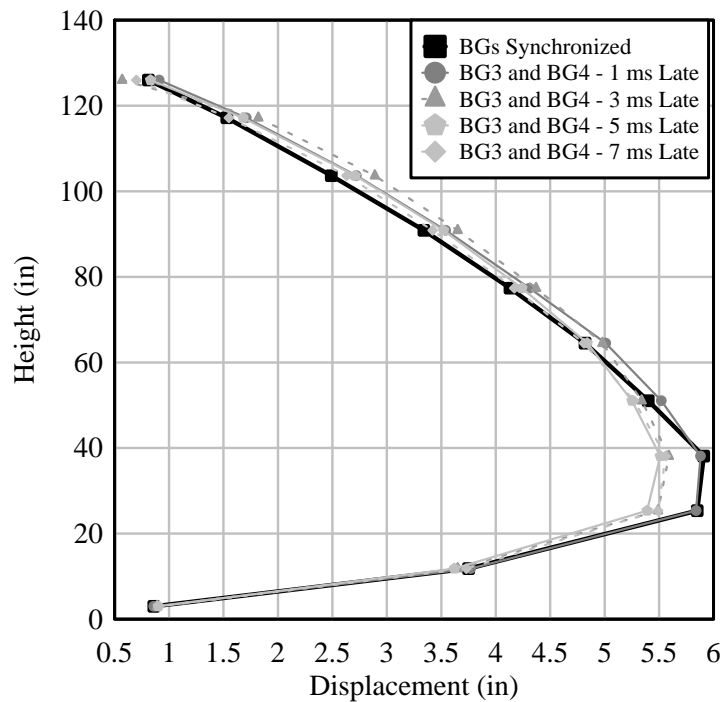
Figure 7.14: Maximum Displacements of BG25s Arriving Late
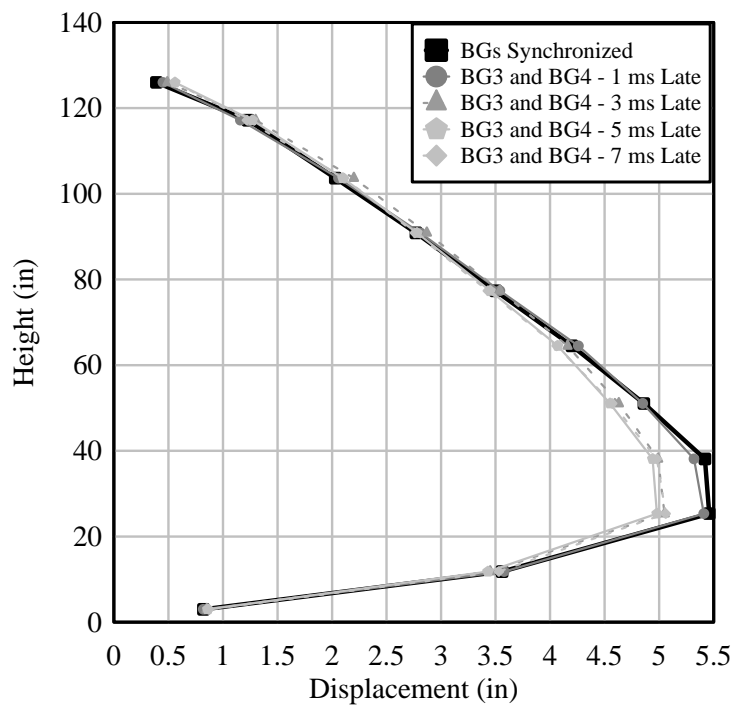
Figure 7.15: Residual Displacements of BG50s Arriving Late

7.1.4 Investigation Conclusions

This investigation used a 10.0% range of error as being an "acceptable" test. This error was chosen based on the relative errors in other areas of the system, such as video tracking and initial point measurement error. Using this range and a similar loading scenario for the column along the height the following conclusions can be drawn:

- For any realistic impact scenario, if the arrival delay time is within 3 ms, it will not contribute greatly to error in the behavior of the column.

- A synchronized impact of the two BG25s and the two BG50s separately does not greatly affect the column response, for impact delays up to 7 ms.

- In a single delayed BG25 impact, there is not a substantial amount of difference in column behavior, regardless of the amount of relevant impact delay.

- Single delayed impacts of the BG50s with arrival times of more than 3 ms late could produce errors of more than 10.0% from a synchronized impact and it is recommended that these delays be incorporated into any modeling or conclusions.

The fact that the synchronicity has little effect on the structure is likely due to the fact that the periods of the specimens are in the range of around 1 s, which is much larger when compared with the impulsive loading time regime is much larger. The structure does not have time to react to any differences in the loading unless they are coupled with very large masses or velocities such as those on the higher velocity hits for the BG50s.

7.2   Effects of BG Mass & Velocity on Impulse and Column Behavior

7.2.1 Motivation

This section investigates the effect of mass and velocity on impulse and the behavior of the specimen. Often during the initial phase of the test design, it is important to consider what target impulse placed on the column is desired and what masses and velocities should be used to achieve that specific impulse. Additionally, during the testing process, it is often necessary to increase or decrease the impulse applied to the next specimen. This can be done in one of two ways: varying the impacting mass and/or varying the impact velocity. Varying these two parameters changes both the momentum (mv) and the kinetic energy (mv^2) of the mass. If the column behavior is more governed by momentum then more likely the mass should be varied; however, if the column behavior is governed by the kinetic energy of the mass, then the relative change in velocity would have a greater impact on the behavior of the column.

7.2.2 Design of Investigation

This experiment again utilized the finite element model from Chapter 4. In this case, both the W10x49 and the W14x132 (Figure 7.16) columns were used, however only the W14x132 column results are given in this section. The results from the W10x49 column, as well as other results, were similar to those presented in this section. In this case, the link system was removed for two main reasons and replaced with just a vertical translational only boundary condition. The first reason was the link system involves many moving parts, and, therefore, contact surfaces and rubber rotation pad. Both of these add to energy losses in the system and an effort was made to remove parts that

contribute to energy losses that could not be fully accounted for. Also, the removal of the link adds to a large decrease in run time for these simulations.
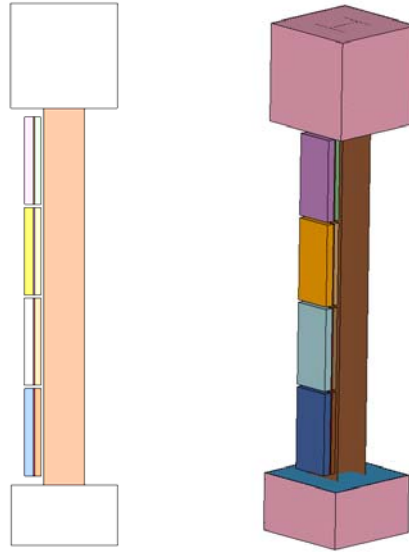
Figure 7.16: W14x132 Finite Element Specimen

Two impacting masses were considered for the initial comparison of each column. The masses were determined using a percentage of the mass of the specimen and that was distributed over each of the four BGs. The mass percentages chosen were 100% and 200% of the specimen mass, which are similar to the experiments. An initial velocity for the 100% mass and 200 % was chosen as a midrange velocity at1181.1 in/s (30 m/s).

This study consisted of two phases. The first phase looked at the effects of momentum transfer and the second phase observed the effects of kinetic energy transfer on the behavior of the column. The first phase test matrix is given in Table 7.9. The momentum of the control case (Run 1 or Run 2) with mass of either 100% or 200% was used to calculate the velocity for masses of 50% and 150% so that momentum in both cases was equal. The second phase consisted of the same set of masses and initial

velocities, but the kinetic energies were equated. A list of those tests is given in Table 7.10.

Table 7.9: Momentum Effects Test Matrix

Run Name	Mass (% of Column)	Mass lb (kg)	Velocity in/s (m/s)	Momentum (kg-m/s)
1	100	354.8 (160.9)	1181.1 (30)	4827.0
mv (1a)	50	177.4 (80.4)	2362.2 (60.0)	4827.0
mv (1b)	150	532.1 (241.4)	787.4 (20.0)	4827.0
2	200	709.6 (321.8)	1181.1 (30)	9654.0
mv (2a)	275	975.7 (442.6)	858.3 (21.8)	9654.0
mv (2b)	125	443.4 (201.1)	1889.8 (48.0)	9654.0

Table 7.10: Kinetic Energy Effects Test Matrix

Run Name	Mass (% of Column)	Mass lb (kg)	Velocity in/s (m/s)	Kinetic Energy (Joule)
1	100	354.8 (160.9)	1181.1 (30.0)	72405
$1/2mv^2$ (1a)	50	177.4 (80.4)	1661.4 (42.4)	72405
$1/2mv^2$ (1b)	150	532.1 (241.4)	964.6 (24.5)	72405
2	200	709.6 (321.8)	1181.1 (30)	144810
$1/2mv^2$ (2a)	275	975.7 (442.6)	1007.9 (25.6)	144810
$1/2mv^2$ (2b)	125	443.4 (201.1)	1492.1 (37.9)	144810

7.2.3 Investigation Results

The results from the 4 similar cases are plotted in Figure 7.17. Equating momentum, depending on the ratio of the mass and velocity, produces a smaller or larger impulse, and therefore displacement, on the column, while equating kinetic energy produced the other extreme of the impulse applied to the column. Because of this, a third case was considered and the results are shown in Figure 7.18. In this case, Equation (7.1) was implemented to see if it would be better at predicting the response of the column.

$$m_1 v_1^{1.5} = m_2 v_2^{1.5} \qquad (7.1)$$
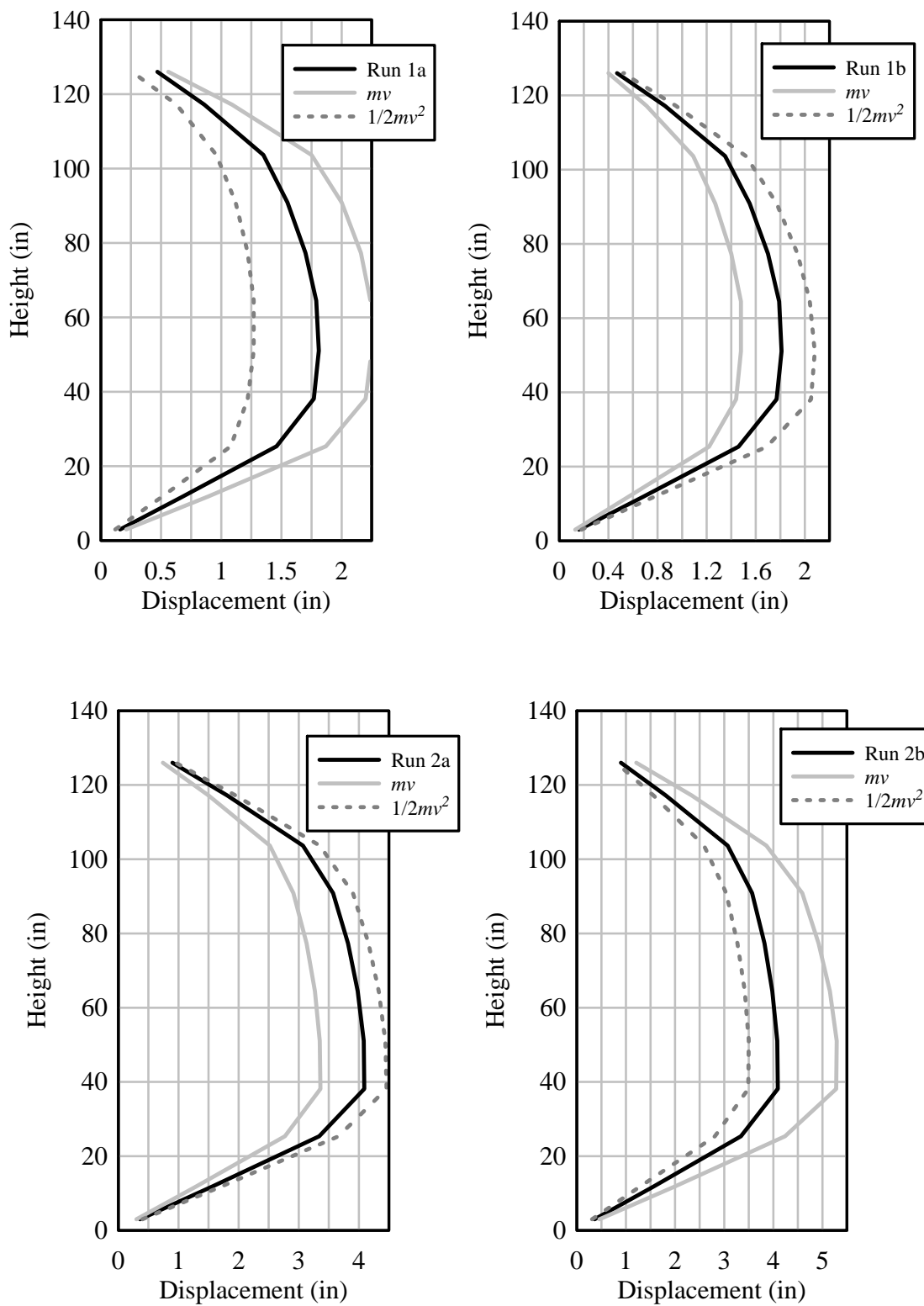
Figure 7.17:Comparisons of Runs with Equated Momentum & Kinetic Energy
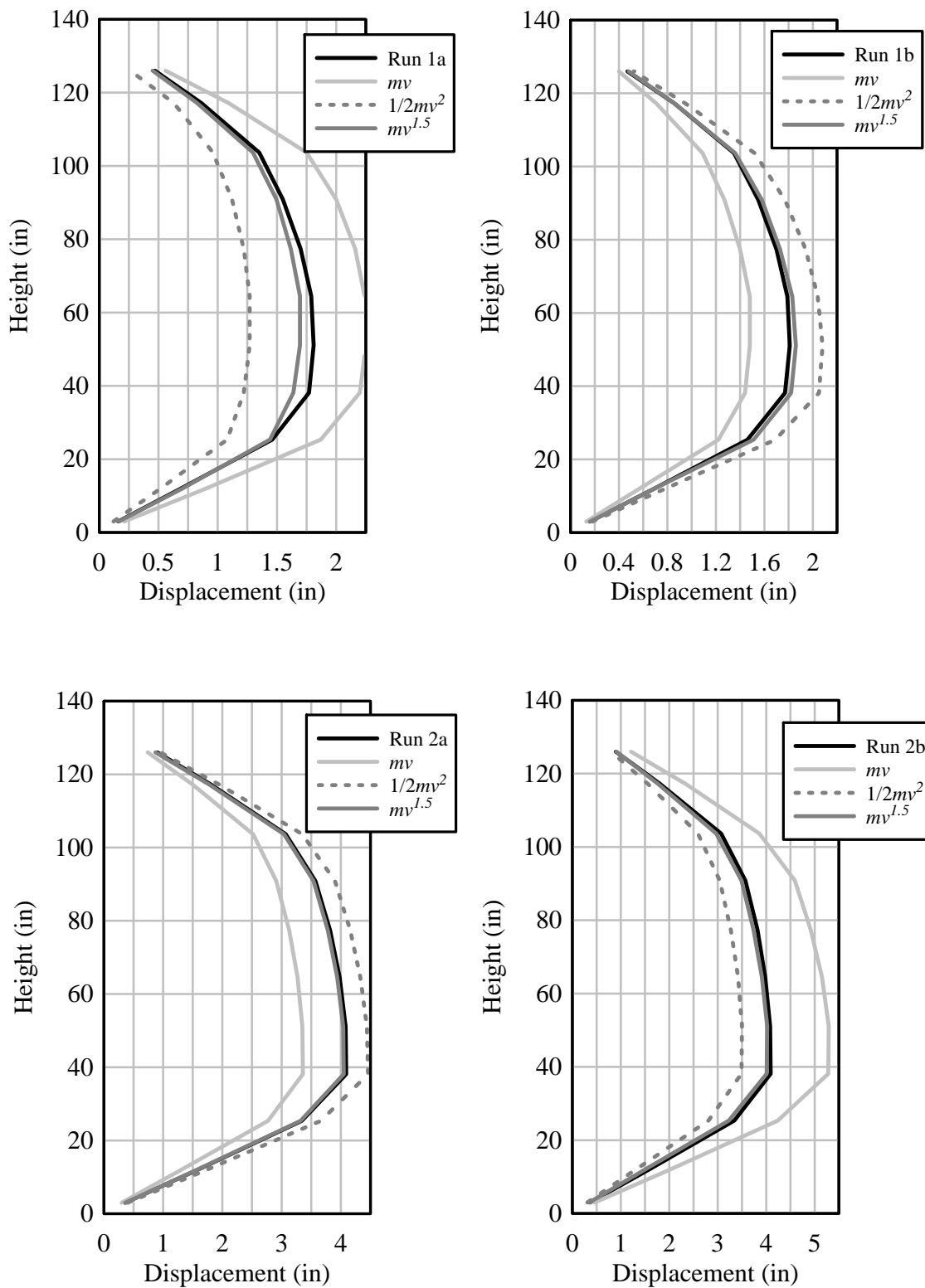
Figure 7.18: Comparisons of Runs with Equated Momentum, Kinetic Energy and $mv^{1.5}$

7.2.4 Investigation Conclusions

This investigation found that neither equating momentum nor kinetic energy for tests with different masses produced the same load and behavior of the column. An alternative approach was considered in which $mv^{1.5}$ was equated for both tests. Although this has no physical basis, it does seem to work phemonologically for accounting for the energy and momentum losses for a wide range of columns, masses and velocities.

7.3 Blast Loads Applied to Strong Axis Steel Column Models

7.3.1 Motivation

This section describes the development of the procedure for applying blast loads to steel columns in the strong axis direction. As discussed in Chapter 2, when a vehicle bomb detonates close to the ground, the wave creates a Mach front which hits the column face. As discussed in Chapter 2, these loads are not easily predicted by commonly used graphical methods and advanced analysis tools are often needed to predict pressure and impulses on the column.

Once the pressure-time histories on the column are known, they must be converted to a procedure that can be applied on finite element models. Using a code that does a coupling of these two types of Eulerian and Lagrangian analysis is an option, but they are often time consuming. One of the goals of this dissertation is to develop a fast running model with only a Lagrangian analysis, therefore a method must be developed that accurately and efficiently applies the correct loads onto the column.

7.3.2 CTH and BLASTX Comparison

To best predict the explosive loads on the column, CTH [23] and BLASTX [34] were both used to model a spherical charge of a given size similar to that of a vehicle bomb. The plane was modeled using just a reflecting surface shown in Figure 7.19 with half symmetry and, therefore, the initial comparison did not take into account clearing effects. Tracers were placed as shown in Figure 7.20 with a finer mesh at the base of the wall and they recorded pressure history data.
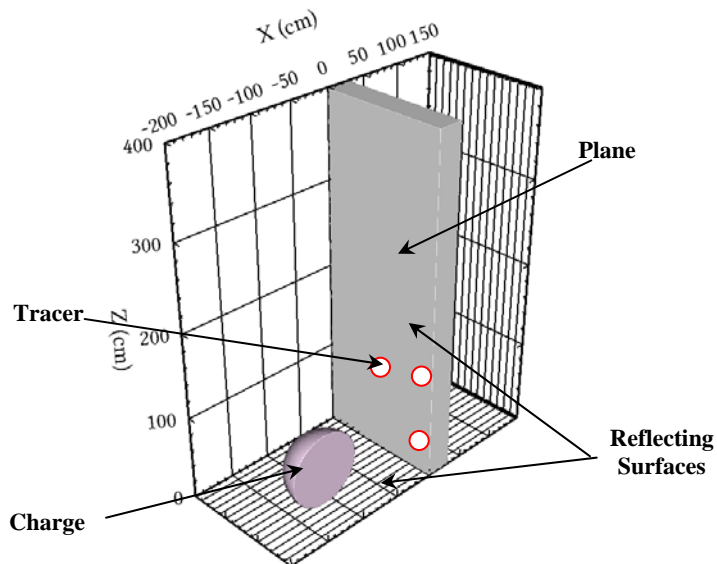
Figure 7.19: CTH Model for Spherical Charge on Strong Axis

An example of the pressure-contours on the wall at 1 ms is shown in Figure 7.21 with pressure-time history data for three locations compared in Figure 7.22, Figure 7.23 and Figure 7.24.
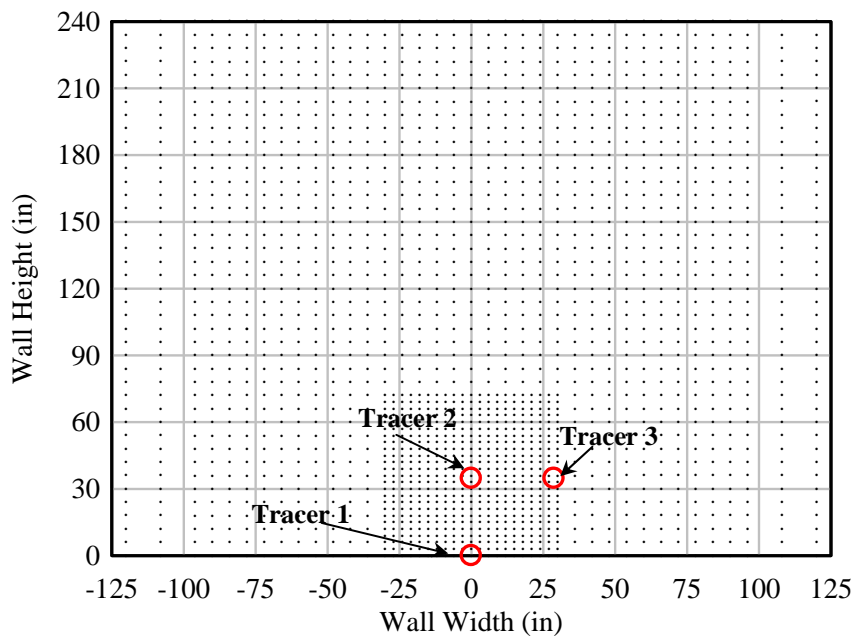
Figure 7.20: Tracer Locations for CTH and BLASTX Comparison
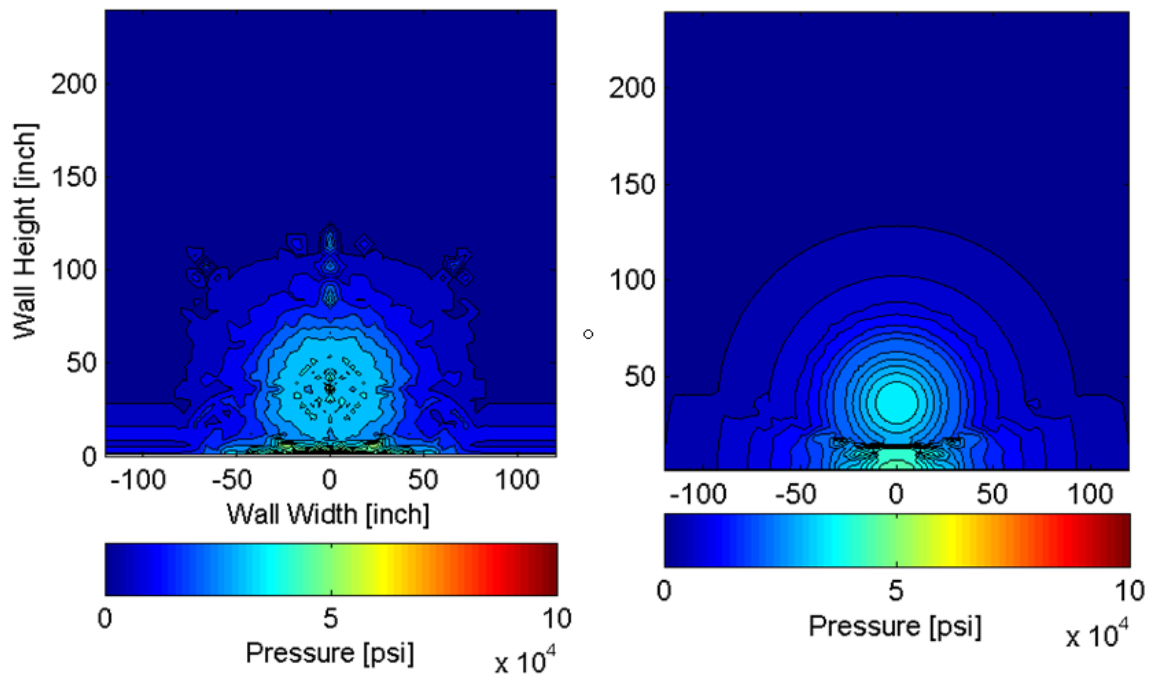
Figure 7.21: CTH (left) vs BLASTX (right) Pressure Comparison
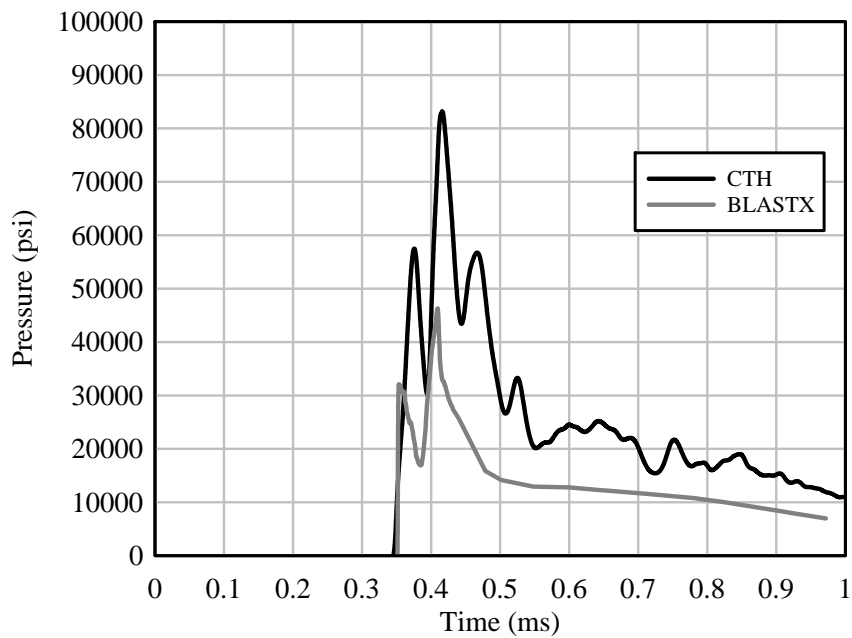
Figure 7.22: CTH vs BLASTX Tracer 1 Comparison
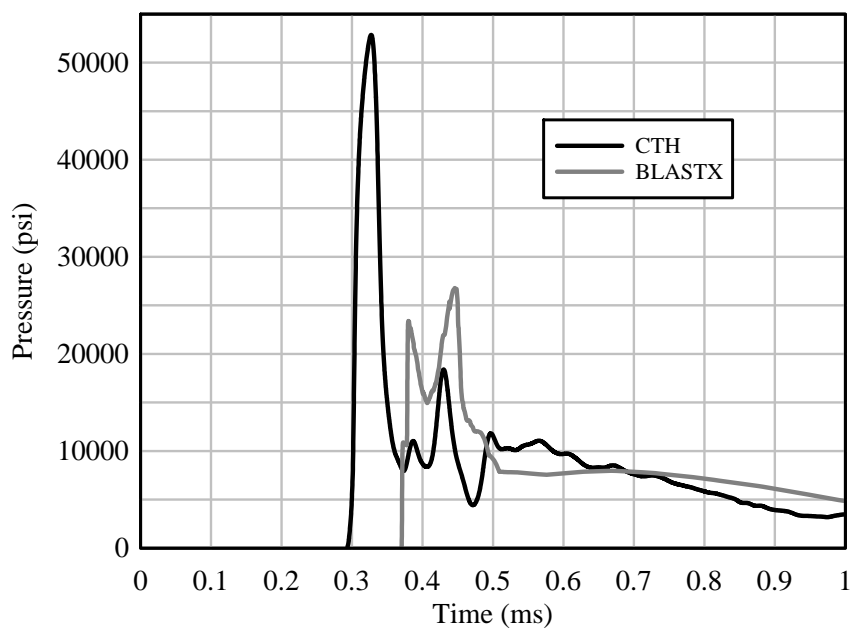
Figure 7.23: CTH vs BLASTX Tracer 2 Comparison
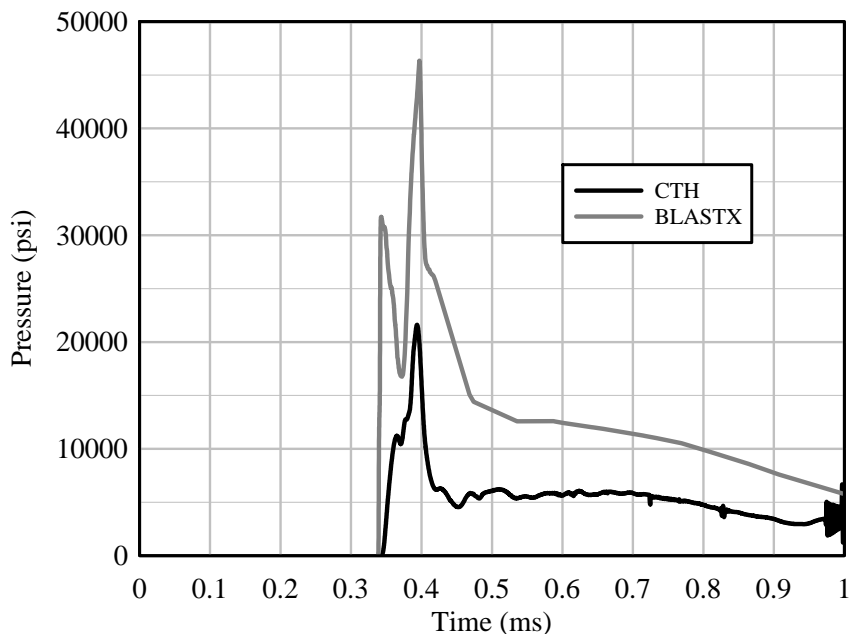
Figure 7.24: CTH vs BLASTX Tracer 3 Comparison

The comparison of CTH and BLASTX pressures give results that are slightly different for each of the three locations, which could be due to a minor offset of the tracers, meaning that a tracer only a small distance away could produce similar results. Because of this, it is important to study and compare the response of the column subjected to both loads.

The results from the column comparison are given in Figure 7.25 and plots of maximum displacements are given in Figure 7.26. These runs were conducted on the FRM finite element model that is discussed in the next chapter in Section 8.2.1. The CTH pressures were greater towards the base and therefore the column buckled earlier and did not result is as much global displacement. From the plots, it is evident that the overall column behavior is not greatly affected (within 15%) by the differences in pressures and impulses predicted by CTH and BLASTX. Because of this, and the fact that BLASTX

has a much smaller computation time, BLASTX was used to predict loads for the rest of
this chapter as well as for the development of the fast running model in Chapter 8.

CTH   **BLASTX**
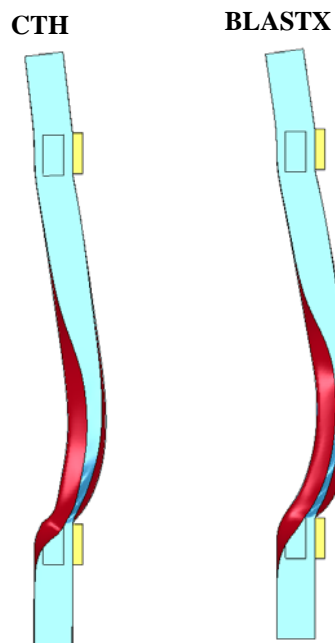
Figure 7.25: CTH and BLASTX Column Response Comparison
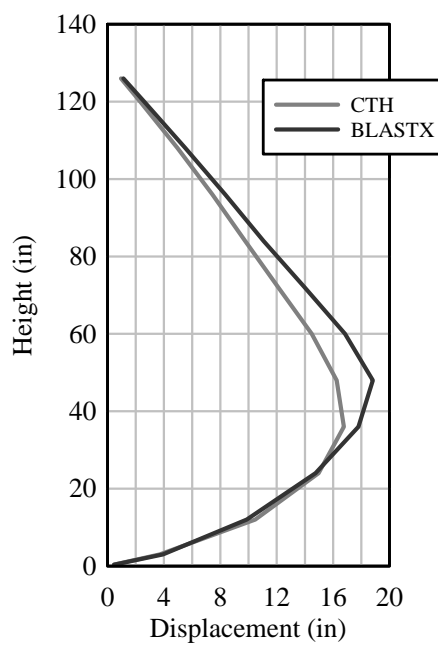
Figure 7.26: CTH and BLASTX Column Displacement Comparison

7.3.3 Approximation of Blast Loads on Strong Axis

In the above comparison, the loads on the column were applied using a variance in pressure and impulse along the width and height of the column at many locations. For modeling, it is often necessary to apply an approximate load on the column that does not utilize as many spatial divisions of tracer data. The next set of comparisons was preformed in order to produce a methodology that can easily approximate these detailed loads.

First, the width shall be considered. Figure 7.27 gives the pressure time histories from tracer locations located at the same height of 36 in from the ground at three locations along the width. Because the width of the column is so small, the differences in the pressures are negligible and it was concluded that the pressure-time history can be assumed to be constant along the width of the column for charges in the range of this dissertation.

Unlike the width, the pressure along the height of the column is much more variable and may not be considered constant. The column was split into three other different configurations. The first spaced the tracers at a finer 3 in pattern toward the base of the column. The second spaced the tracers at 6 in and the third spaced the tracers at 12 in as in Figure 7.28. The column was then loaded with the pressure-time history from the closest tracer over the corresponding tributary area.
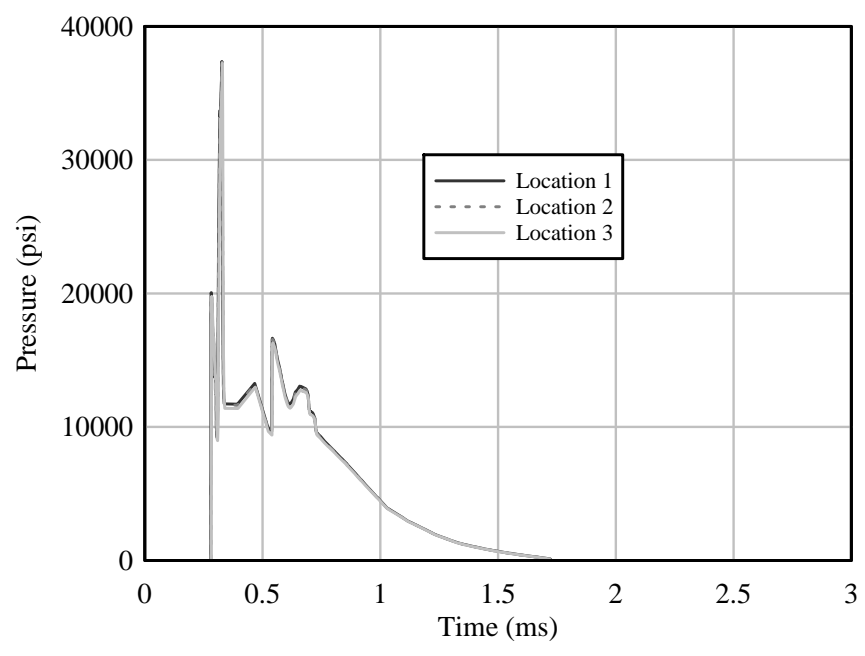
Figure 7.27: Example Pressure-Time Histories at Same Height
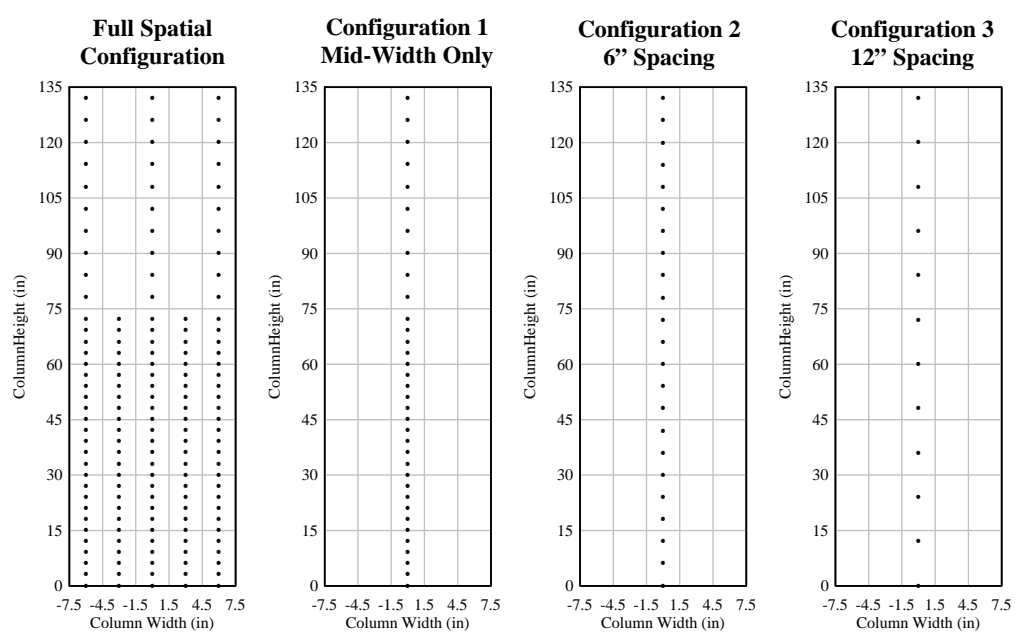
Figure 7.28: Location of Tracers for Applied Load Comparison

The maximum global displacements over the height of the column were again used as the tool for comparison. Maximum displacements were used with the assumption that the unloading of the column would not be sensitive to the loading which occurs much early on in the run, and also because the unloading for a given maximum displacement was verified in Chapter 4. The maximum displacements for the detailed model are listed in Table 7.11 and plotted in Figure 7.29. Based on the results, it was determined that a 12 in spacing is sufficient. A complete set of approximate pressure time histories for various scaled distances are included in Appendix B for use in approximating column response in developing testing protocols as discussed in Section 2.3.3.

Table 7.11: Reduced Segments Maximum Displacements Comparison

Distance from Base (in)	Spatially Distributed Max Disp.(in)	Mid-Width Only Configuration1 Max Disp. (in)	6" Spacing Configuration 2 Max Disp. (in)	12" Spacing Configuration 3 Max Disp. (in)
126.0	1.12	1.13	1.13	1.12
120.0	2.60	2.63	2.62	2.60
108.0	5.51	5.56	5.56	5.50
96.0	8.34	8.42	8.41	8.32
84.0	11.07	11.2	11.17	11.02
72.0	13.99	14.03	14.01	13.80
60.0	16.84	17.04	17.02	16.75
48.0	18.82	19.01	18.91	18.62
36.0	17.79	18.06	17.85	17.43
24.0	14.75	14.93	14.77	14.55
12.0	9.87	9.96	9.86	9.74
3.0	3.92	3.98	3.96	3.97
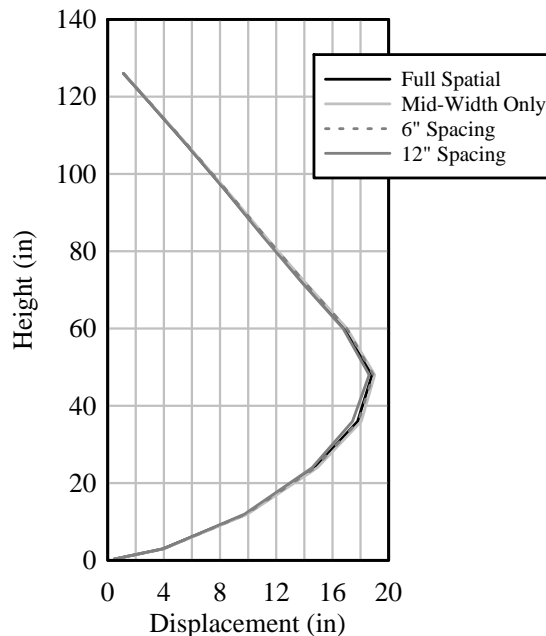
Figure 7.29: Reduced Tracer Maximum Displacements Comparison

7.4   Blast Loads Applied to Weak Axis Steel Column Models

7.4.1 Motivation

Similar to Section 7.3, this section describes the procedure for loading columns in the weak axis direction with pressures-time histories generated from vehicle bomb sized charges. Specifically, this section investigates the loads applied to the flanges since those applied to the web are initially consistent with the loads calculated for the strong axis. Other methods and conclusions from the strong axis model will be assumed to be consistent for use in the weak axis, including segment height.

7.4.2 Approximating Loads for Weak Axis Flanges

In order to approximate the loads on the column, an analysis was conducted with tracers placed on the web, outside flanges and inside flanges using CTH. Figure 7.30

shows pressures on the column web and flanges. From the figures, it is evident that the loads applied to the inside flanges are less than the web and the pressure applied to the outside (if clearing effects are present) are, in comparison, almost negligible.

Using the tracer information from the CTH plot, the impulses were calculated along the height of the column for the middle of the web, middle of the outside flange and the middle of the inside flange as shown in Figure 7.31. The pressure and impulses for both flanges are plotted in Figure 7.32 and Figure 7.33, respectively. Plots of the impulses of the flanges normalized with the web impulses are shown in Figure 7.34. From the plot, it is observed that, consistently for the whole column height, the inside flanges are loaded with about 70% of the web impulse, while the outside flanges are loaded with approximately 10% of the web impulse.
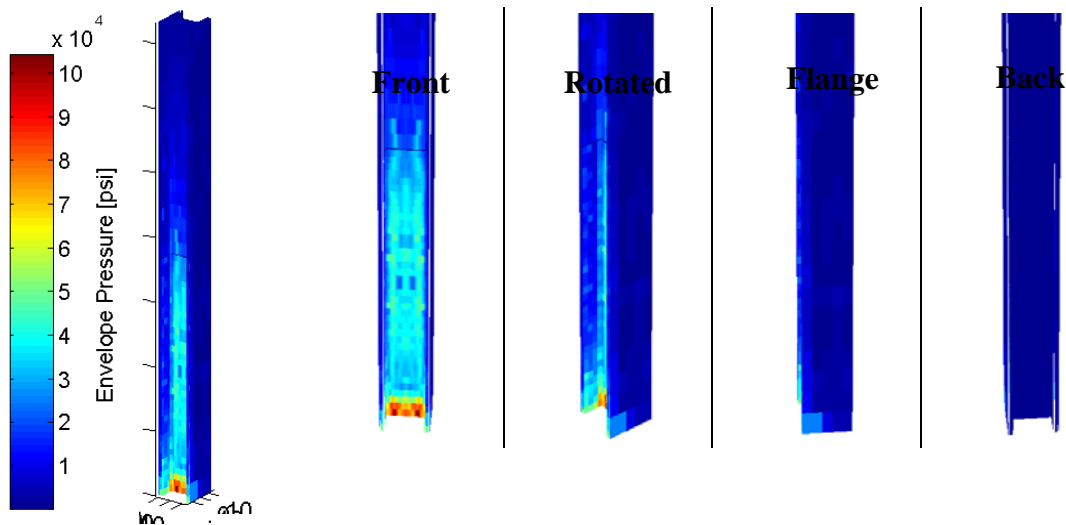
Figure 7.30: CTH Pressure Loads on Weak Axis Column
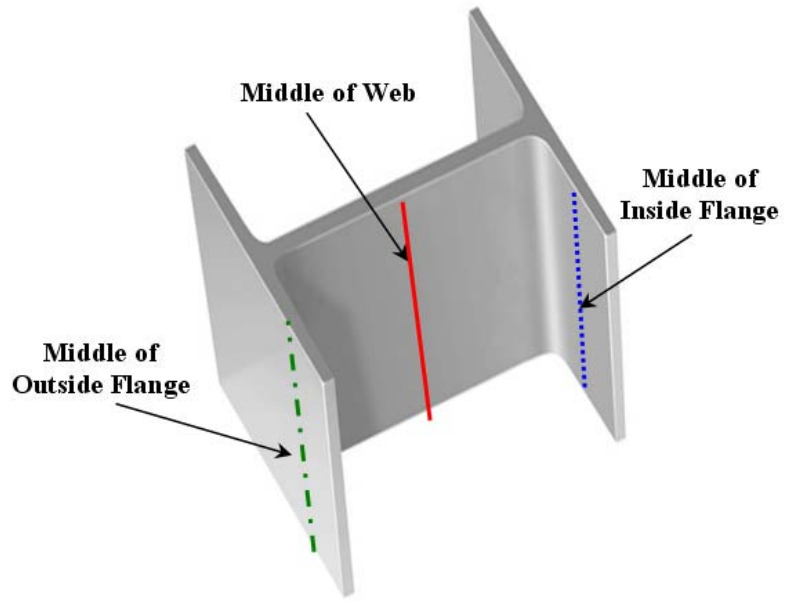
Figure 7.31: Locations for Weak Axis Comparison
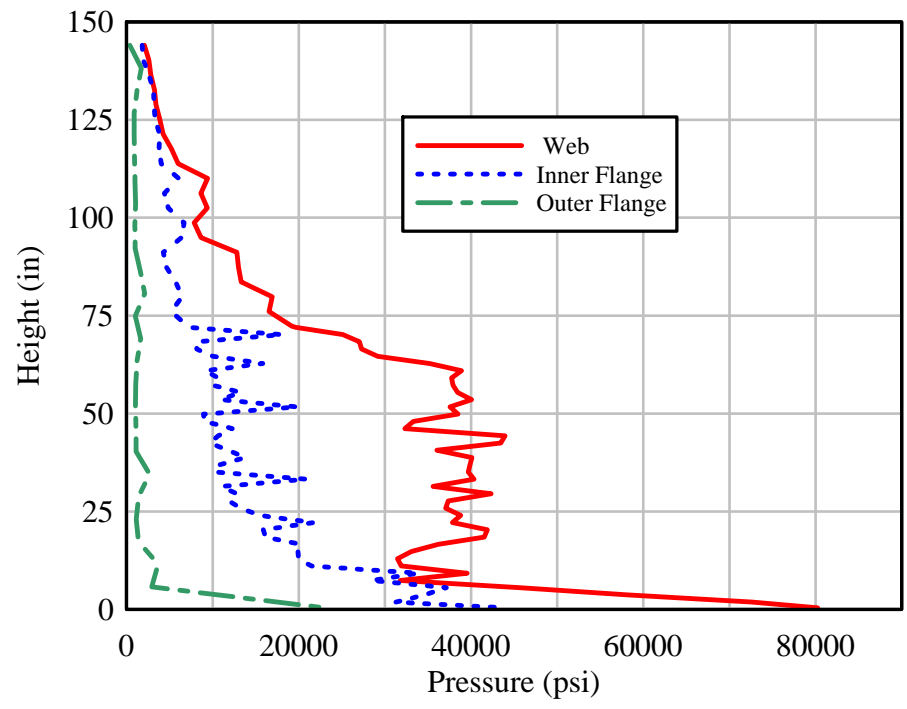
Figure 7.32: Peak Pressure Comparison for Web and Flanges along Column Height
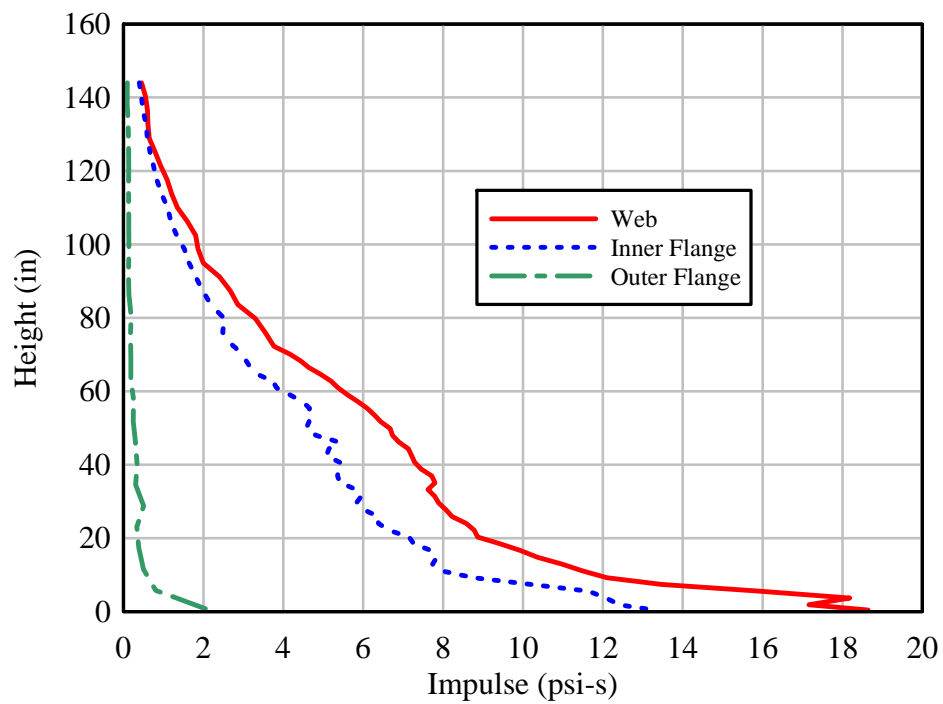
Figure 7.33: Impulse Comparison for Web and Flanges along Column Height
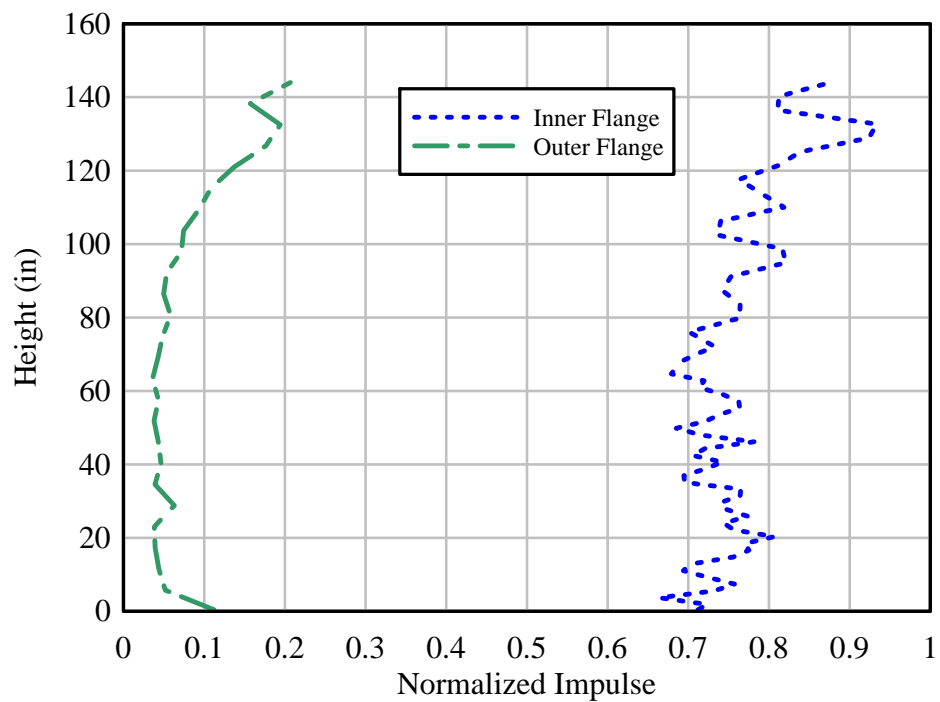
Figure 7.34: Normalized Impulse Comparison

7.5   Protocol for Simulator Testing Steel Columns

This section incorporates the investigations within this chapter and the models and experiments from the previous chapters into the development of a protocol for utilizing the Blast Simulator for testing steel columns. This protocol can be used to design similar column tests or can be used as a basic methodology for testing other components of steel columns such as baseplates and beam-column connections. It can also be used as a guideline and varied for developing tests of other material types. The protocol is shown in the form of a flow chart in Figure 7.35 with notes for each box that are given as follows:

1) Enter flowchart and determine threat scenario. This normally refers to vehicle bomb size and standoff distance. In the case where impulse or pressure histories are given, proceed to step 6.

2) Calculate scaled distance, Z, from Equation 2.2.

3) Decision: Is Z approximately equal to any of the pre-calculated scaled distance scenarios given in Appendix B?

4) YES – Refer to Appendix B for given impulses and pressure-time histories.

5) NO – Predict impulses and pressures along the height of the column using appropriate method. Methods may include CTH, BLASTX, etc.

6) Apply pressure-time histories with equivalent impulses to finite element model developed in Chapter 4 and 6. This can be done using the 12 in spacing suggesting in Section 7.5 and the approximation methods discussed in Chapter 2.

7) Record appropriate displacements and localized failure behavior or any other relevant and desired parameters.

8) Begin design of experiment.

9) Decision: Are the masses pre-fabricated and on site?

  10) YES – Proceed to step 12.

  11) NO – Select a mass equal to that of the portion of the column specimen that it impacts. This does not include the mass of the supports or the reaction structure.

12) Determine first estimate of initial velocity using Equation 3.2. The impulse should be determined using the average impulse over the height of those calculated from Step 4 or Step 5.

13) Run finite element model with appropriate masses and velocities. The masses must also incorporate the weight of the rod and collar for the appropriate BG type.

14) Decision: Does the results of the finite element run adequately resemble those recorded in Step 7?

  15) YES – Proceed to Step 17.

  16) NO – Modify velocity and return to Step 13.

17) Decision: Is the velocity from the run in Step 15 feasible with the limitations of the Simulator including velocity limits, deceleration pressures, deceleration times, stroke length, etc?

  18) YES – Except test design

19) NO – Modify masses and velocity by equating $mv^{1.5}$ to that of $mv^{1.5}$ in Step 15 and return to Step 17 to get a feasible velocity.
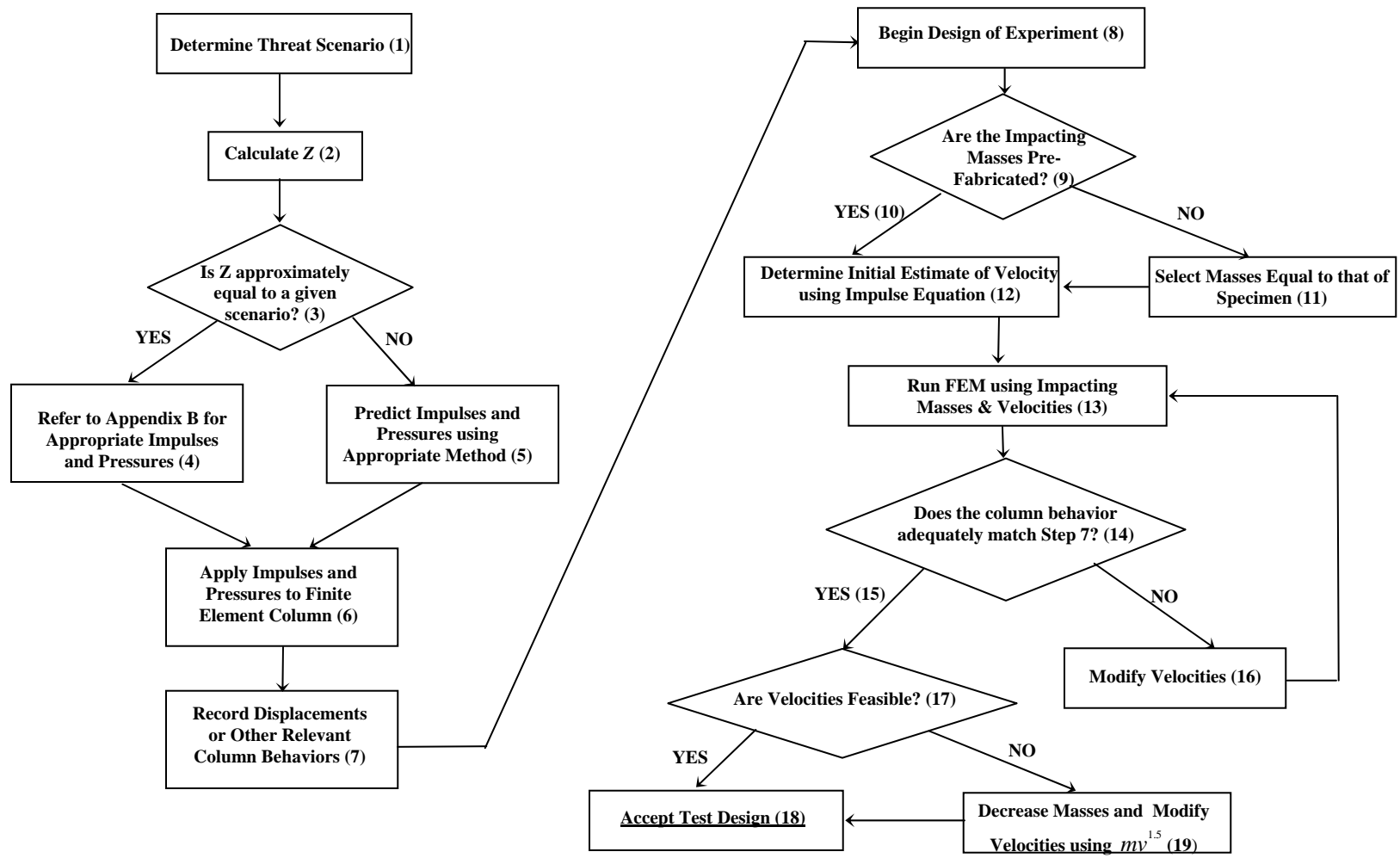
Figure 7.35: Flow Chart for Design of Simulator Tests for Steel Columns

7.6 Summary

This chapter included multiple investigations regarding steel column testing and finite element analysis. The first study considered the effects of BG impact synchronicity on the response of the column. Multiple finite element analyses were conducted for various unsynchronized impacts. It was found that because the periods of the columns are far greater than that of the loads, a reasonably unsynchronized impact does not have a great effect on the column behavior.

The second study involved momentum and kinetic energies of the impacting module and their affect of the displacement and behavior of the column. This study was motivated by a logistical as well as a practical standpoint as one of the most important aspects in obtaining an output of interest is the experimental inputs. A finite element model was used to compare loadings of similar momentum and kinetic energies and it was found that using and equating $mv^{1.5}$ produced more similar results to the control columns than that of only equating momentum or only equating kinetic energy. Because of this, the velocity should be used as the means for varying impulse to its maximum effect and therefore, mass, and materials, can be reduced to some extent.

Methodologies for approximating blast loads on columns were also considered in this chapter. Comparisons of common blast analysis programs showed that they yielded similar results as far as column response is concerned. Also, it was demonstrated that applying a fully distributed load along the width and height of the column is not necessary and an average distribution over a reduced number of tributary areas can be

sufficient. For weak axis impacts it was also found that loading can be simplified by including a scaled web load on the inside flanges of the column.

Lastly, this chapter incorporated the findings in this chapter as well as previous chapters into a loading protocol for testing steel columns with the UCSD Blast Simulator. The test design relates impactor design and velocity to the column behaviors of a structure subjected to various vehicle charge sizes with and certain standoffs. This methodology can be used to design similar future steel column tests or column specimens that incorporate other components such as baseplates or connections.

8 Development of a Fast Running Model for Predicting Capacity of Blast Loaded Steel Columns

This chapter describes the development of a fast running model (FRM) to be used for predicting capacity of steel columns subjected to typical sized vehicle bombs. The model was created using an artificial neural network (ANN) which was trained using data generated from the finite element models validated in the previous chapters. The fast running model is a tool that can be utilized in situations where time consuming, advanced analysis models are not practical. The following sections will explain the development of the model including selection of parameters, data generation, model training and validation. A threat analysis example is also included to highlight the capability of using the FRM as a risk assessment tool.

8.1 Model Motivation & Scope

The implementation of fast running models for prediction of structural behavior due to blast loads has become vital in the evaluation of threats. Often times it is necessary

to evaluate structures and their potential risks in a relatively quick time frame, much quicker than the time a full finite element analysis run would necessitate.

The majority of fast running models, at the current time, heavily rely on single degree of freedom (SDOF) models. In an SDOF analysis [35], the beam/column seen in Figure 8.1 with length, L, and blast load, $w(t)$, is given. The load is typically chosen to be uniform and the boundaries can be modified to represent the configuration of the structure.
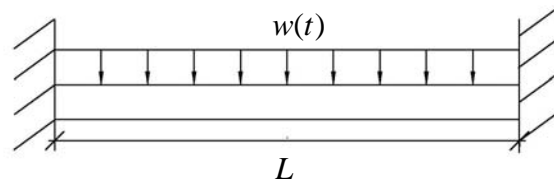
Figure 8.1: Typical Loaded Beam for SDOF Model

The column, which has a continuous displaced shape along the length, is simplified into a mass-spring system, in which the equivalent mass of the structure, M_{eq}, is lumped into a single element and with a time-varying load, $F(t)$, applied. The resistance, R_c, which is a function of the displacement of the mass, Δ, is also incorporated and found using the basic stiffness and boundary conditions of the structure. The displacement is computed by numerically solving the equation of motion given in Equation (8.1).

$$F(t) = M_{eq}\ddot{\Delta}(t) + R_c(\Delta) \tag{8.1}$$

$F(t)$

M_{eq}

$\Delta(t)$

$R_c(\Delta)$
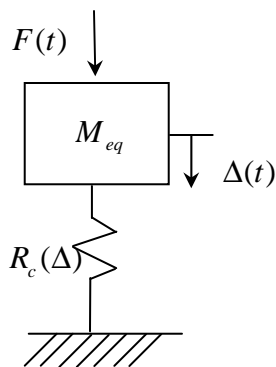
Figure 8.2: Typical SDOF Model

The displacement computed from the SDOF is typically defined as the displacement for the midspan of the column and does not yield any other relevant information. It does not include the variable loading along the height of the column, nor does it include any localized behavior of the system.

In this case of the columns tested and modeled in this dissertation, the behavior of the damaged column was described by many additional factors other than midspan displacement. For the strong axis tests, localized web buckling was evident at the base of the column near the supports, as well as other localized flange bending. In the weak axis tests, observed behavior included flange buckling at the front and the back of the column, web fracture, concrete damage and flange bending, none of which could be described by a SDOF model. Because of this, it was necessary to employ a validated finite element based model that could include the behaviors seen in blast damaged columns to ultimately characterize the capacity of the column.

The finite element based model must be able to accurately predict the column capacity for any subset of given conditions and parameters. Often times, the population of the parameter space can involve hundreds of runs in order to adequately describe the

data set. For this reason, an artificial neural network, discussed in the following sections, was used to process the parameters into an adequate capacity response instead of undergoing a full parametric study.

The model developed in this dissertation is adequate for predicting residual column capacity in both the strong and weak directions for columns free-standing columns with no beam connections or base plates. It is meant to be the starting point for multiple variations and additions as subsequent research is conducted as the methodology described is pertinent for applications to other column configurations and other types of structures.

8.2   Artificial Neural Networks

An artificial neural network is a mathematical or computational model that tries to simulate how biological nervous systems, such as the brain, process information. In the model each single artificial neuron, shown in Figure 8.3, accepts information from a number of given inputs. Each of those inputs comes with a strength (or weight) which corresponds to the synaptic efficiency in a biological neuron. Each neuron has a corresponding threshold or bias value, $\bar{b}$. The weighted sum of the inputs is computed and subtracted from the threshold value, to compute the activation value, $\bar{a}$. This activation value is passed through an activation function (transfer function) to produce the output of the neuron.

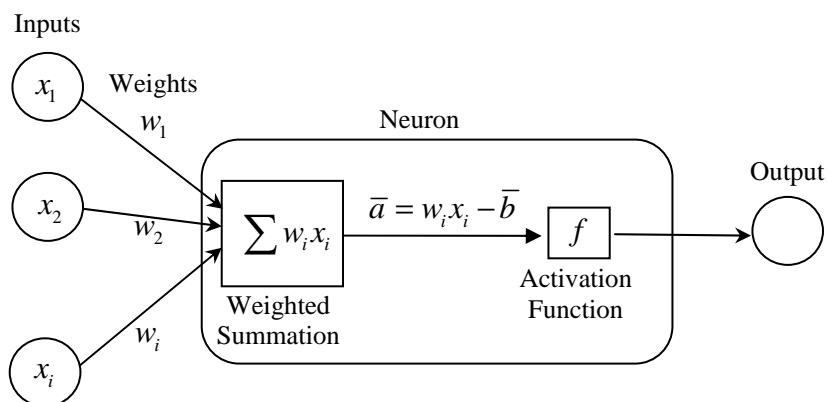Figure 8.3: Single Artificial Neuron Model

A network of neurons is composed of many single element neurons operating in parallel. The connections between the elements are often interconnected by multiple inputs and multiple layers of hidden neurons which can produce multiple outputs. One example of a network on interconnected neurons is given in Figure 8.4.
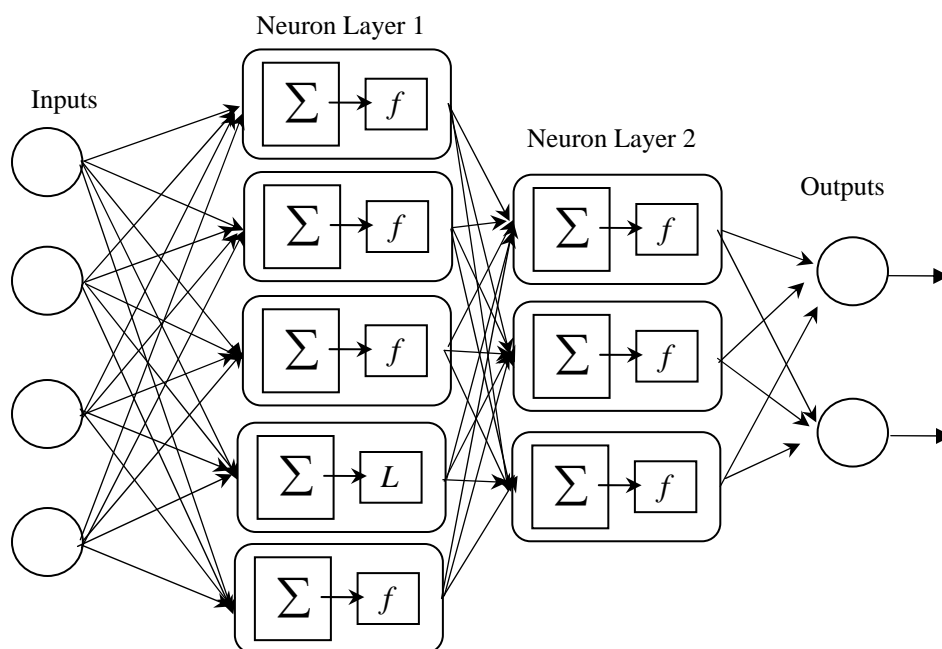
Figure 8.4: Artificial Neural Network Model

For the purpose of this dissertation, a feed-forward network, which can only pass information in one direction, with one layer of hidden neurons and one output parameter will be used and discussed further. Many references such as [36, 37] discuss ANNs in more detail and provide information on additional types of neural net structures.

The procedure of modifying the weights and biases of the network to perform some particular task, i.e. predict column capacity, is done with a training algorithm. The training algorithm can be supervised or unsupervised. This dissertation will use a supervised algorithm were the inputs and outputs of the training sample set are known and applied to the model. In this case, the inputs are applied to the network and outputs are computed. These calculated outputs are compared to the actual target values and the weight and bias values are updated.

There are many training algorithms that can be used to help the model "learn". The majority of the algorithms are methods that seek to provide a numerical/iterative method for the minimization of the error function created over the space of parameters. Some examples of these types of algorithms are the back propagation method, the conjugate gradient descent method, the Quasi-Newton method, and the Levenberg-Marquardt method. Once acceptable values from the weights and biases have been determined, the model can then be used to predict outputs from another set of desired inputs.

8.3   Selection of Parameters

8.3.1 Input Parameters

The input parameters for the neural network were divided into two categories: loading parameters and structural parameters. The loading parameters are needed to adequately describe the loads imparted on the column by a typical vehicle bomb. As discussed in Chapter 2, the loading environment can be described by a charge of a given weight at a given standoff. Typical vehicle bombs are within the range of 500 lbs to 1500 lbs and are normally located a few feet off the ground. For this parameter, a constant charge was chosen as 1000 lbs of TNT and located 3 ft from the ground with the varying parameter being the standoff, R, from the column. If another charge size is of interest, the standoff can be scaled using the scaled distance description from Chapter 2. The standoffs of interest should be within the range of 3 ft to 25 ft from the column. Any standoff closer than 3 ft would be considered a contact charge and is outside the scope and data of this dissertation. Outside of 25 ft and the amount of damage to a typical sized steel column would be minimal.

The structural parameters were chosen to sufficiently describe the geometry of a steel wide flange section. A typical wide flange section is shown in Figure 8.5. The first parameter to be considered is the column depth, d, which is an important parameter because as d increases, the tributary area (for weak axis) increases which, in turn, increases the load on the column. In the strong axis direction, it also contributes to the stiffness in the loaded direction. Column depths of interest are those associated with W8 sections through W14 Sections and range from 7.93 in to 22.84 in.
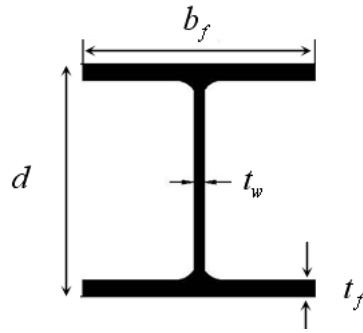
Figure 8.5: Typical Wide Flange Geometry

The second structural parameter of interest is the width-thickness ratio of the depth, d, to the web thickness, t_w. The parameter will therefore be defined as $\dfrac{d}{t_w}$. The ranges for this parameter for columns of W8 to W14 are 6.11 to 37.04.

Because the testing and validation of the finite element model in the previous chapters involved square columns, it will be assumed that the columns used in this analysis will also be relatively square with $\dfrac{b_f}{d} \geq 0.75$. Therefore the length of the flange, b_f, will not be used as a parameter and can be considered to be equal to d in any subsequent calculations used for model training.

The next structural parameter involves the flange thickness, t_f. The thickness of the web will be included in a ratio with the thickness of the flange. The thickness ratio, $\dfrac{t_f}{t_w}$, is appropriate because, among other things, it specifically helps define the amount of local and global damage of the column depending on its orientation. For example, in a strong axis test, if the flange thicknesses are small compared to its web, more local flange

deformation would occur over the global deformation of the column which is more governed by the web. Typical thickness ratios range from 1.62 to 1.77.

The last structural parameter is the column length, L. The column length is significant because as the column height increases, the amount of deformation increases due to an increase of tributary area, as well as the buckling length. Column lengths appropriate for this model range from 8 ft to 20 ft. A summary of the input parameters and their ranges are included in Table 8.1.

Table 8.1: Input Parameters and Ranges

Parameter Type	Parameter	Range	Limitations/Comments
Loading	Standoff, R	3 ft to 25 ft	1000 lbs of TNT, otherwise convert using scaled distance, Z
Structural	Depth, d	7 in to 25 in	Depths of W8 to W14 Columns with $\dfrac{b_f}{d} \geq 0.75$
Structural	Width-Thickness Ratio, $\dfrac{d}{t_w}$	6.11 to 37.04	
Structural	Thickness Ratio, $\dfrac{t_f}{t_w}$	1.37 to 1.77	
Structural	Length, L	8 ft to 25 ft	

8.3.2 Output Parameter

Residual column capacity was determined to be the output parameter of interest in this model. The residual capacity is quantified by the Column Capacity Ratio (CCR). The CCR is defined as the ratio of the residual column capacity after blast damage over the virgin capacity of the column as described in Equation (8.2).

$$CCR = \frac{\text{Blast Damaged Column Capacity}}{\text{Virgin Column Capacity}} \tag{8.2}$$

For example, if a column with a capacity of 800 kips was input into the model and a CCR of 0.75 was outputted, this would indicated that the column could withstand 75% of the capacity or 600 kips before failing. If the column were designed to hold 700 kips, the column would likely fail after the blast.

8.4 Selection of Training Points

The selection of individual training points was performed in an iterative process. An initial set of training points was selected and is described in this section and then modified in the subsequent sections to further define the sample space.

The initial set consisted of 51 samples in both the strong and the weak axis model. These samples each included a different combination of the five parameters described in the previous section. For each parameter, a nominal, minimum and maximum value was assigned based on the distribution and range of values for that parameter. The nominal value is selected as the most representative value of the sample. This can be based on mean, median, distribution, etc. and often times experience aids in the selection.

The minimum standoff, R, was set at 5 ft, the nominal was defined as 10 ft and the maximum was set as 20 ft. It should be noted that these are not the full minimum and maximum ranges because the model is able to extrapolate, to some extent, outside of the minimum and maximum ranges defined.

This model considers W8 through W14 sized columns with $\dfrac{b_f}{d} \geq 0.75$. The corresponding depths, d, and width-thickness ratio, $\dfrac{d}{t_w}$, associated with these sections are plotted in Figure 8.6. From the distribution of this plot, it was decided that a nominal depth of 14 in would be used with a minimum and maximum of 8 in and 22 in, respectively. 8 was chosen as the minimum for the width-thickness ratio, 20 in for the nominal and 35 for the maximum.
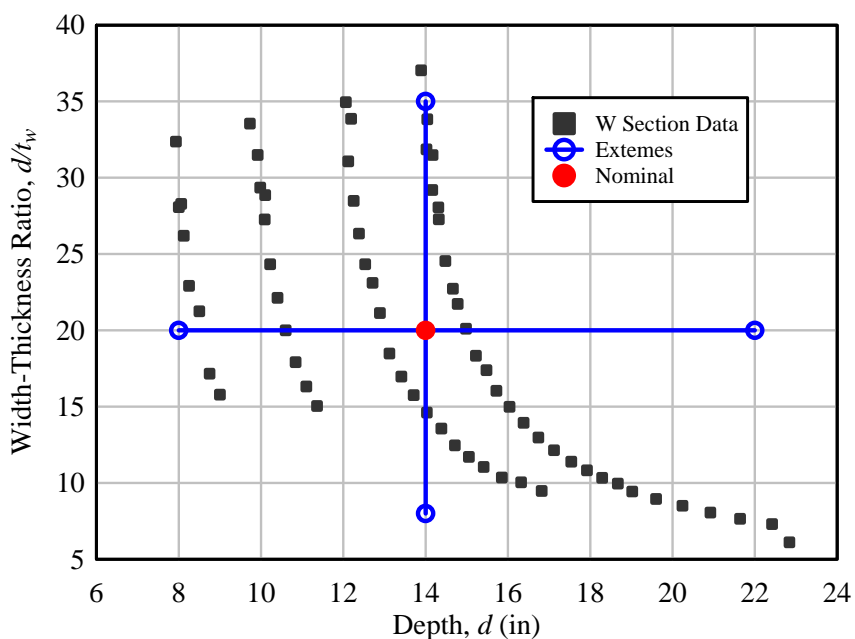

Figure 8.6: W8 – W14 Depths and Width-Thickness Ratios

Figure 8.7 gives a plot of the depths versus the thickness ratio, $\dfrac{t_f}{t_w}$. In this case, the nominal for the thickness-ratio parameter was chosen as 1.60 because that value seemed to best represent the distribution of points. The minimum and maximum were selected as 1.45 and 1.75, respectively.
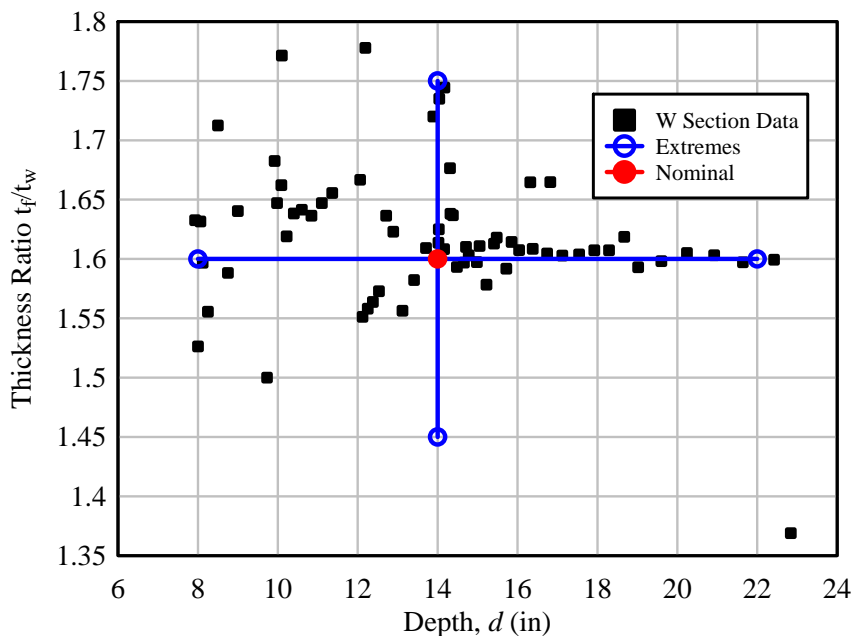
Figure 8.7: W8 – W14 Depths and Thickness Ratios

The last parameter is the column length, L. A minimum height was chosen as 8 ft and a maximum was chosen as 20 ft. The nominal was decided to be 12 ft because that could be considered an average height for typical structures. A summary of all the parameters and their values is given in Table 8.2.

Table 8.2: Summary of Nominal and Extreme Parameter Values

Parameter	Model Range	Minimum	Nominal	Maximum
Standoff, R	3 ft to 25 ft	5 ft	10 ft	20 ft
Depth, d	7 in to 25 in	8 in	14 in	23 in
Width-Thickness Ratio, $\dfrac{d}{t_w}$	6.11 to 37.04	8	20	35
Thickness Ratio, $\dfrac{t_f}{t_w}$	1.37 to 1.77	1.45	1.60	1.75
Length, L	8 ft to 25 ft	8 ft	12 ft	20 ft

The parameters were combined in a systematic fashion for the initial data set. The five parameter combinations span a five dimensional space that is difficult to visualize. For this reason, a three-dimensional data set will be used for explanation purposes. If a three parameter space, x_1, x_2, x_3, is considered and plotted as a cube with the nominal of each value at the center of the axis and the minimum and maximum as the two extremes, as shown in Figure 8.8, then the center point would correspond to the sample with $x_1 =$ nominal, $x_2 =$ nominal, and $x_3 =$ nominal.
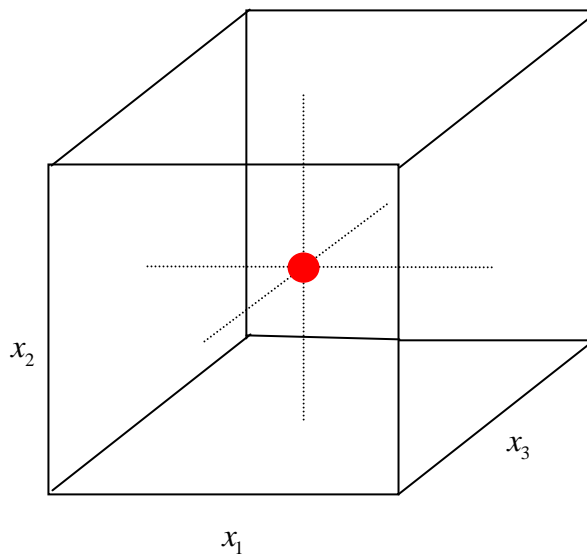
Figure 8.8: Three Dimensional Sample Space with Nominal Point

The next set of points is found by varying one parameter to an extreme and keeping the remaining parameters fixed and the nominal. For example, $x_1 =$ minimum, $x_2 =$ nominal and $x_3 =$ nominal. These points are shown in the cube in Figure 8.9 as the blue dots. For a given number of parameters, n_s, the number of samples corresponding to varying one parameter is $2n_s$.
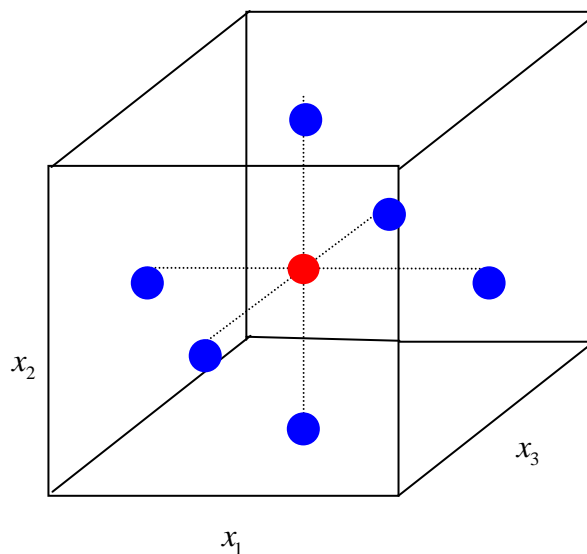
Figure 8.9: Three Dimensional Sample Space Varying One Parameter

The last set of points used in this initial data set is found by varying two parameters to all combinations of extremes and keeping the third parameter fixed as nominal. For example, $x_1 =$ minimum, $x_2 =$ maximum and $x_3 =$ nominal. These points are shown in the cube in Figure 8.10 as the green dots. For a given number of parameters, n_p, the number of samples corresponding to varying two parameters is $2n_p(n_p - 1)$.
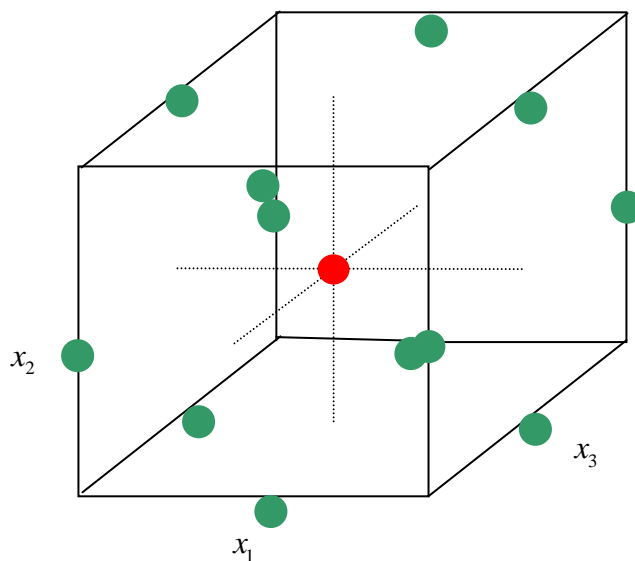

Figure 8.10: Three Dimensional Sample Space Varying Two Parameters

If all of the above mentioned samples are considered, then the total number of initial samples, S_0, for n parameters is given by Equation (8.3).

$$S_0 = 1 + 2n_p{}^2 \tag{8.3}$$

For the five input parameters in this model, the number of initial samples is 51. The combinations of values for these parameters are given in Table 8.3.

Table 8.3: Parameter Values for Initial Sample Set

Case #	Description	R	d	$\dfrac{d}{t_w}$	$\dfrac{t_f}{t_w}$	L
1	All Values Nominal	10	14	20	1.6	12
2	R Min, Rest Nominal	5	14	20	1.6	12
3	R Max, Rest Nominal	20	14	20	1.6	12
4	d Min, Rest Nominal	10	7.93	20	1.6	12
5	d Max, Rest Nominal	10	22.84	20	1.6	12
6	$\dfrac{d}{t_w}$ Min, Rest Nominal	10	14	6.1	1.6	12
7	$\dfrac{d}{t_w}$ Max, Rest Nominal	10	14	37.04	1.6	12
8	$\dfrac{t_f}{t_w}$ Min, Rest Nominal	10	14	20	1.368	12
9	$\dfrac{t_f}{t_w}$ Max, Rest Nominal	10	14	20	1.777	12
10	L Min, Rest Nominal	10	14	20	1.60	8
11	L Max, Rest Nominal	10	14	20	1.60	20
12	R Min, d Min, Rest Nominal	5	7.93	20	1.60	12
13	R Min, d Max, Rest Nominal	5	22.84	20	1.60	12
14	R Max, d Min, Rest Nominal	20	7.93	20	1.60	12
15	R Max, d Max, Rest Nominal	20	22.84	20	1.60	12
16	R Min, $\dfrac{d}{t_w}$ Min, Rest Nominal	5	14	6.1	1.60	12
17	R Min, $\dfrac{d}{t_w}$ Max, Rest Nominal	5	14	37.04	1.60	12

Table 8.3 (cont.): Parameter Values for Initial Sample Set

Case #	Description	R	d	$\dfrac{d}{t_w}$	$\dfrac{t_f}{t_w}$	L
18	R Max, $\dfrac{d}{t_w}$ Min, Rest Nominal	20	14	6.1	1.60	12
19	R Max, $\dfrac{d}{t_w}$ Max, Rest Nominal	20	14	37.04	1.60	12
20	R Min, $\dfrac{t_f}{t_w}$ Min, Rest Nominal	5	14	20	1.368	12
21	R Min, $\dfrac{t_f}{t_w}$ Max, Rest Nominal	5	14	20	1.777	12
22	R Max, $\dfrac{t_f}{t_w}$ Min, Rest Nominal	20	14	20	1.368	12
23	R Max, $\dfrac{t_f}{t_w}$ Max, Rest Nominal	20	14	20	1.777	12
24	R Min, L Min, Rest Nominal	5	14	20	1.60	8
25	R Min, L Max, Rest Nominal	5	14	20	1.60	20
26	R Max, L Min, Rest Nominal	20	14	20	1.60	8
27	R Max, L Max, Rest Nominal	20	14	20	1.60	20
28	d Min, $\dfrac{d}{t_w}$ Min, Rest Nominal	10	7.93	6.1	1.60	12
29	d Min, $\dfrac{d}{t_w}$ Max, Rest Nominal	10	7.93	37.04	1.60	12
30	d Max, $\dfrac{d}{t_w}$ Min, Rest Nominal	10	22.84	6.1	1.60	12
31	d Max, $\dfrac{d}{t_w}$ Max, Rest Nominal	10	22.84	37.04	1.60	12
32	d Min, $\dfrac{t_f}{t_w}$ Min, Rest Nominal	10	7.93	20	1.368	12
33	d Min, $\dfrac{t_f}{t_w}$ Max, Rest Nominal	10	7.93	20	1.777	12
34	d Max, $\dfrac{t_f}{t_w}$ Min, Rest Nominal	10	22.84	20	1.368	12

Table 8.3 (cont.): Parameter Values for Initial Sample Set

Case #	Description	R	d	$\dfrac{d}{t_w}$	$\dfrac{t_f}{t_w}$	L
35	d Max, $\dfrac{t_f}{t_w}$ Max, Rest Nominal	10	22.84	20	1.777	12
36	d Min, L Min, Rest Nominal	10	7.93	20	1.60	8
37	d Min, L Max, Rest Nominal	10	7.93	20	1.60	20
38	d Max, L Min, Rest Nominal	10	22.84	20	1.60	8
39	d Max, L Max, Rest Nominal	10	22.84	20	1.60	20
40	$\dfrac{d}{t_w}$ Min, $\dfrac{t_f}{t_w}$ Min, Rest Nominal	10	14	6.1	1.368	12
41	$\dfrac{d}{t_w}$ Min, $\dfrac{t_f}{t_w}$ Max, Rest Nominal	10	14	6.1	1.777	12
42	$\dfrac{d}{t_w}$ Max, $\dfrac{t_f}{t_w}$ Min, Rest Nominal	10	14	37.04	1.368	12
43	$\dfrac{d}{t_w}$ Max, $\dfrac{t_f}{t_w}$ Max, Rest Nominal	10	14	37.04	1.777	12
44	$\dfrac{d}{t_w}$ Min, L Min, Rest Nominal	10	14	6.1	1.60	8
45	$\dfrac{d}{t_f}$ Min, L Max, Rest Nominal	10	14	6.1	1.60	20
46	$\dfrac{d}{t_w}$ Max, L Min, Rest Nominal	10	14	37.04	1.60	8
47	$\dfrac{d}{t_w}$ Max, L Max, Rest Nominal	10	14	37.04	1.60	20
48	$\dfrac{t_f}{t_w}$ Min, L Min, Rest Nominal	10	14	20	1.368	8
49	$\dfrac{t_f}{t_w}$ Min, L Max, Rest Nominal	10	14	20	1.368	20
50	$\dfrac{t_f}{t_w}$ Max, L Min, Rest Nominal	10	14	20	1.777	8

Table 8.3 (cont.): Parameter Values for Initial Sample Set

Case #	Description	R	d	$\dfrac{d}{t_w}$	$\dfrac{t_f}{t_w}$	L
51	$\dfrac{t_f}{t_w}$ Max, L Max, Rest Nominal	10	14	20	1.777	20

8.5   Generation of CCR Data

The data for use in this model was generated using a finite element model similar to that which was validated in Chapter 4 and Chapter 6 for the strong and weak axis columns, respectively. The model was simplified specifically in the boundary conditions to make for a more realistic scenario and also to allow for a faster run time of the model. Details regarding the two models and the loading conditions are described in the next two sections. Further applications and future additions to the model are discussed in Section 8.6.

8.5.1   Strong Axis Model

Finite Element Model

The FRM model developed for training calculations is shown in Figure 8.11. The model is capable of capturing a variety of loading conditions and configurations within one generalized model. The model is also adaptable to the creation of additional parameters such as beam/column connections and boundary condition variations, allowing the data generated in this dissertation to help train any future models.
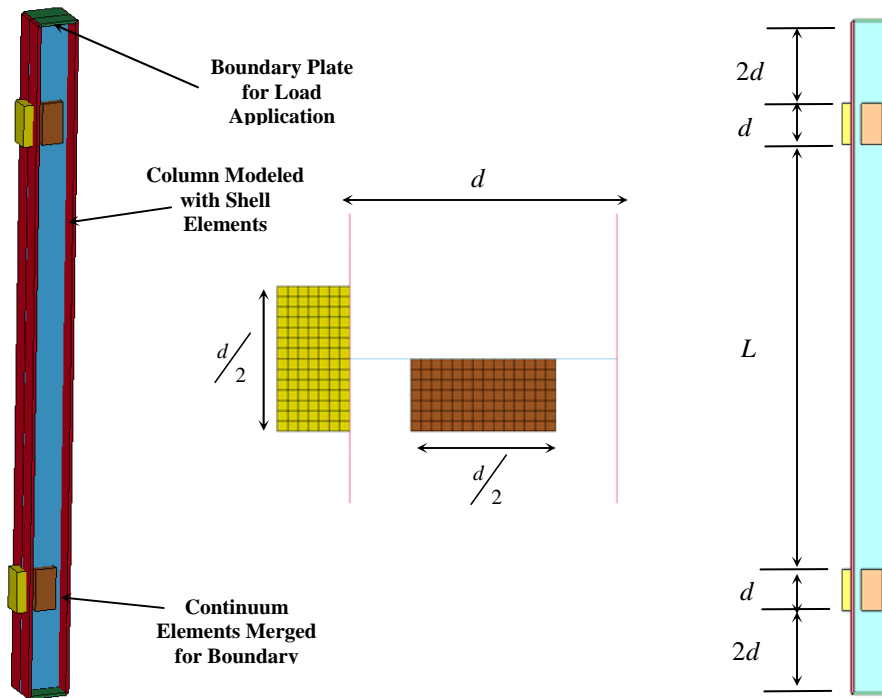
Figure 8.11: FRM Finite Element Model Geometry

The column mesh dimensions and geometry were generalized according to the FRM input parameters. The model was made with shell elements consistent in size and material with those used previously in this dissertation. The column length, L, was defined as the clear length between the supports, which are modeled by solid element support "pads" that have dimensions which are functions of the column geometry. The column was left continuous through the supports both top and bottom to allow the column web and flange to deform near the supports. This was also done to represent the case of typical of multistory construction, where the columns run continuous between floors and often go below ground level to basement floors.

The column boundary conditions, shown in Figure 8.12, were chosen primarily to avoid an over-constraining of the column which would be dominated by flexural

response. They were chosen to allow the local shear and buckling deformation to occur that were observed in various field tests. Roller boundary conditions were applied to the solid element "pads" to prevent horizontal and vertical translations during loading and during rebound. A roller support was also placed at the bottom of the column to prevent vertical uplift. Node sets were placed at all boundary "pads" and supports to allow for the future restraint of the model if a fixed condition or spring addition is later desired.
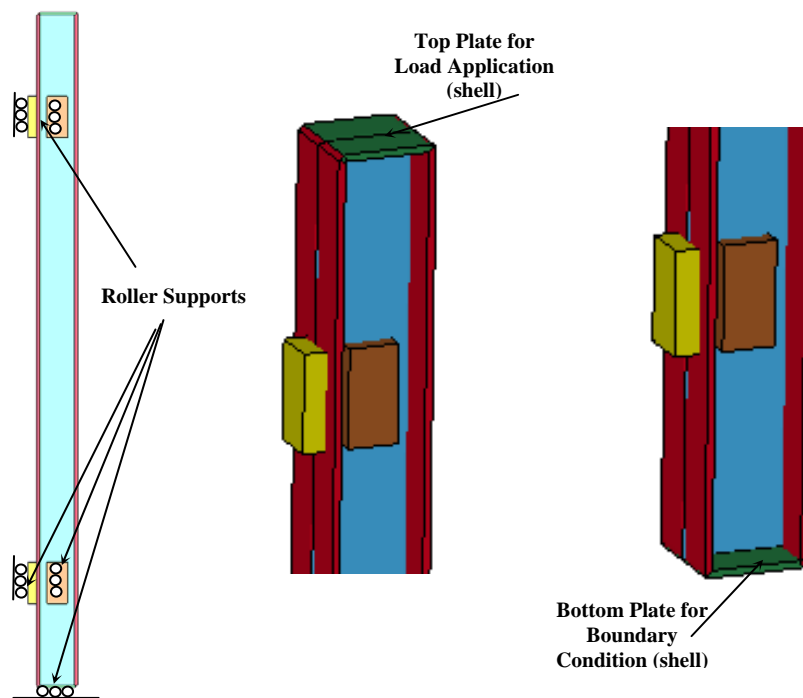
Figure 8.12: FRM Finite Element Model Boundary Conditions for Strong Axis

Loading

For the strong axis runs, the load was applied to the flange opposite the support boundary as shown in Figure 8.13. The loads were determined using BLASTX and were distributed over the height of the column using the procedure highlighted in Chapter 7. The loads did not take into account any clearing effects and therefore are considered to be

conservative if clearing effects are appropriate. Additional information on clearing effects and cladding is given at the end of this chapter.
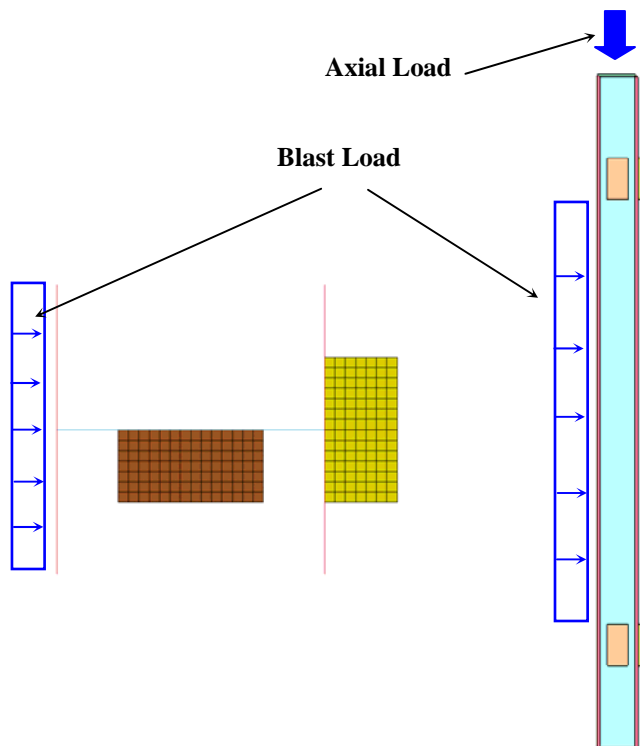
Figure 8.13: Description of FRM Loading for Strong Axis

The blast load was applied along the height of the column at time, $t = 0$. The column was allowed to respond to the blast load for 300 ms. Additional cases were run with a longer time frame, but it was found that it did not affect the results greatly. After 300 ms, an axial load was applied in the form of a displacement controlled boundary condition at a rate of 12 in/s. For the virgin capacity, the blast load was omitted and the axial load was applied at the same loading rate, with the hope that any rate effects from the high loading rate would nearly cancel out.

Results

The 51 finite element model cases were run according to the loading described in the previous section. Results from two representative cases are given below. The first set of results is from Case # 48. The standoff was 10 ft, the column had a depth of 14 in, a width-thickness ratio of 20, a thickness ratio of 1.368 and a 8 ft length. A summary of the behavior through loading is given in Figure 8.14. The first two figures show the column being loaded by the blast load. The third figure shows the column being initially loaded axially and the last figure given the column buckling due to the damage at the base (from an alternate view).
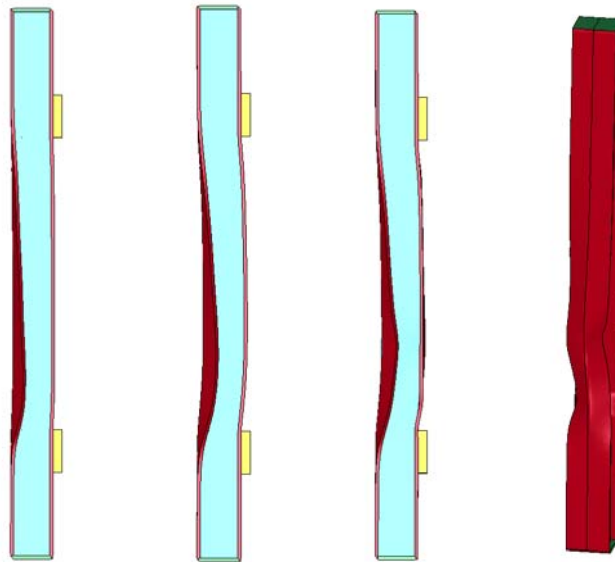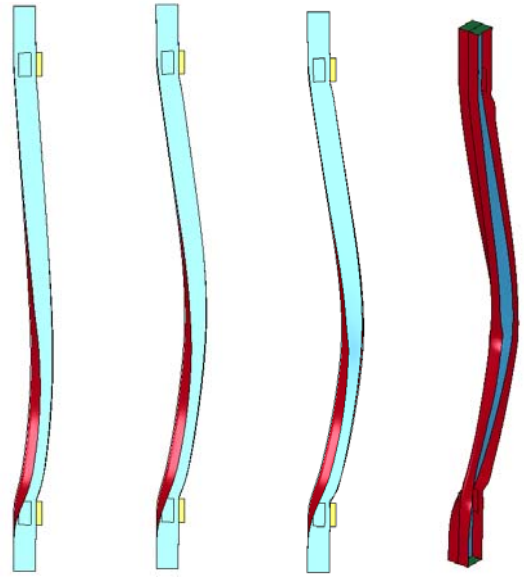

Figure 8.14: Column Behavior, Strong Axis – Example 1

The corresponding force diagram from this sample is given in Figure 8.15. From this plot, the capacity of the column at failure was 2,210 kips. This is compared to a virgin capacity test of 2,552 kips. The associated CCR is 0.866.
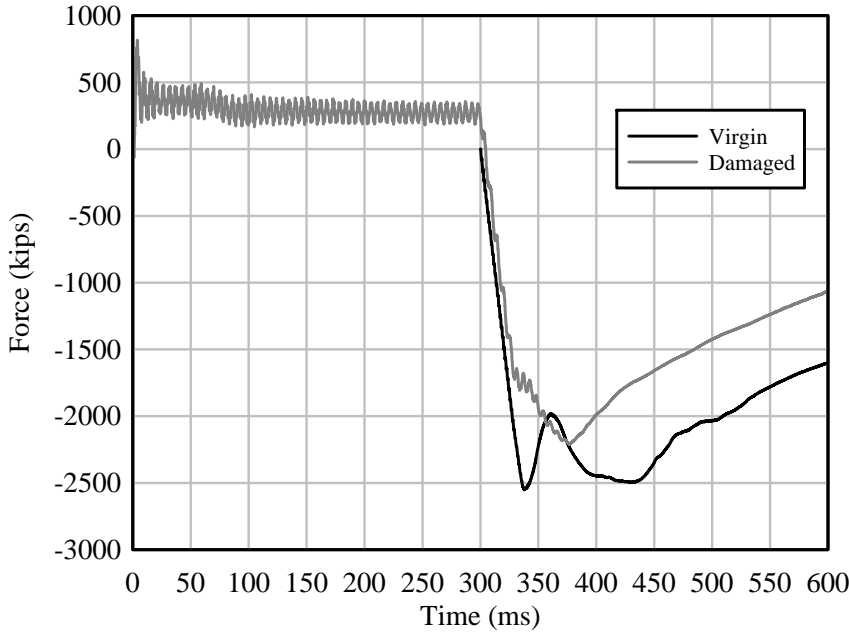
Figure 8.15: Column Force, Strong Axis – Example 1

The second set of results is from Case #32. This standoff was 10 ft, the column had a depth of 7.93 in, a width-thickness ratio of 20, a thickness ratio of 1.368 and a 12 ft length. A summary of the behavior through loading is given in Figure 8.16.

Figure 8.16: Column Behavior, Strong Axis – Example 2

The corresponding force diagram from this sample is given in Figure 8.17. From this plot, the capacity of the column at failure was 297 kips. This is compared to a virgin capacity test of 829 kips. The associated CCR is 0.358. The results from the remaining samples are summarized in Table 8.4.
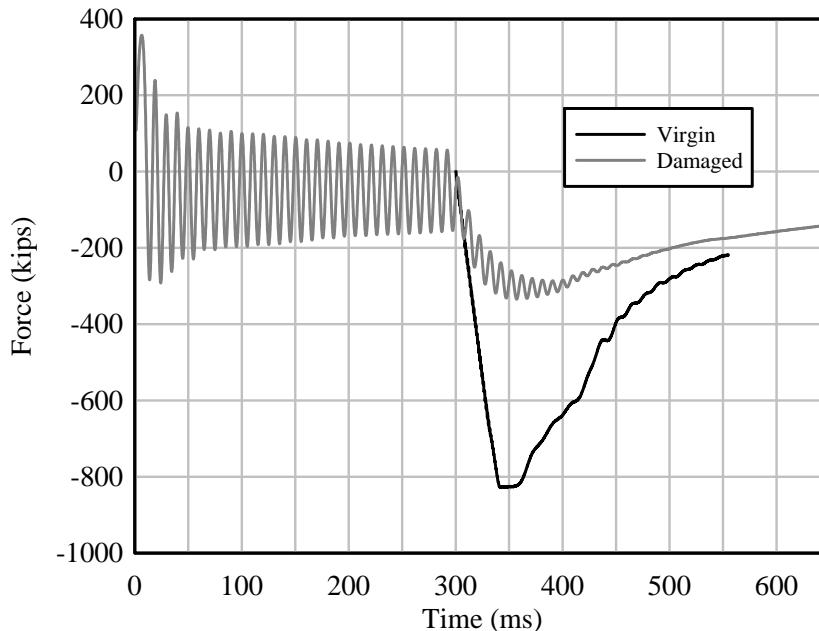
Figure 8.17: Column Force, Strong Axis – Example 2

Table 8.4: Strong Axis Initial Sample CCR Results

Case #	R	d	$\dfrac{d}{t_w}$	$\dfrac{t_f}{t_w}$	L	CCR
1	10	14	20	1.6	12	0.914
2	5	14	20	1.6	12	0.316
3	20	14	20	1.6	12	0.979
4	10	7.93	20	1.6	12	0.358
5	10	22.84	20	1.6	12	0.962
6	10	14	6.1	1.6	12	0.996
7	10	14	37.04	1.6	12	0.410
8	10	14	20	1.368	12	0.908
9	10	14	20	1.777	12	0.919
10	10	14	20	1.60	8	0.904

Table 8.5 (cont.): Strong Axis Initial Sample CCR Results

Case #	R	d	$\dfrac{d}{t_w}$	$\dfrac{t_f}{t_w}$	L	CCR
11	10	14	20	1.60	20	0.973
12	5	7.93	20	1.60	12	0.001
13	5	22.84	20	1.60	12	0.828
14	20	7.93	20	1.60	12	0.774
15	20	22.84	20	1.60	12	0.999
16	5	14	6.1	1.60	12	0.909
17	5	14	37.04	1.60	12	0.002
18	20	14	6.1	1.60	12	0.994
19	20	14	37.04	1.60	12	0.823
20	5	14	20	1.368	12	0.314
21	5	14	20	1.777	12	0.413
22	20	14	20	1.368	12	0.989
23	20	14	20	1.777	12	0.977
24	5	14	20	1.60	8	0.322
25	5	14	20	1.60	20	0.371
26	20	14	20	1.60	8	0.998
27	20	14	20	1.60	20	0.940
28	10	7.93	6.1	1.60	12	0.938
29	10	7.93	37.04	1.60	12	0.130
30	10	22.84	6.1	1.60	12	0.998
31	10	22.84	37.04	1.60	12	0.779
32	10	7.93	20	1.368	12	0.373
33	10	7.93	20	1.777	12	0.406
34	10	22.84	20	1.368	12	0.985
35	10	22.84	20	1.777	12	0.991
36	10	7.93	20	1.60	8	0.490
37	10	7.93	20	1.60	20	0.278
38	10	22.84	20	1.60	8	0.999
39	10	22.84	20	1.60	20	0.995
40	10	14	6.1	1.368	12	0.987
41	10	14	6.1	1.777	12	0.992
42	10	14	37.04	1.368	12	0.351
43	10	14	37.04	1.777	12	0.992
44	10	14	6.1	1.60	8	0.997
45	10	14	6.1	1.60	20	0.984
46	10	14	37.04	1.60	8	0.511

Table 8.5 (cont.): Strong Axis Initial Sample CCR Results

Case #	R	d	$\dfrac{d}{t_f}$	$\dfrac{t_f}{t_w}$	L	CCR
47	10	14	37.04	1.60	20	0.441
48	10	14	20	1.368	8	0.866
49	10	14	20	1.368	20	0.812
50	10	14	20	1.777	8	0.965
51	10	14	20	1.777	20	0.948

8.5.2 Weak Axis Model

Finite Element Model

The finite element model used for the weak axis direction FRM is identical to that of the strong axis model described in section 8.5.1 except for the weak axis runs, the other support "pad" is used as shown in Figure 8.18. All other geometry and mesh boundaries are the same.
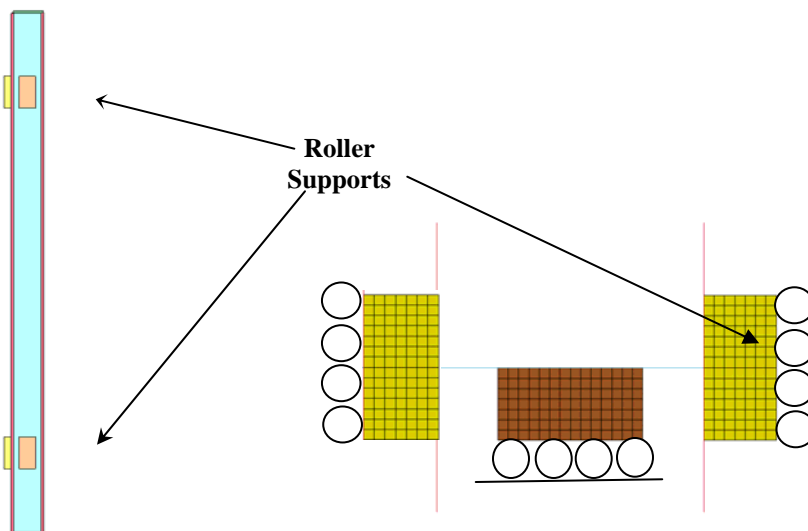
Figure 8.18: FRM Finite Element Model Boundary Conditions for Strong Axis

Loading

For the strong axis runs, the pressure load was applied to the web opposite the support as shown in. The loads were determined using BLASTX and were distributed over the height of the column using the procedure from Chapter 7. 70% of the web loads were applied to the inside of the flanges to remain consistent with loads without clearing effects. Additional modifications could be made to the model to incorporate clearing effects and cladding with more information given at the end of this chapter.
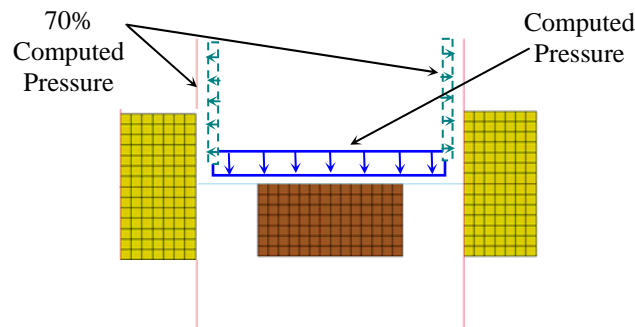
Figure 8.19: Description of FRM Loading for Weak Axis

Results

The 51 finite element model cases were run according to the loading described in the previous section. Results from two representative cases are given below. The first set of results is from Case # 1, which was the nominal case. The standoff was 10 ft, the column had a depth of 14 in, a width-thickness ratio of 20, a thickness ratio of 1.6 and a 12 ft length. A summary of the behavior through loading is given in Figure 8.20. The first three figures show the column being loaded by the blast pressure load. The third figure shows the column being initially loaded axially and the last figure given the column buckling in a first mode response in the region with the most blast damage.
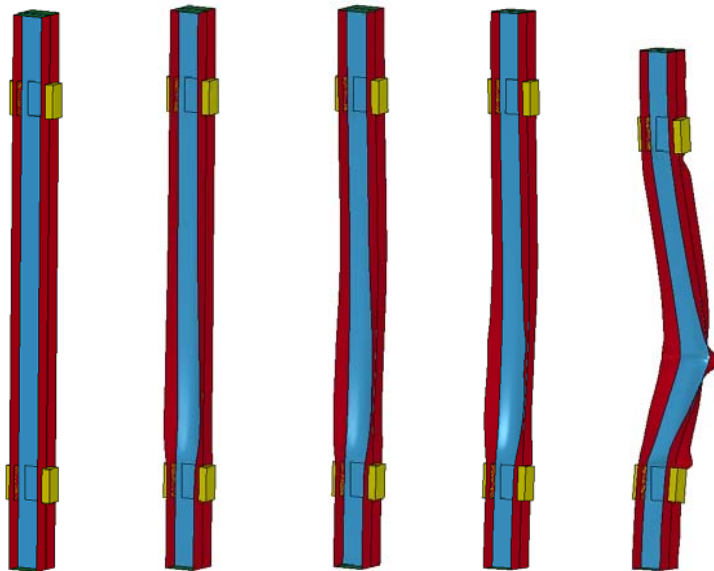
Figure 8.20: Column Behavior, Weak Axis – Example 1

The corresponding force diagram from this sample is given in Figure 8.21. From this plot, the capacity of the column at failure was 2,164 kips. This is compared to a virgin capacity test of 2,723 kips. The associated CCR is 0.792.
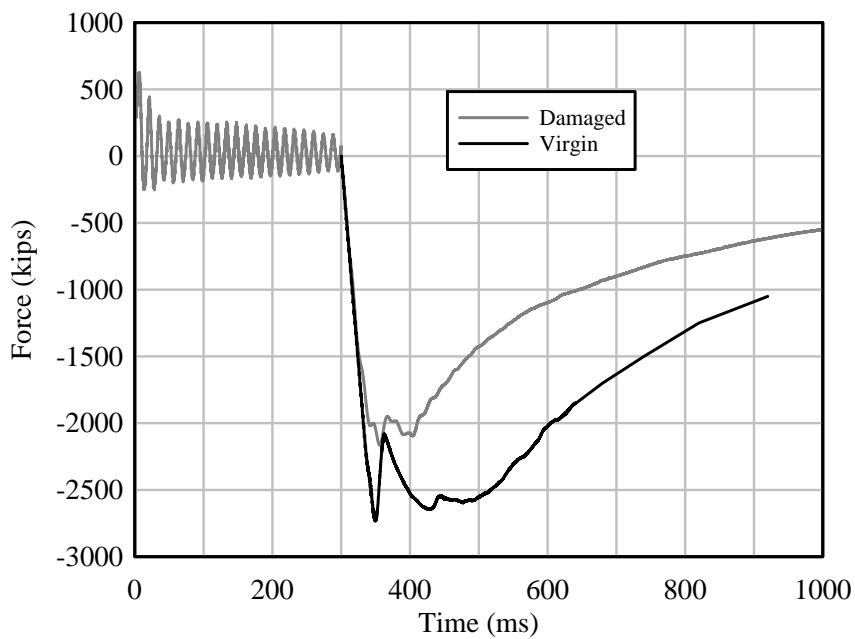
Figure 8.21: Column Force, Weak Axis – Example 1

The second set of results is from Sample # 7. This standoff was 10 ft, the column had a depth of 14 in, a width-thickness ratio of 37.04, a thickness ratio of 1.6 and a 12 ft length. A summary of the behavior through loading is given in Figure 8.22.
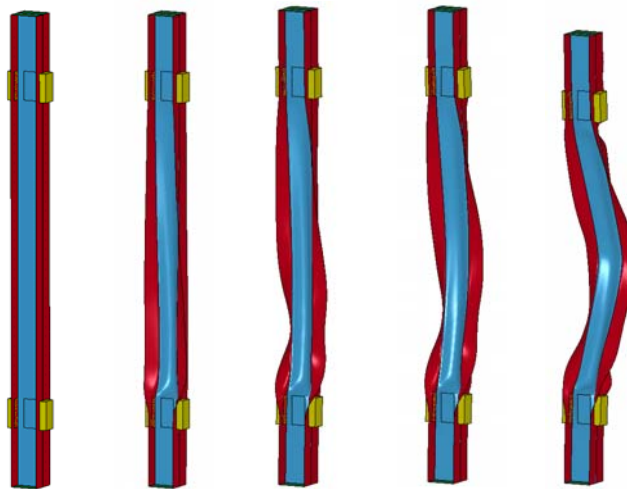
Figure 8.22: Column Behavior, Weak Axis – Example 2

The corresponding force diagram from this sample is given in Figure 8.23. From this plot, the capacity of the column at failure was 356 kips. This is compared to a virgin capacity test of 1,345 kips. The associated CCR is 0.265. The results from the remaining samples are summarized in Table 8.4.
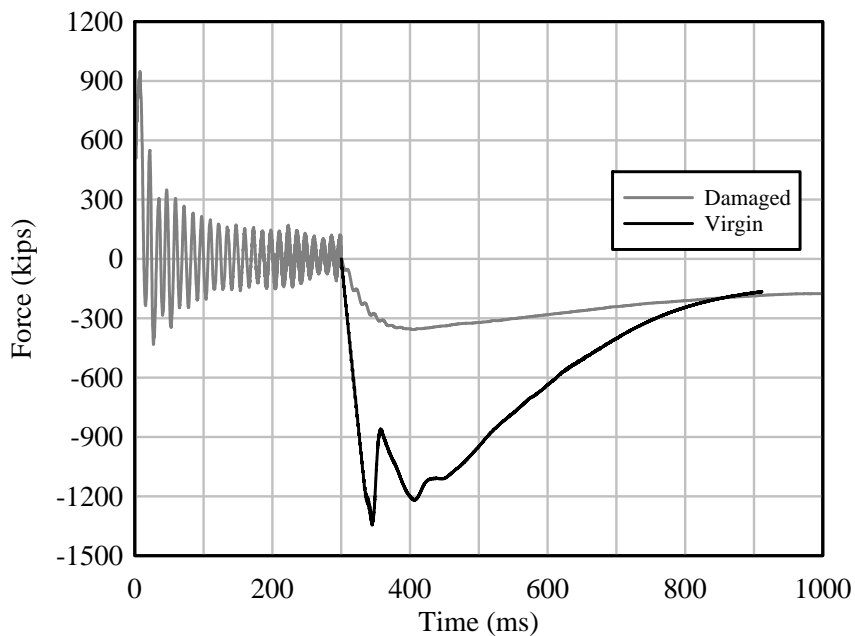
Figure 8.23: Column Force, Weak Axis – Example 2

Table 8.5: Weak Axis Initial Sample CCR Results

Case #	R	d	$\dfrac{d}{t_w}$	$\dfrac{t_f}{t_w}$	L	CCR
1	10	14	20	1.6	12	0.792
2	5	14	20	1.6	12	0.238
3	20	14	20	1.6	12	0.951
4	10	7.93	20	1.6	12	0.326
5	10	22.84	20	1.6	12	0.907
6	10	14	6.1	1.6	12	0.923
7	10	14	37.04	1.6	12	0.265
8	10	14	20	1.368	12	0.693
9	10	14	20	1.777	12	0.735
10	10	14	20	1.60	8	0.765
11	10	14	20	1.60	20	0.405
12	5	7.93	20	1.60	12	0.139
13	5	22.84	20	1.60	12	0.543
14	20	7.93	20	1.60	12	0.698
15	20	22.84	20	1.60	12	0.986
16	5	14	6.1	1.60	12	0.706
17	5	14	37.04	1.60	12	0.022

Table 8.5 (cont.): Weak Axis Initial Sample CCR Results

Case #	R	d	$\dfrac{d}{t_w}$	$\dfrac{t_f}{t_w}$	L	CCR
18	20	14	6.1	1.60	12	0.988
19	20	14	37.04	1.60	12	0.632
20	5	14	20	1.368	12	0.382
21	5	14	20	1.777	12	0.262
22	20	14	20	1.368	12	0.898
23	20	14	20	1.777	12	0.964
24	5	14	20	1.60	8	0.397
25	5	14	20	1.60	20	0.069
26	20	14	20	1.60	8	0.962
27	20	14	20	1.60	20	0.829
28	10	7.93	6.1	1.60	12	0.700
29	10	7.93	37.04	1.60	12	0.038
30	10	22.84	6.1	1.60	12	0.969
31	10	22.84	37.04	1.60	12	0.554
32	10	7.93	20	1.368	12	0.315
33	10	7.93	20	1.777	12	0.364
34	10	22.84	20	1.368	12	0.838
35	10	22.84	20	1.777	12	0.931
36	10	7.93	20	1.60	8	0.486
37	10	7.93	20	1.60	20	0.099
38	10	22.84	20	1.60	8	0.913
39	10	22.84	20	1.60	20	0.786
40	10	14	6.1	1.368	12	0.892
41	10	14	6.1	1.777	12	0.943
42	10	14	37.04	1.368	12	0.096
43	10	14	37.04	1.777	12	0.151
44	10	14	6.1	1.60	8	0.910
45	10	14	6.1	1.60	20	0.823
46	10	14	37.04	1.60	8	0.239
47	10	14	37.04	1.60	20	0.059
48	10	14	20	1.368	8	0.712
49	10	14	20	1.368	20	0.306
50	10	14	20	1.777	8	0.794
51	10	14	20	1.777	20	0.491

8.6 Model Training & Validation

Training for both the strong and the weak axis models was done using the same procedure. The description of the methodology is shown with the strong axis data in this section and both trained models will be validated in the next section.

Before the sample sets were placed into the training algorithm, a visual assessment of the CCR data was completed to insure that the initial sample set was sufficiently representative of the problem domain. For each parameter, the parameter value was plotted against the CCR. These are shown in Figure 8.24, Figure 8.25, Figure 8.26, Figure 8.27, Figure 8.28 for standoff, depth, width-thickness ratio, thickness ratio and column length, respectively.

From these plots, it was decided additional sample points were needed to get a better distribution on some of the parameters. From the plot of standoff, Figure 8.24, it was determined that both the 5 ft and the 10 ft standoff have a relatively even distribution of CCR values. The 20 ft standoff however, has mostly higher values for CCR and the transition between 10 ft and 20 ft standoff may not be easily defined. Also, in the 5 ft to 10 ft range, it is known that column behaviors can vary much more with closer charges, so additional points between these values were added as well.

The depth vs. CCR plot shows a clear distribution of CCR values. It shows that, for the most part, a larger depth creates a larger column capacity were as a smaller depth leads to a smaller capacity. The nominal values of depth have a good distribution of values. There are a few values of CCR in the higher range for lower depths and therefore additional points were added to focus on this transition.

Figure 8.26 shows the values of CCR for varying width to thickness ratio. The values for CCR are distributed over the range for both the nominal and the maximum values. The minimum value of this ratio yielded results that are mostly in the higher range of CCR. Additional points between the minimum and the nominal may need to be considered to correctly model this transition.

The plots for both thickness ratio, Figure 8.27, and length, Figure 8.28 both showed to have a good distribution in their data as well, having a spread of values over the CCR range. From this information, a few sample runs were considered before training the data. A summary of these runs is shown in Table 8.6 and the points are indicated on the CCR distributions in red.

Table 8.6: Additional Cases used for Training ANN

Case #	R	d	$\dfrac{d}{t_w}$	$\dfrac{t_f}{t_w}$	L	CCR Strong Axis	CCR Weak Axis
52	12	10	15	1.5	15	0.804	0.507
53	12	10	12	1.5	15	0.836	0.615
54	15	9	15	1.5	15	0.784	0.572
55	15	7	12	1.5	15	0.747	0.535
56	7	12	15	1.5	15	0.646	0.322
57	7	14	15	1.5	15	0.832	0.454
58	9	8	20	1.65	10	0.265	0.380
59	12	8	28	1.65	10	0.370	0.263
60	12	8	20	1.65	10	0.557	0.483
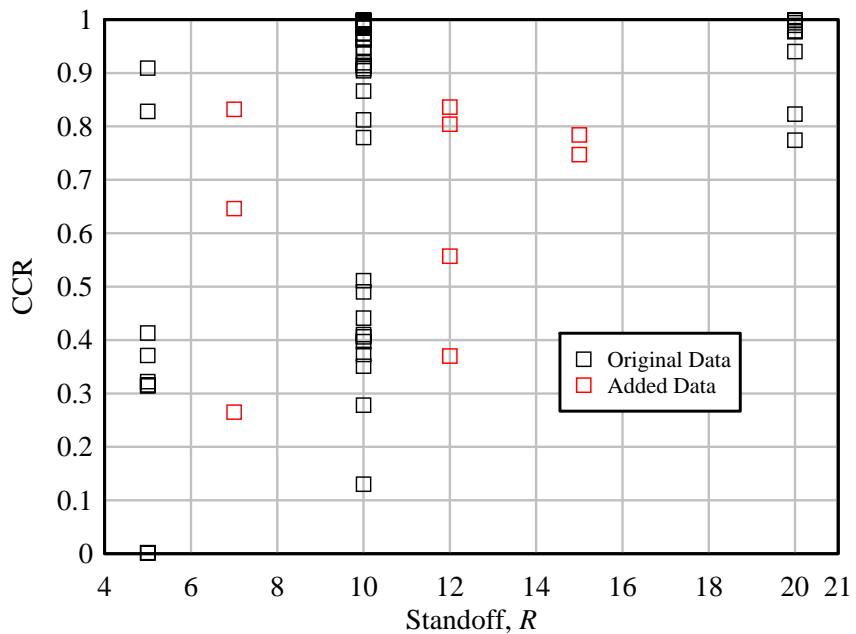
Figure 8.24: Initial Sample Set Data – Standoff vs. CCR
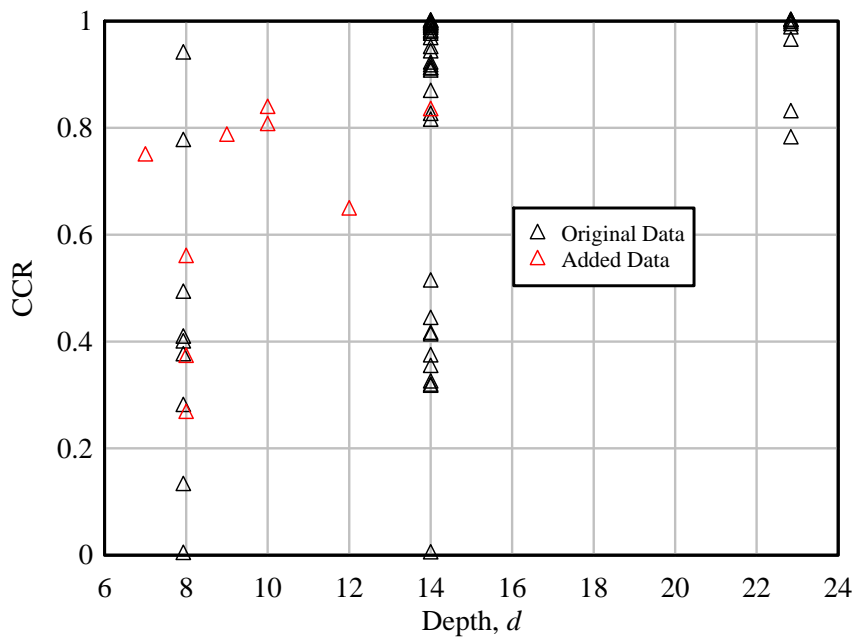
Figure 8.25: Initial Sample Set Data – Depth vs. CCR
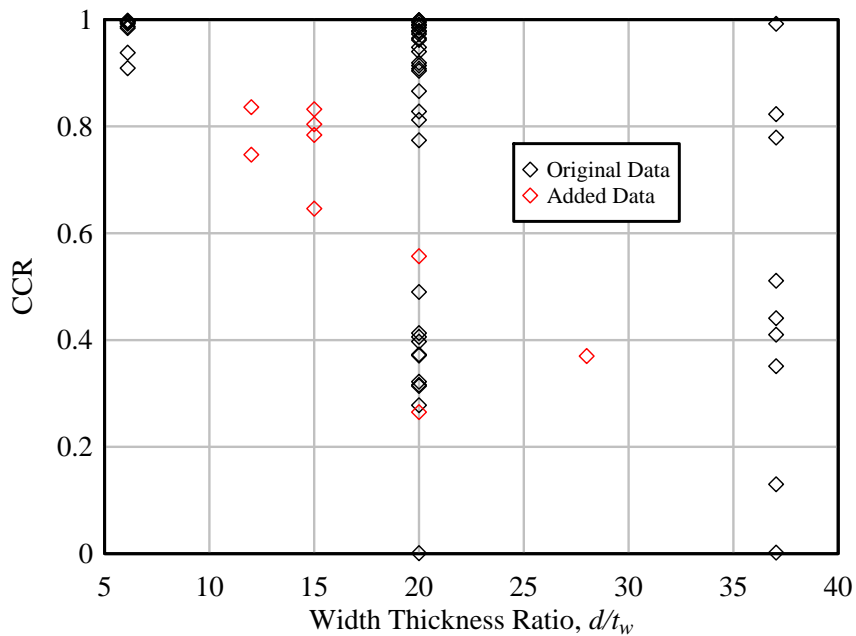
Figure 8.26: Initial Sample Set Data – Width-Thickness Ratio vs. CCR
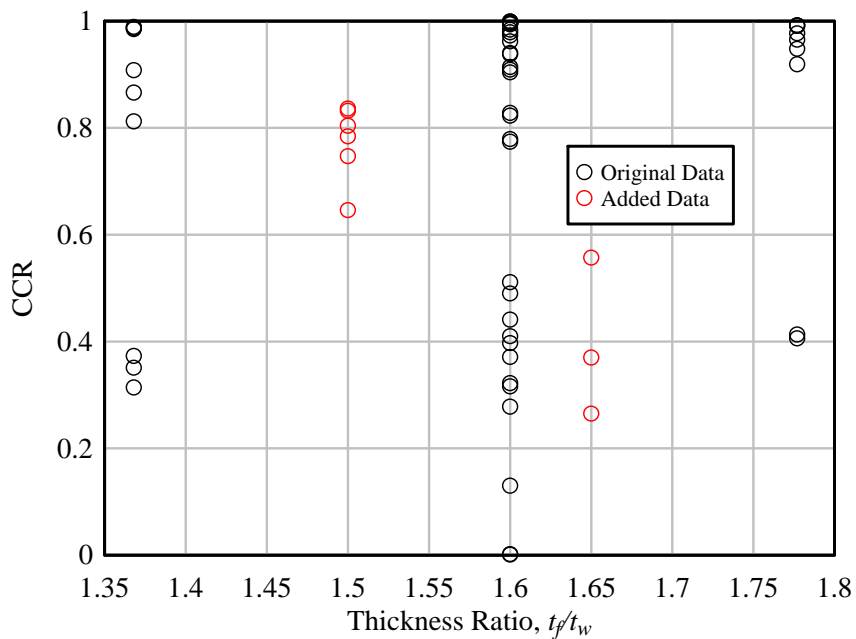
Figure 8.27: Initial Sample Set Data – Thickness Ratio vs. CCR
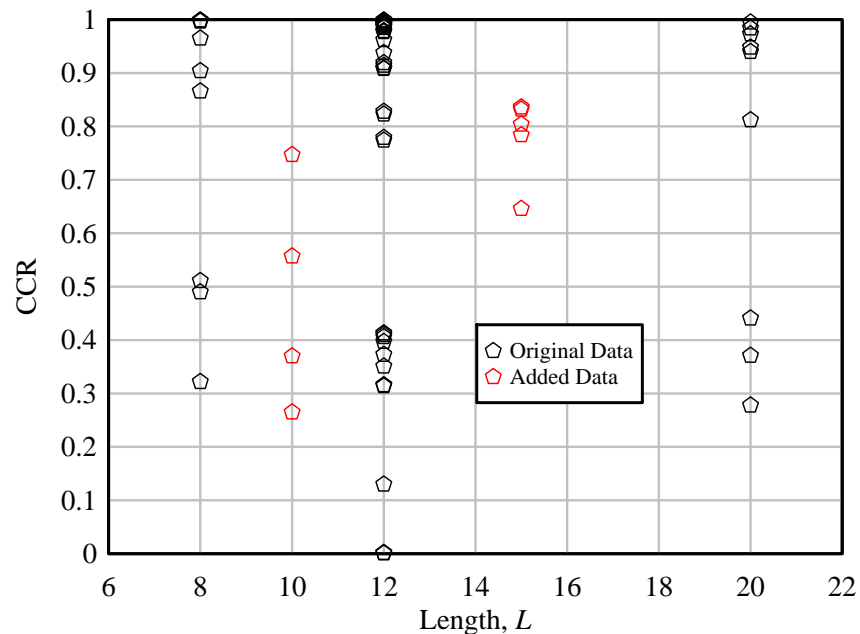
Figure 8.28: Initial Sample Set Data – Length vs. CCR

The structure of the neural network was set up to accommodate the five input parameters and the one output parameter and is given in Figure 8.29. Initially, six hidden neurons were chosen for the first neuron layer. A logarithmic transfer function was used for both the hidden layer and the output layer because values of CCR are restricted from 0 to 1.

The Levenberg-Marquardt Algorithm (LMA) [38, 39] was used as the training algorithm for this dissertation and is built into the MATLAB Neural Network Toolkit [40]. The LMA provides a numerical solution for the minimization of a function created over a space of parameters by making the assumption that the underlying function being modeled by the neural network is linear. Based on this calculation, the minimum can be determined exactly in a single step. The calculated minimum is tested, and if the new error there is less, the algorithm moves the weights to this new point [37].
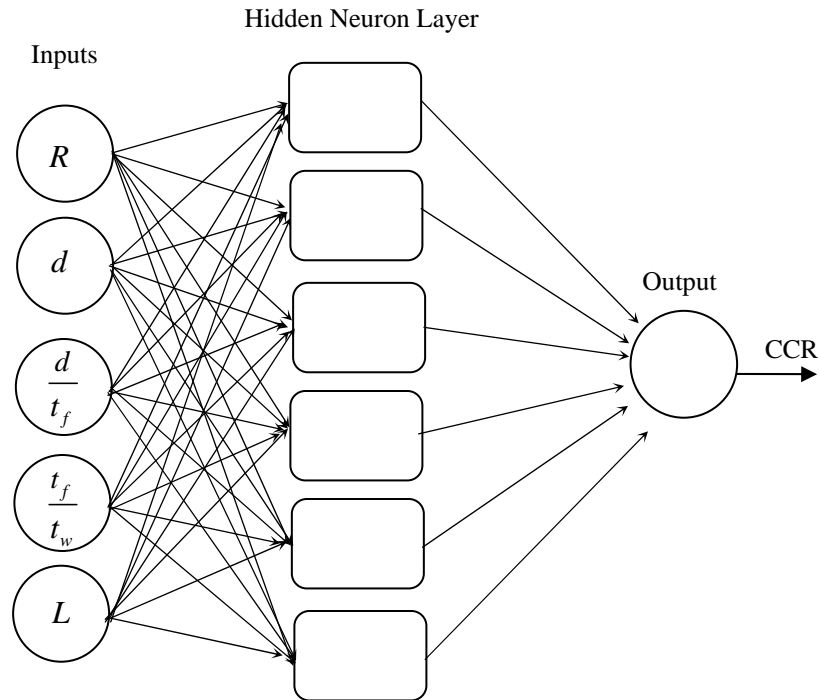
Figure 8.29: Steel Column Neural Network Structure

The 60 sample input sets were randomly divided into 51 training data samples and 9 validation data samples. The LMA algorithm was trained with the training data sample as long as the network continued to reduce the error in the validation sample output. A plot of the mean square error versus iteration is given in Figure 8.30. From this plot, it is evident that the model was learning and reducing error with each iteration.

The network can also be tested by using the initial training data (FE inputs) as inputs and having the model determine the outputs. If the outputs are compared to the targets (FE outputs) a regression analysis can be conducted. The results from this regression analysis are shown in Figure 8.31. The R value for the regression was 0.965.
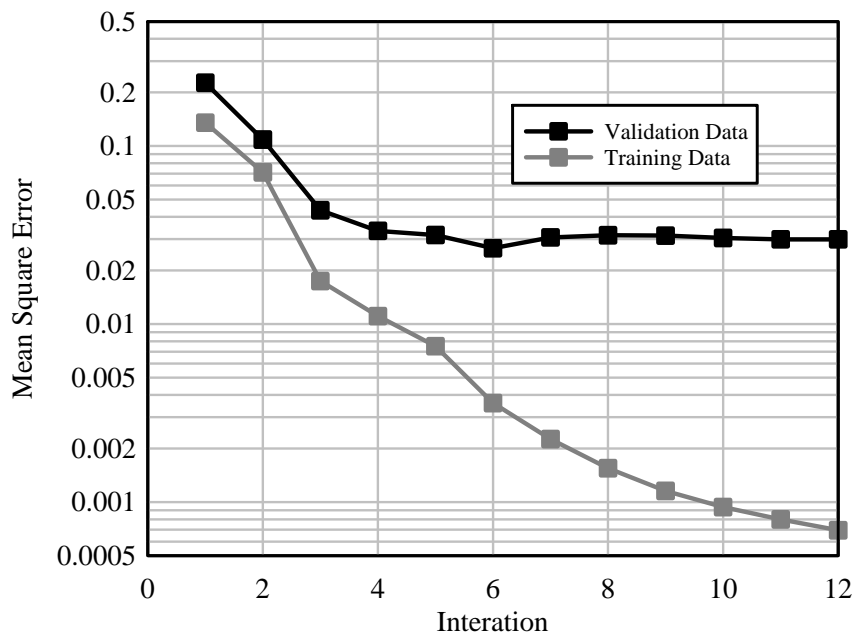
Figure 8.30: Neural Network Training Performance
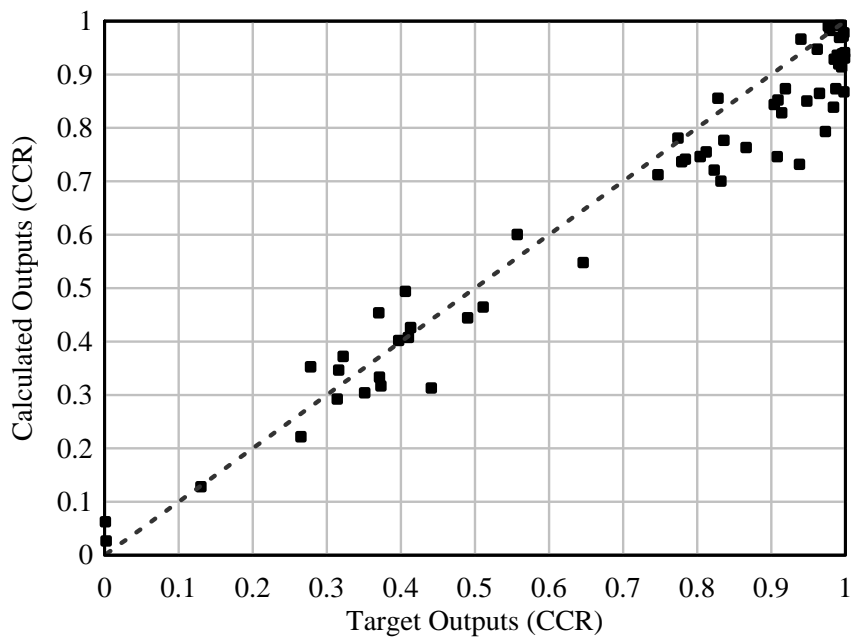
Figure 8.31: Comparison of Target Outputs and Calculated Outputs

8.7   Model Testing

The model was tested versus one randomly selected column in each of the four depth ranges (W8, W10, W12, W14). Each column was randomly assigned a standoff from 3 ft to 25 ft and a column length from 8 ft to 25 ft. The results from the random selection are given in Table 8.7. For each column, the finite element model was run given the loading condition described by the standoff. The residual capacity of the column was calculated and compared to the output from the FRM. The results for both the strong and the weak axis models are given in Section 8.7.1 and 8.7.2, respectively.

Table 8.7: Randomly Selected Test Points

Test #	W Section	R (ft)	d (in)	$\dfrac{d}{t_w}$	$\dfrac{t_f}{t_w}$	L (ft)
Strong Axis						
1	W8x48	18	8.5	21.25	1.71	12
2	W10x112	18	11.36	15.05	1.66	21
3	W12x79	4	12.38	26.3	1.56	14
4	W14x99	15	14.16	22.73	1.6	10
Weak Axis						
5	W8x40	18	8.25	22.92	1.5	18
6	W10x33	7	9.73	33.55	1.68	20
7	W12x152	6	13.71	15.76	1.61	22
8	W14x68	20	14.04	33.83	1.73	20

8.7.1   Strong Axis Direction Results

The results from the finite element runs for the four tests cases are given in Figure 8.1. These plots include the force time history for the virgin, as well as, the damaged capacity column. The column in Test 3 failed during the blast and therefore no residual capacity was computed. The results are compared to the CCR values calculate from the FRM and are summarized in Table 8.8 along with the calculated error between the FRM

and the finite element model calculations. The results from the FRM are all within 8% of the finite element calculations which is well within an acceptable range of this dissertation. If a lesser error was desired, additional data point could be added and the model could be retrained.
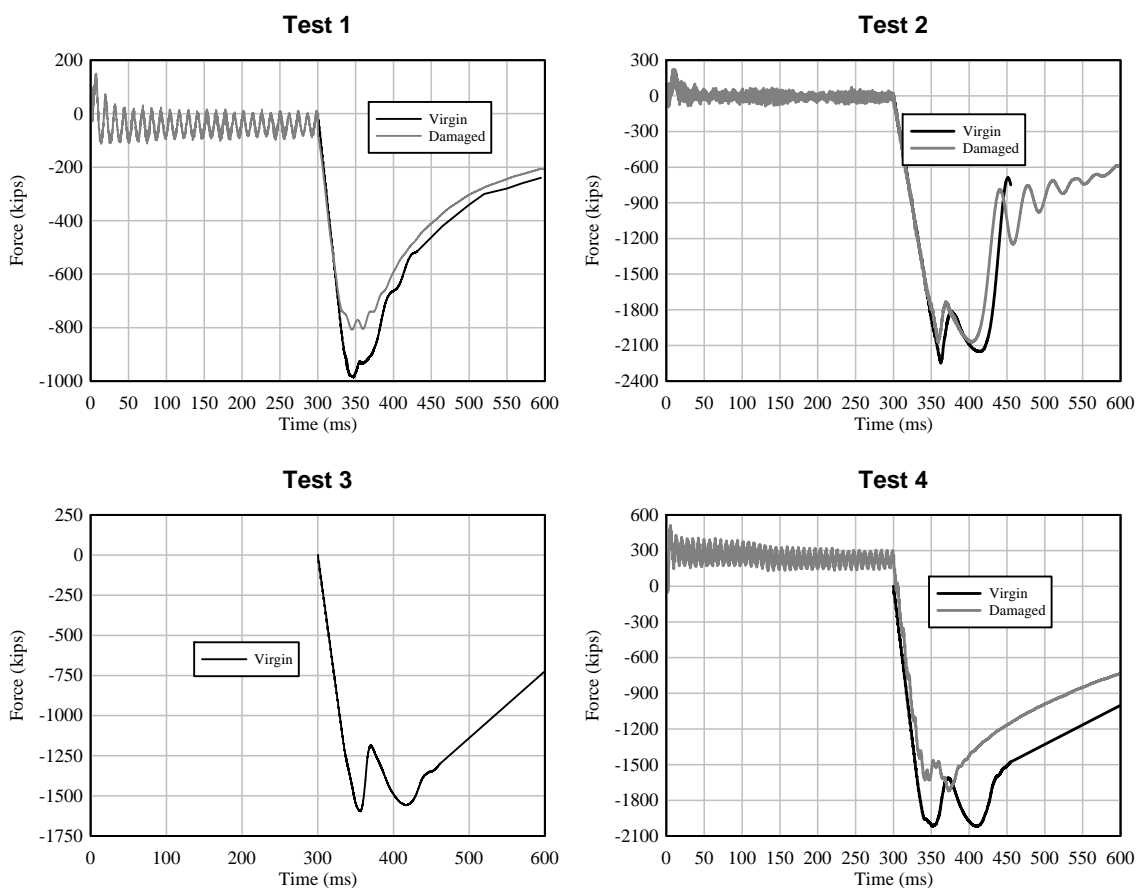
Figure 8.32: Force Results from Strong Axis Test Cases

Table 8.8: Results from Strong Axis Test Cases

Test #	W Section	Finite Element CCR	FRM CCR	Difference
1	W8x48	0.800	0.739	0.061
2	W10x112	0.924	0.906	0.018
3	W12x79	0.001	0.050	0.049
4	W14x99	0.853	0.884	0.031

8.7.2 Weak Axis Direction Results

The force time histories from the virgin and damaged columns are shown in Figure 8.33 for the test cases. Table 8.9 summarizes the results from the FEA and from the FRM. All CCR values for the weak axis FRM are within 0.09 of the actual CCR. Adding additional data points, is again, an option if a lesser error is required.
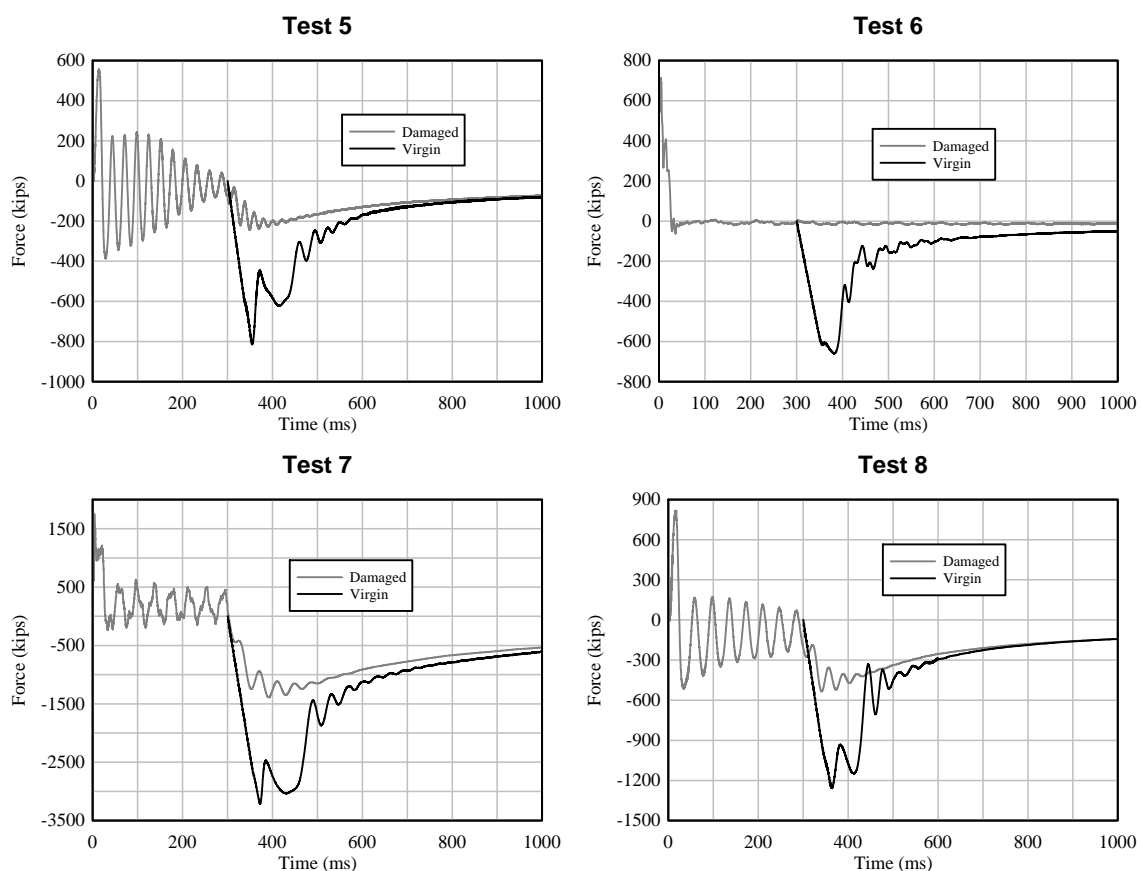
Figure 8.33: Force Results from Weak Axis Test Cases

Table 8.9: Results from Weak Axis Test Cases

Test #	W Section	Finite Element CCR	FRM CCR	Difference
1	W8x48	0.300	0.387	0.087
2	W10x112	0.002	0.006	0.004
3	W12x79	0.231	0.231	0.000
4	W14x99	0.425	0.477	0.052

8.7.3 Threat Assessment Example Using Fast Running Model

8.7.4 Threat Scenario

A threat assessment and recommendation is necessary for a steel structure with 14 ft, W12x136 columns. The building is located along a street with a curb and concrete barriers located 7 ft from the structure with the strong axis facing the street as in Figure 8.34. Vehicle ANFO bombs in the range of 500 to 1,500 lbs are being considered. The task is to determine if 7 ft standoff is sufficient or is additional standoff required.
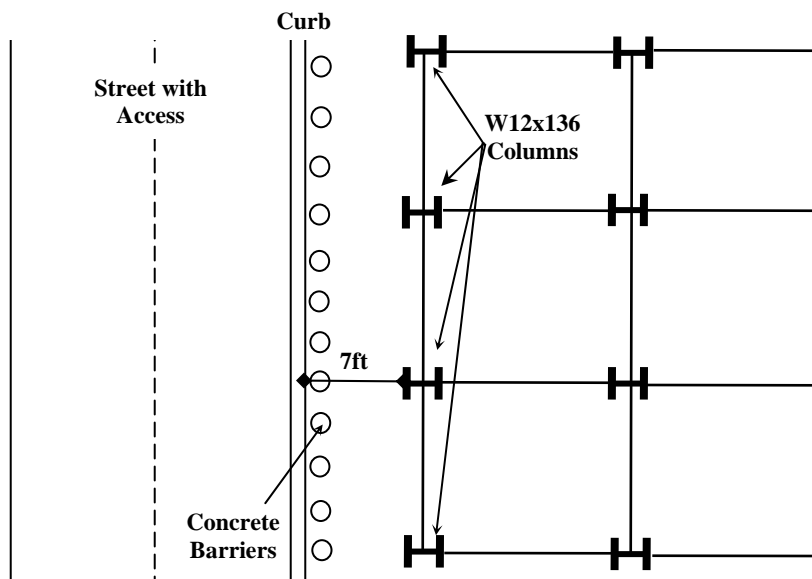
Figure 8.34: Threat Scenario Example

8.7.5 Threat Assessment

The assessment can be conducted using the FRM with the steps highlighted below. This assessment does not include any factors of safety, but it is possible to place a factor (> 1.0) on the charge or the standoff (< 1.0) to increase the conservativeness of the assessment.

1) Because the FRM is based on 1,000 lbs of TNT, if the maximum charge is not 1,000 lbs of TNT, calculated scaled distance, Z, using the largest charge equivalent TNT charge and given standoff.

$$TNT_{eq} = (0.82)(1{,}500 \text{ lbs ANFO}) = 1{,}230 \text{ lb of TNT} \tag{8.4}$$

$$Z \equiv \frac{R}{W^{1/3}} = \frac{7\,ft}{(1{,}230lbs)^{1/3}} = 0.65 \tag{8.5}$$

2) Convert the scaled distance found in (1) to an effective standoff, R_{eff}, for 1,000 lbs of TNT.

$$Z \equiv \frac{R}{W^{1/3}} \tag{8.6}$$

$$0.65 = \frac{R_{eff}}{(1{,}000lbs)^{1/3}} \tag{8.7}$$

$$R_{eff} = 6.5\,ft \tag{8.8}$$

3) Input dimensions of given column into Fast Running Model and run model to produce output CCR.

R_{eff}	d	$\dfrac{d}{t_w}$	$\dfrac{t_f}{t_w}$	L	CCR (Output)
6.5 ft	13.4 in	16.97	1.58	14	0.721

4) If CCR > 0.95, Column is likely not to fail. If CCR < 0.95, run FRM for larger

R_{eff} .

R_{eff}	d	$\dfrac{d}{t_w}$	$\dfrac{t_f}{t_w}$	L	CCR (Output)
7 ft	13.4 in	16.97	1.58	14	0.799
8 ft	13.4 in	16.97	1.58	14	0.895
9 ft	13.4 in	16.97	1.58	14	0.956

The required R_{eff} is therefore 9 ft.

5) Convert 1,000 lbs of TNT at R_{eff} to 1,500 lbs ANFO at required standoff, R_{req} .

$$\frac{R_{eff}}{R_{req}} = \left(\frac{W_{eff}}{W_{req}} \right)^{1/3} \tag{8.9}$$

$$\frac{9\,ft}{R_{req}} = \left(\frac{1,000lbs}{1,230lbs} \right)^{1/3} \tag{8.10}$$

$$R_{req} = 9.64 \text{ ft} \tag{8.11}$$

Therefore the required standoff is 10 ft. Additional security or barricades should be placed to increase the standoff from the existing curb.

8.8 Applications to Additional Loading Scenarios

The FRM described in the above sections was meant to serve as the initial column model for which additions, modifications and improvements can be made. It represented the most basic column loaded with blast pressures which do not take into account clearing effects or cladding. This section serves to describe the ways in which the model could be modified for different loading scenarios and additions of other components.

8.8.1 Clearing Effects

Clearing on a finite surface occurs when the diffraction of blast waves around the leading edges of the cross section and the propagation of rarefaction waves from the leading edges to the column centerline causes a more rapid reduction in pressure and impulse than in on an infinite plane as shown in Figure 8.35 [41]. Clearing effects can develop on columns when the columns are not shielded from the blast by architectural cladding or glass. The FRM model developed in this dissertation was trained using loads calculated for an infinite surface and then those loads were placed on a column. In order to take into account clearing effects, the loads on the columns must be scaled
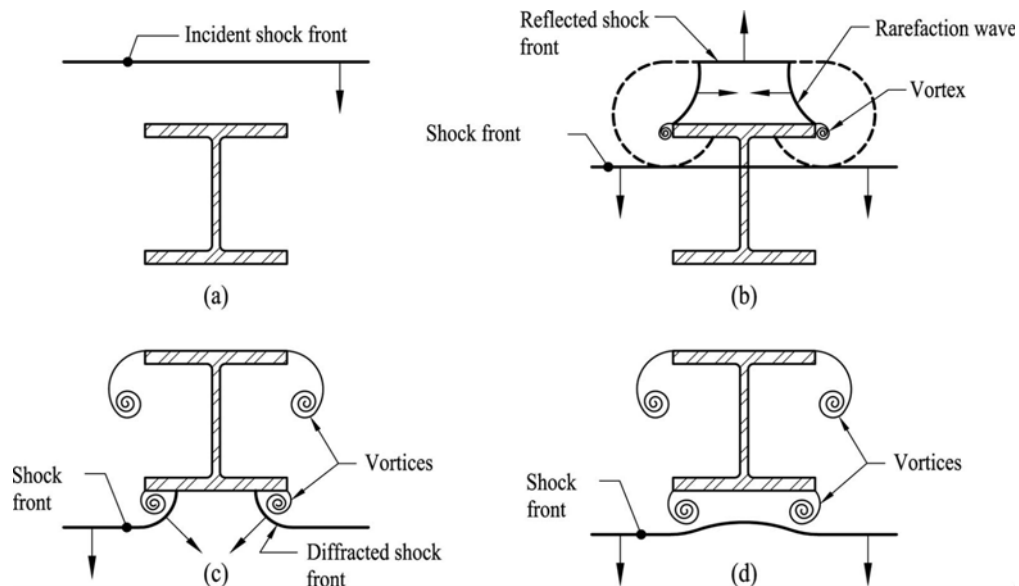
Figure 8.35: Propagation of a Shockwave around a W-Shape from [40]

Numerical research for columns in the strong axis direction has been conducted by [41]. It was found that for a given charge mass, held constant for a range of standoff distances, impulse is approximately proportional to $1/R$ when considering an infinite surface. If clearing is considered, the reflected impulse is still proportional to $1/R$, but

can be 50% lower than the value computed for an infinite surface. This was found to be valid for scaled distance values from approximately 1 to 10.

The 50% reduction in reflected impulse can be implemented into the model by scaling the standoff distance, R. To do this, the value of scaled distance, Z, should be computed for the given threat scenario from Equation 2.7. The computational methods from Chapter 2 can then be used to estimate a new scaled distance, Z_{clear}, that corresponds to a 50% loss in reflected impulse as shown in . The Z_{clear} should then be converted back to the equivalent clearing standoff, R_{clear}, which can be input as a parameter in the FRM.
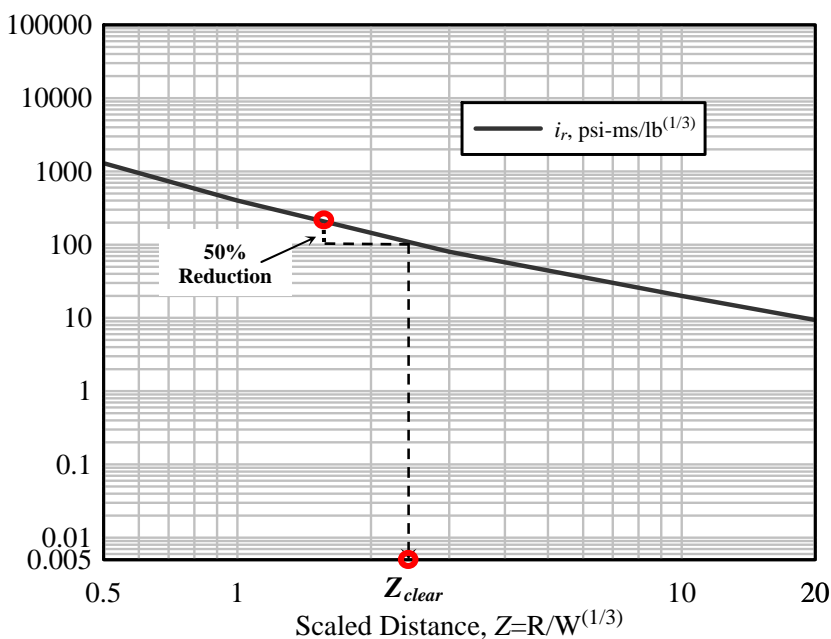
Figure 8.36: Graphical Method for Clearing Impulse from Reflected Impulse

The effects of clearing on the weak axis were discussed in Section 7.4 and it was found that the waves travel inside the web and flange region and are essentially trapped. There is almost no reduction in load to what is calculated for an infinite surface. From

Figure 7.32, it is shown that the effects of wrap-around are minor and only up to about 5% of the impulses felt on the inside web. For this reason, it can be assumed that the FRM can be used to predict column behavior with clearing for the weak axis without any modification.

8.8.2 Cladding

The effects of cladding on columns are currently being researched at UCSD. Due to the increase in mass and prevention of clearing, cladding can contribute to additional impulse on the column. An initial series of tests have been conducted on various dimensions of concrete cladding using the UCSD Blast Simulator. These tests utilize the same setup as the experiments for fracture, discussed in Section 6.6 with the addition of a piece of cladding that is accelerated toward the specimen as seen in the schematic in Figure 8.37 and the photo in Figure 8.38.
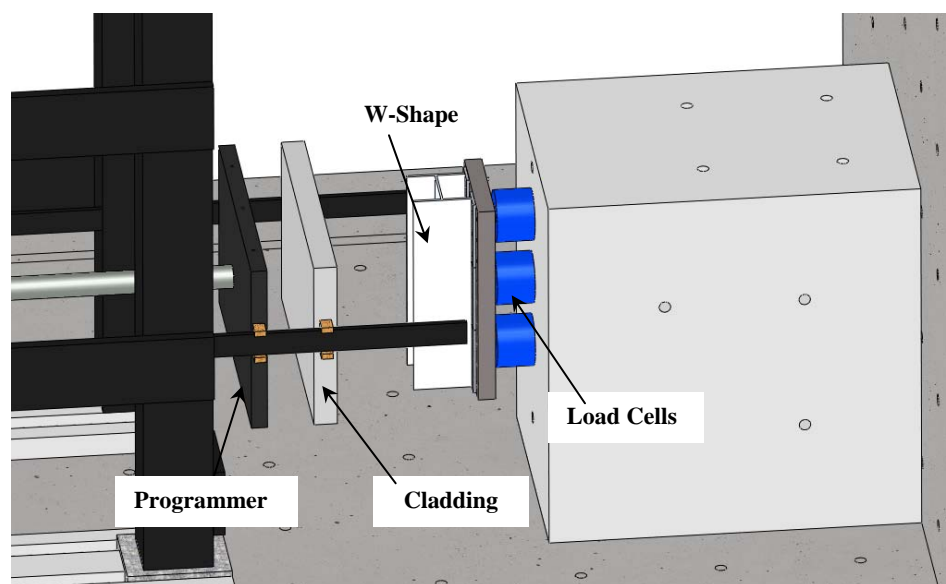
Figure 8.37: Schematic of Cladding Test Setup
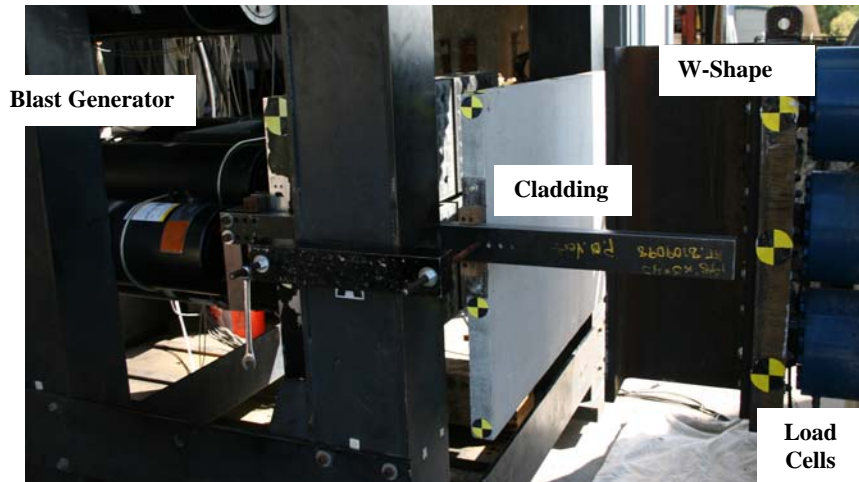
Figure 8.38:Photo of Cladding Test Setup

The high speed cameras were able to capture the progression of breakup of the concrete and photos from an experiment are given in Figure 8.39. Load cells measured the force applied to the column for various sizes of cladding. Initial tests have shown that the addition of mass and width of the cladding increases the impulse on the column up to some effective width. Additional research is necessary in order to quantify this effect. Once a scale factor, c, on the impulse can be determined as was done for clearing, it can be incorporated into the FRM using $R_{cladding} = cR$.

Figure 8.39:Strong Axis Cladding Propagation of Damage

The effects of clearing on the weak axis have shown to change the behavior of the load entirely. The cladding does not allow pressure to initially enter into the open area and impact the web. Instead, the cladding loads the flanges and then breaks up and the web is loaded. This was evident in one of the tests, shown in Figure 8.40, in which the cladding was stuck in between the flanges and the web was not loaded, but a force value was recorded by the load cells. The addition of cladding on the weak axis to the FRM would require additional research as well as additional finite element runs due to the fact that the FRM did not load the flanges directly.
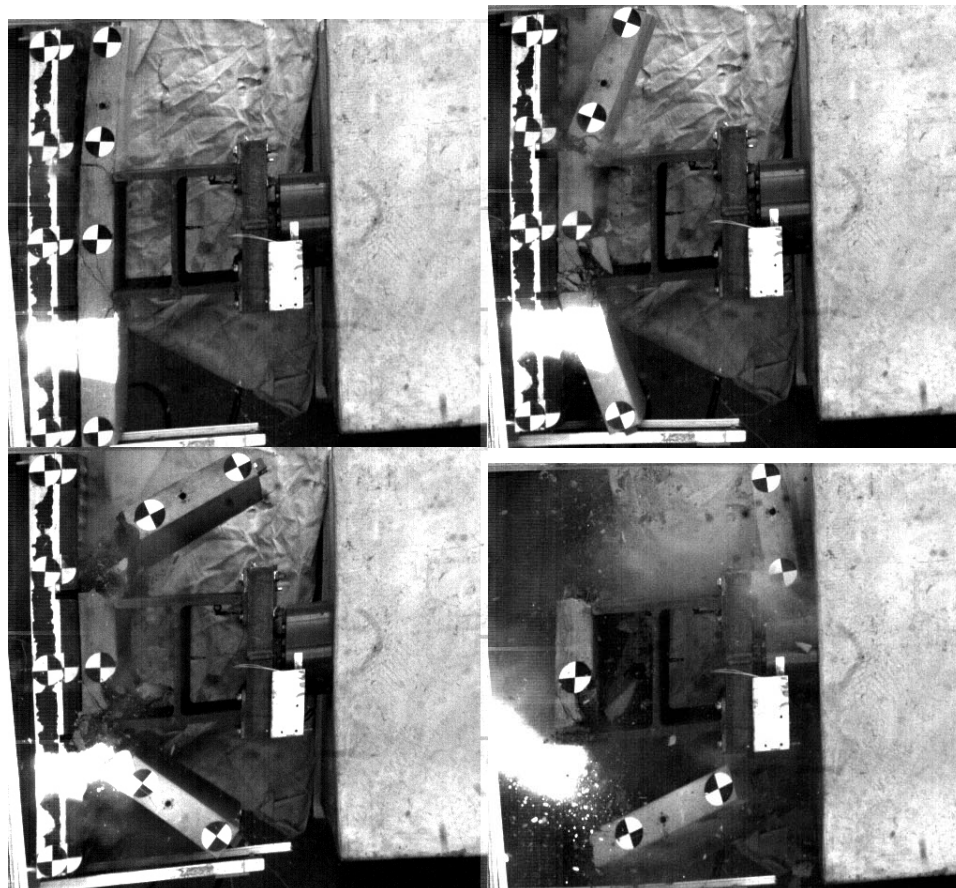
Figure 8.40: Weak Axis Cladding Propagation of Damage

8.8.3 Future Model Adaptations

The FRM was developed to allow for modification as data becomes available. Effects of components such as beam, connections, baseplates and splices could be added by adapting the model to incorporate those systems or by simulating the system with springs or rotational constraints. The use of the artificial neural network makes the addition of other features much less difficult than other methods because a large subset of the data is already in use and the inclusion of other parameters requires minimal runs and not an entire parameterization study.

8.9 Summary

This chapter responded to the growing necessity of a fast running model to predict column capacity that, unlike typical methods such as SDOFs, could take into account column effects that can vary with a standoff and charge size such as localized web buckling, flange bending and web fracture. The model was created using a simplified finite element model to populate a data set. The input parameters were chosen based on typical column dimensions as well as typical threat scenarios. The output, CCR, was selected to be a ratio of the damaged column capacity to the virgin column capacity.

An artificial neural network was used to predict the output parameter and the methodology for the development including parameterization and model training was described. The FRM was tested with four cases in both the strong and weak axis model which all produced responses close to that of the finite element runs. It was concluded that the model, using 60 finite element runs, is able to predict the response of relevant columns with an adequate (<10% error) level of confidence.

This chapter also discussed the current and future research that is being conducted and the incorporation of that research into the FRM. Different loading scenarios, such as clearing effects and the application of cladding, were included, as well as the future additions of components such as baseplates, beams and connections.

9 Conclusions

9.1 Summary & Conclusions

This dissertation presented research that was conducted with the UCSD Blast Simulator on steel W-Shape columns. The research produced methodologies and guidelines for testing steel columns in both the strong and weak axis directions that sufficiently replicated blast loads. The high quality experimental data that was generated during the testing was used to develop and validate numerical models which were utilized to further study the Blast Simulator and other column behaviors. Finally, the results of the studies were incorporated into the creation of a fast running model that can adequately predict the capacity of columns subjected to blast loads. Summaries for each individual chapter along with conclusions based on principal findings are included below.

Chapter 2 provided background information and a literature review of reference material. It included an overview of the quantification of blast loading, a description of the UCSD Blast Simulator, a literature review of previous field and simulator

experiments, information regarding relevant material models and an introduction to finite element analysis.

Chapter 3 presented research conducted experimentally on full-scale steel columns using the Blast Simulator oriented in the strong axis direction. The chapter described the experimental design, data acquisition and analysis techniques for applying blast-like loads onto the specimens. Also incorporated in the chapter was a method for utilizing the Blast Simulator to achieve a distribution of loadings, similar to those seen with vehicle bombs that are variable along the height of the column, using both blast generator types. Additionally, the chapter served to validate the Blast Simulator for these types of tests by demonstrating the close correlation of the behavior of the columns to that observed during field tests which included local and global deformations as well as web buckling.

A finite element model was calibrated and validated in Chapter 4 for steel columns loaded in the strong axis direction. The model was created from a combination of shell, solid and beam elements and is able to simulate the response of the columns for all experiments conducted and described in Chapter 3. Of particular importance to the simulation was the accuracy of the boundary condition modeling. It was found that the upper link boundary conditions did not provide the constraints that were initially desired during the experiments and therefore the link system had to be fully modeled to include rotation, which varied with velocity. The rotation was accounted for with the addition of a layer of rubber solid elements that allowed for additional rotation for the higher velocity impacts.

Chapter 5 provided the design, results and data analysis from a series of simulated blast tests on as-built steel wide-flange sections impacted in the weak axis direction with uniform and variable load along the height of the column. These tests were unique because they involved the use of a loading medium to transfer the loads from the flat impacting modules to the non-flat geometries inside the web and the flanges which are both loaded during a blast. Both water and sand were explored as medium and it was found that while they both effectively transferred the loads, the sand was the optimal choice because it did not impede the high speed camera views. Qualitative comparisons were included for a variety of tests in which confirmed that the Simulator was able to generate behavior and failures, including web fracture, column buckling and global deformations similar to those seen in the field.

Data generated from the test series described in Chapter 5 was used to generate and validate a numerical model for steel columns loaded in the weak axis direction which is discussed in Chapter 6. Smooth Particle Hydrodynamics were used to model the sand elements that underwent large deformations. The model was validated using the three Simulator sand tests and it was found that the finite element analysis could accurately predict the global behavior and buckling of the columns in all tests, but modeling fracture of the k-region proved to be problematic. The model was capable of producing a response that physically modeled fracture and the behavior associated with it, but predicting a failure strain that could be incorporated, with confidence, for future tests was not feasible due to the lack of data.

Chapter 7 included multiple investigations regarding steel column testing and finite element analysis. The first study considered the effects of BG impact synchronicity

on the response of the column through multiple finite element analyses. It was found that because the periods of the columns are far greater than that of the loads, a reasonably unsynchronized impact does not have a great effect on the column behavior and therefore, in most situations, does not have to be included in any associated modeling.

The second study involved momentum and kinetic energies of the impacting module and their affect of the displacement and behavior of the column. A finite element model was used to compare loadings of similar momentum and kinetic energies and it was found that using and equating $mv^{1.5}$ produced more similar results to the control columns than that of momentum or kinetic energy. Because of this, the velocity should be used as the means for varying impulse to its maximum effect and therefore, mass, and materials, can be reduced to some extent.

Methodologies for approximating blast loads on columns were also considered in this Chapter 7. Comparisons of different blast analysis programs which yielded slightly different pressures and impulses produced similar column behaviors and therefore the most time efficient program was utilized. It was also demonstrated that applying a fully distributed load along the width and height of the column is not necessary and an average distribution over a reduced number of locations is sufficient. For weak axis impacts it was determined that loading can be simplified by including a 70% scaled web load on the inside flanges of the column instead of conducting a full hydrocode simulation.

Lastly, Chapter 7 incorporated the findings of the dissertation into a loading protocol for testing steel columns with the UCSD Blast Simulator. The test design related impactor design and velocity to the column behaviors of a structure subjected to vehicle bombs and certain standoffs. This methodology is valid for designing similar future steel

column tests or column specimens that incorporate other components such as baseplates or connections.

A fast running model was developed and implemented in Chapter 8. The model was created using a simplified finite element model to populate a data set with input parameters chosen based on typical column dimensions as well as typical threat scenarios. The output was selected to be a ratio of the damaged column capacity to the virgin column capacity. An artificial neural network was used to predict the output parameter and the methodology for the development including parameterization and model training was included. The FRM was tested and validated with four cases in both the strong and weak axis directions which all produced responses close to that of the finite element simulations. This chapter also discussed the possibility for FRM use in different loading scenarios, such as clearing effects and the application of cladding, as well as the future additions of components such as baseplates, beams and connections.

9.2   Recommendations for Future Work

This section serves to give recommendations for future work relevant to blast loading of steel columns to be performed using the Blast Simulator or other testing methods.

The dissertation discussed the methods and testing for steel columns with a simplified boundary design of a concrete footer at the base. In order to generalize column behaviors, additional base and header designs still need to be considered. This would include the testing and modeling of various baseplate configurations as well as the case where the column is continuous to a basement level. The setup for this type of testing

could be easily incorporated into the testing design for the columns in this research. Additionally, further investigations into the response of the beam/column connections and quantification of the tension membrane forces developed in the beams should be considered due to the fact that connection damage could disrupt alternate load paths.

The addition of cladding on the front face of columns has demonstrated an increase in column impulse and deformation. Because of this, it is important to quantify the amount of increased load introduced by the cladding and any change to the distribution of loading on the column. Also, it should be determined if an effective width of the cladding does exist which could be used for design purposes.

There is also need to develop and test hardening strategies for as-built design, especially those cases where increasing standoff conditions is not possible. This may include the addition of stiffening plates or the use of kinetic energy defeat devices which are currently being researched.

From a modeling standpoint, a research effort to produce a fully characterized programmer model is still needed that can predict loads without calibration for each testing scenario. It is also recommended that an effort be placed on developing a material card to be implemented into LS-DYNA from the research findings.

Finally, as discussed in Chapter 4, it is suggested that research be continued to characterize the fracture and propagation of damage in the k-region during weak axis loading scenarios. It is likely that this would necessitate a large experimental effort and the creation of a new material model that could handle these types of behaviors.

APPENDIX A

This appendix presents additional results from the synchronicity study included in Chapter 7. The plots included in the body of the dissertation described analysis results from Scenario 2 with a maximum BG velocity of 40 m/s. The appendix presents results from Scenario 1 with BG velocities of a maximum of 20 m/s. Additional explanation of the plots can be found in Section 7.1.

BG Synchronicity Study Test Matrix

Test #	BG Impact Description	BG1 Impact Time (ms)	BG2 Impact Time (ms)	BG3 Impact Time (ms)	BG4 Impact Time (ms)
1	BGs Synchronized	0	0	0	0
2	BG1 Late	1	0	0	0
3	BG2 Late	0	1	0	0
4	BG3 Late	0	0	1	0
5	BG4 Late	0	0	0	1
6	BG1 Late	3	0	0	0
7	BG2 Late	0	3	0	0
8	BG3 Late	0	0	3	0
9	BG4 Late	0	0	0	3
10	BG1 Late	5	0	0	0
11	BG2 Late	0	5	0	0
12	BG3 Late	0	0	5	0
13	BG4 Late	0	0	0	5
14	BG1 Late	7	0	0	0
15	BG2 Late	0	7	0	0
16	BG3 Late	0	0	7	0
17	BG4 Late	0	0	0	7
18	BG1 and BG2 Late	1	1	0	0
19	BG1 and BG2 Late	3	3	0	0
20	BG1 and BG2 Late	5	5	0	0
21	BG1 and BG2 Late	7	7	0	0
22	BG 3 and BG 4 Late	0	0	1	1
23	BG 3 and BG 4 Late	0	0	3	3
24	BG 3 and BG 4 Late	0	0	5	5
25	BG 3 and BG 4 Late	0	0	7	7

Displacement Comparison for a Single BG 1 ms Late

Test #	Test Description	Maximum Displacement (in)	Maximum Displacement Error (%)	Residual Displacement (in)	Residual Displacement Error (%)
1	BGs Synchronized	1.67		1.17	
2	BG1 1 ms Late	1.73	3.59%	1.36	16.24%
3	BG2 1 ms Late	1.73	3.59%	1.26	7.69%
4	BG3 1 ms Late	1.67	0.00%	1.08	7.69%
5	BG4 1 ms Late	1.66	0.60%	1.15	1.71%

Displacement Comparison for a Single BG 3 ms Late

Test #	Test Description	Maximum Displacement (in)	Maximum Displacement Error (%)	Residual Displacement (in)	Residual Displacement Error (%)
1	BGs Synchronized	1.67		1.17	
2	BG1 3 ms Late	1.68	0.60%	1.27	8.55%
3	BG2 3 ms Late	1.53	8.38%	1.07	8.55%
4	BG3 3 ms Late	1.59	4.79%	1.10	5.98%
5	BG4 3 ms Late	1.64	1.80%	1.16	0.85%

Displacement Comparison for a Single BG 5 ms Late

Test #	Test Description	Maximum Displacement (in)	Maximum Displacement Error (%)	Residual Displacement (in)	Residual Displacement Error (%)
1	BGs Synchronized	1.67		1.17	
2	BG1 5 ms Late	1.48	11.38%	1.11	5.13%
3	BG2 5 ms Late	1.59	4.79%	1.09	6.84%
4	BG3 5 ms Late	1.54	7.78%	1.08	7.69%
5	BG4 5 ms Late	1.54	7.78%	1.16	0.85%

Displacement Comparison for a Single BG 7 ms Late

Test #	Test Description	Maximum Displacement (in)	Maximum Displacement Error (%)	Residual Displacement (in)	Residual Displacement Error (%)
1	BGs Synchronized	1.67		1.17	
2	BG1 7 ms Late	1.28	23.35%	0.91	22.22%
3	BG2 7 ms Late	1.55	7.19%	1.03	11.97%
4	BG3 7 ms Late	1.63	2.40%	1.13	3.42%
5	BG4 7 ms Late	1.64	1.80%	1.16	0.85%
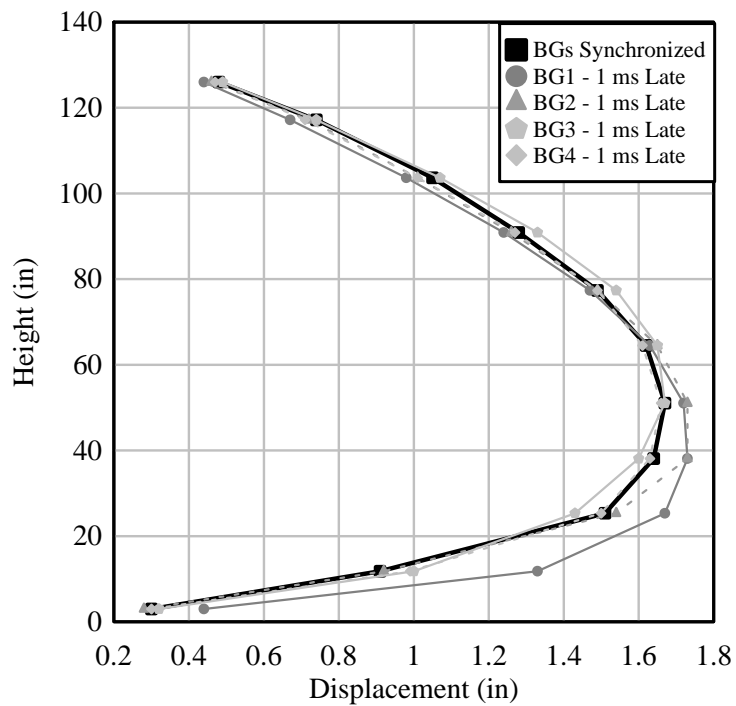
Maximum Displacements of Single BG, 1 ms Late
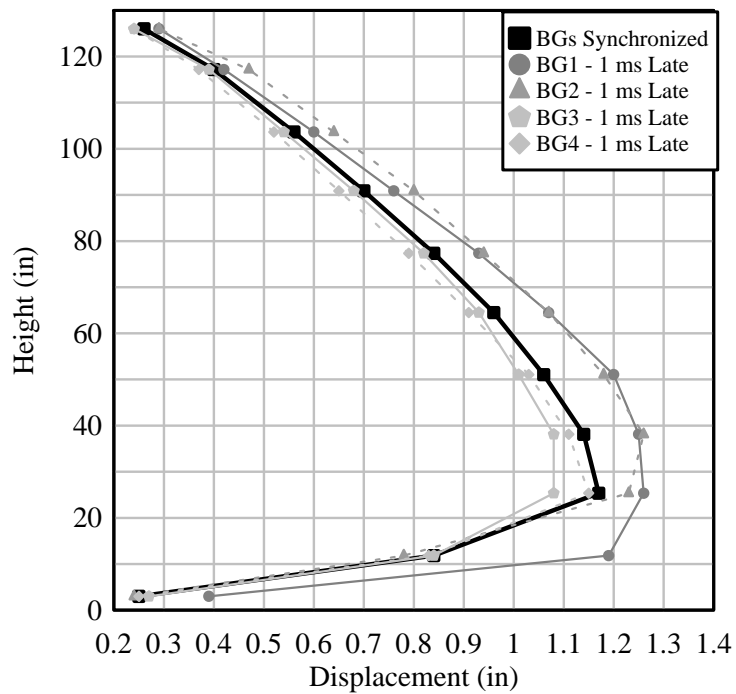
Residual Displacements of Single BG, 1 ms Late
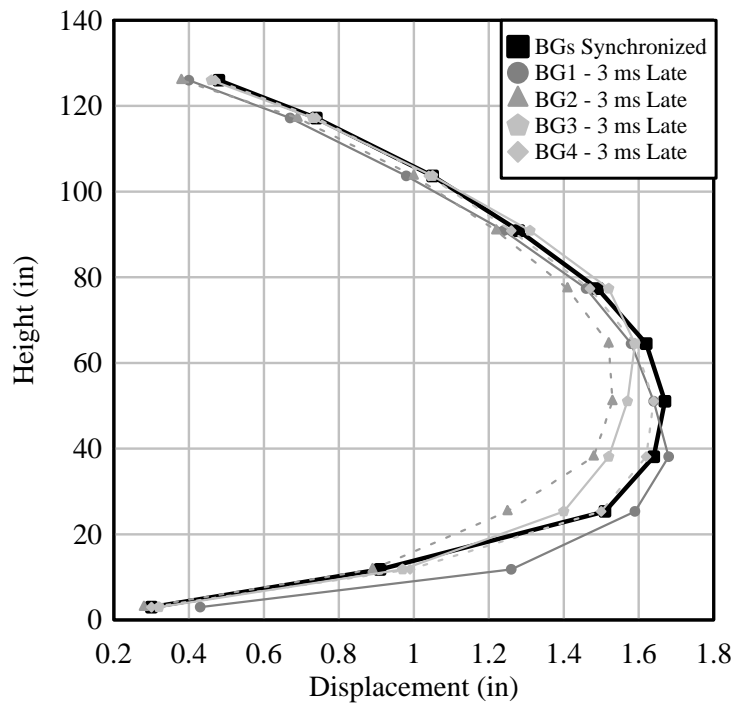
Maximum Displacements of Single BG, 3 ms Late
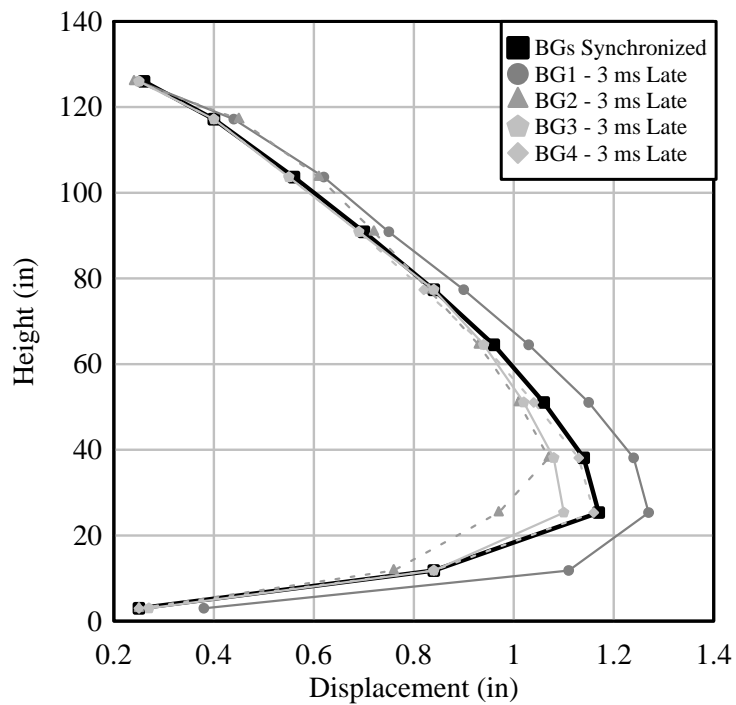
Residual Displacements of Single BG, 3 ms Late
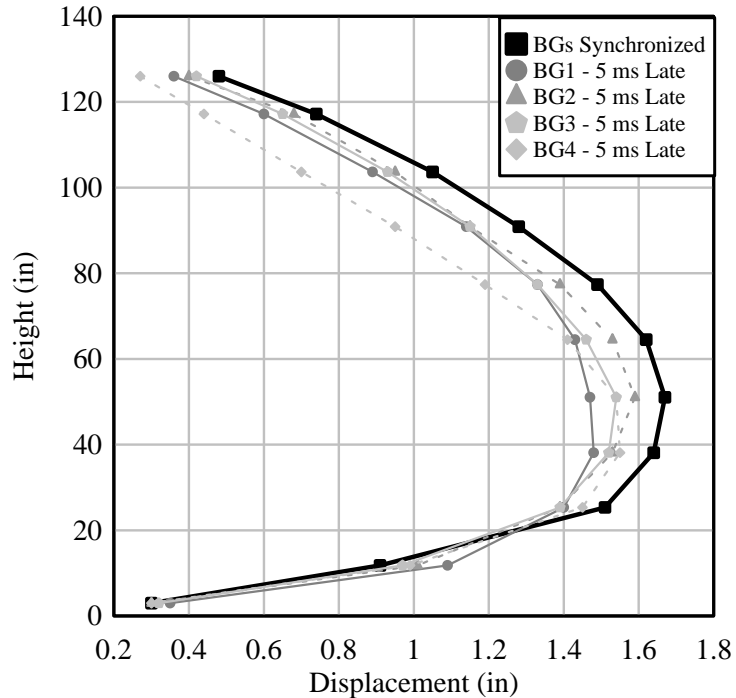
Maximum Displacements of Single BG, 5 ms Late
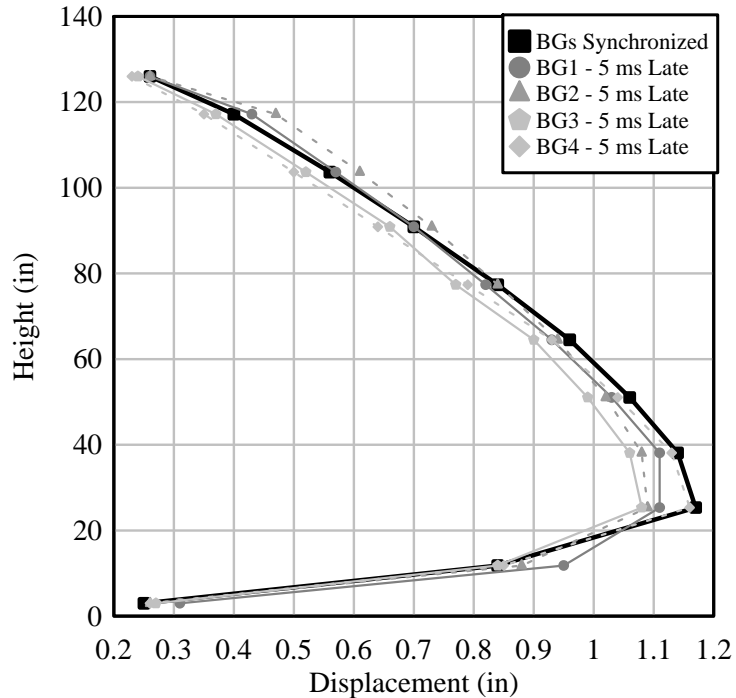
Residual Displacements of Single BG, 5 ms Late
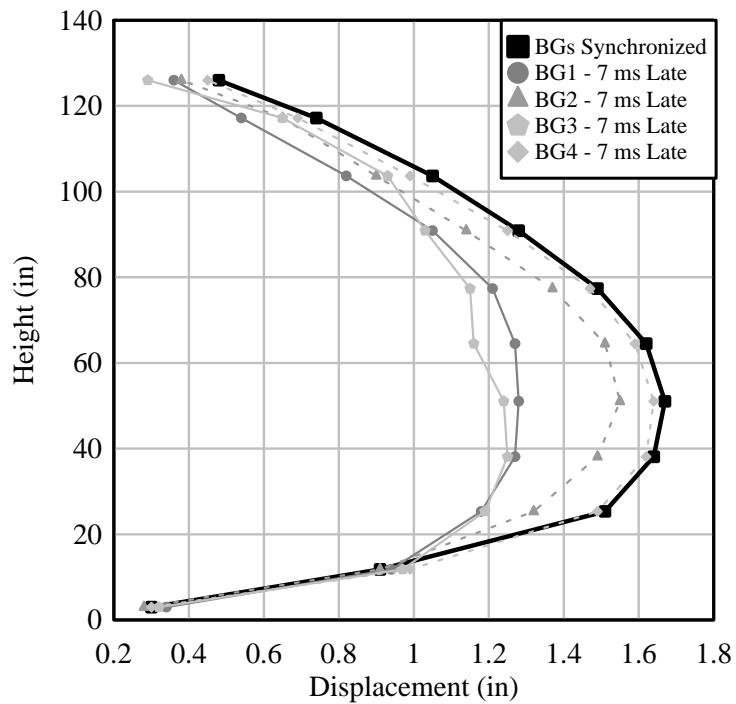
Maximum Displacements of Single BG, 7 ms Late
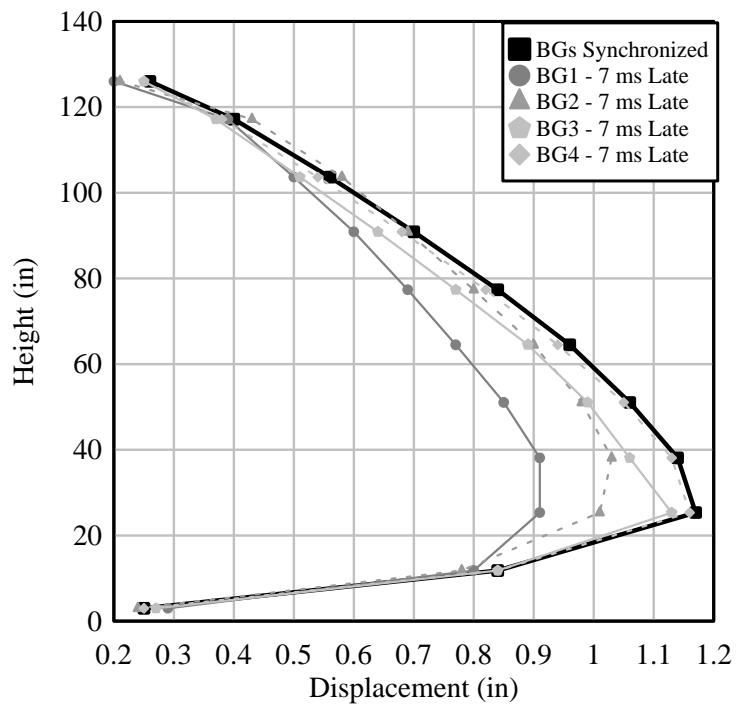
Residual Displacements of Single BG, 7 ms Late

Displacement Comparison for BG 50s Arriving Late

Test #	Test Description	Maximum Displacement (in)	Maximum Displacement Error (%)	Residual Displacement (in)	Residual Displacement Error (%)
1	BGs Synchronized	1.67		1.17	
2	BG1 & BG2 1 ms Late	1.86	11.38%	1.37	17.09%
3	BG1 & BG2 3 ms Late	1.77	5.99%	1.26	7.69%
4	BG1 & BG2 5 ms Late	1.68	0.60%	1.18	0.85%
5	BG1 & BG2 7 ms Late	1.63	2.40%	1.11	5.13%

Displacement Comparison for BG 25s Arriving Late

Test #	Test Description	Maximum Displacement (in)	Maximum Displacement Error (%)	Residual Displacement (in)	Residual Displacement Error (%)
1	BGs Synchronized	1.67		1.17	
2	BG3 & BG4 1 ms Late	1.61	3.59%	1.04	11.11%
3	BG3 & BG4 3 ms Late	1.52	8.98%	1.03	11.97%
4	BG3 & BG4 5 ms Late	1.48	11.38%	1.04	11.11%
5	BG3 & BG4 7 ms Late	1.48	11.38%	1.03	11.97%
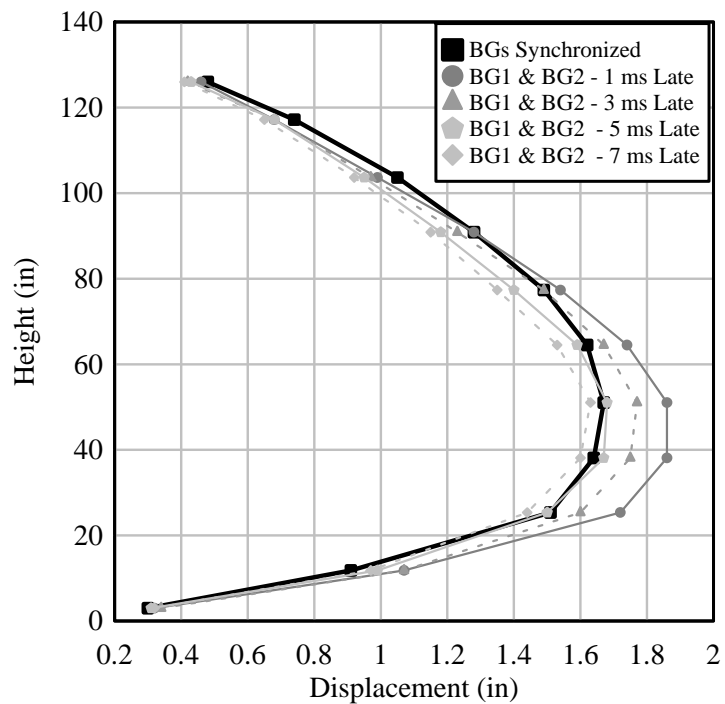
Maximum Displacements of BG50s Arriving Late
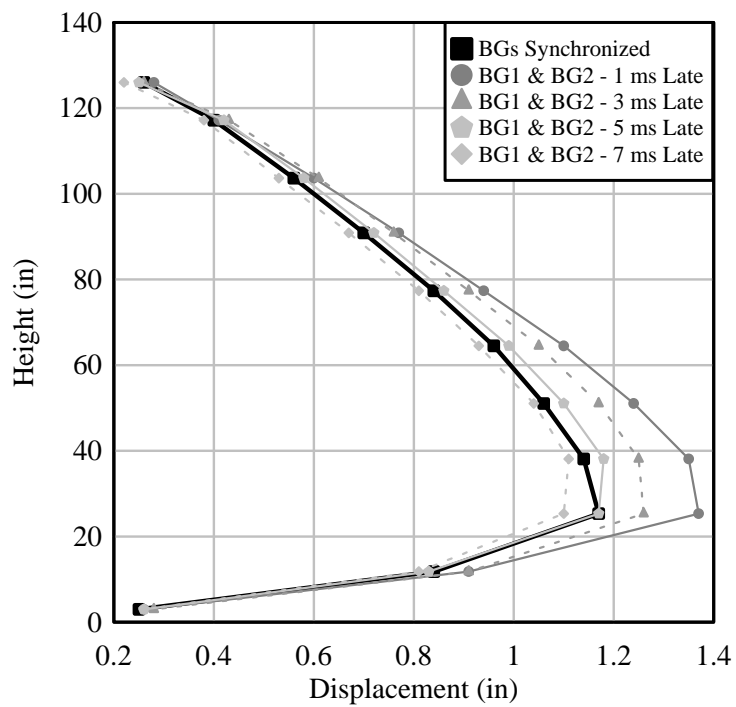
Residual Displacements of BG50s Arriving Late
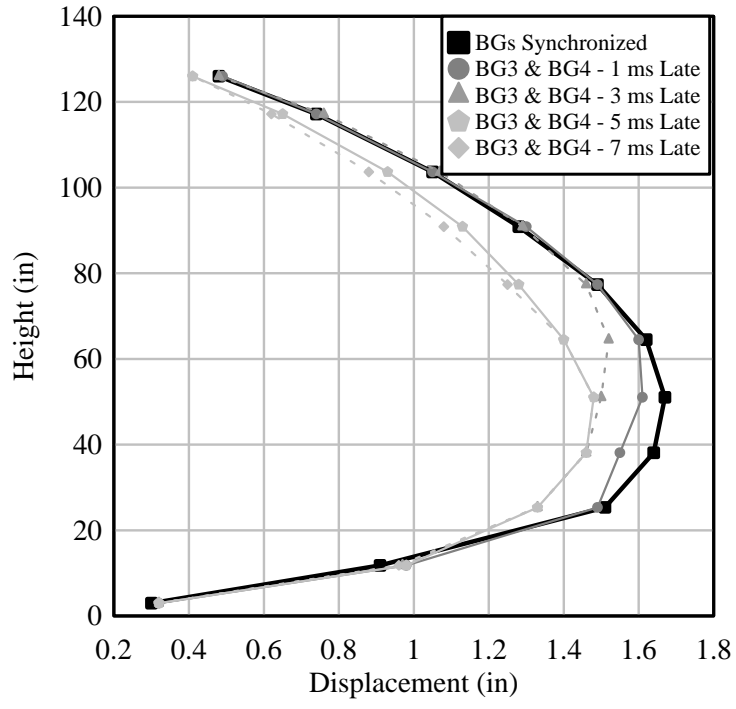
Maximum Displacements of BG25s Arriving Late
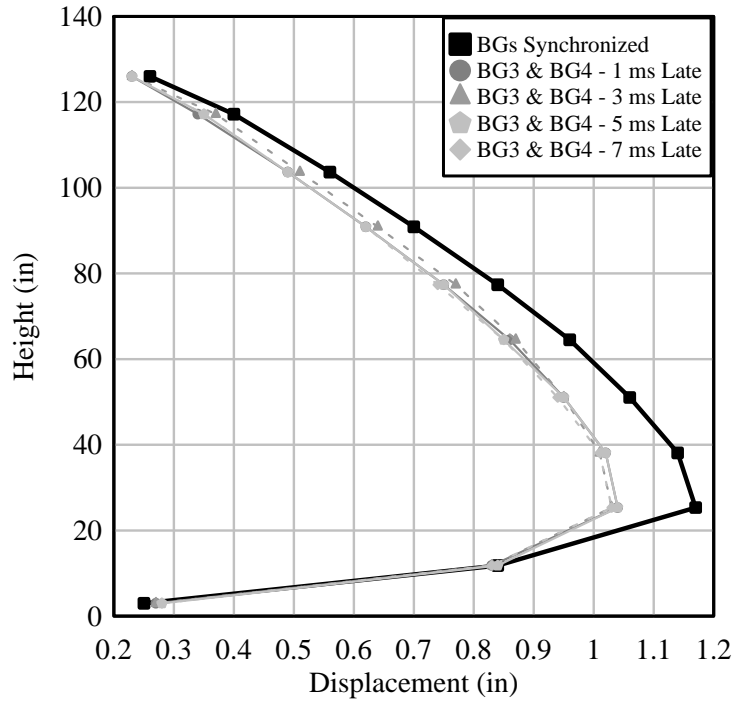
Residual Displacements of BG50s Arriving Late

APPENDIX B

This appendix provides pressure-time histories and impulses for various scaled distances to be used to apply blast loads to columns. The plots are provided at heights of every 12 inches which was proven to be sufficient for applying vehicle bomb loads on steel columns in Chapter 7. The plots do not include the negative phase and only include the pressures and any reflections up to about 10 ms.

$Z = 0.4$

Height = 6 in

Height = 18 in

Height = 30 in

Height = 42 in

Height = 54 in

Height = 66 in

$Z = 0.4$

Height = 78 in

Height = 90 in

Height = 102 in

Height = 114 in

Height = 126 in

Height = 138 in

$Z = 0.4$

Height = 150 in

Height = 162 in

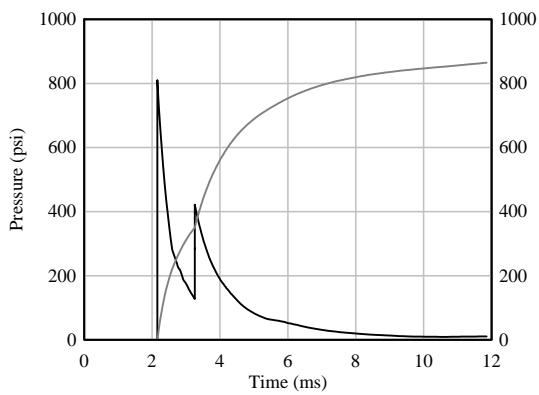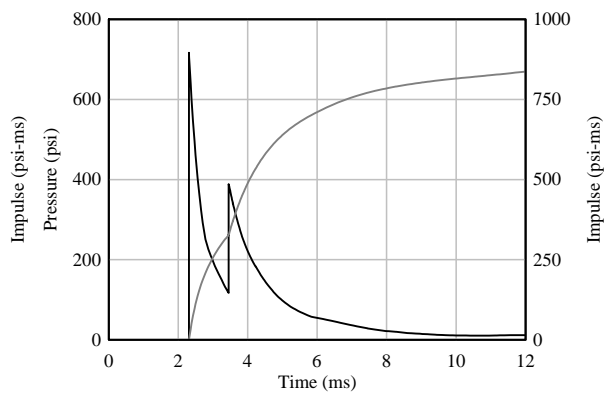**Height = 174 in**

Height = 186 in

Height = 198 in

Height = 210 in

$$Z = 0.4$$

Height = 222 in

Height = 234 in

$Z = 0.5$

Height = 6 in

Height = 18 in

Height = 30 in

Height = 42 in

Height = 54 in

Height = 66 in

$Z = 0.5$

Height = 78 in

Height = 90 in

Height = 102 in

Height = 114 in

Height = 126 in

Height = 138 in

$Z = 0.5$

Height = 150 in

Height = 162 in

Height = 174 in

Height = 186 in

Height = 198 in
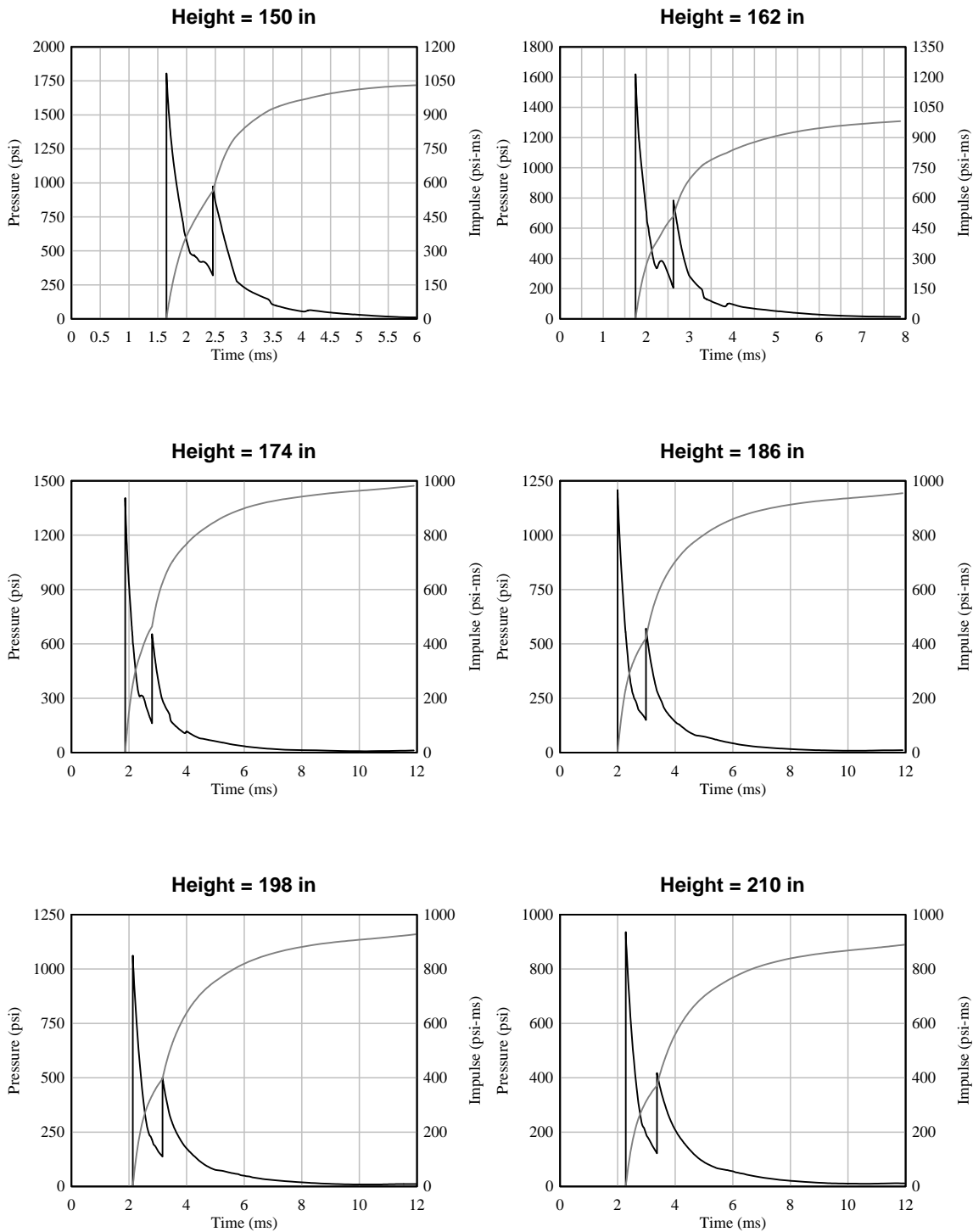

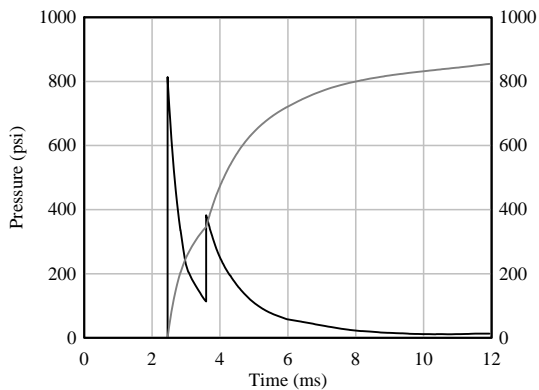**Height = 210 in**

$Z = 0.5$

Height = 222 in

Height = 234 in

$$Z = 0.6$$

Height = 6 in

Height = 18 in

Height = 30 in

Height = 42 in

Height = 54 in

Height = 66 in

$$Z = 0.6$$

Height = 78 in

Height = 90 in

Height = 102 in

Height = 114 in

Height = 126 in

Height = 138 in

$$Z = 0.6$$

Height = 150 in

Height = 163 in
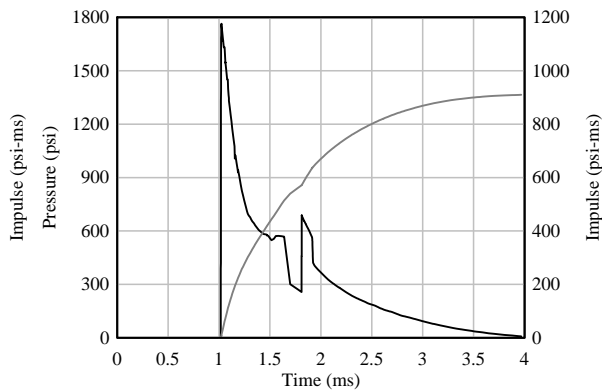
Height = 174 in

Height = 186 in

Height = 198 in

Height = 210 in

$$Z = 0.6$$

Height = 222 in

Height = 234 in

$$Z = 0.7$$

Height = 6 in

Height = 18 in

Height = 30 in

Height = 42 in

Height = 54 in

Height = 66 in

$Z = 0.7$

Height = 78 in

Height = 90 in

Height = 102 in

Height = 114 in

Height = 126 in

Height = 138 in

$$Z = 0.7$$

Height = 150 in

Height = 162 in

Height = 174 in

Height = 198 in

Height = 198 in

Height = 210 in

$$Z = 0.7$$

Height = 222 in

Height = 234 in

$$Z = 0.9$$

Height = 6 in

Height = 18 in

Height = 30 in

Height = 42 in

Height = 54 in

Height = 66 in

$$Z = 0.9$$

Height = 78 in

Height = 90 in

Height = 102 in

Height = 114 in

Height = 126 in

Height = 138 in

$$Z = 0.9$$
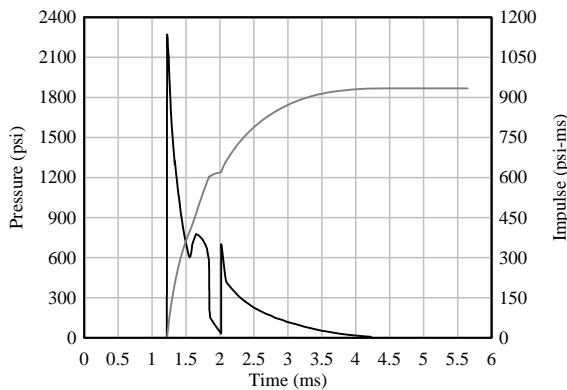
Height = 150 in
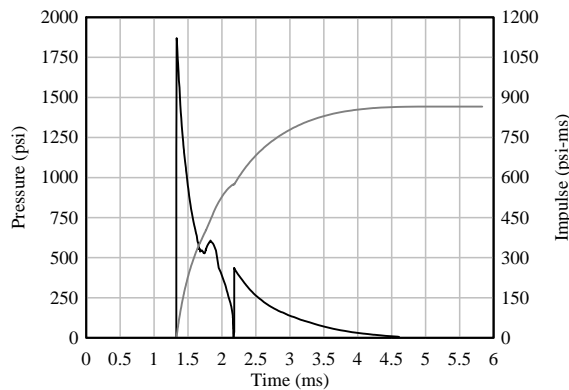
Height = 162 in
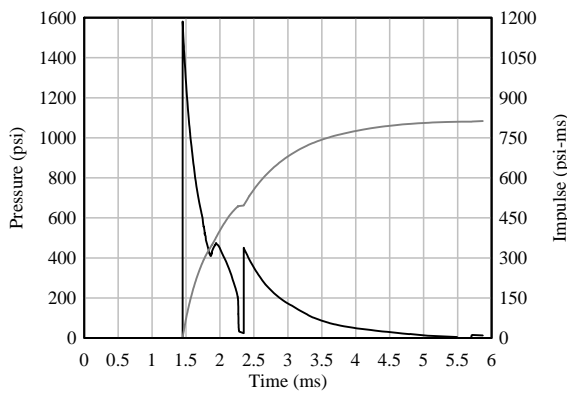
Height = 174 in
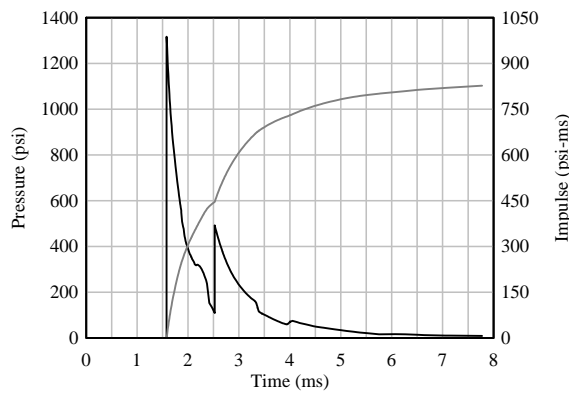
Height = 186 in
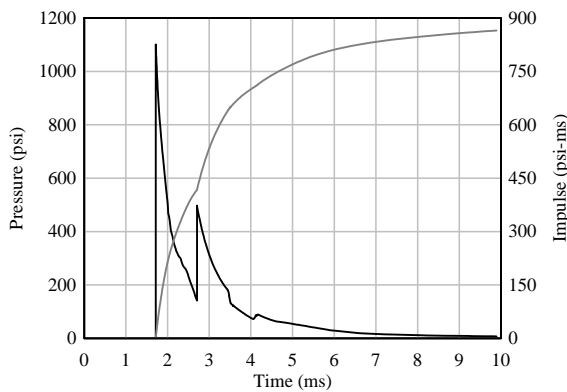
Height = 198 in

Height = 210 in

$$Z = 0.9$$

Height = 222 in

Height = 234 in

$$Z = 1.0$$

Height = 6 in

Height = 18 in

Height = 30 in

Height = 42 in

Height = 54 in

Height = 66 in
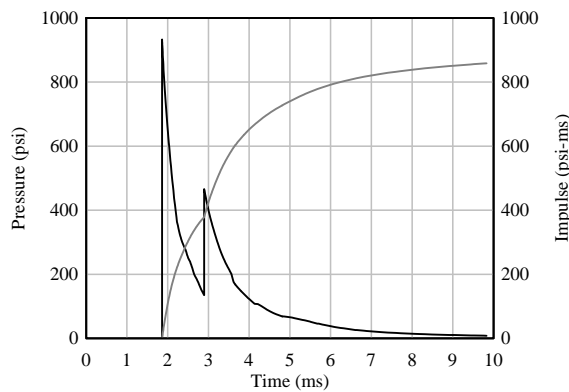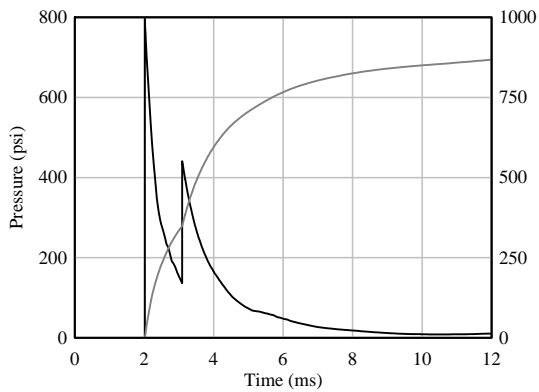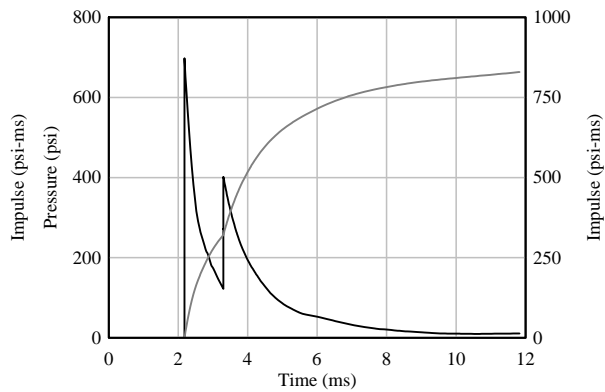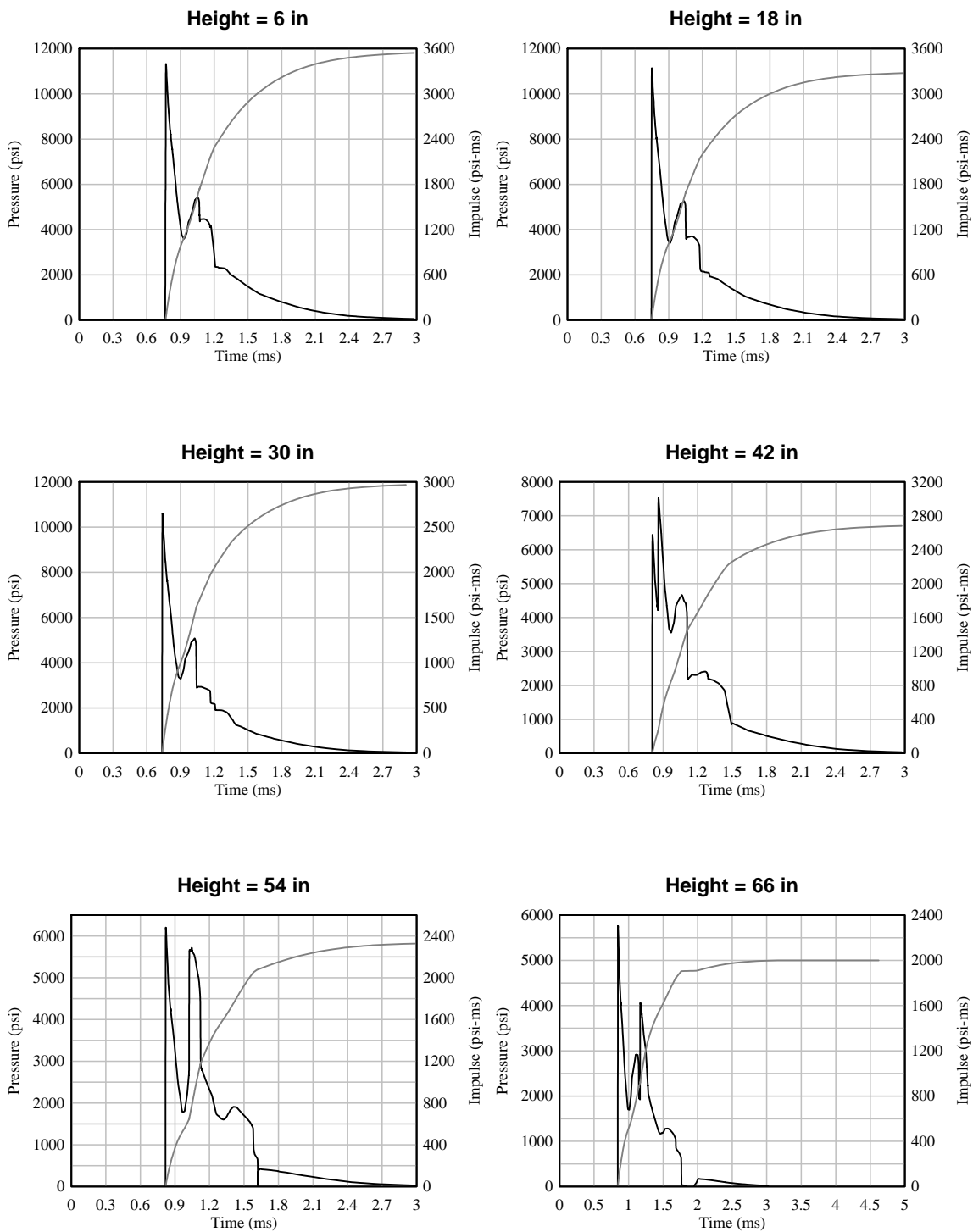
$Z = 1.0$

Height = 78 in
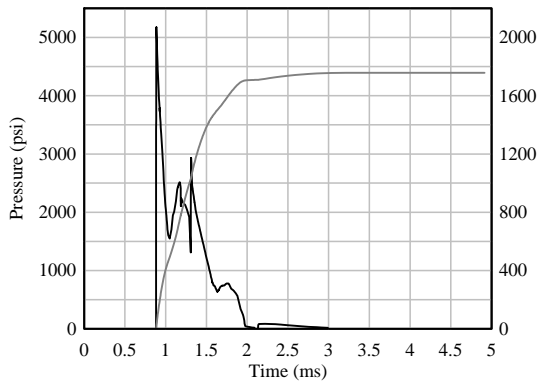
Height = 90 in
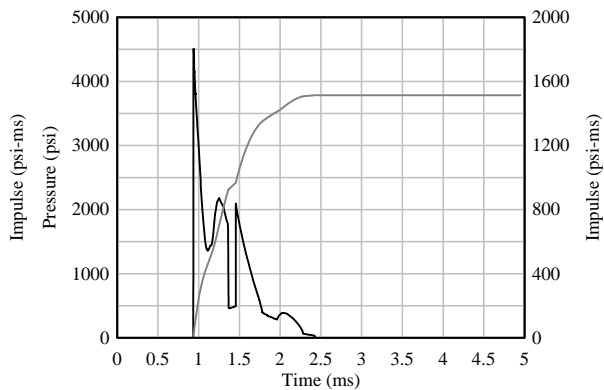
Height = 102 in
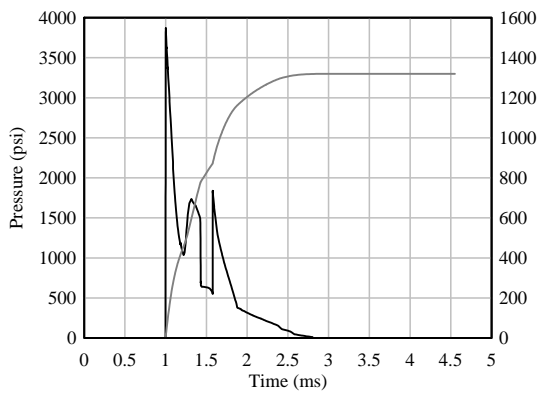
Height = 114 in
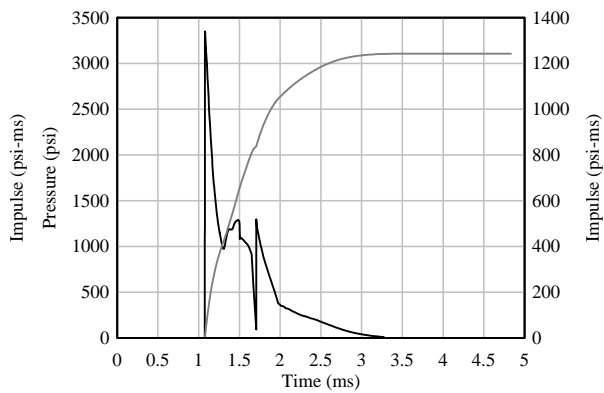
Height = 126 in
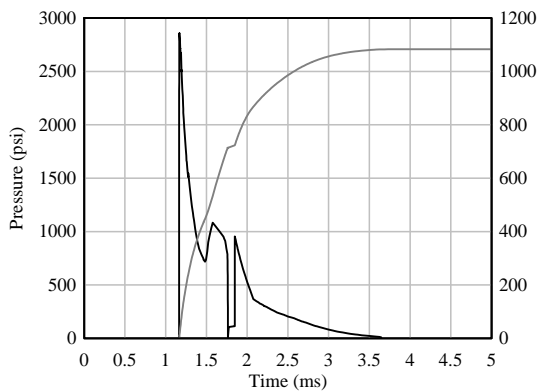
Height = 138 in
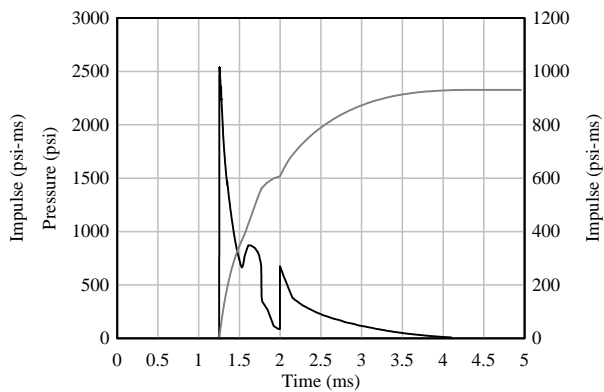
$Z = 1.0$

Height = 150 in
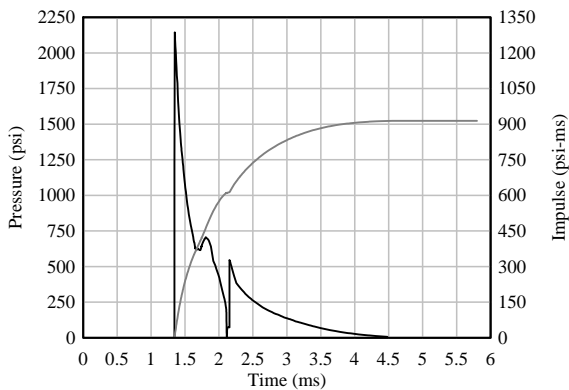
Height = 162 in
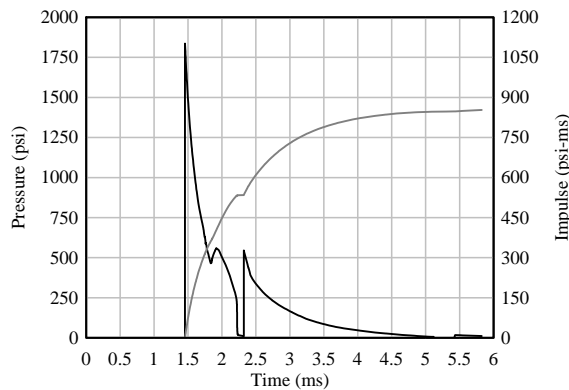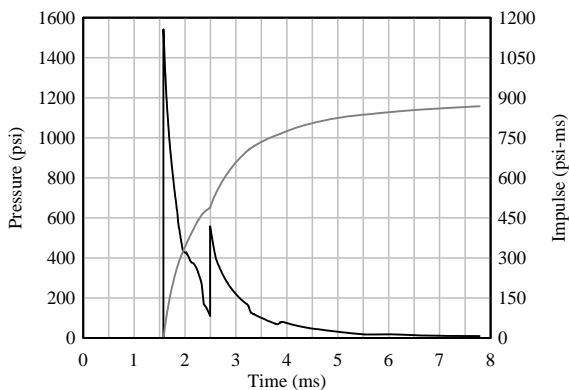
Height = 174 in
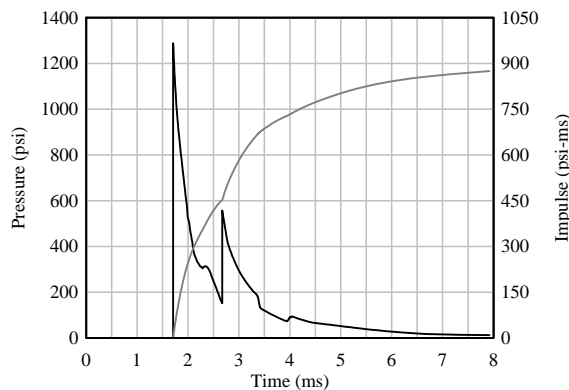
Height = 186 in
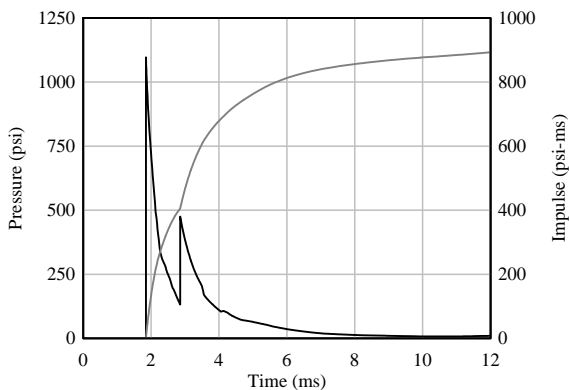
Height = 198 in

Height = 210 in

$$Z = 10\,ft$$

Height = 222 in

Height = 234 in

$Z = 1.0$

Height = 6 in

Height = 18 in

Height = 30 in

Height = 42 in

Height = 54 in

Height = 66 in

$$Z = 1.2$$

Height = 78 in

Height = 90 in

Height = 102 in

Height = 114 in

Height = 126 in

Height = 138 in

$Z = 1.2$

Height = 150 in

Height = 162 in

Height = 174 in

Height = 186 in

Height = 198 in

Height = 210 in

$$Z = 1.2$$

Height = 222 in

Height = 234 in

$$Z = 1.5$$

Height = 6 in

Height = 18 in

Height = 30 in

Height = 42 in

Height = 54 in

Height = 66 in

$$Z = 1.5$$

Height = 78 in

Height = 90 in

Height = 102 in

Height = 114 in

Height = 126 in

Height = 138 in
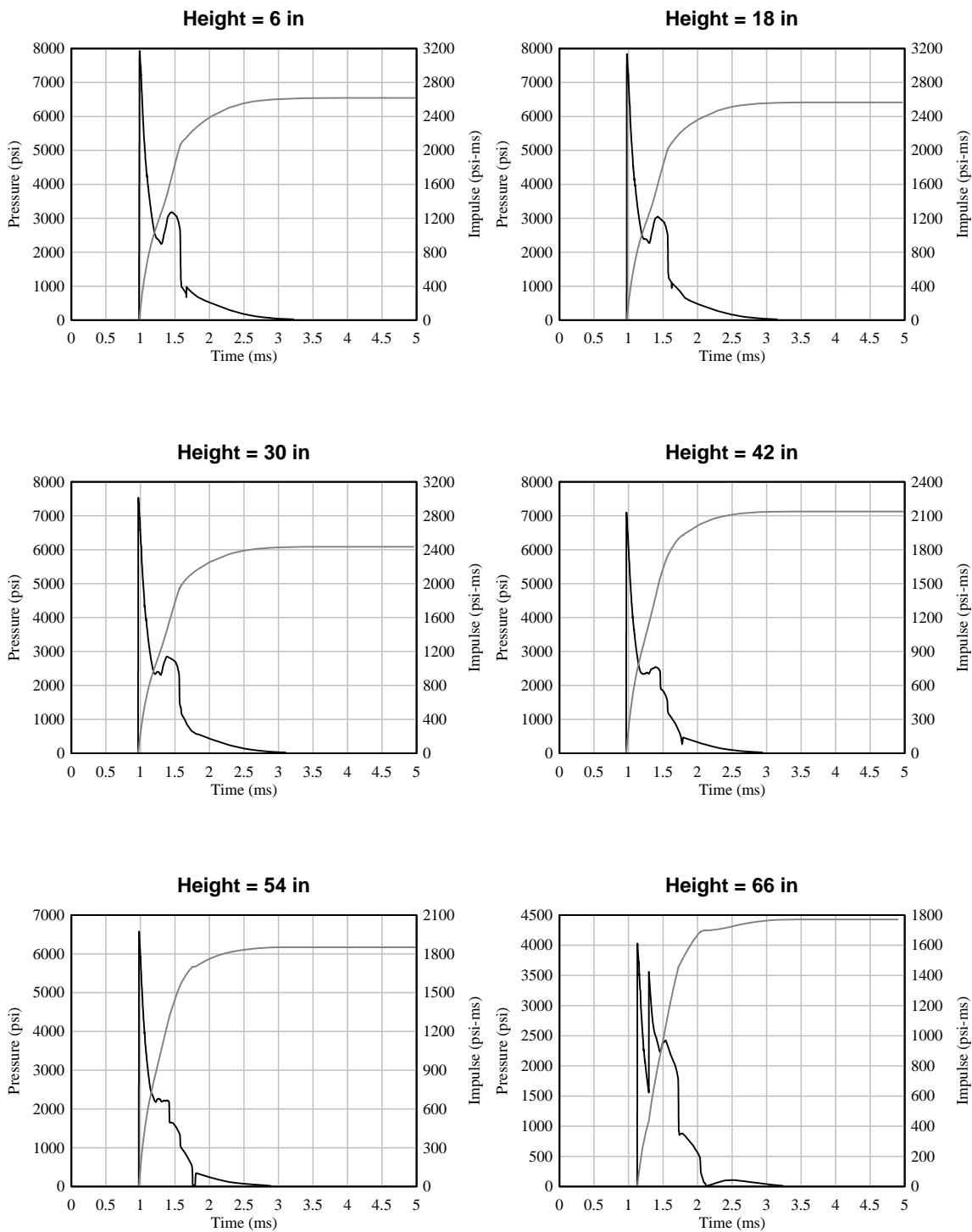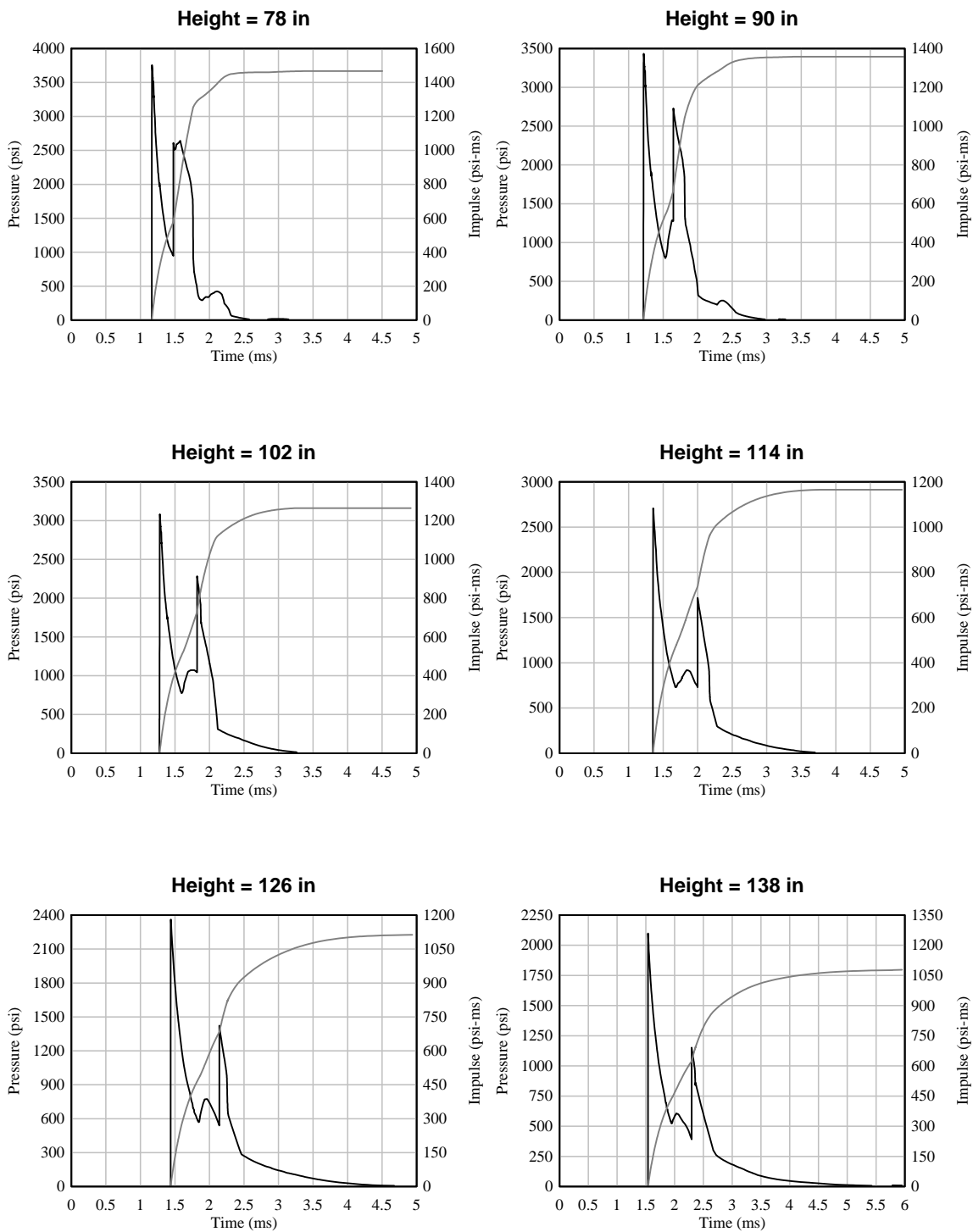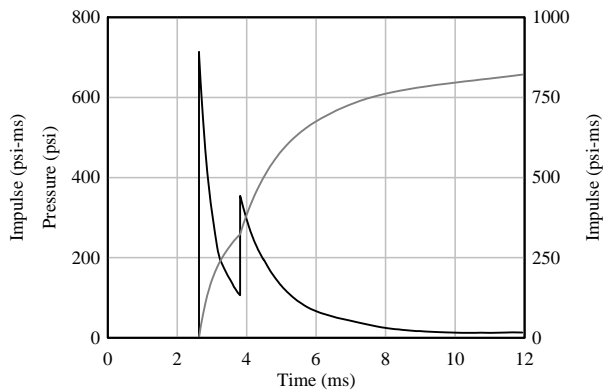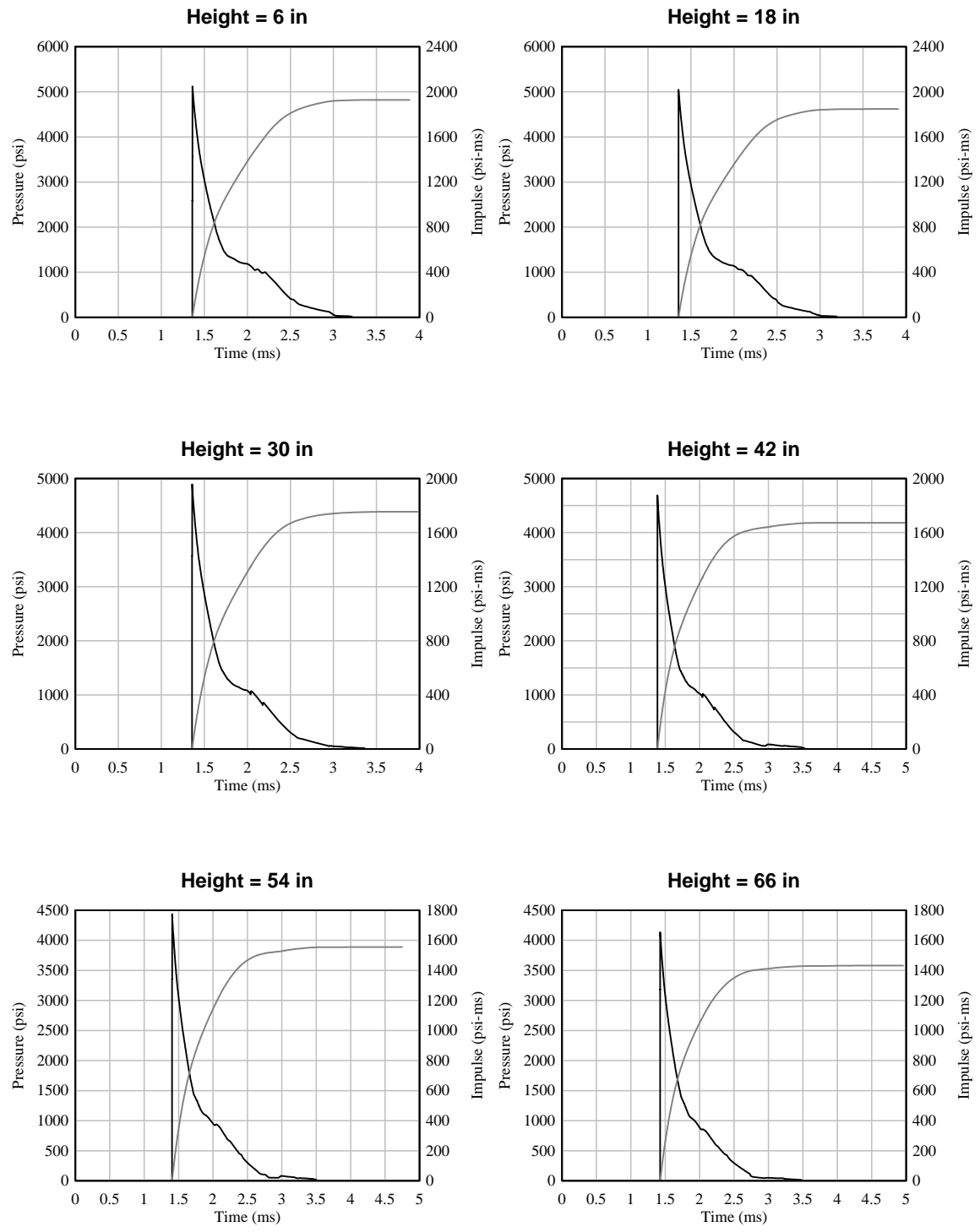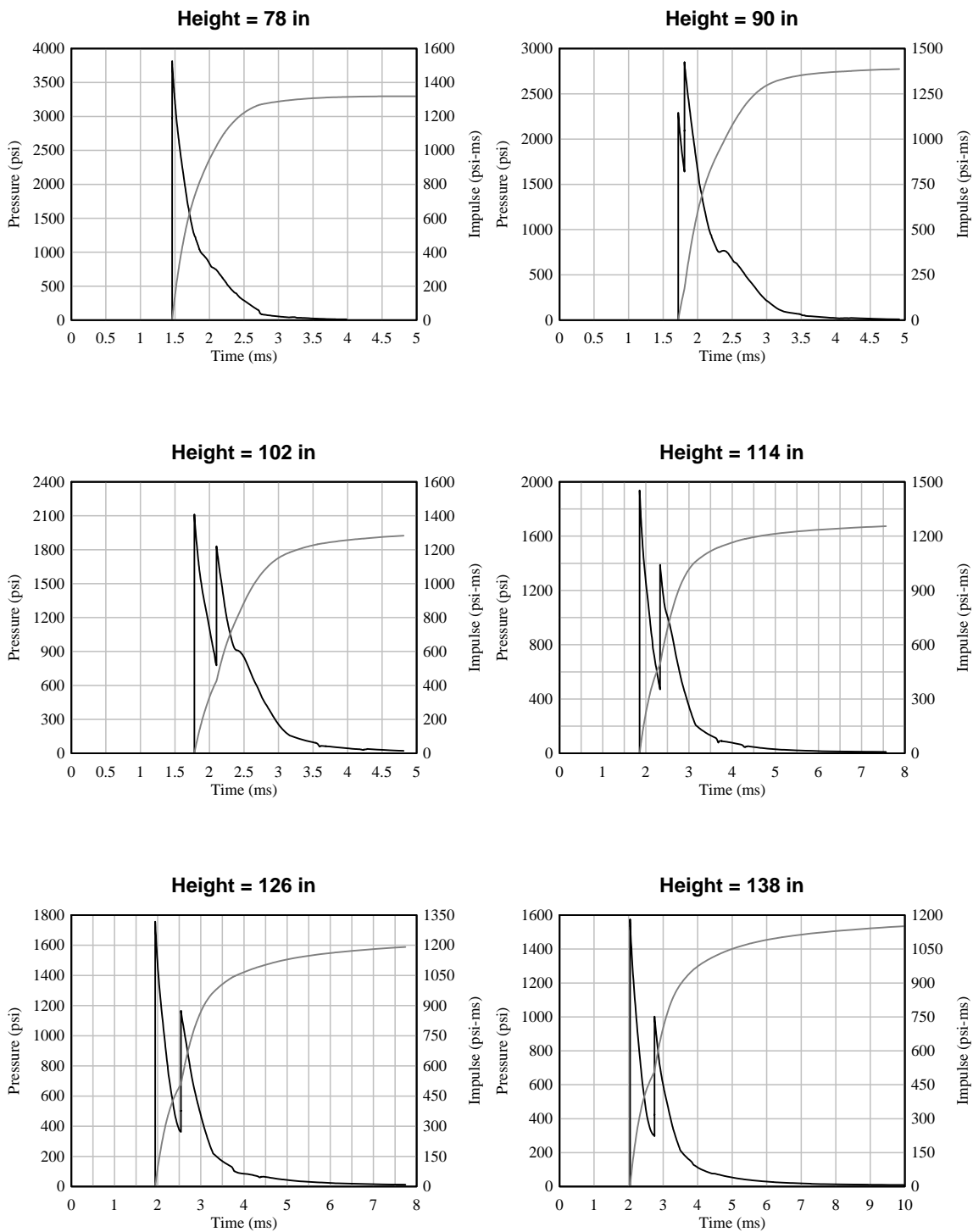
$$Z = 1.5$$
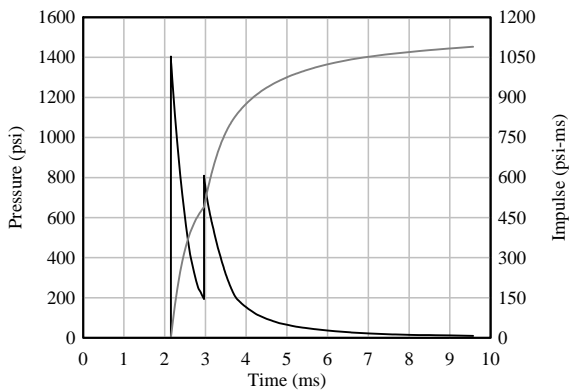
Height = 150 in
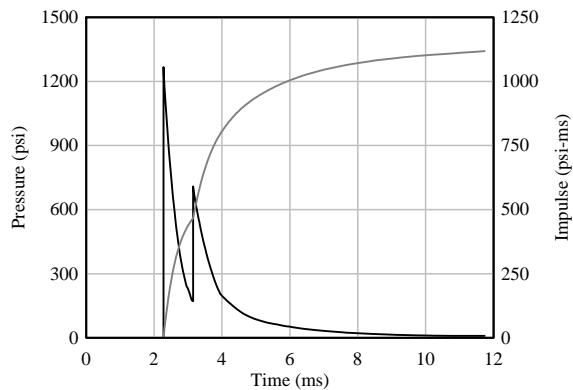
Height = 162 in
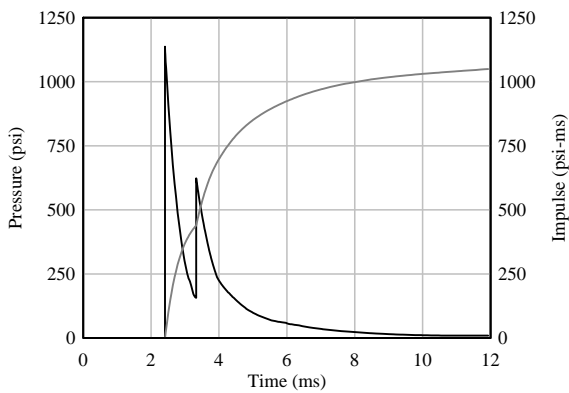
Height = 174 in
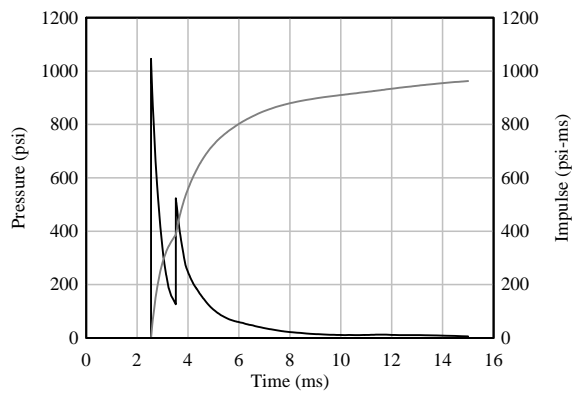
Height = 186 in
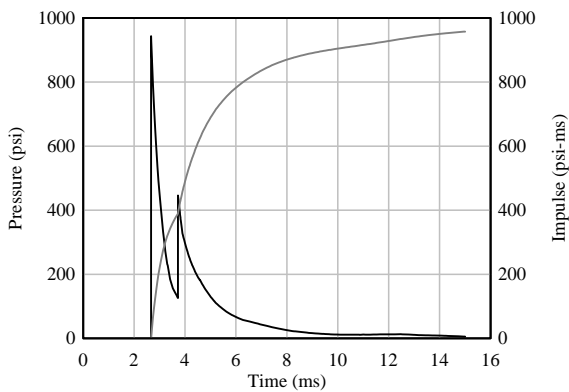
Height = 198 in

Height = 210 in

$$Z = 1.5$$

Height = 222 in

Height = 234 in

$Z = 1.8$

Height = 6 in

Height = 18 in

Height = 30 in

Height = 42 in

Height = 54 in

Height = 66 in

$$Z = 1.8$$

Height = 78 in

Height = 90 in

Height = 102 in

Height = 114 in

Height = 126 in

Height = 138 in
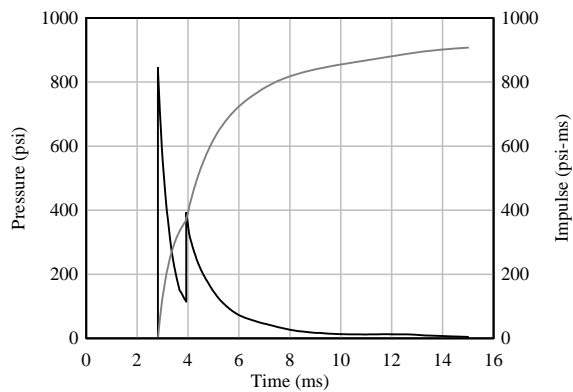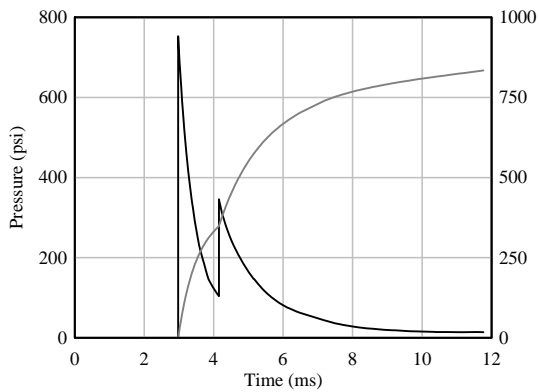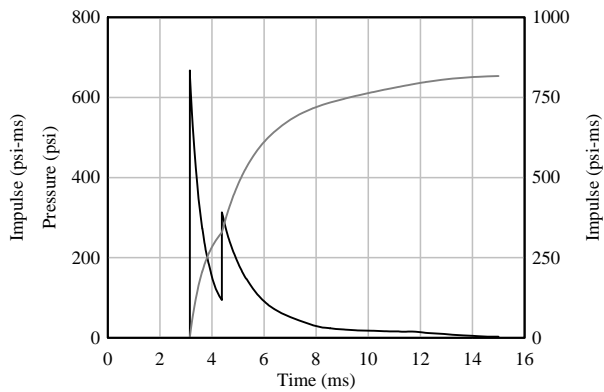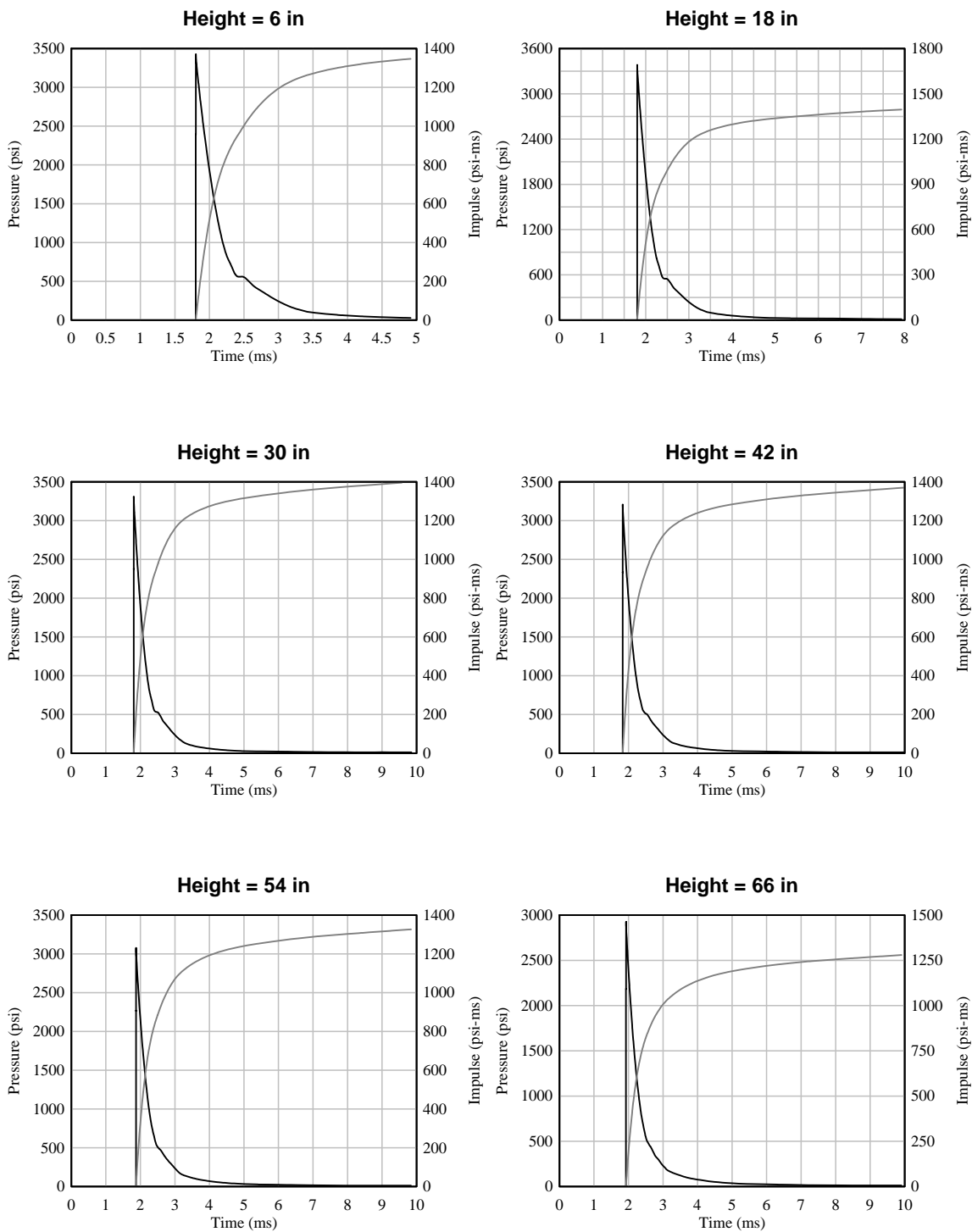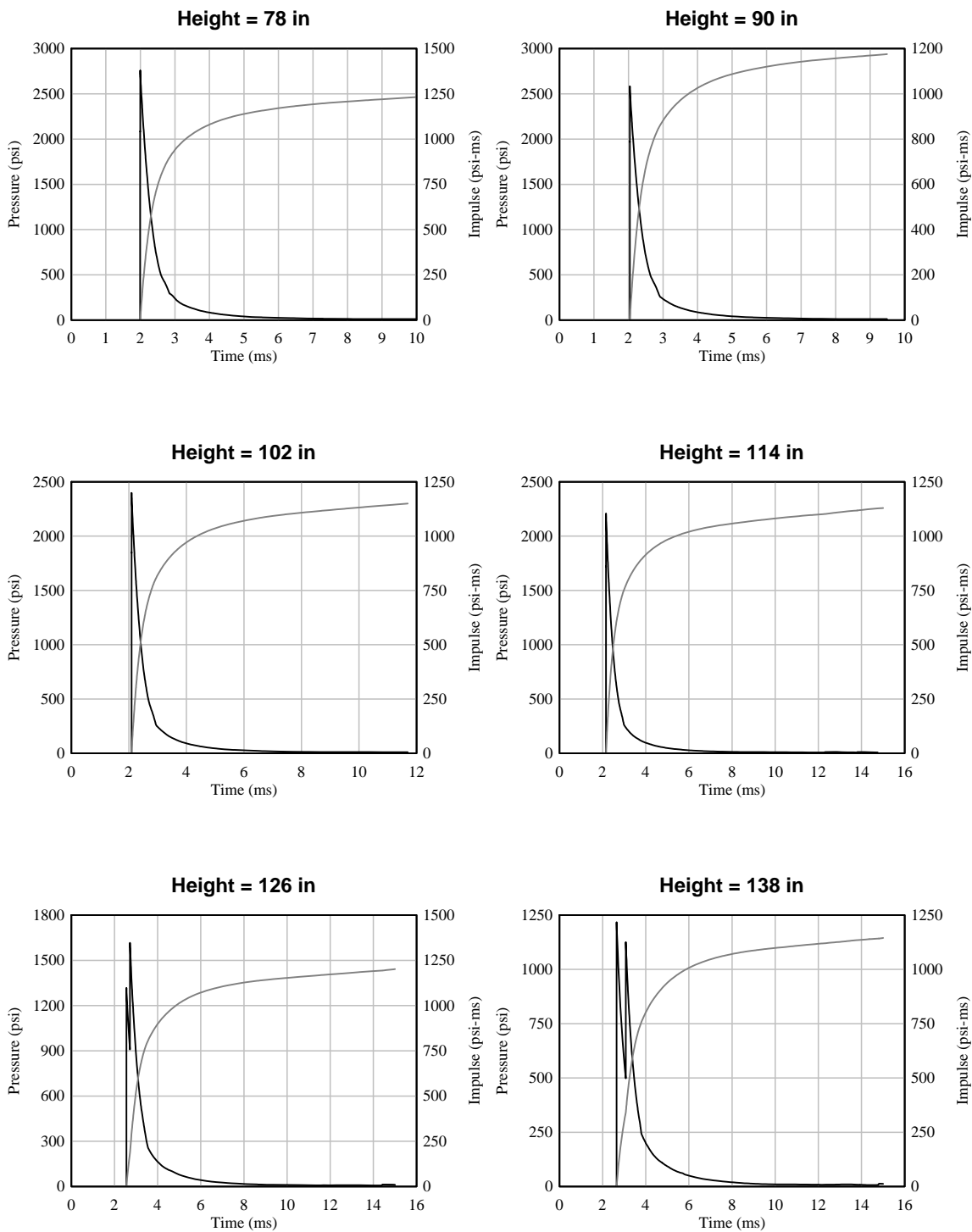
$Z = 1.8$
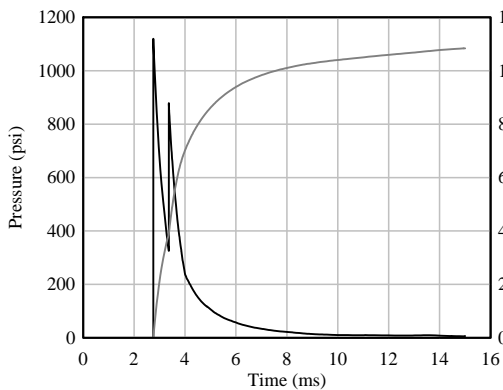
Height = 150 in
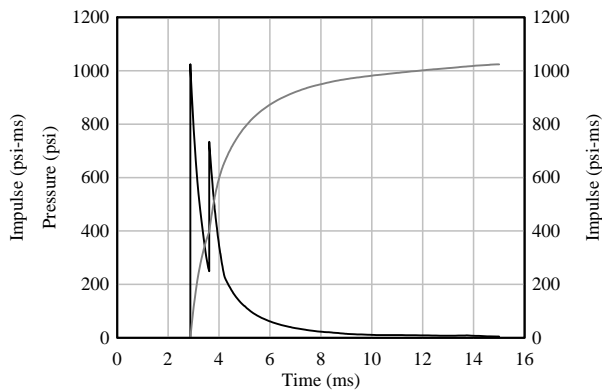
Height = 162 in
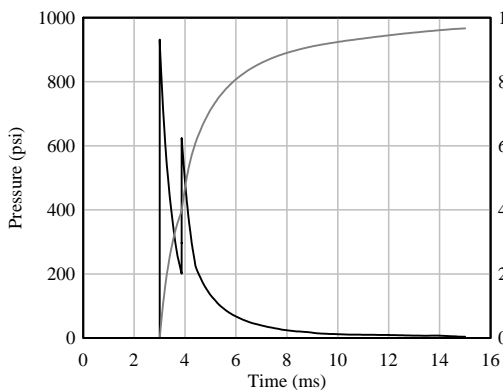
Height = 174 in
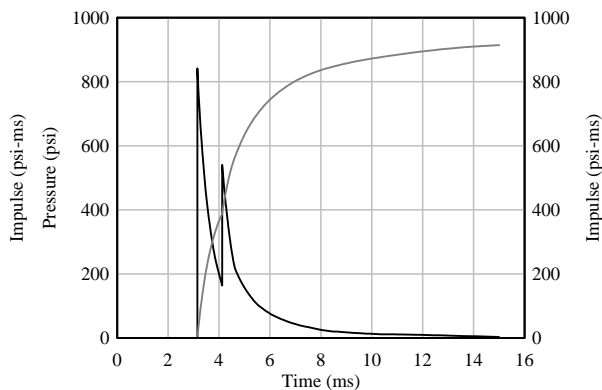
Height = 186 in
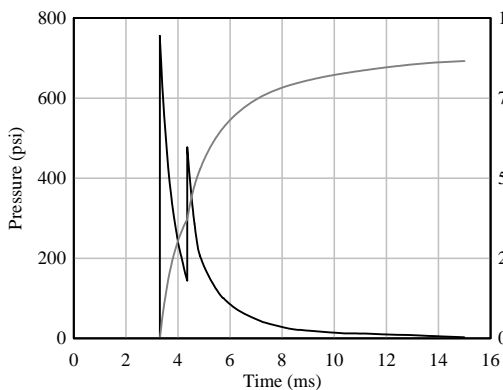
Height = 198 in

Height = 210 in

$Z = 1.8$

Height = 222 in

Height = 234 in

$Z = 2.0$

Height = 6 in

Height = 18 in

Height = 30 in

Height = 42 in

Height = 54 in

Height = 66 in

$$Z = 2.0$$

Height = 78 in

Height = 90 in

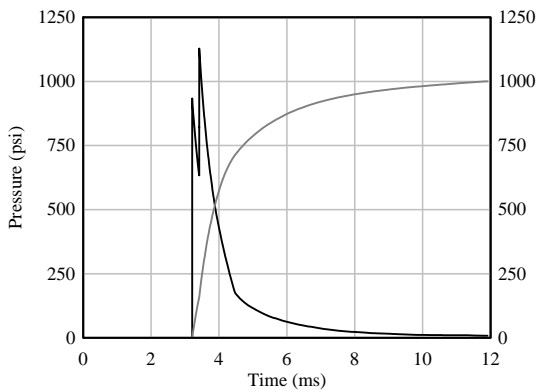**Height = 102 in**

Height = 114 in

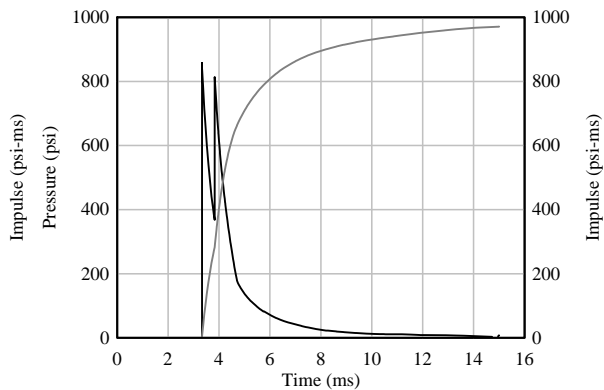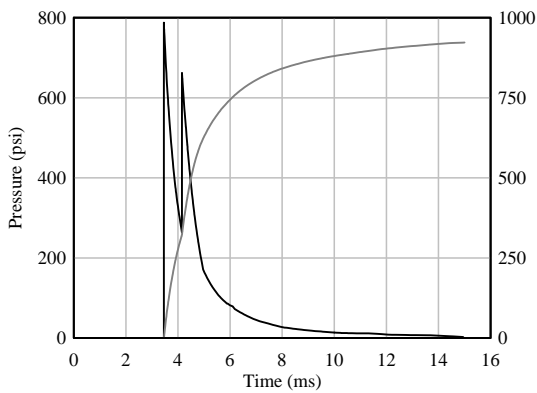**Height = 126 in**

Height = 138 in
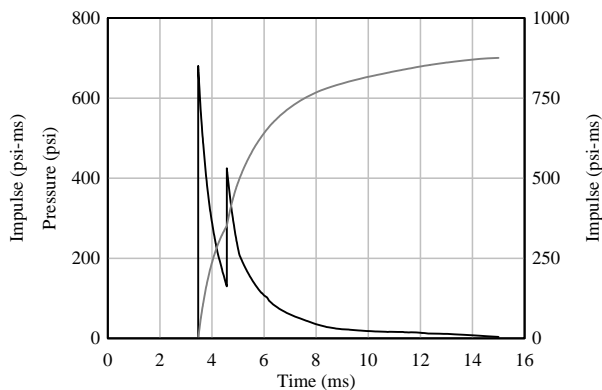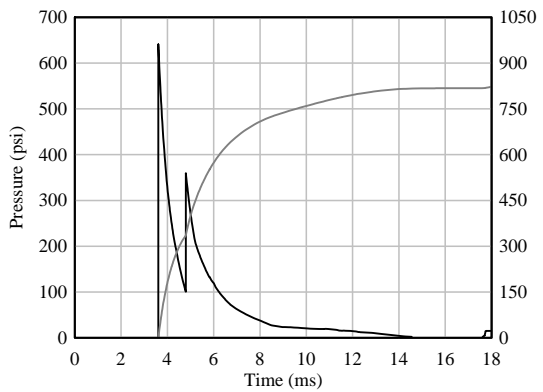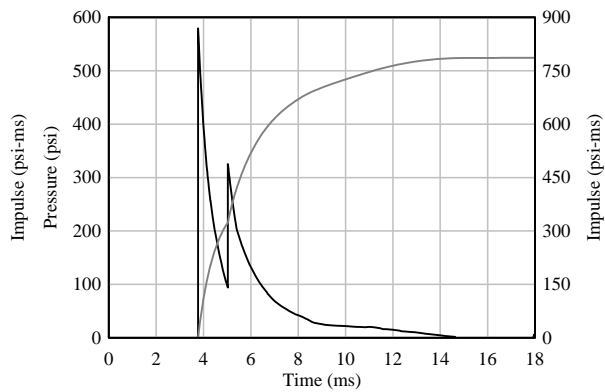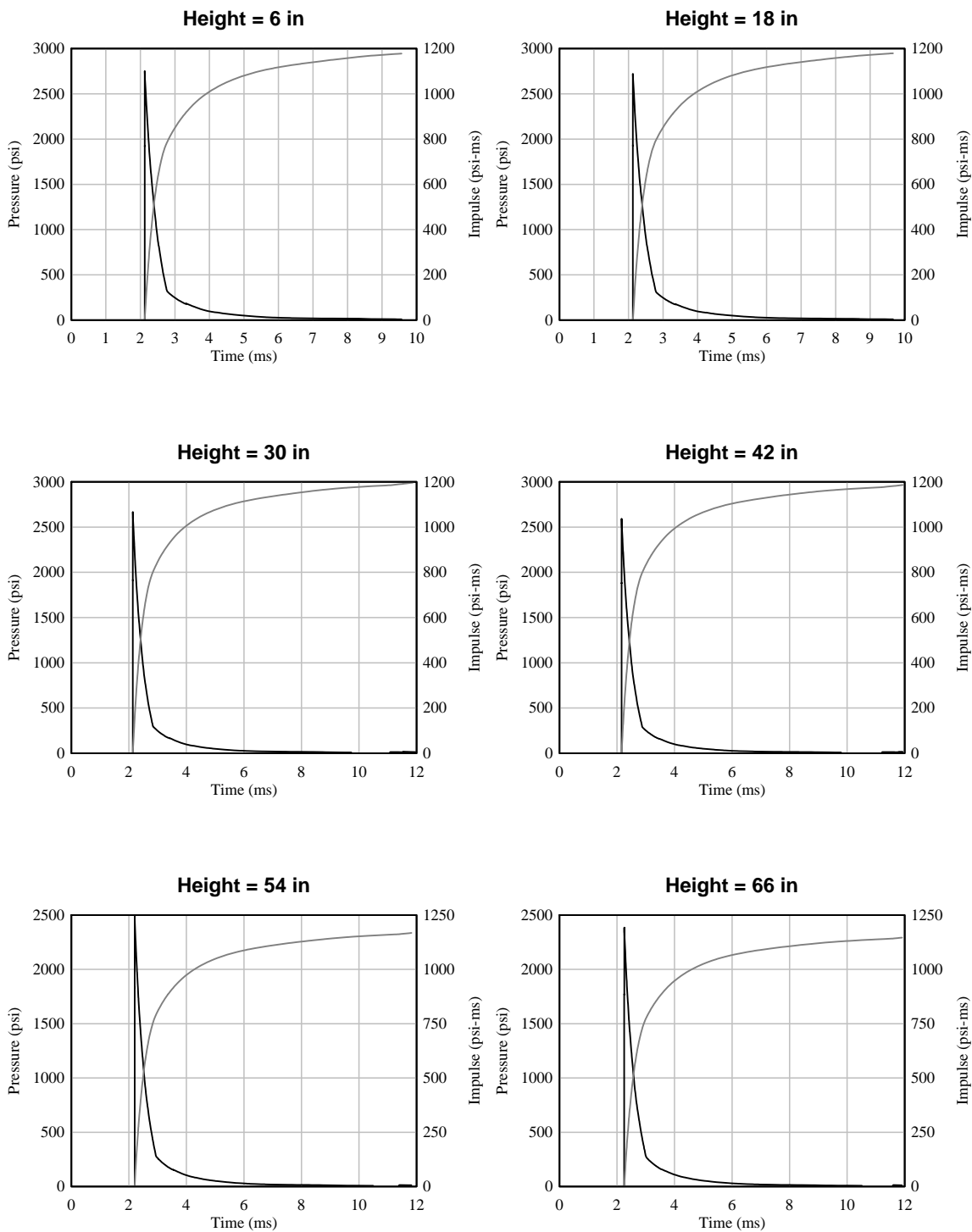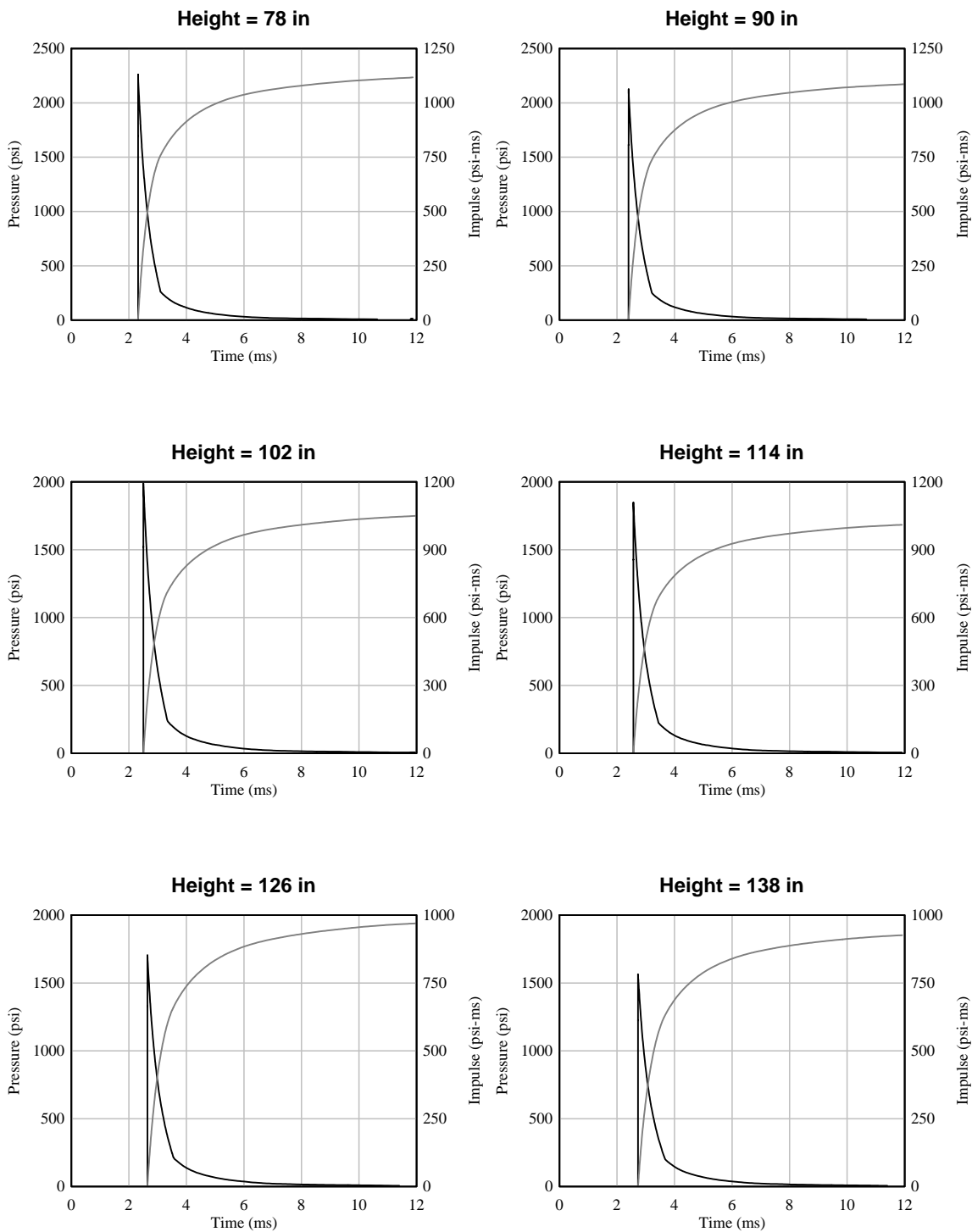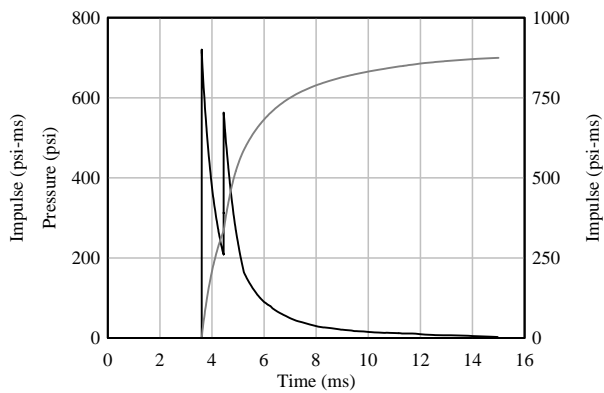
$$Z = 2.0$$

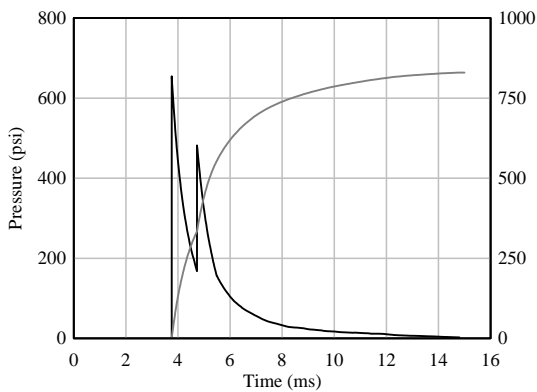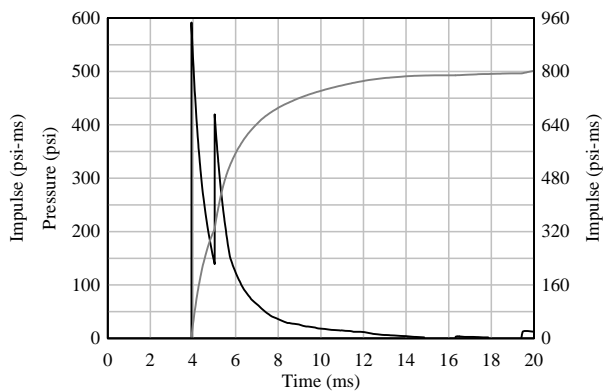**Height = 150 in**

Height = 162 in

Height = 174 in
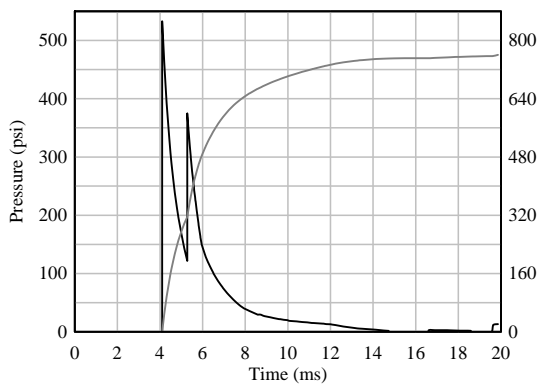

Height = 186 in

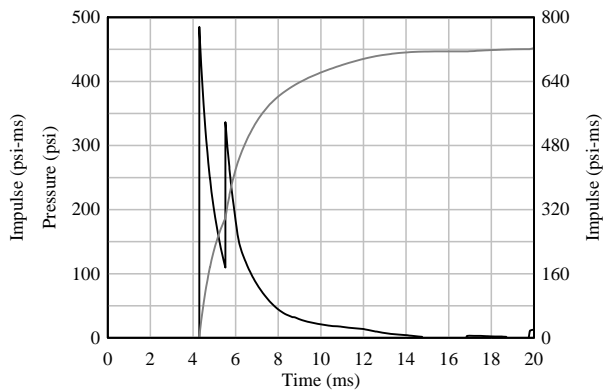**Height = 198 in**

Height = 210 in

$$Z = 2.0$$

Height = 222 in

Height = 234 in

REFERENCES

1. Mays, G.C. and Smith, P.D. (1995), *Blast Effects on Buildings: Design of Buildings to Optimize Resistance to Blast Loading*. New York. Thomas Telford.

2. Smith, P.D. and Herrington, J.G. (1994), *Blast and Ballistic Loading of Structures*. Oxford; Boston: Butterworth-Heinemann.

3. Krauthammer, T. (2006). "Modern Protective Structures: Design, Analysis and Evaluation." Course Notes.

4. Hopkinson, B. British ordinance board minutes 13565, 1915.

5. Cranz, C. *Lehrbuch der Ballistik*. Springer, Berlin, 1926.

6. TM 5-1800 (1990). "Structures to Resist the Effects of Accidental Explosions," U.S. Department of the Army.

7. Rankine, W.J.H. (1870) Phil. Trans. Roy. Soc, (160), pp 277-288.

8. Zhang, J., Maaleh, M., Quek, S.T. and Teo, Y.Y. "Drop Weight Impacts on Hybrid Fiber ECC Blast/Shelter Panels." National University of Singapore, Singapore.

9. Gardner, K.D., John, A.G., and Lu, F.K. "Development of a Shock Loading Simulation Facility." Aerodynamic Research Center. Arlington, TX.

10. Segars, R.A. and Carboni, M.G. (2008). "A Shock Tube for Downselecting Material Concepts for Blast Protection, Part1." U.S. Army Natick Soldier Research Center. Technical Report. Natick, MA.

11. Hegemier, G., Seible, F., Arnett, K., Rodriguez-Nikl, T., Oesterle, M., Wolfson, J. Gram, M. and Clark, A. (2006). "The UCSD Blast Simulator." *77th Shock and Vibration Symposium. Monterey*, CA.

12. Rodriguez-Nikl, T. (2006). "Experimental Simulations of Explosive Loading on Structural Components: Reinforced Concrete Columns with Advanced Composite Jackets." PhD Dissertation, Structural Engineering, University of California, San Diego, La Jolla.

13. Oesterle, M. (2009). "Blast Simulator Wall Tests: Experimental Methods and Mitigation Strategies for Reinforced Concrete and Concrete Masonry." PhD

Dissertation, Structural Engineering, University of California, San Diego, La Jolla.

14. von Mises, R. (1913). *Mechanick der Festen Korper im plastiscn deformablen Zustand*. Gottin. Nachr. Math. Phys. (1), pp 582-592.

15. Krieg, R.D. and Krieg, D.B., (1977). "Transactions of the ASME", *Journal of Pressure Vessel Technology*, (1), pp 510-515.

16. Livermore Software Technology Corporation (2007). *LS-DYNA Keyword Theory Manual.* Livermore, CA.

17. DiMaggio, F.L. and Sandler, I.S. (1971). "Material Model for Granular Soils." *Journal of the Engineering Mechanics Division Proceedings of the American Society of Civil Engineers*.

18. Prager, W (1959). "A Introduction to Plasticity." Reading, MA: Addison-Wesley.

19. Hughes, T.J.R. (2000), *The Finite Element Method: Linear Static and Dynamic Finite Element Analysis*. Mineola, NY: Dover Publications.

20. Courant, R. (1942). "Variational Methods for the Solution of Problems of Equilibrium and Vibrations." *Trans American Mathematics Society*, 1-23.

21. Livermore Software Technology Corporation (2007). *LS-DYNA Keyword User's Manual Version 971*. Livermore, CA.

22. Wu, S.R. and Qiu, W. (2008). "Nonlinear Transient Dynamic Analysis by Explicit Finite Elements with Iterative Consistent Mass Matrix." *Communications in Numerical Methods in Engineering*.

23. McGlaun, J.M., Thompson, S.L., Kmetyk, L.N. and Elrick, M.G. (1990). "CTH: A Three Dimensional Shock Wave Physics Code." *International Journal of Impact Engineering*. 10, (1) pp. 351-360.

24. Malvar, L. J., "Review of Static and Dynamic Properties of Steel Reinforcing Bars," *American Concrete Institute Materials Journal,* Vol. 95, No. 5, pp 609-616, September -October 1997.

25. Malvar, L.J., Crawford, J.E., Wesevich, J.W. and Simons, D. (1997). "A Plasticity Concrete Material Model for DYNA3D." *International Journal of Impact Engineering*. 19, (9-10) pp. 847-873.

26. Chen, W.F. (1982), *Plasticity in Reinforced Concrete*. New York: McGraw-Hill.

27. Sallay, J. and Gurtman, G. (2008). "Characterization of Blast Simulator Programmers." Final Report, Science Applications International Corporation.

28. Lucy, L.B. (1977). "An Numerical Approach to the Testing of the Fission Hypothesis." *Astronomy Journal*. 92 1013.

29. Gingold, R.A. and Monaghan, J.J.,(1977). "Smoothed Particle Hydrodynamics: Theory and Applications to Non-Spherical Stars." Mon. Not. R. Astr. Soc. 181, 375.

30. Randles, P.W. and Libersky, L.D. (1996). "Smoothed Particle Hydrodynamics: Some Recent Improvement and Applications." Computational Methods in Applied Mechanical Engineering. Vol 130 pp 375-408.

31. Dunn, B. (2005). "AISC Steel Materials Testing Final Report."

32. Green, M. L., "Shear Friction Test Support Program: Laboratory Test Results for WES Flume Sand Backfill", US Army Waterways Experiment Station Structures Laboratory Vicksburg, Mississippi, September 1984.

33. Kaufman, E.J. and Fisher, J.W. (2001). "The Effect of Straightening Method on the k Area Loading Behavior of Rolled Column Sections." Final Report to American Institute of Steel Construction. Bethlehem, PA.

34. Britt, J.R. (1992). "Enhancements of the BLASTX Code for Blast and Thermal Propagation in Protective Structures: BLASTX Version 2.0." U.S. Army Engineer Waterways Experiment Station.

35. Chopra, A.K. (2001), *Dynamics of Structures: Theory and Applications to Earthquake Engineering*. 2nd ed. Prentice-Hall International Series in Civil Engineering and Engineering Mechanics. Upper Saddle River, NJ: Prentice Hall.

36. Anderson, J. (1995). *An Introduction to Neural Networks*: The MIT Press, Cambridge, MA.

37. Fausett, L. (1994). Fundamentals of Neural Networks. New York: Prentice Hall.

38. Levenberg, K. (1944). "A Method for the Solution of Certain Non-linear Problems in Least Squares." *The Quarterly of Applied Mathematics*. Vol 2. pp 164-168.

39. Roweis, S. "Levenberg-Mardquardt Optimization." *Numerical Recipes in C*, 2nd Edition, pp 683-685.

40. Demuth, H., Beale, M., and Hagan, M. "Matlab Neural Network Toolbox User's Guide." The MathWorks Inc. Natick, MA

41. Ballantyne, G., Whittaker, A., Dargush, G., and Aref, A. (2010). "Air-Blast Effects on Structural Shapes of Finite Width." *Journal of Structural Engineering*. Vol 136, No 2.